

UNCLASSIFIED

SECURITY CLASSIFICATION OF THIS PAGE

AD-A261 366

2

REPORT DC

1a. REPORT SECURITY CLASSIFICATION
Unclassified

2a. SECURITY CLASSIFICATION

DTIC

ELECTE

S MAR 9 1993

2b. DECLASSIFICATION/DOWNGRADING SCHEDULE

4. PERFORMING ORGANIZATION REPORT NUMBER(S)

6a. NAME OF PERFORMING ORGANIZATION
Department of Aeronautics
and Astronautics6b. OFFICE SYMBOL
(If applicable)

31-264

6c. ADDRESS (City, State, and ZIP Code)

77 Massachusetts Ave.
Cambridge, MA 021398a. NAME OF FUNDING/SPONSORING
ORGANIZATION

AFOSR

8b. OFFICE SYMBOL
(If applicable)

NA

8c. ADDRESS (City, State, and ZIP Code)

AFOSR,
Building 410
Bolling AFB, DC 20332-6448

11. TITLE (Include Security Classification)

Active Stabilization of Aeromechanical Systems

12. PERSONAL AUTHOR(S)

J. Dugundji, A.H. Epstein, E.M. Greitzer, G.R. Guenette, L. Malavani

13a. TYPE OF REPORT

Final Technical

13b. TIME COVERED

FROM 11/1/89 to 10/31/91

14. DATE OF REPORT (Year, Month, Day)

1/5/93

15. PAGE COUNT

220

16. SUPPLEMENTARY NOTATION

17. COSATI CODES		
FIELD	GROUP	SUB-GROUP

18. SUBJECT TERMS (Continue on reverse if necessary and identify by block number)

Active Control Compression System Flow Instabilities
Unsteady Flow, Fluid-Structure Interaction

19. ABSTRACT (Continue on reverse if necessary and identify by block number)

This report details the work on the active control of surge and stall in gas turbine engines. The use of small amplitude waves predicted by theory as stall precursors were tested with experimental data. The nonlinear behavior of such waves was shown to explain much of the data in the literature. This theory was used to design an active stabilization system for rotating stall which was tested on both a single-stage and a three-stage axial compressor, increasing the stable operating range of the single-stage compressor by 25%. The dynamics of the three-stage compressor were shown to match closely with theory. The open-loop forced response characteristics of the compressors were measured and methodology developed in which this data was used to design the compressor control system. The models then developed were used to evaluate alternate control strategies. Engineering of the structural dynamics of the compression system was also shown to be successful in damping rotating stall and surge.

20. DISTRIBUTION/AVAILABILITY OF REPORT

UNCLASSIFIED/UNLIMITED

 SAME AS RPT. DTIC USERS

22a. NAME OF RESPONSIBLE INDIVIDUAL

MAJ. D. FANT

DD FORM 1473, 84 MAR

22b. TELEPHONE (Include Area Code) 22c. OFFICE SYMBOL

202-767-0471

SECURITY CLASSIFICATION OF THIS PAGE

83 APR edition may be used until exhausted.
All other editions are obsolete.

UNCLASSIFIED

Gas Turbine Laboratory
Department of Aeronautics and Astronautics
Massachusetts Institute of Technology
Cambridge, MA 02139

Final Technical Report on Grant AFOSR-90-0059

entitled

Accession for	
NTIS	CRA&I
DTIC	TAB
Unclassified	
Justification	
By	
Distribution/	
Availability Codes	
Dist	Avail and/or Special
A-1	

ACTIVE STABILIZATION OF AEROMECHANICAL SYSTEMS

submitted to

Air Force Office of Scientific Research
Building 410
Bolling AFB, DC 20332-6448

ATTN: Major Daniel Fant
Aerospace Sciences

PRINCIPAL
INVESTIGATORS: Alan H. Epstein
Professor and Associate Director, Gas Turbine Laboratory

Edward M. Greitzer
Professor and Director, Gas Turbine Laboratory

CONTRIBUTORS: John Dugundji
Vincent H. Garnier
Gerald R. Guenette
Daniel L. Gysling
Joel M. Haynes
Gavin J. Hendricks
John P. Longley
James D. Paduano
Jon S. Simon
Lena Valavani

93 3 8 056

PERIOD OF
INVESTIGATION: November 1, 1989 - October 31, 1992

January 1993

93-04944



TABLE OF CONTENTS

- I. Summary
- II. Rotating Stall Inception
 - 1. Rotating Waves as a Stall Inception Indication in Axial Compressors
 - 2. Modeling Axial Compressor Nonlinear Rotating Stall Phenomena for Control
- III. Active Control of Rotating Stall Experiments
 - 1. Active Control of Rotating Stall in a Low Speed Axial Compressor
 - 2. Active Stabilization of Rotating Stall in a Three-Stage Axial Compressor
- IV. Modelling for Control and System Identification
 - 1. Modeling for Control of Rotating Stall
 - 2. Parameter Identification of Compressor Dynamics During Closed-Loop Operation
- V. Evaluation of Alternate Control Approaches
 - 1. Evaluation of Approaches to Active Compressor Surge Stabilization
 - 2. A Theoretical Study of Sensor-Actuator Schemes for Rotating Stall Control
- VI. Control of Surge and Stall With Structural Dynamics
 - 1. Dynamic Control of Centrifugal Compressor Surge Using Tailored Structures
 - 2. Dynamic Control of Rotating Stall in Axial Compressors Using Aeromechanical Feedback

I. SUMMARY

The active stabilization of rotating stall and surge has been studied with the aim of increasing the stable operating range of aircraft engine compression systems and thereby realizing improved performance and decreased weight. The work during this contract has progressed from theoretical speculation, through experimental investigation, development of control procedures, large scale demonstration, and the evaluation of alternate control approaches.

The initial efforts centered on establishment of the mechanisms by which axial compressors enter rotating stall. In particular, the linear 2-D stability theory of Moore and Greitzer was shown to match well with data from low speed axial compressors measured at MIT and high speed data provided by an engine company. It was realized that the compressor stability could be thought of in terms of an oscillator (second order system) rotating about the compressor annulus. Disturbances would manifest themselves as small amplitude waves travelling about the compressor annulus with the mature form of the waves being rotating stall. Thus, the compressor stability would be equivalent to the wave stability, which is exactly what was found experimentally. The linear assumptions of the model (used for mathematical simplicity) were then relaxed and the nonlinear form was shown to explain the differences observed in the stall inception process in different compressors described in the literature.

Using the Moore-Greitzer hydrodynamic stability theory as a starting point, a rotating stall control system was designed for a single-stage, low speed research compressor. The low amplitude circumferential travelling waves were sensed by a computer which then "wiggled" a circumferential array of individually actuated vanes so as to damp the travelling waves, thereby increasing the stability of the compressor. The small amplitude (linearity) of the waves was exploited by breaking the waves into spatial Fourier components, and controlling each spatial Fourier component separately. This approach succeeded in extending the flow range of the compressor by 25%. This was the first time that compressor rotating stall was successfully stabilized.

This control approach was then extended to a three-stage research compressor. The data

from this experiment was used to refine the Moore-Greitzer stability theory, in particular to include the effect of time lags within the compressor. The modified theory was shown to quantitatively agree well with the experimental stability data including prediction of the onset of instability (i.e. predicting when the compressor will go into rotating stall).

The above-described experiments were greatly aided by the development of control theoretic models of the compressor and the application of parameter identification methodology to compressor fluid mechanics. Specifically, state-space models of the compressor stability were formulated which proved very accurate, contributing in no small way to experimental gains realized. The high speed actuators were used to excite the compressor open loop and thereby established the forced response characteristic of the system. The measured system characteristics were shown to closely match those calculated from the modified hydrodynamic stability model. Given the system characteristics (either measured or calculated) and the control model framework, then the controller design could be carried out in a straightforward and systematic manner. The experimental controlled compressor performance was then shown to match well with that predicted by the control design.

Since the theoretical models of the controlled compressor were shown to agree well with data, the model could be used to explore alternate strategies for the active stabilization of compressors. Variables studied included the selection and placement of actuators and sensors, the effects of control bandwidth constraints, and the role played by the disturbance structure exciting the compression systems. Both surge and stall control were examined. In all cases, mass flow was the most effective variable to be sensed. For surge, actuators mostly closely coupled to the compressor worked best such as a close-coupled valve or mass injection at the inlet. For rotating stall, a peripheral array of jets at the compressor inlet, injecting both mass and momentum, proved the most effective, extending the stable operating range of the compressor by a factor of four over that demonstrated on the three-stage compressor equipped with wiggly guide vanes as actuators. These calculations highlighted the importance of adequate control system bandwidth, showing that the actuators must respond at least three times faster than the system characteristic frequency (the

engine Helmholtz frequency for surge, the wave rotation rate for stall). These bandwidths are extremely challenging for the current actuator state of the art.

Understanding surge and rotating stall in the context of a second order system instability is a powerful concept which enables new approaches to these old problems. One such approach is to damp the perturbations in this fluid oscillator by coupling it to a structural oscillator with suitable dynamic characteristics. This is analogous to the tuned pendulum damper concept employed on WWII aircraft piston engines. Surge control was studied first and several concepts were analytically evaluated, including moving walls, throttle valves, and Helmholtz resonators. A moving plenum wall concept was implemented experimentally, with the wall engineered to have the proper dynamic characteristics (frequency, damping, phase shift, etc.) as predicted by linear theory. A nonlinear simulation was also performed to evaluate such phenomena as friction. The moving wall structural damper worked quite well and proved as effective as active control in extending the surge-free operating range of the centrifugal compressor on which it was tested. The experimental results agreed well with the theoretical predictions.

This approach of using tailored structural dynamics to damp fluid mechanic instabilities has been extended to two-dimensional disturbances – rotating stall. Several concepts were evaluated analytically. Then, a single-stage research compressor was outfitted with a peripheral array of jets on the outer annulus wall, upstream of the rotor. The jets are controlled by composite reed valves actuated by local pressure perturbations. The structural dynamics of the valves are such that jet amplitude and phase shift are those needed to damp the incipient rotating stall. Although the experiments are still in the preliminary phase, initial results are quite promising, showing a 7% increase in the compressor stable operating range due to the dynamic behavior of the structurally controlled jets.

The active stabilization of compressors has progressed quite far over the course of the work described herein. There are still challenges ahead, both in the basic research and applied areas.

II. ROTATING STALL INCEPTION

J. H. Garnier

A. H. Epstein

E. M. Greitzer

Gas Turbine Laboratory,
Massachusetts Institute of Technology,
Cambridge, MA 02139

Rotating Waves as a Stall Inception Indication in Axial Compressors

Stall inception has been studied in two low-speed compressors (a single-stage and a three-stage) and in a high-speed three-stage compressor, using temporally and spatially resolved measurements. In all three machines, rotating stall was preceded by a period in which small-amplitude waves were observed traveling around the circumference of the machine at a speed slightly less than the fully developed rotating stall cell speed. The waves evolved smoothly into rotating stall without sharp changes in phase or amplitude, implying that, in the machines tested, the prestall waves and the fully developed rotating stall are two stages of the same phenomenon. The growth rate of these disturbances was in accord with that predicted by current analytical models. The prestall waves were observed both with uniform and with distorted inflow, but were most readily discerned with uniform inflow. Engineering uses and limitations of these waves are discussed.

Introduction

Axial compressors are subject to two distinct aerodynamic instabilities, rotating stall and surge, which can severely limit compressor performance. Rotating stall is characterized by a wave traveling about the circumference of the machine, surge by a basically one-dimensional fluctuation in mass flow through the machine. Whether these phenomena are viewed as distinct (rotating stall is local to the blade rows and dependent only on the compressor, while surge involves the entire pumping system: compressor, ducting, plenums, and throttle) or as related (both are eigenmodes of the compression system with surge being the zeroth order mode), they cannot be tolerated during compressor operation. Both rotating stall and surge reduce the pressure rise in the machine, cause rapid heating of the blades, and can induce severe mechanical distress.

The instabilities are commonly avoided by operating the compressor at a reduced pressure rise so as to leave a safety margin, the so-called "surge margin," between the operating point of the compressor and the point at which the machine surges. The requirement for surge margin reduces the available operating pressure rise from a given machine and often reduces the operating efficiency as well. Reduction of surge margin can then translate directly into compressor weight and efficiency improvement so that there is practical incentive to reducing the surge margin required. In the high-speed compressors common to aircraft engines, rotating stall and surge are closely coupled. As the machine moves along a constant speed operating line toward lower mass flow (Fig. 1), it generally first encounters rotating stall, which then (loosely)

"triggers" the surge, often after only one or two rotor revolutions. Thus, surge and stall must both be considered; the compressor surge line could really be considered the rotating stall line, and the surge margin as stall margin.

We are aware of several alternate approaches under investigation for reducing the stall margin required. They can be considered to fall into one of two categories: those based on moving the operating point close to the stall line in situations

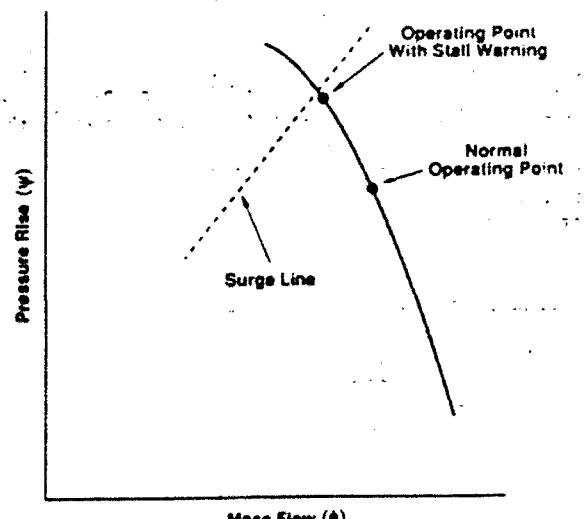


Fig. 1 Compressor performance is characterized by the constant speed line shown (solid line); the compressor cannot be safely operated to the left of the surge line

Contributed by the International Gas Turbine Institute and presented at the 35th International Gas Turbine and Aeroengine Congress and Exposition, Brussels, Belgium, June 11-14, 1990. Manuscript received by the International Gas Turbine Institute, February 7, 1990. Paper No. 90-GT-156.

when surge and stall do not threaten, and those based on moving the surge line itself and thus increasing the stable range of the compressor. Efforts in the former category include: (a) a real-time assessment of the stall margin by correlation of the instantaneous aircraft flight parameters with the measured compressor stall behavior; and (b) stall avoidance in which the control system detects rotating stall and then quickly moves the compressor operating point away from stall.

Dynamic compressor stabilization is based on an alternate approach. Here, the stall point is moved to lower mass flows by active feedback control. This scheme, and stall avoidance also, rely on the use of real-time measurements within the compressor to assess the machine stability. Clearly, the earlier a control system can detect a stall or even an incipient stall, the more effective (and less demanding) the control becomes.

This paper describes an experimental study of the rotating stall inception and growth process in three axial compressors. Its goals were both to illuminate the manner in which stall cells are born and develop, as well as to establish, as suggested by theory, whether real-time information can be extracted from the compressor, which would warn of an impending stall before the stall actually developed. This stall warning or "precursor" could have significant practical benefit if the warning is sufficiently in advance of the stall so as to permit time for control system response. The longer the warning, the greater the potential utility.

In the following sections, we review the relevant theoretical background on rotating stall development, describe the experimental arrangement, present data for three compressors under a variety of operating conditions, and finally comment on the generality of these findings and their usefulness.

Background

A large amount of experimental data taken over the last 20 years shows that, if measured at a single point in the compressor, rotating stall is seen as a sudden event with a growth period on the order of the stall cell period. Stall detection schemes based on this sort of measurement have thus not been successful in providing appreciable warning time. During the same period, however, a theoretical basis for the description of rotating stall has arisen based on the understanding of rotating stall as one class of the natural instabilities of the compression system. At its current state of development (e.g., Moore and Greitzer, 1986), the model describes the time evolution of surge and rotating stall in a compressor treated mathematically as a two-dimensional incompressible device (i.e., large hub-to-tip ratio), with three-dimensional phenomena represented only through empirical inputs. The results of a prediction by this model for a representative three-stage compressor (Fig. 2) show an instability evolving as a small-amplitude wave in axial velocity, which grows as it travels around the circumference of the compressor until, through nonlinear interaction, it causes a large-amplitude disturbance in annulus average axial velocity (surge). This type of model provides the background for the present work.

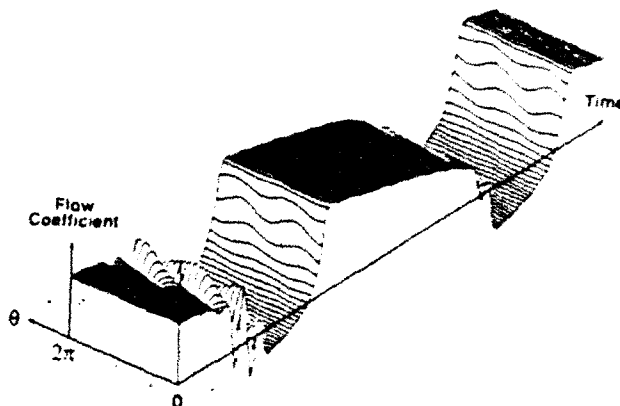


Fig. 2 The time evolution of the nondimensional axial velocity (C_x/U) distribution about the circumference ($0 \leq \theta \leq 2\pi$) of a three-stage compressor during compression system instability; mean level of C_x/U prior to instability is 0.5

As shown in the appendix, we can describe the stability of a compressor in terms of the time evolution of an asymmetric perturbation of the velocity potential, Φ , namely

$$\Phi = \sum_{|k| \neq 0} b_k (e^{ik\theta - \omega_k t}) (e^{ik\eta - \omega_k t}) \quad (1)$$

Each Fourier mode (k) is the product of two exponentials. The term $\exp(ik\theta - \omega_k t)$ represents a traveling wave function of circumferential position (θ) and time (t); ω_k is the wave frequency. The term $\exp(ik\eta - \omega_k t)$ gives the dependence of the wave on axial position (η) and time; ω_k is the damping of the wave. Equation (1) can be viewed as analogous to the behavior of an oscillator rotating about the circumference of the compressor. The growth of the wave (i.e., the stability of the compressor) is determined by the instantaneous damping ω_k . When the damping is negative, oscillations grow and the flow in the compressor is unstable. Active control schemes aim to increase this damping. Here we make use of equation (1) in designing an experiment to detect the rotating waves and measure the instantaneous stability of the compressor.

McDougall (1988) and McDougall et al. (1990) were the first persons known to the authors to have made measurements of these rotating waves. Examining a single-stage, low-speed compressor, he found small disturbances rotating about the machine just prior to the onset of stall, in qualitative accord with the above theory. He included a good summary of previous experimental work.

To explore the use of the traveling waves as a stall precursor or warning, we pose the following questions:

- Do prestall waves exist in most (many, all) compressors?
- At what rate do these waves grow? How long do they persist?
- At what rate do they travel?
- How can they be observed?

Nomenclature

a_k, b_k = Fourier components of disturbance velocity potential
 c_k = Fourier component of axial velocity disturbance
 k = harmonic number
 δP = pressure perturbation
 R = compressor midspan radius
 u = axial velocity perturbation (see Appendix)
 U = rotor speed at midspan

V = measured axial velocity
 η = nondimensional axial coordinate = axial distance/ R
 θ = circumferential coordinate
 λ, μ = compressor inertia parameters
 ξ = nondimensional time = $(\text{time} \cdot U)/R$
 σ = nondimensional damping ra-

tio (see equation (1))
 ϕ = compressor flow coefficient = axial velocity/ U
 Φ = nondimensional compressor velocity potential
 ψ = compressor pressure rise = $P_{ext} - P_{turb}/\frac{1}{2}\rho U^2$
 ω = nondimensional frequency = frequency $\cdot (U/R)$

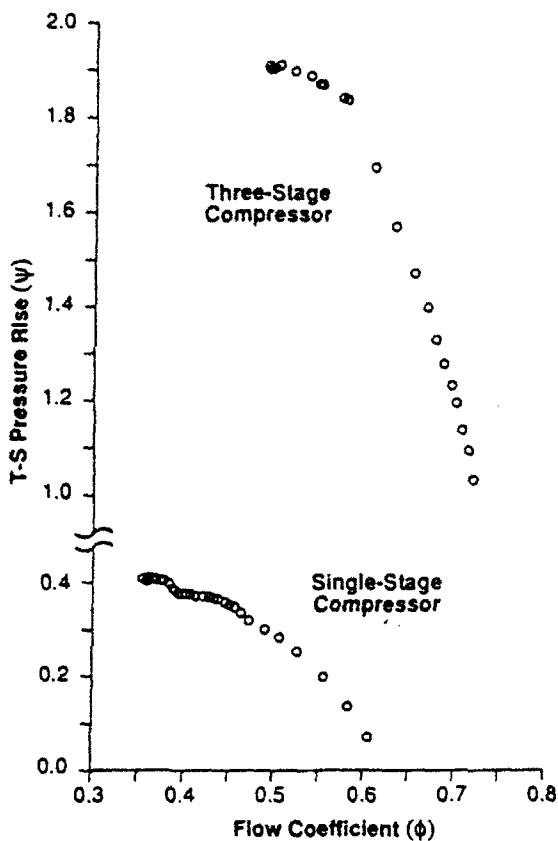


Fig. 3 Compressor characteristics of the two low-speed compressors examined in this study

- How is this behavior affected by inlet distortion and mass flow transients?
- Do high-speed (compressible) machines behave similarly?

In sum, these questions address both the basic assumptions inherent in the Moore/Greitzer model and its utility in providing real-time warning of an impending compressor stall. In the following, we experimentally examine these issues.

Experimental Apparatus

Prestall behavior of three compressors were examined: two low-speed and one high-speed machine. The low-speed, single-stage compressor consisted of IGV's, rotor, and stator. It is described in more detail by Johnson and Greitzer (1987) and Lee (1988). The low-speed, three-stage compressor is described by Gamache and Greitzer (1986) and Lavrich (1988). Nondimensional inlet total to exit static pressure compressor characteristics are shown for the two machines in Fig. 3. Both low-speed compressors were operated at tip speeds below 100 m/s, so that compressibility effects were negligible. The high-speed, three-stage compressor is a modern experimental design run at Pratt & Whitney Div., United Technologies Corp. This machine was equipped with fast-acting bleed valves, which quickly moved the operating point away from stall when it occurred to prevent mechanical damage. Experiments on that machine were conducted by Pratt & Whitney personnel and the raw data provided to the authors.

Instrumentation

All the compressors were outfitted with standard time-averaged instrumentation to provide the steady-state operating characteristics of the machines. Time-resolved instrumentation

consisted of hot-wire anemometers in the low-speed compressors (oriented so as to measure axial velocity), and wall-mounted, high response, static pressure transducers in the high-speed compressor. The high-speed machine had eight transducers mounted about the circumference at each of four axial stations. The low-speed machines had either eight hot wires at a time at one axial station or three rows of four mounted at various stations. The low-speed data were digitized in real time (with suitable low pass anti-aliasing filters), while the high-speed data were first recorded on analog magnetic tape. All data were d-c coupled.

The hot wires were calibrated in place prior to each test to a velocity accuracy of ± 3 percent. The net resolution of the anemometers was 0.8 percent of the average prestall axial velocity. The pressure transducers in the high-speed experiment were calibrated by Pratt & Whitney personnel. One pressure transducer had significantly less amplitude than all its neighbors so that its gain was raised in post-test processing to yield the same level of rms fluctuations.

Signal Processing and Probe Placement Considerations

Experiments were conducted to look for small-amplitude traveling waves whose spatial and temporal structure was important. Probe placement and signal processing were therefore carefully considered. Also, because the measurements in both time and space were discrete, aliasing was of concern in both dimensions.

Probe number was determined by the number of spatial harmonics (N) to be examined. $2N+1$ measurement points are required about the circumference at each axial station. Eight were used in most cases, providing definition of the first three spatial harmonics. We expected most of the energy in the lowest order modes but were concerned about aliasing of the higher order modes and blade passing phenomena. Since small upstream disturbances due to the compressor are irrotational, they decay exponentially with upstream distance. Thus, the first measurements were made one-half compressor radius upstream so that high-order (short length scale) disturbances would be filtered out fluid dynamically. These disturbances appeared not to be a problem and measurements were subsequently made throughout the compressors.

We expect the waves to travel about the circumference at close to the rotating stall frequency, 20-50 percent of rotor shaft speed. Thus, the data was digitally band-pass filtered in the computer, with a passband 0.1 to 1.2 times rotor shaft frequency. These frequencies were determined by trial and error comparison to the unfiltered data.

The filtered time histories of the individual sensors can be used to calculate the modal information by taking a discrete Fourier transform in space about the circumference of the compressor at each point in time. Given N measurements about the machine, the complex Fourier coefficients for each mode k are given by

$$C_k = \frac{1}{N} \sum_{n=0}^{N-1} V_n \exp \left[-\frac{2ikn\pi}{N} \right] \quad (2)$$

where V_n is the measured axial velocity at angular position n . For most measurements described herein, eight sensors were used so that $N = 8$, $-3 \leq k \leq 4$, and, since V_n is real, C_k and C_{-k} are complex conjugates. The Fourier coefficients contain all the information on the wave position and amplitude as a function of time.

Low-Speed Compressor Experiments

The low-speed single-stage and three-stage compressors were used to explore the nature of the stall initiation process and the prestall traveling wave behavior, examine alternate sensor placements, establish the traveling wave statistical behavior,

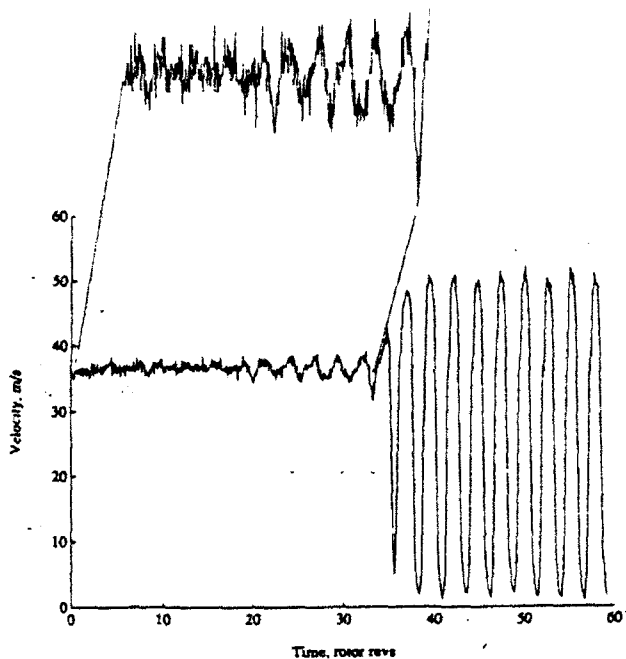


Fig. 4 Time history of axial velocity from a single hot wire positioned upstream of the single-stage compressor; the machine is in rotating stall after a time of 35 rotor revolutions

and determine the influence of inlet distortion and throttle (mass flow) transients.

Quasi-Steady Stalling Behavior. During these experiments, the compressor operation was first stabilized very close to stall (within 0.005 in flow coefficient from the stall point in Fig. 3) and then the throttle closed very slowly so that machine would stall within 10 to 20 seconds. Data were taken during this entire period from the eight hot wires about the compressor annulus. Unless otherwise specified, the hot wires were positioned 0.5 compressor radii upstream of the IGV's.

Figure 4 shows the time history of the axial velocity as measured by a single sensor during the stalling transient. Here, time equal to zero has been defined, somewhat arbitrarily, as the time at which the velocity nonuniformity has grown to 50 percent of the fully stalled maximum value. The period of a rotor revolution is used as the unit of time since this is a characteristic time scale for the phenomena. As can be seen, the prestall fluctuations have a small amplitude compared to the rotating stall itself, during which the velocity fluctuations are greater than 100 percent of the prestall mean velocity. The time history of all eight sensors about the circumference is shown in Fig. 5 on a magnified scale, and regular disturbances can be observed here for a considerable time before the stall. The amplitude of the first Fourier component (the modulus of C_1), calculated from these data with equation (2), is shown in Fig. 6. This is a measure of the strength of the first mode of the rotating wave. Although small compared to the amplitude during fully developed rotating stall ($r > 0$), it is nonzero for a long period (90 revs) before the stall. The argument of C_1 is the phase angle of the traveling wave, and this is shown in Fig. 7 along with the phase of the second harmonic (arg C_2). The slopes of these lines are the speeds at which the harmonics of the waves travel around the compressor annulus (the annulus has been unwrapped in the figure so that 2π radians is one trip around). This coarse scale is used deliberately to show the overall trend. The key point from Fig. 7 is that phase speed of the first harmonic of the traveling waves is essentially constant and readily discernible for almost 90 rotor revolutions before the stall. There is a small shift in wave speed

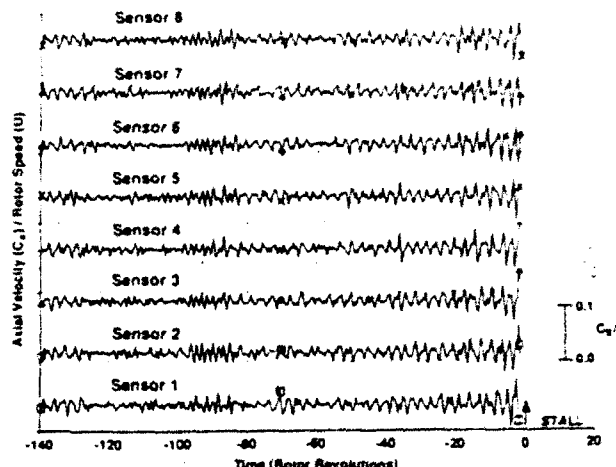


Fig. 5 Time history of axial velocity before stall as measured by eight hot wires equally spaced about the circumference 0.4 compressor radii upstream of the IGV's

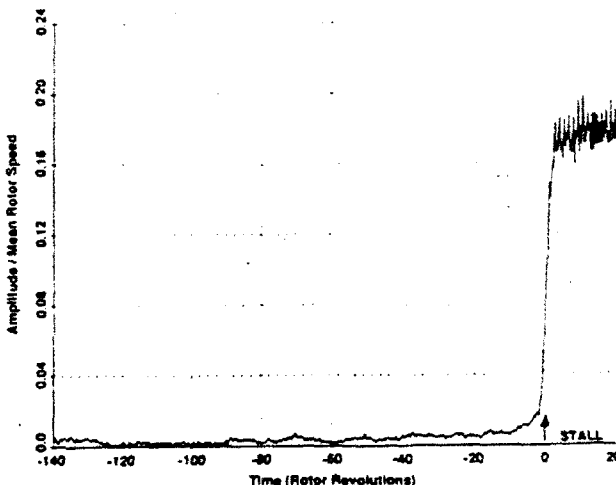


Fig. 6 Amplitude of the first Fourier harmonic ($|C_1|$) of the data in Fig. 5

at the stall point, from 0.35 rotor speed before the stall to 0.38 rotor speed with fully developed stall. The curve marked "second harmonic" shows that, for this experiment, the second harmonic signal is too weak (i.e., the signal-to-noise ratio is too small with the instrumentation used) to give useful information.

A three-dimensional representation of the C_1 component during the last 20 revs before stall is shown in Fig. 8 in a format similar to that of the calculation shown in Fig. 2. The wave nature of the disturbance in this machine is evident.

The amplitude of the oscillations in the compressor flowfield (in this case the traveling waves about the circumference) reflects not only the operating point but also the level of disturbances in the system (the forcing). Near the neutral stability point (damping, σ , close to zero), the flowfield should behave like a narrow band system. Re-examining Fig. 7 we see that there is a stretch of constant phase speed between -140 and -125 revs, followed by a period of ill-defined speed to -95 revs, and then finally constant phase speed until stall at 0. In the context of the model, we interpret this to imply that the damping of the compressor (σ) is very close to zero, so that the traveling waves are very lightly damped. They can grow and then decay, depending upon the level of external disturbances. Thus, we might expect to see some test-to-test variation

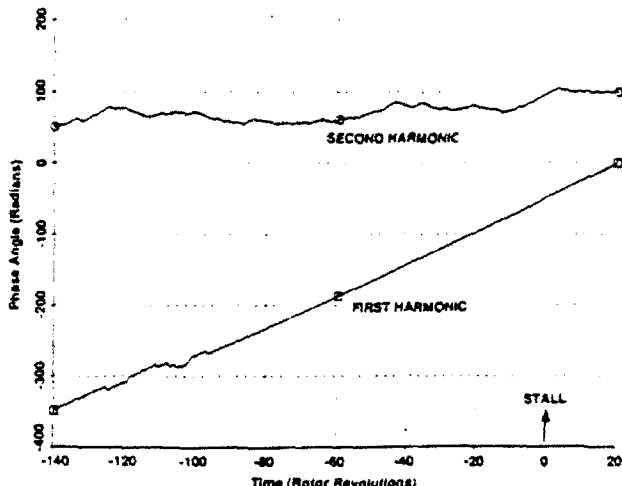


Fig. 7 The time history of the phase of the first and second Fourier coefficients measured upstream of the low-speed, three-stage compressor

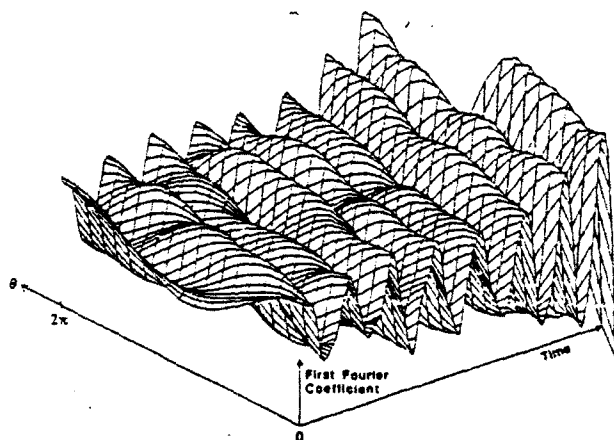


Fig. 8 Measured first harmonic behavior in a format comparable to that of Fig. 2

in the time during which the prestall waves propagate strongly enough to be evident. This was examined by carrying out nine tests on the three-stage compressor under nominally identical conditions. The mean prestall period of constant wave propagation was approximately 60 rotor revolutions with a high of 250 and a low of 30. (In all cases, the wave speed was 33 percent of rotor speed before stall and 38 percent during stall.) There is thus considerable statistical variation in the time during which the prestall waves were tracked. We have not characterized the source of these variations; they may be related to low-amplitude external disturbances (noise) convected into the compressor inlet. Overall, these data establish that rotating stall starts as a small amplitude travelling wave in the two low-speed compressors studied.

Throttle Transient and Inlet Distortion Effects. The influence of throttle (mass flow) transients and inlet distortion (spatially nonuniform inlet total pressure) is of interest since we know from engine experience that rotating stall is often associated with these phenomena. Experiments were conducted on both the one- and three-stage compressors with qualitatively similar findings.

The throttle transient experiments were conducted at three different throttle rates, which varied by a factor of 150 to 1, the fastest corresponding to a flow coefficient range of roughly 0.1 (Fig. 3) per 100 rotor revolutions. Distortion was generated

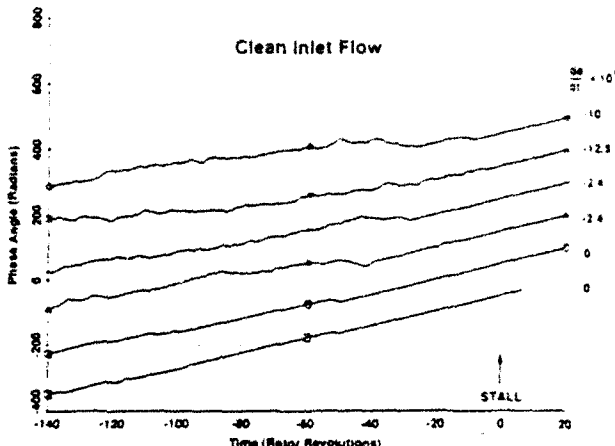


Fig. 9 Phase angle of first harmonic measured on the low-speed, three-stage compressor at different throttle rates

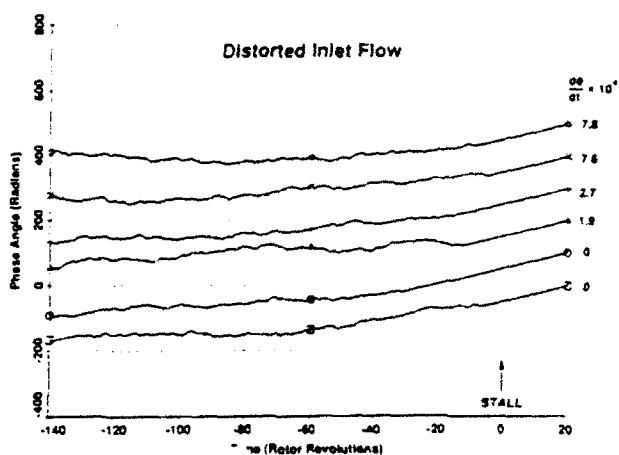


Fig. 10 A. Fig. 9, but with inlet distortion

by blocking off 180 deg of the annulus approximately one compressor diameter upstream of the IGVs, creating a roughly square wave total pressure distortion with an amplitude of 0.5 dynamic head, based on mean velocity. The time-resolved mass flow for these experiments was obtained using the average of the hot-wire measurements. The time derivative of the mass flow was obtained by a least-squares fit to the last second of data preceding stall. The absolute uncertainty of these measurements was estimated at 5 percent.

The prestall behavior of the three-stage compressor with a uniform (Fig. 9) and distorted (Fig. 10) inlet flow was measured at three throttle rates. In both cases, the rotating stall was always preceded by low-amplitude waves traveling at constant speed. The prestall duration of these waves is roughly inversely proportional to the throttle rate. This is consistent with the stability model in that the higher the throttle rate, the less time the machine spends at the low flow (ϕ) region of the speedline, which has low damping (σ) and, thus, the shorter the period during which the prestall waves can propagate for an appreciable time.

The flow coefficient (ϕ) at which prestall waves are first discerned is shown in Fig. 11 for the single-stage compressor as a function of nondimensional throttle rate ($d\phi/dt$), where t is measured in rotor revolutions, i.e., $t = \text{time/rotor revolution period}$. The waves appear at nearly the same value of ϕ independent of the throttle rate (over the rates examined, the waves appear slightly later as $d\phi/dt$ increases). The prestall

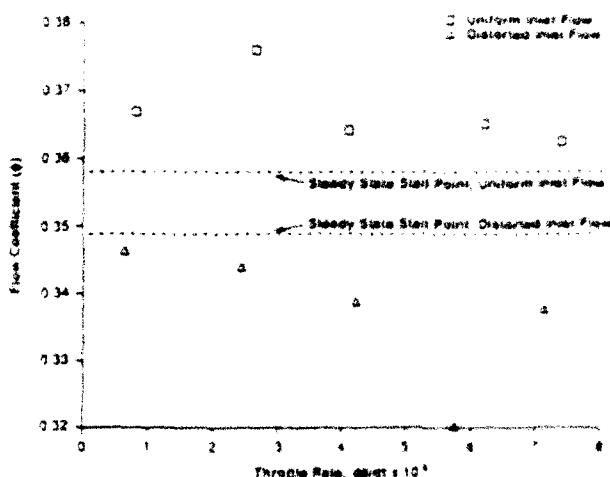


Fig. 11 Flow coefficient (ϕ) at which pre stall waves are first discerned in the low-speed, single-stage compressor as a function of throttle rate

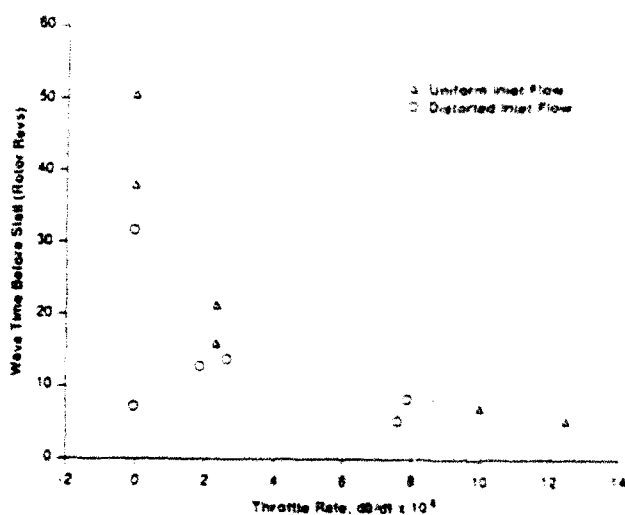


Fig. 12 Period during which the pre stall wave is discerned as a function of throttle rate

period of constant traveling wave speed (the straight line segments in Figs. 9 and 10) is plotted in Fig. 12 as a function of the throttle rate and exhibits (roughly) a $1/(d\phi/dt)$ dependence.

The effects of inlet distortion are evident in Figs. 9-11. The pre stall period at near-zero throttle rate is an order of magnitude smaller with the inlet distortion than without. This behavior is also consistent with a model such as that described by equation (1) if we consider that wave propagation velocity and amplitude are functions of the local flow conditions and thus will vary about the annulus in the case of distorted inflow. We infer that the signal processing technique used here (equation (2)), which looks only for sinusoidal waves, is not optimal with inlet distortion. Instead, a method based on the true eigenmodes of the system—and thus independent of wave shape—should be used. These could be calculated using the procedure outlined by Hynes and Greitzer (1987), but we have not yet taken this step.

Sensor Placement Influence. Data were taken with the circumferential array of sensors at five different axial stations upstream, downstream, and between the blade rows of the single-stage compressor to evaluate the influence of sensor placement on traveling wave detection. The waves were discernible at all axial stations. The amplitude increased as the sensors were moved downstream but so did the noise. This is

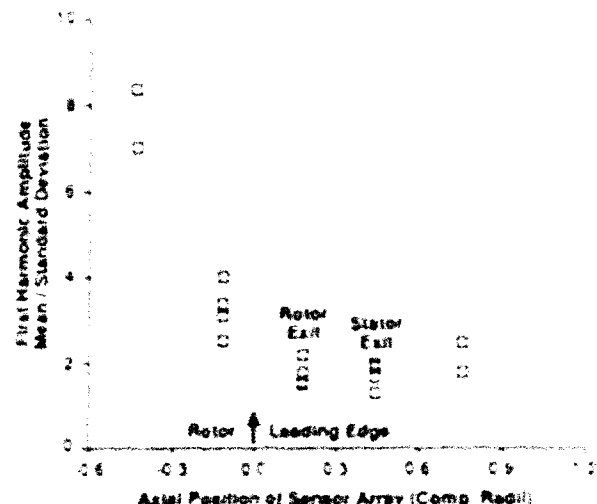


Fig. 13 Signal-to-noise ratio of first Fourier coefficient amplitude measured at various axial stations in the single-stage compressor

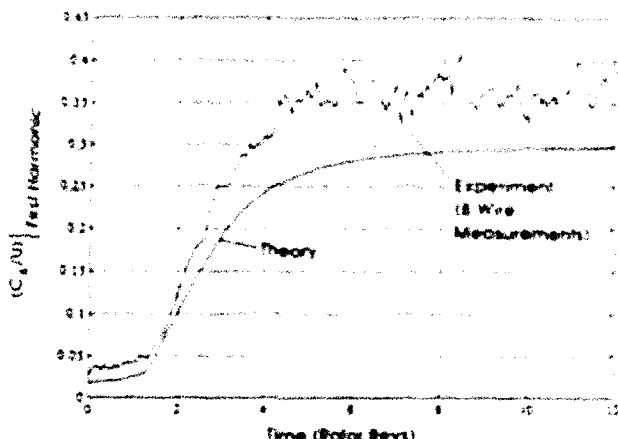


Fig. 14 Time evolution of the first harmonic of the axial velocity in the three-stage compressor during the inception of rotating stall

reflected in Fig. 13, which shows the signal-to-noise ratio, defined as the mean of the amplitude of the first harmonic ($\langle C_1 \rangle$) of the wave divided by the standard deviation. The signal is cleanest upstream of the IGVs.

Disturbance Growth Rate. The general nonlinear model that gives rise to equation (1) describes the evolution of the traveling wave system in the compressor and it should be capable of quantitatively predicting the growth of the waves. The inputs required for the calculation are the compressor geometry (lengths, blade stagger angles, etc.) and the steady-state compressor characteristic. Comparison of model prediction with experimental measurement for the three-stage low-speed compressor (Fig. 14) shows good agreement. (Note that, since the initial conditions for the model are not known, the zero time reference for the data and the calculation are arbitrary.) In our view, this agreement helps establish the validity of the model.

High-Speed Compressor Experiments

The wall static pressure history measured just upstream of the first stage stator in a three-stage high-speed compressor with uniform inlet flow during a slow throttle transient is shown in Fig. 15. The data are for eight circumferential locations. The phase speed of the first two spatial harmonics of these data as calculated using equation (2) shows that the second

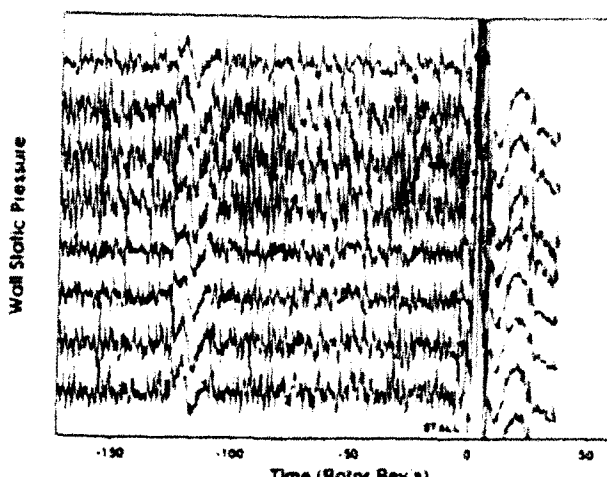


Fig. 15 Time history of eight wall static pressure transducers located about the circumference ahead of the first stator row in a high-speed, three-stage compressor

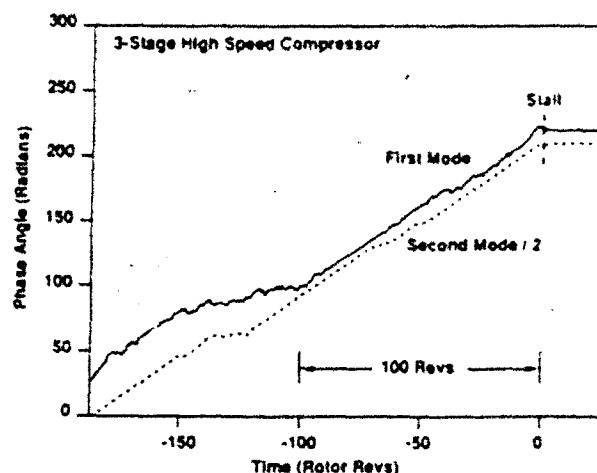


Fig. 16 The phase history of the first two spatial harmonics calculated from the high-speed compressor data of Fig. 15

harmonic is most readily discerned (Fig. 16). The prestall amplitude [$|C_{N1}|$] is considerably higher for the second harmonic as well. The wave speed is constant for more than 100 rotor revolutions, showing a behavior similar to that of the low-speed compressors. Comparison of the phase speed of the second harmonic as measured at the leading edge of each of the three stator rows (Fig. 17) shows the signal to be the clearest at the first stage. Other measurements and calculations indicate that the first stage stalls first under these flow conditions.

Time history of the wall static pressure on the high-speed compressor with a 180 deg inlet distortion during a slow throttle transient is shown in Fig. 18. Here we see that the prestall disturbance level is not uniform about the circumference. The phase speeds of the first two spatial harmonics of this data are not readily discerned (Fig. 19) except for a short stretch of the second harmonic. The reason for this may be inferred from the time histories in Fig. 18, which show prestall disturbances of relatively high amplitude originating on sensor 7 (low flow region) being strongly attenuated as they move by sensors 6 and 5 (high flow region). Cross correlations of adjoining sensors were taken, which indicated a maximum at a time delay corresponding to 13 percent of rotor speed. A time history of the maximum value of the cross correlation between sensors 0 and 1 shows (Fig. 20) strong correlation for the period (-100 to -140 revs) during which constant phase speed of the second harmonic can be discerned. The correlation increases again as stall is approached.

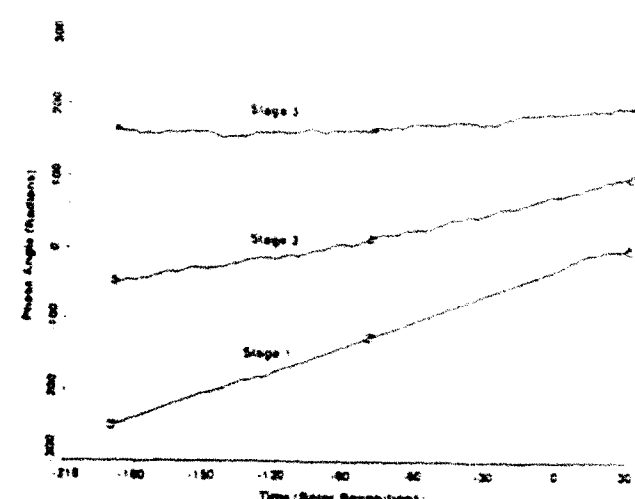


Fig. 17 Phase history of first spatial harmonic from measurements taken at the stator leading edges in a high-speed, three-stage compressor

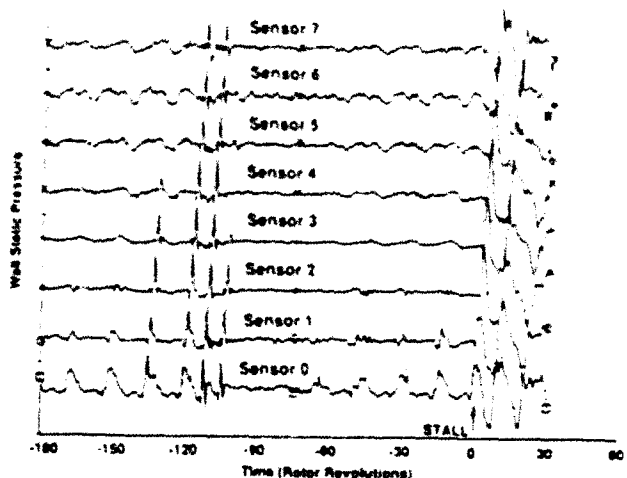


Fig. 18 As Fig. 15, but with inlet distortion

These high-speed data support the view that the distorted compressor acts (crudely) as parallel compressors with wave speed and damping varying about the circumference as a result of the locally varying flow field. The cross correlations of both high and low-speed compressor data show that there is local real-time information available on the instantaneous compressor stability, which may require more sophisticated data processing than represented by equation (2).

Application of Signal Processing to Compressor Stability Estimation

We believe that the experimental data presented have verified the applicability of the compressor stability model represented by equation (1), at least to the three machines studied. In this view, compressor stability is directly linked to the growth or decay of the traveling waves and rotating stall is simply the mature form of this wave evolution. The question of stall warning thus becomes one of identification of the waves and estimation of their growth rate. The practical implementation of this approach is complicated by two factors. The first is that, during transients, the growth of the disturbance may not be slow compared to its fundamental period, and this reduces the effectiveness of the more simple time spectra techniques such as fast Fourier transforms (FFT). The second is that the circumferentially uniform flowfield of a compressor with inlet

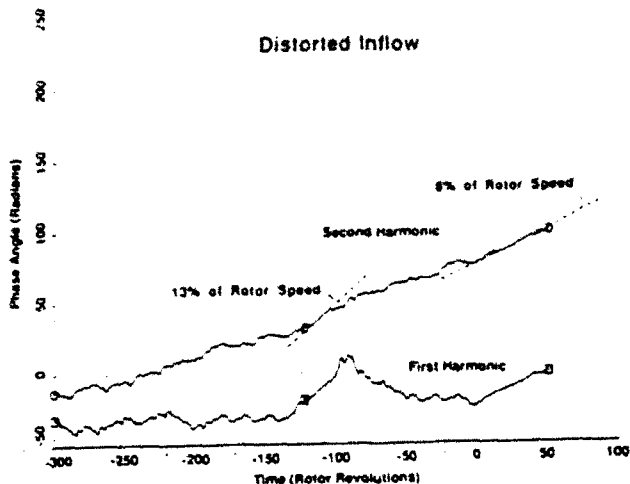


Fig. 19 Phase angle history of the first two spatial harmonics of the high-speed compressor with inlet distortion

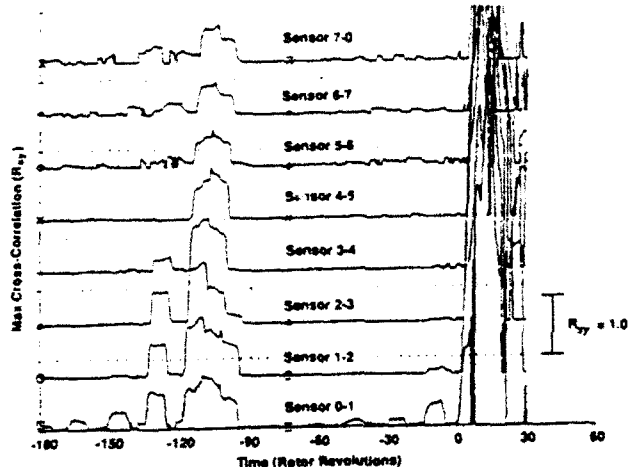


Fig. 20 The maximum value of the cross correlation of the adjacent transducers of Fig. 8 in a high-speed, three-stage compressor

distortion means that wave growth and propagation rates are nonuniform about the circumference, reducing the effectiveness of the simple spatial analysis approach of equation (2). To extract the maximum information available from the compression system, more sophisticated signal processing is thus required to cope with temporal and spatial variations. In the following sections, we address only the problem of temporal variability, leaving the spatial variation problem to a later time.

As sketched in the Appendix, the wave behavior of equation (1) is associated with the temporal behavior of the Fourier modes (a_k) of the velocity potential of the form

$$\frac{da_k}{d\xi}(\xi) = C_k a_k(\xi) \quad (3)$$

which is the description of a first-order system in which C is a constant that depends on geometry. Two interrelated approaches can be brought to bear on this system: spectral analysis and system identification techniques.

Spectral Analysis. In its simplest form, spectral analysis can be used to estimate the power spectral density (PSD) of each important spatial harmonic of the flowfield. A peak should be present at the frequency of the traveling waves (20–40 percent of rotor rotation) with its height being proportional to the power in the wave. Monitoring the time evolution of this

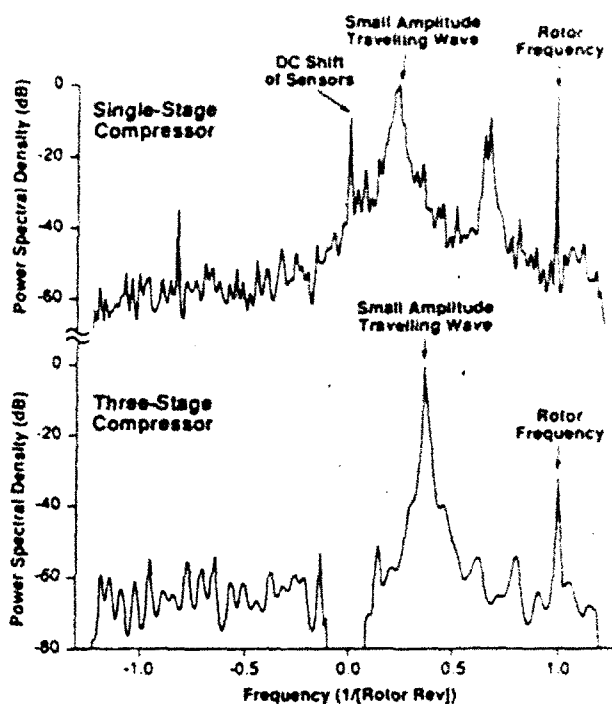


Fig. 21 Power spectral density (PSD) of first spatial harmonic of the axial velocity before stall in two low-speed compressors

peak yields information on the wave growth and thus the compressor stability. This should be a more discerning technique than the simple-phase speed plots (as in Figs. 7, 9, 10, and 15), since the phase is driven by the strongest frequency component present in the signal, which is not necessarily that of the traveling waves of interest, while the PSD will not be so affected.

The fast Fourier transform (FFT) is often used to calculate PSDs but has two limitations that are important in this application. The first is that the frequency resolution is proportional to the time interval available for analysis. The second is that the absence of information outside this interval distorts the spectral response. These problems can be particularly troublesome with very short data records and data with time varying spectral content, both of which are present in this application. Other techniques have been developed, however, which largely overcome these problems. The one adopted here is based on the fitting of a linear model to the data (Kay and Marple, 1981), which has the advantage of resolving sharp spectral features from short data records.

The power spectral densities of the first spatial harmonic of the axial velocity before stall in the single-stage and the three-stage low-speed compressors are shown in Fig. 21. The traveling wave is readily apparent in both compressors, at 0.24 of rotor frequency for the single-stage and 0.35 for the three-stage. (The three-stage data were low pass filtered to remove the d-c component; the single-stage data were not.) Figure 21 shows the power spectra at one flow coefficient at one instant of time. The power in the traveling wave (i.e., the height of the peak at the traveling wave frequency of Fig. 21) is plotted in Fig. 22 as a function of flow coefficient. The amplitude of this peak at the traveling wave frequency increases as the flow coefficient is decreased, implying that the power in the waves is related to the compressor stability. Note that the power in this first spatial harmonic is considerably reduced when inlet distortion is present. This is most likely a result of the signal processing technique used here, which was aimed at discerning sinusoidal waveforms traveling about the compressor circumference. The distorted inflow waveforms are not so simple,

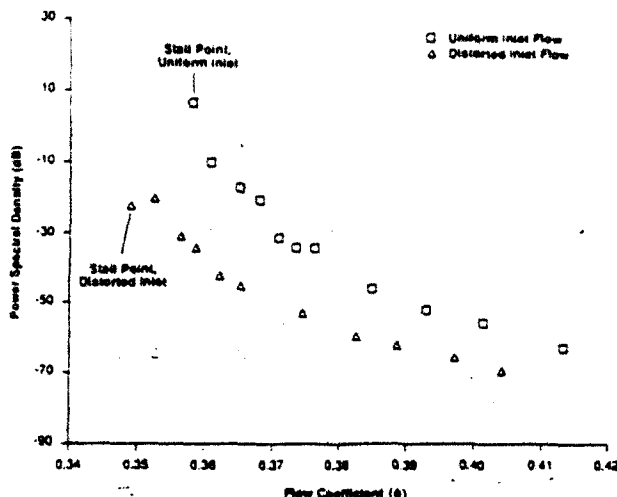


Fig. 22 The peak power of the first spatial harmonic as a function of flow coefficient (σ) on the single-stage, low-speed compressor

thus more sophisticated processing techniques may be required. The direct spectral approach lets us identify flow features but does not directly yield information on compressor stability, since the height of the peak is a function both of the damping of the system and the amplitude of the excitation. System identification techniques are of use in this respect.

System Identification. We have a model (equation (1)) that we believe to be a relevant description of the physical system, compressor stability. System identification is a technique that allows us to estimate the values of the physical parameters describing the compressor stability by fitting data to the model in real time. A discrete time series y_n can be modeled as the solution of a difference equation

$$y_n = b_1 y_{n-1} + \dots + b_p y_{n-p} + v_n \quad (4)$$

where v_n is a noise term (turbulence, electrical noise, convected disturbances, etc.). The p coefficients of b_i in equation (4) can be estimated by fitting a p th order linear model to the data. The advantage in this application is that only the parameters need be estimated since the form of the model has been established. Filtering can be used to enhance the results by removing unmodeled dynamics and correlated noise.

The model can be fitted to the data in either the time or frequency domain. The time domain was used here since it is well suited to real-time implementation. Least-squares techniques can be used recursively by updating the model parameter estimates for each new data point (Goodwin and Sin, 1984; Friedlander, 1984) and "forgetting" old data to track time varying parameters. We refer the reader to Garnier (1989) for further details.

We rewrite the wave model of equation (3) for each spatial harmonic in the form of equation (4) as an ordinary differential equation

$$\frac{dC_{-k}(\xi)}{d\xi} = (\sigma_k - i\omega_k) C_{-k}(\xi) + V(\xi) \quad (5)$$

where C_{-k} is the harmonic defined by equation (2), σ_k the traveling wave damping, ω_k the wave frequency, and $V(\xi)$ the driving noise. In fitting this model to the data at any instant in time, we have estimated the wave damping and frequency for each spatial harmonic. To the degree to which the model is valid, wave damping and compressor stability are equivalent. A real-time estimate of σ is thus an instantaneous measure of the compressor stability.

The fit of equation (5) to the power spectral density of the first spatial harmonic of the single-stage low-speed compressor is shown in Fig. 23 for undistorted flow and Fig. 24 for dis-

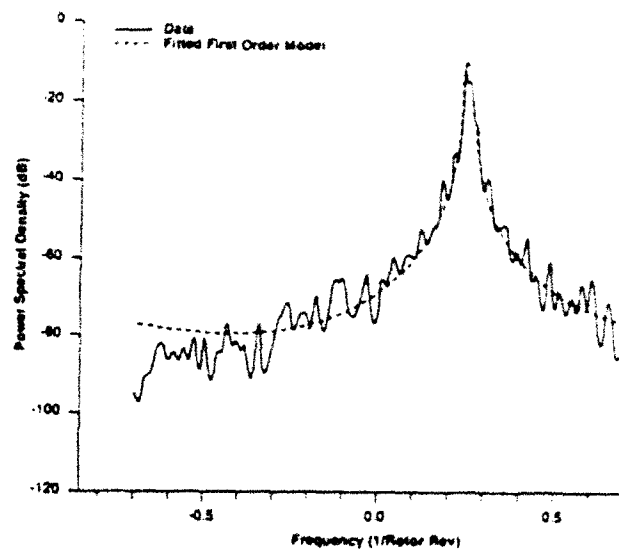


Fig. 23 Comparison of the linear model and measurement of the power spectral density of the first spatial harmonic on the low-speed, single-stage compressor

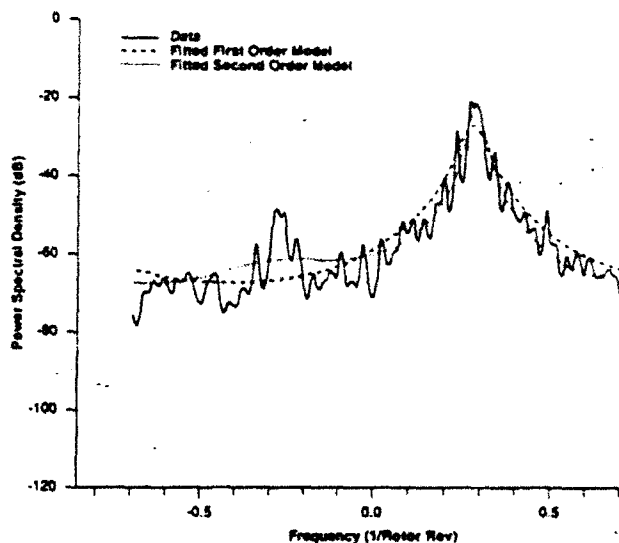


Fig. 24 As Fig. 23, but for second spatial harmonic

torted inflow. In both cases, the model fits the general shape of the data well. The distorted data shows a peak frequency of -0.3 , which is too close to traveling wave frequency to simply filter, so a second-order model was employed to account for this peak. All of the distorted inlet data subsequently used a second-order model.

The damping coefficient (σ_1) of the first spatial harmonic estimated with this technique from the data is shown as a function of flow coefficient in Fig. 25, with and without inlet distortion. With undistorted inflow, the compressor is stable until the damping approaches zero. With inlet distortion, the damping is greater than for the undistorted case away from stall, but drops much faster with flow coefficient until the machine stalls at a somewhat higher value of σ . The frequency of the first spatial harmonic (ω_1) is the same with and without inlet distortion and independent of flow coefficient. The influence of throttle transients is apparently to steepen the drop in damping with flow coefficient as well as delay the stall to a somewhat lower flow coefficient (Fig. 26). How much of the delay is due to unmodeled inertia effects within the compressor and how much is due to time lags in the algorithm has not been determined.

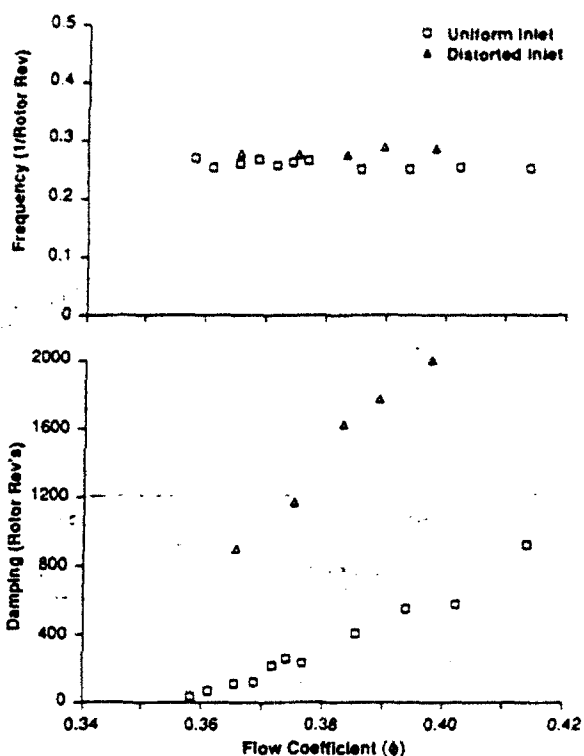


Fig. 25 First spatial harmonic wave damping (σ) and frequency (ω) estimated from the single-stage compressor measurements using parameter identification techniques

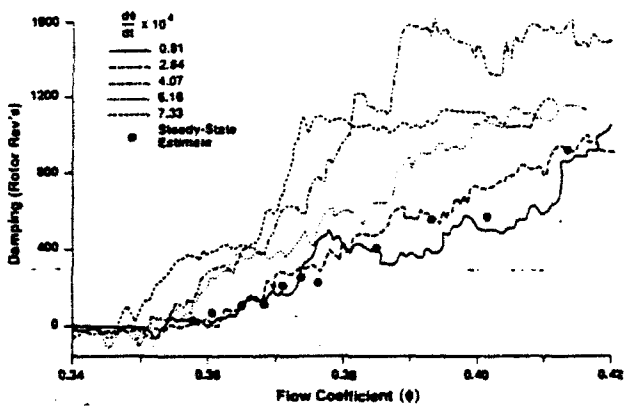


Fig. 26 First spatial harmonic damping, as in Fig. 25, but estimated for various throttle transient rates ($d\phi/dt$)

Discussion—Engineering Uses of Prestall Waves

As we have demonstrated, the compressor damping can be directly estimated on-line, given sufficient experimental data. The damping is a direct measure of the compressor stability over the period represented by the data and is thus an indication of the likelihood of stall. Whether a machine stalls at a given time is determined not just by the system damping, however, but also by the nature and level of the system forcing, which we have not addressed here. The damping by itself, though, is an indication of the susceptibility to the excitation and thus to stall.

One use of this information would be to establish the surge line of a new compressor on the test stand without the necessity of actually stalling the machine. This avoids the requirement to "dump" the compressor automatically to a higher mass flow each time surge is encountered (necessary to prevent mechanical damage), and can provide a savings in test time. A second possible use is to determine the location within a mul-

tistage compressor of the blade row in which the stall starts. The data from the high-speed compressor indicated that the waves are most clearly discerned at this axial station.

One of the most intriguing and challenging uses would be as a real-time prestall indicator in an operational engine. The limited data presented herein suggest that sufficient warning time may be available (tens to hundreds of rotor revolutions) for a more or less conventional engine control system to take corrective action (changing fuel flow, nozzle area, vane settings, etc.), thus reducing the surge margin required and the associated penalties. There are many questions that must be examined before the practicality of such a scheme could be established—not just ones of compressor dynamics as addressed here but also more applied ones such as sensor reliability, computational requirements, system complexity, overall dependability, and cost.

An even more challenging use of these prestall waves is as a control signal for an actively stabilized compressor, one in which external feedback control is used to increase the compressor stability by increasing the wave damping (σ). Epstein et al. (1989) first suggested this approach and an ongoing effort was described by Dugundji et al. (1989), where the inlet guide vanes of a single-stage low-speed compressor were being "wiggled" to suppress the traveling waves and thus increase the compressor stability.

For any of these applications to become practical, considerably more work than presented here must be done on the sensing and identification of these circumferentially traveling waves. In particular, the sinusoidal nature of the signal processing inherent in equation (2) must be relaxed in order to account for more complex flows, such as those with inlet distortion. Algorithm selection and adaptation to minimize the length of time data must be taken to identify the waves is another area where work is needed. We believe these extensions of the present work are straightforward, although not necessarily simple. Somewhat more complicated (or at least tedious) is the analytical inclusion of compressibility to model high-speed machines accurately (although the high-speed data examined to date are quite similar to that from low-speed machines).

An extremely fundamental question is how general are the results presented herein; do some, most, or all compressors exhibit this prestall wave behavior? We make no claims beyond the results for the compressors we have examined. All exhibit similar behavior, behavior in accord with the theoretical models of compression system stability.

We know of no reason why such waves should not exist in all compressors, although we would not be at all surprised if their strength and duration varied to such a degree as to render them very difficult to discern in some machines. Only more data can answer this question.

Conclusions and Summary

We have examined the flow in two low-speed and one high-speed compressor. The experiments in these machines show that:

- 1 Small-amplitude (less than 5 percent of the stall amplitude) waves can be discerned traveling about the compressor annulus at close to the rotating stall speed for 10–200 rotor revolutions prior to the onset of rotating stall.

- 2 These waves grow into a fully developed rotating stall without apparent sharp changes in either phase or amplitude.

- 3 The prestall period during which these waves were discerned varied by a factor of 5 at a single flow condition, apparently stochastically.

- 4 The behavior was similar in both the high and low-speed compressors, except that the first spatial harmonic was the strongest in the low-speed machines and the second in the high-speed.

5 In multistage compressors, the prestall waves are clearest in the stage that stalls first.

6 Inlet distortion reduces the period during which the prestall waves were discerned, using techniques based on the assumption of sinusoidal waves about the circumference.

7 The data fit the model of Moore and Greitzer, including both the qualitative behavior of the prestall waves and the quantitative prediction of the growth rates.

Overall, we believe that recognition of this wave behavior can be a useful tool in the study of compressor stability. Future work should encompass more sophisticated signal processing to account for distorted inflow, include the effects of compressibility, and extend the experimental work to a larger number of compressors.

Acknowledgments

The authors would like to acknowledge the assistance of Mr. James Paduano, Dr. G. R. Guenette, and Professor L. Valavani. We thank our colleagues Dr. I. J. Day and Dr. J. P. Longley for their stimulating discussions and thoughtful comments. The authors are grateful to Pratt & Whitney Government Engines Business for providing the high-speed compressor data and permission to publish it. This work was supported by the Office of Naval Research, Dr. R. J. Hansen technical monitor, and by the Air Force Office of Scientific Research, Captain H. Helin and Dr. J. McMichael technical monitors. We thank these gentlemen both for their support and active encouragement.

References

Dugundji, J., Epstein, A. H., Garnier, V., Greitzer, E. M., Guenette, G. R., Paduano, J., Siklowski, P., Simon, J., and Valavani, L., 1989, "A Progress Report on Active Control of Flow Instabilities: Rotating Stall Stabilization in Axial Compressors," AIAA Paper No. 89-1008.

Dunham, J., 1965, "Non-Axisymmetric Flows in Axial Compressors," *Mech. Eng. Sci. Monograph No. 3, IMechE, Oct.*

Epstein, A. H., Ffowcs Williams, J. E., and Greitzer, E. M., 1989, "Active Suppression of Aerodynamic Instabilities in Turbomachines," *Journal of Propulsion and Power*, Vol. 5, No. 2, pp. 204-211.

Friedlander, B., 1984, "The Overdetermined Recursive Instrumental Variable Method," *IEEE Transactions on Automatic Control*, Vol. AC-29, No. 4, pp. 353-356.

Garnier, R. N., and Greitzer, E. M., 1986, "Reverse Flow in Multistage Axial Compressors," AIAA Paper No. 86-1747, to appear in *Journal of Propulsion and Power*, 1990.

Garnier, V., 1989, "Experimental Investigation of Rotating Waves as a Rotating Stall Inception Indication in Compressors," M.S. Thesis, Dept. of Aeronautics and Astronautics, MIT, Cambridge, MA.

Goodwin, G. C., and Sin, K. S., 1984, *Adaptive Filtering, Prediction and Control*, Prentice-Hall, New Jersey.

Graupe, D., 1984, *Time Series Analysis, Identification and Adaptive Filtering*, Robert E. Krieger Publishing Company, Malabar, FL.

Greitzer, E. M., 1976, "Surge and Rotating Stall in Axial Compressors, Part I: Theoretical Compression System Model; Part II: Experimental Results and Comparison With Theory," *ASME Journal of Engineering for Gas Turbines and Power*, Vol. 98, pp. XX-XX.

Greitzer, E. M., and Moore, F. K., 1986, "A Theory of Post-Stall Transients in Axial Compressors: Part II—Applications," *ASME Journal of Engineering for Gas Turbines and Power*, Vol. 108, pp. 231-239.

Hynes, T. P., and Greitzer, E. M., 1987, "A Method for Assessing Effects of Circumferential Flow Distortion on Compressor Stability," *ASME Journal of TURBOMACHINERY*, Vol. 109, pp. XX-XX.

Johnson, M. C., and Greitzer, E. M., 1987, "Effects of Slotted Hub and Casing Treatments on Compressor Endwall Flowfields," *ASME Journal of TURBOMACHINERY*, Vol. 109, pp. 380-387.

Kay, S. M., and Marple, L. S., 1981, "Spectrum Analysis—A Modern Perspective," *IEEE Proceedings*, Vol. 69, No. 11, pp. 1380-1419.

Lavrich, P. L., 1988, "Time Resolved Measurements of Rotating Stall in Axial Flow Compressors," MIT Gas Turbine Laboratory Report #194.

Lee, N. K. W., 1988, "Effects of Compressor Endwall Suction and Blowing on Stability Enhancement," MIT Gas Turbine Laboratory Report #192.

Ljung, L., Mørk, M., and Falcoover, D., 1978, "Fast Calculations of Gain Matrices for Recursive Estimation Schemes," *International Journal of Control*, Vol. 27, No. 19, pp. 1-19.

Marple, L. S., 1980, "A New Autoregressive Spectrum Analysis Algorithm," *IEEE Transactions on Acoustics, Speech, and Signal Processing*, Vol. ASSP-28, No. 4, pp. 441-454.

McDougall, N. M., 1988, "Stall Inception in Axial Compressors," PhD Thesis, Cambridge University, United Kingdom.

McDougall, N. M., Cumpsty, N. A., and Hynes, T. P., 1990, "Stall Inception in Axial Compressors," *ASME JOURNAL OF TURBOMACHINERY*, Vol. 112, pp. 116-125.

Moore, F. K., 1983, "A Theory of Rotating Stall of Multistage Axial Compressors: Part I—Small Disturbances," *ASME Journal of Engineering for Power*, Vol. 105, pp. XX-XX.

Moore, F. K., and Greitzer, E. M., 1986, "A Theory of Post-Stall Transients in Axial Compressors: Part I—Developments of the Equations," *ASME Journal of Engineering for Gas Turbines and Power*, Vol. 108, pp. 68-76.

Stennings, A. H., 1980, "Rotating Stall and Surge," *ASME Journal of Fluids Engineering*, Vol. 102, pp. 14-20.

APPENDIX

Brief Description of the Basic Stall Inception Model

The underlying ideas of stall inception and the approach to the sensing are connected by a simple model, which provides a framework to view the phenomenon. Two points concerning rotating stall onset should be stressed at the outset. First, when one considers the actual flow, there are several disparate length scales involved. What is needed is a description of the interaction between flow on the blade element scale (length scales on the order of blade pitch or smaller) and the wave structure in the annulus (flow phenomena with length scale of the radius of the machine). Second, there is strong evidence that the "region" of the blade passage that is responsible for rotating stall is the endwall. Put another way, the mechanism of stall is generally *not* two dimensional, and the treatments that view it as such miss the essential fluid mechanics of the situation.

The model that we use was developed by Moore (1983) for rotating stall and later extended by Moore and Greitzer (1986) to encompass generalized disturbances, i.e., combined rotating stall and surge in multistage machines. Here we examine only onset of the former. In the model, the disturbances upstream and downstream of the compressor are viewed as two dimensional; this would be expected to be the case in compressors of high hub-tip radius ratio. The blade row description, however, makes use of the measured steady-state compressor pressure rise characteristic, with correction to account for unsteadiness. In a very real sense, then, three-dimensional effects are accounted for because the behavior at the endwalls, which can be a strong contributor to the "turnover" in the pressure rise versus flow curve, has been included. Although both the blade row modeling and the coupling between large scale disturbance field and blade element dynamics are crude, the model does appear to contain the necessary elements for a description of the stall process. It is this point, with the simplicity as a secondary issue, that suggests use of such a description in the sensing and control problem.

The derivations of the relevant equations have been given several times elsewhere, so that we will only sketch out the steps leading to the equations that we need. The flow fields considered are two dimensional, inviscid, and incompressible upstream and downstream of the compressor. The flow in these two regions is coupled by three matching conditions across the compressor, two kinematic and one dynamic. With these conditions, representing the modeling of the unsteady and non-axisymmetric compressor performance, we describe the flow in each region as follows.

Upstream Flow Region. Upstream of the compressor the flow is irrotational, and a velocity potential can be used. We express the velocity as a uniform steady flow plus a small asymmetric perturbation, which is the gradient of a potential, Φ , satisfying the two-dimensional Laplace equation, with periodic boundary conditions and vanishing far upstream. Φ can thus be expressed in terms of its spatial Fourier coefficients as

$$\Phi(\eta, \theta, \xi) = \sum_{k=1}^{\infty} a_k(\xi) e^{ik\theta} e^{i\eta k} \quad (A1)$$

The quantity η is the nondimensional axial coordinate x/R and ξ is a nondimensional time, where $\xi = \text{time} \cdot (U/R)$.

Across the Compressor. As stated, there are three matching conditions that are applied across the compressor. The first is that the local axial velocity distribution is the same at all axial stations through the compressor. This approximation is made on the basis of the small opportunity for circumferential redistribution within typical compressors. Order of magnitude arguments imply that it is most correct for disturbances with low order harmonic content, and these are precisely the ones of interest here. Discussion of the assumption can be found in the papers by Dunham (1965) or Stenning (1980).

Explicitly, the matching condition is

$$u_u(0, \theta, \xi) = u_d(0, \theta, \xi)$$

where the subscript u refers to just upstream and d to just downstream of the compressor.

The second matching condition is constant leaving angle at compressor exit. This is also an approximation, but it should be reasonable for the solidities of practical concern.

The last matching condition can be expressed in terms of a relation between the pressure difference across the compressor and the local axial velocity and its derivative. As developed by Moore (1983) (see also Moore and Greitzer, 1986) the matching condition can be written in a linearized form as

$$\left[\frac{\delta P_d - \delta P_u}{\rho U^2} = \left(\frac{d\psi}{d\phi} \right)_{\phi=0} - \lambda \frac{\partial \delta \phi}{\partial \theta} - \mu \frac{\partial \delta \phi}{\partial \xi} \right]_{(0, \theta, \xi)} \quad (A2)$$

The quantity $(d\psi/d\phi)$ is the slope of the steady-state compressor characteristic, and λ and μ are nondimensional parameters associated with the inertia of the fluid in the compressor blade passages. Their precise values are not critical here since what is of most interest is the general form of the solution, but for reference μ is roughly twice λ and is of order unity.

Downstream Flow Region. The linearized flow field in the downstream region is periodic and obeys the equation

$$\nabla^2 \delta P_d = 0 \quad (A3)$$

with the boundary condition far downstream of constant static pressure. The downstream pressure field is thus of the form

$$\delta P_d = \sum P_{n_d}(\xi) e^{-ik_1 \eta + i\theta} \quad (A4)$$

Using the linearized forms of the equations of motion in the upstream and downstream region equations, (A1), (A2), and (A4) may be combined into a single equation for $a_k(\xi)$, the Fourier component of the upstream velocity disturbance potential. This is

$$\frac{da_k(\xi)}{d\xi} = \frac{ik_1 \left| \left(\frac{d\psi_c}{d\phi} \right) - ik\lambda \right|}{(2 + ik_1 \mu)} a_k(\xi) \quad (A5)$$

If we define

$$\sigma_k = - \left(\frac{d\psi_c}{d\phi} \right) \frac{ik_1}{2 + ik_1 \mu} \quad (A6)$$

$$\omega_k = k\lambda \frac{ik_1}{2 + ik_1 \mu} \quad (A7)$$

The solution of equation (A5) can be written

$$a_k(\xi) = b_k e^{(-\sigma_k - i\omega_k \xi)} \quad (A8)$$

and thus

$$\Phi = \sum_{k=0} b_k e^{(ik_1 \eta - \sigma_k \xi)} e^{(ik\theta - i\omega_k \xi)} \quad (A9)$$

As stated in the main text, therefore, the Fourier mode is the product of two exponentials. The term $e^{(ik\theta - i\omega_k \xi)}$ represents a traveling wave, with ω_k the wave frequency. The other exponential, $e^{(ik_1 \eta - \sigma_k \xi)}$, gives the dependence of the wave amplitude on axial position (η) and time; σ_k is the damping of the wave.

DISCUSSION

Y. N. Chen,¹ U. Haupt,² and M. Rauteberg³

The paper presents a series of interesting experimental results about the prestall wave. Figure 4 shows that this wave is amplified within about one cycle into the rotating stall wave of nearly the same frequency. The explanation of this extremely strong amplification is based on the two-dimensional theory of the velocity potential given in equation (1), as introduced by Moore and Greitzer (1986). This equation represents a traveling wave around the circumference of the rotor with dependence on the axial position. Equation (1) is viewed in the paper as analogous to the behavior of an oscillator rotating about the circumference of the compressor. The growth of the wave (i.e., the instability of the compressor) is determined by the instantaneous damping. When the damping is negative, oscillations grow and the flow in the compressor is unstable.

The prestall wave in the form of a stall precursor is thus considered in the paper as an axially transverse wave traveling around the circumference of the rotor. As the corresponding annular space is occupied by a lot of blades, it may be difficult to realize how such a traveling wave can cross the barrier in the form of these blades.

If the alignment of the stall cells of multistage axial compressors in the axial direction is considered, the waves associated with rotating stall of each of the stages are blocked in the axial direction. In other words, the waves penetrate through the whole depth of the compressor from the rotor of the first stage to the rotor of the last stage in the axial direction without changing in the global pattern. This depth-independent nature reveals that the waves of the different stages have the capability of blocking each other in the axial direction on one hand, and crossing the blade channels of the rotor on the other.

The writers of this discussion found in their previous publications (Chen, 1990; Chen et al., 1987, 1989, 1990a, 1990b, 1991; Haupt et al., 1987) that the baroclinic waves in combination with the Rossby waves and the associated transient vortices (a circular Karman vortex street) possess the capability required.

It was shown by the writers that on the verge of rotating stall the compressed reverse flow comes from the annular space behind the outlet of the rotor along the casing/shroud to meet the fresh forward flow on a ring-shaped front. Due to the different entropies and temperatures of the two opposite flows, a baroclinic instability deforms the ring into a wavy motion. This front was, in addition, confirmed by the measurements of Koch (1970) and Inoue et al. (1990) as cited in Chen et al. (1989, Fig. 14, and 1990a, Fig. 17). The wavy motion of the front is then developed into Rossby waves, the velocity field of which was detected from the measurement of Breugelmans and Sen (1982) on a centrifugal turbomachine (Chen, 1990, Fig. 10), and from the measurement of Lavrich (1988) on an axial compressor (Chen et al., 1990b, Fig. 20, and 1990a, Fig. 4).

There are two kinds of secondary recirculations in the rotor, which control the activity of the Rossby waves and the rotating stall.

The first kind of secondary recirculation, composed of the reverse flow along the casing/shroud and the forward flow along the hub, primarily promotes the Rossby waves and thus the rotating stall. There is a close analogy between the Rossby waves in the annular spaces in front of and behind the rotor of an axial compressor on one hand, and the Rossby waves (baroclinic waves) on the upper and bottom layers of a rotating

¹Sulzer Brothers Ltd., Winterthur, Switzerland.

²Institute for Turbomachinery, University of Hannover, Federal Republic of Germany.

fluid annulus with an artificial recirculation between the outer and inner cylindrical walls found by Douglas et al. (1972) in their laboratory experiment (see Chen et al., 1987, Fig. 9) on the other hand. The pressure rise of the rotor corresponds to the gravity field in the experiment of the rotating annulus. The Rossby waves in the two annular spaces/layers are coupled with each other by their blocking effect.

In the case of the rotor, the communication of the activity of the Rossby waves between the blade channels is carried out by the second kind of secondary recirculation around each of the blades, as shown by Chen et al. (1990a, Figs. 14, 15, and 16).

Furthermore, each blade channel of the rotor of an axial compressor generates its own Rossby wave (see Chen et al., 1990b, Fig. 22), which serves as a communicating member between the Rossby waves in the two annular spaces in front of and behind the rotor. In this manner, the field of the Rossby waves around the entire rotor forms an ensemble, renewing from blade channel to blade channel under the guidance of the activity of the Rossby waves in the frontal and rear annular spaces.

The formation of the Rossby wave in each of the blade channels of centrifugal compressors can be also verified, as shown in a further paper of the writers (1991).

The Rossby waves in the turbocompressors and pumps are similar to those in the ocean and the middle atmosphere (e.g., 500 mbar height). In the latter case they guide the polar front on the earth's surface (i.e., between the warm westerly from the subtropical region and the cold easterly from the polar region, and thus subjected to the baroclinic instability for forming the meteorological vortices "low and high" of the unstable weather event), and the jet stream in the high atmospheric level (200 mbar).

The Rossby waves of the rotor have their velocity components primarily in the tangential and radial directions u and v . These two components correspond to the west-east direction of the zonal flow and its deflection to the north-south direction in the Rossby waves of the atmosphere. The axial velocity component w , which initiates the first and second kinds of secondary recirculations of the rotor mentioned above, is not directly involved in the Rossby waves. These tangential and radial components u and v of the Rossby waves are then capable of being communicated between the blade channels as stated previously.

The paper under discussion is based on the wave motion of the axial velocity component w around the rotor. This corresponds to a wave motion in the atmosphere in the direction normal to the earth's surface. Such a wave is observed as an internal wave in stratified flow on the earth, e.g., the lee wave downstream of a mountain as a barrier. This wave cannot cause a rotating disturbance around the earth. In other words, the axial disturbance in a rotor cannot stay in any direct connection with the rotating stall, which has the major property of a rotating disturbance.

The rotating stall of the axial compressor usually has one stall cell. The Rossby number of the accompanying Rossby wave was determined to be 0.083 by the writers (1990b). The rotating stall of the centrifugal compressor with its two-cell pattern has then a Rossby number of 0.17 (Chen, 1990). These values correspond well to those of the Rossby waves in nature.

The writers are quite aware that their Rossby-wave theory is still in a developing stage. It needs further mathematical and physical treatments. An advanced step for this will be carried out in the near future (Chen et al., 1991).

References

- Chen, Y. N., Haupt, U., and Rautenberg, M., 1987, "On the Nature of Rotating Stall in Centrifugal Compressors With Vaned Diffuser, Part II: Karman Vortices as the Controlling Mechanism," *1987 Tokyo International Gas Turbine Congress*, Vol. II, pp. 169-182.
- Chen, Y. N., Haupt, U., and Rautenberg, M., 1989, "The Vortex-Filament Nature of the Reverse Flow on the Verge of Rotating Stall," *ASME JOURNAL OF TURBOMACHINERY*, Vol. 111, pp. 450-461.
- Chen, Y. N., Haupt, U., Seidel, U., Jin, D., and Rautenberg, M., 1990a, "The Behavior of the Rossby Waves of Rotating Stall in Turbocompressors," *Interfluid-Dokumente*, Druckhaus K. Schmitz Wwe, Frankfurt Main, pp. 403-416.
- Chen, Y. N., Haupt, U., and Rautenberg, M., 1990b, "Rossby Waves and Associated Transient Rotating Stall Vortices in Radial and Axial Turbocompressors," *Zeitschrift für Flugwissenschaften und Weltraumforschung*, Vol. 14, No. 4.
- Chen, Y. N., 1990, "Rotating Stall in Radial Compressors and Pumps as Rossby Waves Associated With Transient Vortices," *Swizer Technical Review*, No. 1, pp. 51-56.
- Chen, Y. N., Seidel, U., and Rautenberg, M., 1991, "The Rossby Waves of Rotating Stall in Impellers, Theory and Application," to be published.
- Haupt, U., Chen, Y. N., and Rautenberg, M., 1987, "On the Nature of Rotating Stall in Centrifugal Compressors With Vaned Diffusers, Part I: Detection of Reverse Flow," *1987 Tokyo International Gas Turbine Congress*, Vol. II, pp. 161-168.

Authors' Closure

The authors thank Drs. Chen and Haupt and Profesor Rautenberg for their comments. We do not, however, agree with the points that are made. In particular, we do not see that any scientific evidence at all has been presented connecting rotating stall with either Rossby waves (which occur at high ratios of Coriolis to inertial forces) or baroclinic instability. To be more explicit, we have not seen, either in their discussion or in previous expositions, any clearly stated body of assumptions, a mathematical statement of the problem, calculations based on this statement, or predictions about the form of such waves in an axial compressor. We feel strongly that such a rational development is needed to demonstrate the appropriateness, let alone the correctness, of any proposed theory. Figure 14 of Garnier et al. is the result of such a process: a computation based on a clearly stated theory. Its agreement with experiment seems to us to show that the theory contains much of the essential physics of the stall cell wave evolution, but if this is disputed then there are specific statements that one examines to see the cause of any disagreement.

In addition to this overall view, there are clear errors of concept in the discussion. For example, baroclinic instability (which depends on density not being solely a function of pressure) is invoked by the discussers to explain some aspects of rotating stall. The flows examined by Garnier and predecessors, however, had low Mach numbers (on the order of 0.1 in some cases) and temperature rises much less than the ambient level. Under these conditions, the flow can be considered constant density, the entropy has no dynamic significance, and there is no role played by baroclinic instability. Further, in the theory presented in the paper, the propagation of the stall cell depends on a balance between inertial effects in the compressor and the upstream and downstream flow fields; there is no relationship to Rossby waves.

In summary, while some of the statements concerning Rossby waves made by the discussers may be correct, we have seen no factual trail leading to their connection with rotating stall. We would be pleased to consider such evidence if presented in a well-reasoned and unambiguous manner, rather than as the vague analogies that appear in the discussion.

Modeling Axial Compressor

Nonlinear Rotating Stall Phenomena for Control

James D. Paduano

Daniel L. Gysling

*Massachusetts Institute of Technology
Cambridge, MA 02139*

Abstract

A formulation of the Moore-Greitzer rotating stall model is presented which allows nonlinearity to be represented in a control-theoretic framework. To test the validity of the nonlinear model, stall inception experiments are compared to simulated stall inception transients. The shape of the nonlinear compressor characteristic is shown to be important in characterizing the transient behavior. The effects of the throttle characteristic and unsteady losses are also discussed.

Introduction

Rotating stall and surge are violent limit cycle -type oscillations in axial compressors which result when perturbations (in flow velocity, pressure, etc.) become unstable. Originally treated separately, these two phenomena are now recognized to be coupled oscillation modes of the compression system -surge is the zeroth order or planar oscillation mode, while rotating stall is the limit cycle resulting from higher-order, rotating-wave disturbances. The importance of these phenomena to the safety and performance of gas turbine engines is widely recognized [1], and various efforts to either avoid or control both rotating stall and surge have been studied [2,3,4].

A turning point in these attempts came with the development of relatively simple models for surge and rotating stall [5,6,7], which relied on modeling the global behavior of the compression system rather than detailed internal flow characterization. These models, which we will call the Moore-Greitzer models, were simple enough to be used in the design and implementation of stabilizing controllers. In fact, it has been shown that in centrifugal compressors [8,9], and in some low-speed axial compressors [10,11], the linearized versions of the surge and

rotating stall models are accurate and useful representations in the context of stabilization.

The nonlinear forms of these models have also received attention as tools for studying stabilization and control [12,13]. In this respect, nonlinear modeling of surge is more mature: experimental studies indicate that the details of surge initiation and the surge limit cycle are well characterized by the nonlinear surge model [14, 21]; all indications to date are that nonlinear control law design based on this model is justified and would work in implementation.

The nonlinear rotating stall model, on the other hand, is more complicated, involves more assumptions and simplifications, and is more difficult to verify experimentally. Lavrich [15] conducted the most thorough study of the assumptions of the Moore-Greitzer model, and found that during *fully developed* stall, significant radial and circumferential flow occurs, which makes the model assumptions less accurate. Thus care must be exercised in using the rotating stall model without first verifying its usefulness in characterizing the instability to be controlled.

Fortunately, characterizing *fully-developed* rotating stall is not our primary goal. Since a stabilizing controller would keep perturbations relatively small, it is only small-perturbation waves and stall inception waves that we must accurately model. The former have been shown to obey the linearized dynamics satisfactorily, and to be stabilizable over a certain range of unstable operating conditions. Stall inception waves, on the other hand, involve large enough perturbations that nonlinear effects must be taken into account. These nonlinearities may be important for controllers of severely nonlinear compressors, or to extend the stabilized operating range of existing active control research compressors.

In this paper, we first present the coupled nonlinear surge/rotating stall model, in a form which is useful for control law design. We then look at experimental rotating stall inception data, and compare it to simulation results. Our goal is to show that, for the perturbations which lead to rotating stall, the Moore-Greitzer model adequately characterizes compressor dynamic behavior. In the process, the important effects of the nonlinearities will be elucidated.

Low Speed (Incompressible) Compressor Modeling

Consider the schematic diagram of an axial compressor in Figure 1. It consists of an upstream annular duct, a compressor modeled as an actuator disk, a downstream annular duct, and a throttle. During stable operation, flow through the

compressor can be assumed to be circumferentially uniform (axisymmetric), and a single non-dimensional measure of flow through the compressor determines the system state. This measure is the 'flow coefficient', which is simply the nondimensionalized value of the axial velocity:

$$\phi = \frac{\text{(axial velocity)}}{\text{(rotor speed)}} \quad (1)$$

During quasi-steady operation, the total-to-static pressure rise delivered by the compressor is simply determined by its 'pressure rise characteristic,' denoted $\Psi_C(\phi)$. The pressure rise is balanced by a pressure loss across a throttling device, which can be either a simple flow restriction (used for testing compressors as components) or the combustor and turbine in a gas turbine engine. The balance between pressure rise across the compressor and pressure drop across the throttle is depicted as an intersection between the characteristics of the two devices, $\Psi_C(\phi)$ and $\Psi_T(\phi)$, where, for low pressure ratios, $\Psi_T(\phi)$ is usually taken to be a quadratic function of ϕ :

$$\Psi_T = \frac{1}{2} K_T \phi^2. \quad (2)$$

K_T depends on the degree of throttle closure. In a typical experiment, the throttle is slowly closed, the throttle characteristic becomes steeper (modeled by adjustment of K_T above), the intersection point between $\Psi_C(\phi)$ and $\Psi_T(\phi)$ changes, and the equilibrium operating point of the compressor moves from high flow to low flow (see Figure 2).

The stability of the equilibrium point represented by the intersection between $\Psi_C(\phi)$ and $\Psi_T(\phi)$ has been the topic of numerous studies, due to its importance in the safe, high performance operation of gas turbine engines. In our model, the system state under unsteady, possibly non-axisymmetric (i.e. circumferentially varying) conditions is characterized by three terms: the annulus averaged pressure rise delivered by the compressor, $\bar{\Psi}$, the annulus averaged flow coefficient, $\bar{\phi}$, and the spatially distributed perturbation on $\bar{\phi}$, denoted $\delta\phi$:

$$\phi(\eta, \theta, \tau) = \bar{\phi} + \delta\phi(\eta, \theta, \tau) \quad (3)$$

where η is the nondimensional axial position in the compressor (the origin is chosen to be at the compressor face), θ is the circumferential position, and τ is non-dimensional time (in rotor revolutions).

Note that evaluation of Ψ_C and Ψ_T must now be conducted more carefully due to the unsteady and non-axisymmetric character of the flow: Ψ_C is evaluated at $\eta = 0$ (the compressor face), and varies with both τ and θ – i.e. we evaluate $\Psi_C(\bar{\phi} + \delta\phi(0, \theta, \tau))$. Thus the compressor is viewed as a distributed memoryless nonlinearity operating on the local flow coefficient. On the other hand, due to the

nature of the downstream flowfield, Ψ_T can be evaluated for the annulus averaged flow; thus the pressure loss across the throttle is simply $\Psi_T(\bar{\phi})$.

One additional variable must be introduced in order to set up the system of equations. The upstream flowfield, being two dimensional, admits both axial velocity perturbations ($\delta\phi$) and circumferential velocity perturbations. Rather than introduce a circumferential velocity variable, we will introduce the perturbation velocity potential $\delta\Phi$, such that

$$\frac{\partial(\delta\Phi)}{\partial\eta} = \delta\phi \quad \text{and} \quad \frac{\partial(\delta\Phi)}{\partial\theta} = \delta(\text{circ. vel.}) \quad (4)$$

We will see that $\delta\Phi$ can ultimately be eliminated from the equations, along with all of the partial derivatives with respect to space, leaving an operator-theoretic ordinary-differential relationship.

This discussion serves only to introduce the relevant states of the system. Derivation of a model for the dynamics of the compression system is presented in other documents, and is beyond the scope of this paper. Our purpose is to present the model in a format which is coherent and accessible from a control theoretic point of view, and to discuss the dynamic implications of the model. Thus we present the dynamics without further derivation, referring the interested reader to the relevant literature [5,6,7,10,16].

- 1) For the upstream flow field we assume no incoming vorticity (clean inlet conditions) and thus the flow in this region is potential:

$$\nabla^2\delta\Phi = 0 \quad \eta \leq 0. \quad (5)$$

- 2) The annulus average (a.a.) pressure rise across the compressor lags behind that imposed by the throttle characteristic, due to mass storage in the downstream ducting and plenum chamber:

$$\frac{\partial\Psi}{\partial\tau} = \frac{1}{4l_c B^2} [\bar{\phi} - \Phi_T(\bar{\Psi})]. \quad \eta = 0. \quad (6)$$

- 3) The a.a. flow coefficient changes to try to balance the difference between the a.a. pressure rise delivered by the compressor and the a.a. pressure rise that actually exists across the compressor (in unsteady situations these can be different):

$$\frac{\partial\bar{\phi}}{\partial\tau} = \frac{1}{l_c} \{ [\Psi_C(\bar{\phi} + \delta\phi)]_{\text{a.a.}} - \bar{\Psi} \} \quad \eta = 0. \quad (7)$$

- 4) Finally, the non-axisymmetric (n.a.) part of the pressure rise delivered by the compressor acts to accelerate the flow through the rotor and stator passages, where part of this acceleration is due to the rotor moving through a non-uniform flow perturbation (this is represented by the presence of a partial with respect to θ):

$$m \frac{\partial(\delta\Phi)}{\partial\tau} + \mu \frac{\partial(\delta\phi)}{\partial\tau} + \lambda \frac{\partial(\delta\phi)}{\partial\theta} = [\Psi_C(\bar{\phi} + \delta\phi)]_{\text{n.a.}} \quad \eta = 0. \quad (8)$$

5) Definitions: l_C , B , m , μ , λ are scalar geometric parameters defined in [16], $\phi_T(\cdot)$ is the inverse of Ψ_T , and the definitions of the a.a. and n.a. part take the expected forms:

$$[\Psi_C]_{a.a.} = \frac{1}{2\pi} \int_0^{2\pi} \Psi_C d\theta \quad \text{, and} \quad (9)$$

$$[\Psi_C]_{n.a.} = \Psi_C - [\Psi_C]_{a.a.}$$

note that only through the nonlinearity of Ψ_C are the axisymmetric and the non-axisymmetric dynamics coupled. Furthermore, if the n.a. dynamics (rotating stall) dynamics are fast compared to the a.a. (surge) dynamics, then it is reasonable when studying surge to represent the system using only the a.a. part, *provided the compressor characteristic is properly modified* to reflect the effect of instability of the n.a. part. Such modification for high-efficiency, multi-stage, high hub/tip axial compressors will invariably lead to an a.a. characteristic which is discontinuous and has a hysteresis loop (as in [7]).

The system of equations (5-8) is a coupled set of partial differential equations, in which two space dimensions and time are present. For clean inlet flow conditions, however, the space dimensions can be eliminated by introducing the solution for the upstream velocity potential as follows:

$$\delta\Phi = \sum_{\substack{n=-\infty \\ n \neq 0}}^{\infty} \tilde{\Phi}_n(\tau) e^{in\theta} e^{in\eta} \quad \eta \leq 0. \quad (10)$$

This solution satisfies Laplace's equation, and the other boundary conditions of clean inlet flow experiments as described in [10]. Using Equation (4), we can also write a solution for $\delta\phi$ in the upstream flowfield:

$$\delta\phi = \sum_{\substack{n=-\infty \\ n \neq 0}}^{\infty} \tilde{\phi}_n(\tau) e^{in\theta} e^{in\eta} \quad \eta \leq 0, \quad (11)$$

where $\tilde{\phi}(\tau) = |\eta| \tilde{\Phi}(\tau)$. These relationships allow $\delta\Phi$ to be eliminated from the system, and Equation (8) to be written

$$\sum_{\substack{n=-\infty \\ n \neq 0}}^{\infty} \left\{ \left(\frac{m}{|n|} \tilde{\phi}_n + \mu \tilde{\phi}_n + \lambda n \tilde{\phi}_n \right) e^{in\theta} \right\} = [\Psi_C(\tilde{\phi} + \delta\phi)]_{n.a.} \quad (12)$$

where the need for partials has been eliminated, and $\tilde{\phi}_n(\tau)$ is the n^{th} spatial Fourier coefficient of the axial velocity perturbation at the compressor face ($\eta=0$).

Introduction of the Fourier series solutions to eliminate spatial derivatives is a well-known method for handling distributed systems. The modal (or 'spectral') form of the equations allows linear control techniques to be applied. This approach

has proven successful in laboratory stabilization of rotating stall [10,11]. To study the effects of nonlinearity on the system, an operator-theoretic form is often more useful. By substituting the Fourier transform definition of $\tilde{\phi}_n$ into (12), we can write the system (6-8) as follows:

$$\begin{bmatrix} \dot{\psi} \\ \dot{\phi} \\ E(\delta\phi) \end{bmatrix} = \begin{bmatrix} 0 & -1 & 0 \\ \frac{1}{4l_c B^2} & 0 & 0 \\ 0 & 0 & A(\cdot) \end{bmatrix} \begin{bmatrix} \bar{\psi} \\ \bar{\phi} \\ \delta\phi \end{bmatrix} + \begin{bmatrix} \frac{1}{4l_c B^2} \Phi(\cdot) & 0 & 0 \\ 0 & \frac{1}{l_c} [\psi_C(\cdot) \dots]_{a.a.} \\ 0 & [\psi_C(\cdot) \dots]_{n.a.} \end{bmatrix} \begin{bmatrix} \bar{\psi} \\ \bar{\phi} \\ \delta\phi \end{bmatrix}, \quad (13)$$

where:

$$\begin{aligned} E(\cdot) &= f^{-1}\left(\left(\frac{m}{|n|} + \mu\right)f(\cdot)\right) \\ &= \sum_{\substack{n=-\infty \\ n \neq 0}}^{\infty} \left(\frac{m}{|n|} + \mu\right) \left(\frac{1}{2\pi} \int_0^{2\pi} (\cdot) e^{in(\theta-\zeta)} d\zeta\right) = f^{-1}\left(\left(\frac{m}{|n|} + \mu\right)f(\cdot)\right) \end{aligned} \quad (14)$$

and

$$\begin{aligned} A(\cdot) &= f^{-1}(\lambda n \cdot f(\cdot)) \\ &= \sum_{\substack{n=-\infty \\ n \neq 0}}^{\infty} \lambda n \cdot \left(\frac{1}{2\pi} \int_0^{2\pi} (\cdot) e^{-in(\theta-\zeta)} d\zeta\right). \end{aligned} \quad (15)$$

E and A are linear operators which represent spectrally the effect of the upstream flowfield, as well as allowing derivatives with respect to θ and η to be evaluated. The linear and nonlinear parts of Equation (13) have been separated for illustrative purposes, but the equations are clearly in the desired form, i.e. $\dot{x} = F(x)$.

Equations (13) can be further recast into a number of different forms, depending on the application, by repeated application of the Fourier transform and its inverse. For instance, we have implemented an update equation for $E(\delta\phi)$ in our simulation, and then used the proper Fourier relationships to recover $\delta\phi$. It is also possible, by choosing appropriate state variables, to reduce the system to one involving convolution with influence functions in the circumferential variable θ , and thus eliminate the summations over n . Finally, discretization of $\delta\phi$ in θ and substitution of matrix Fourier transformations in place of summations and integrals allows the system to be written as a finite-dimensional state-space system, with good numerical properties for simulation and control work [10].

The purpose of this section was to introduce the Moore-Greitzer model in a form which is useful to control theorists. Simplification of the model to state-space form, as well as approximations such as the surge-only and rotating-stall only approximations, can be made with (13) as a starting point. Because of the assumptions on the upstream flowfield, the partial-differential nature of the original system of equations has been eliminated, and the dependence on axial position has been 'solved out' of the system, leaving a simpler set of equations.

Refinement of the above model to include the effects of unsteadiness on the compressor characteristic has been conducted by Hendricks et. al. [18], for the linearized system. Their refinement recognizes that the compressor characteristic is not in reality a memoryless nonlinearity. They show that the lags inherent in the compressor pressure-rise response have a strong effect on both the damping and the rotation frequency of pre-stall waves. Although this modification is not yet available in the nonlinear simulation used here, an approximation has been implemented which allows the *damping* effect of unsteadiness to be taken into account. We will show in the next section that with this modification, and with an adjustment of λ to account for the rotation frequency change, a nonlinear simulation of Equation [13] accurately models stall inception in experimental low-speed axial compressors.

Comparison of Simulated and Experimental Stall Inception

The nonlinear functions Ψ_C and Ψ_T in (13) govern both the stall inception and the fully developed stall behavior. Fully developed stall behavior has been treated by other researchers, and for the purpose of stabilization, it is the character and subsequent avoidance of stall *inception* that is of primary interest. Thus we will concentrate here on the effect of Ψ_C and Ψ_T on nonlinear stall inception behavior, showing both experimental and theoretical results.

Stall inception - that is, transition from axisymmetric flow to fully developed stall - is of interest because only during this transition process are two important criteria met by the flow field: 1) relatively small axial flow perturbations 2) strong influence of the nonlinearities. Meeting the first criterion is important to insure that the assumptions inherent in the model described above and in [7] are reasonable. Specifically, the "semi-actuator disk" assumption used to simplify the representation of the flow across the compressor is a more severe approximation during fully developed stall than during pre-stall and stall-inception conditions [15]. Restricting the model validation to waves of small amplitude relative to fully developed stall

does not pose a problem to control law development, because presumably any working controller would stabilize the system and avoid the fully-developed stall condition.

The second criterion mentioned above is important in the present study because understanding and accurately modeling nonlinear stall inception behavior is our goal. In some compressors, over a certain range of flow coefficients, linearization of the dynamics in (13) is a workable approach [3]. However, to further extend the operating range of these compressors, and to control compressors in which nonlinearities are more severe, we must understand the nonlinear behavior. Although fully developed stall is a nonlinear phenomenon, it violates our first criterion. Thus we are left with stall inception, where nonlinear effects are beginning to influence the behavior, but the flow perturbations across the compressor are still relatively small.

Our approach in the present study is to carefully model three experimental, low speed compressors which have different stall inception behaviors. For convenience we will label these compressors C1, C2, and C3. The details of the experimental setup for each compressor are described in references [3], [18], and [19] respectively. The geometric details of the compressors (those necessary to perform the simulation) are presented in Tables I and II, and the compressor and throttle characteristics are shown in Figures 3, 4, and 5. Note the following deviations from strict physical interpretation of the model parameters:

- 1) The Greitzer 'B' parameter [5] is set to 0.1 in the experimental compressors - this represents in all cases a 'worst case' maximum. Even using this maximum, the surge dynamics are very stable for the experiments we will present; thus we have for Equations (6,7)

$$\bar{\phi} \equiv \phi_T(\bar{\psi}) ; \quad (16)$$
$$\bar{\psi} \equiv [\psi_C(\bar{\phi} + \delta\phi)]_{a.a.}$$

i.e. the mean flow will follow the throttle characteristic very closely in these experiments.

- 2) The unsteady loss parameter is set to 0.3 in all three compressors. A priori prediction of this parameter is difficult [18], so we have chosen to use an approximate value which is the same for all three compressors. The value chosen is roughly the non-dimensional convection time across one blade row (which happens to be approximately the same in all three compressors).
- 3) Two simulations will be presented for each compressor. The first will use the geometrically determined value of λ , and the second will use an 'effective λ ',

which has been adjusted to account for the rotation frequency change caused by unsteady losses. Since only the damping effect of unsteady losses are currently modeled in the simulation, this approach is deemed appropriate (see [20]). λ is the only parameter (in the simple version of the model presented here) which can be used to change the frequency of rotating stall - modeling other effects (which do in fact increase the rotating stall frequency) would require additional dynamics in the simulation.

In order to determine the compressor characteristics in Figures 3-5, the following procedure was followed: First, the experimental data for each compressor was fit with polynomial segments. The experimental data extends only to the mark 'X' on each figure, because beyond this point the compressor is unstable and does not operate axisymmetrically. The region between the 'X' and the 'O' marks on these figures is the actively stabilized region of operation. Compressors C1 and C2 have had their stable operating range augmented through active control. This allows us to more fully characterize the compressor characteristic in a very important region for this study; when the active control is switched off in these compressors, nonlinear stall inception proceeds from the operating point 'O', and the region between the 'O' and the 'X' is the first region accessed by transient velocity perturbations.

The next step in determining Ψ_C is to utilize the simulation to qualitatively iterate on the correct shape for its unstable part. This trial-and-error procedure is necessary because no directly measured data for Ψ_C exist in this unstable region. Our hypothesis is that stall inception provides a measure of the effects of Ψ_C which is distinct enough to allow the deduction of the shape of Ψ_C beyond the measurable range. Such deduction requires an understanding of the impact of various 'shape parameters' for Ψ_C on stall inception behavior. Implicit in this approach is the assumption, which we will verify through application, that the character and qualitative features of the stall inception process are driven primarily by the nonlinearities, and that informed choices for the shape of the unstable side of the characteristic can be made which allow the qualitative stall inception features to be simulated.

Several features of the shape of the unknown part of Ψ_C are shared by most compressors, so these provide a general framework within which to search. Pressure rise generally reaches a maximum at some flow coefficient, dropping off below this flow value due to separation and other loss-producing factors at low flows. During reverse flow (negative $\delta\phi$), however, pressure rise becomes roughly

quadratic and increasing, because the compressor looks roughly like a throttle to reverse flow. The details of the drop in pressure rise below the peak, the depth of the low-pressure-rise region between zero flow and the peak, and the steepness of Ψ_C for negative flow values are the parameters which are adjusted to attempt to match the experimental stall inception behavior.

For our purposes, the most important feature of Ψ_C is its shape near the peak -specifically its steepness on the unstable (low flow side) compared to the stable (high flow) side of the peak. Compressor C1 is steeper on the stable side than the unstable side over a large range of flow coefficients. Compressor C2 is roughly symmetrical about its peak, and compressor C3 has a steeper slope on the unstable side. (See Figures (3-5)). This qualitative observation may be made conceptually precise by specifying the sign of the leading coefficient of a cubic polynomial fit to the peak of the characteristic:

$$\Psi_C(\phi) = A\phi^3 + B\phi^2 + C\phi + D \quad (17)$$

With this description of the peak, C1 would have $A < 0$, C2 would have $A = 0$ and C3 would have $A > 0$.

Differences in the shape of Ψ_C near its peak are used to account for the observed differences in stall inception behavior. The other features mentioned above are chosen so that the simulation gives roughly the measured magnitude and depth of the fully developed stall cell; these are less important for stall inception than the conditions around the peak, at which stall inception occurs.

Figures 3-5 also show the transient of the annulus-averaged operating point during the transition into rotating stall. Note that the annulus-averaged compressor *no longer operates on the axisymmetric characteristic* - although the local flow does. Since most compressors are tested using only annulus averaged measurements, their measured characteristics *cannot be considered as the axisymmetric (local) characteristic* for use in 2-D simulations. Conversely, when one studies the 1-D dynamics of a compression system, the axisymmetric characteristic should *not* be used: The 1-D dynamic system sees the 1-D (annulus averaged) effect of rotating stall, so this effect should be modeled by using the annulus-averaged compressor characteristic, which, for the compressors tested here, is a discontinuous, dual-valued function (due to hysteresis in rotating stall recovery).

The unstable parts of the compressor characteristics presented in Figures 3-5 are the results of our search, in each case, for the shape of Ψ_C beyond the peak that allows the simulation to best mimic the experimentally observed stall inception

behavior. The 'best fits' to the transient data obtained in this way are shown in Figures 6, 7, and 8. In all cases the salient features are similar between the experiment and simulation, although the three compressors have very different stall inception behavior. Compressor C1 has a very long, slow growth of perturbation waves into rotating stall. Compressor C2, on the other hand, has relatively small perturbation waves, followed by a sharp inception wave which leads quickly into fully developed rotating stall. Compressor C3 is even more severe in this regard: nonlinear influences are seen while the waves are still quite small, and the stall wave grows extremely quickly into violently a nonlinear event.

It is clear from Figures 6-8 that during stall inception (and even during fully developed stall) the proper choice of the shape of Ψ_C can allow experimental observations to be closely modeled by the Moore-Greitzer model. It is also clear that without the adjustment of λ , the model is only qualitatively correct; the rotation frequency is not well predicted by the basic model presented in Equation (13). The explanation for this behavior is given by Hendricks et. al. [18] for the linearized case; extension of the nonlinear model to include the unsteady loss effects they discuss (as well as other effects, such as swirl sensitivity and deviation) is here approximated by increasing λ so that the rotation frequencies match. With this adjustment (which we feel is justified due to its basis in the extended model [18],[20]), the ability of the simulation to capture the nonlinear stall inception behavior is remarkable for compressors C1 and C2. The discrepancies in C3 will be discussed in the next section.

Discussion

To understand the influence of Ψ_C on stall inception, consider a sinusoidal velocity perturbation being mapped through a compressor characteristic, shown in Figure 9. Here it is clear that at the peak of the characteristic, a linear representation of is rarely sufficient; the slope of the characteristic is near zero, so higher order derivatives become important. The high velocity portion of the wave experiences attenuating pressure forces, because it accesses the stable side of the characteristic, while the low flow side experiences destabilizing pressure forces. Because of the interaction caused by partials with respect to θ and τ (Equation 8), the pressure rise does not act alone to accelerate the flow. Instead there is an 'integrating action' of, for instance, the first sinusoidal harmonic. If the integral effect of the positive and negative parts of the characteristic causes a net attenuating effect, then the wave will

die away (or converge to a small amplitude limit cycle). If the integral effect is amplifying, the wave will continue to grow, with a speed which depends at each instant on the wave shape and its mapping through Ψ_C .

The two extremes of this general behavior are: 1) extremely gradual characteristics, whose behavior can be adequately characterized using a linearized analysis (with the proper choice of slope), and 2) characteristics which have very abrupt changes in slope. In the latter case (when the unstable side is much steeper ($A>0$), as in Figure 9), a sharp drop in pressure rise is experienced by the low-flow part of the wave (if it is large enough to access the sharp change in slope). This pressure drop overrides other influences and causes a quick, *localized* deceleration of the flow (as in Figure 8). The drop in flow further reduces the overall pressure rise delivered by the compressor, which moves the mean operating point towards lower values (in order to satisfy the throttle characteristic, Equation 16). The system is thus 'dragged' into rotating stall at a rate which is premature when viewed from a linearized standpoint. In fact, with the proper initial condition, some compressor models can go into stall while they are at annulus-averaged operating points which are still 'stable' in the linearized sense. In these cases, the domain of attraction of the operating point has become very small, because of the existence of a nearby abrupt change in the nonlinear mapping Ψ_C .

Of somewhat secondary importance to the stall inception behavior is the slope of the throttle characteristic, Ψ_T . If Ψ_T is steep at the nominal operating point ($\partial\Psi_T/\partial\bar{\phi}$ large), the annulus-averaged flow coefficient is insensitive to changes in the pressure rise delivered by Ψ_C . This is the case in C1 (Figure 6), in which the throttle discharges to a plenum below atmospheric pressure, so the throttle line is very steep during stall initiation. This, combined with the shape of Ψ_C , accounts for the slow transient into rotating stall.

When Ψ_T is shallow ($\partial\Psi_T/\partial\bar{\phi}$ small), on the other hand, the nonlinearity of Ψ_C couples more immediately into changes in the mean flow as follows: Ψ_C maps energy from higher harmonics into the zeroth harmonic (this effect is represented by the function $[\Psi_C(\bar{\phi} + \delta\phi)]_{a.a.}$, and can be seen in Figure 9). This causes a loss in annulus-averaged pressure rise, which must be accompanied by a relatively large drop in $\bar{\phi}$, if Ψ_T is shallow (see Equation (18)). Thus the rate at which the system is 'dragged' into rotating stall depends in part on the slope of Ψ_T . Compressor C3 is the best example of this type of behavior - the transient from stall inception to fully developed stall is well under one rotor revolution, partially because of the shape of Ψ_T .

Figure 8 indicates that there is a bigger discrepancy between the simulated and the measured stall inception behavior for compressor C3 than for C1 and C2. Several factors contribute to this discrepancy. Most important is the effect of non-axial flow on the measurements. Hot-wire anemometers are used to measure the flow velocity in the experiments; these devices effectively measure the *absolute value* of axial *plus* radial flow perturbations. In the C3 experiment, the hot wires are mounted very close to the compressor face ($\eta = 0$), where significant non-axial and reverse flow perturbations exist. In the C1 and C2 experiments, on the other hand, the hot wires are mounted further upstream of the compressor ($\eta = -0.5$ and $\eta = -0.2$ respectively) where the measured perturbations are primarily axial; a 'fluid dynamic filter' exists (Equation (11)) which smoothes out the internal flow details, allowing the more global influences (those modeled by Moore-Greitzer) to be observed.

The philosophy that modeling global effects is sufficient for studying transient rotating stall behavior is not universally applicable in low-speed axial compressors. Day [19] has measured stall inception behavior which *must* be observed in detail to be fully understood. In such cases, the Moore-Greitzer model requires further refinement; radial flow effects as well as secondary flows may need to be at least partially accounted for to properly model these stall phenomena. Including these effects would make the model 3-dimensional (radial variations not ignored) instead of 2-dimensional, and increase their complexity considerably.

Another important conclusion that one can draw from the results presented here is that nonlinear effects, when they are important, often manifest themselves as *high spatial frequencies* in the stall transients. In both C2 and C3, the rotating stall precursor wave starts as a sinusoidal wave (first spatial harmonic). During stall inception, however, significant spatial harmonic content above the first harmonic exists in the wave shape as it transitions into rotating stall. Figure 9 is an example of how this comes about - it shows a first harmonic perturbation $\delta\phi$ being transformed into a 2nd harmonic acceleration term $\delta\psi$. Figure 10 shows the result - during stall inception, what began as a 1st harmonic perturbation becomes a multi-harmonic perturbation, eventually transitioning again to a 1st-harmonic dominated fully developed stall cell. This complex behavior may indicate that approximations which model only the first spatial harmonic (Galerkin approximation, [7]) do not capture the important nonlinear effects *at stall inception* accurately enough to allow realistic control law design.

Conclusions

A nonlinear, control-theoretic form for the Moore-Greitzer model has been presented. This form is sufficient to accurately model nonlinear stall-inception behavior provided a) the unstable part of the compressor characteristic is properly adjusted, and b) the effects of unsteadiness on the pressure rise delivered by the compressor are included (either theoretically, as in [18], or approximately, which involves adjusting the inertia parameter λ). Stall inception, rather than fully developed stall, is used as a means to verify the Moore-Greitzer model of rotating stall. The effects of the shape of the pressure rise characteristic have been elucidated through evaluation and comparison of experimental and simulation results. The most important conclusions are:

- a) The steepness of the characteristic on its unstable side compared to its stable side determines, to a large extent, the character of stall inception.
- b) second and higher harmonics often interact strongly with the first harmonic during stall inception.

References

1. Greitzer, E. M., "Review - Axial Compressor Stall Phenomena," *ASME Journal of Fluids and Engineering*, vol. 102, 1980, pp. 134-151.
2. Ludwig, G. R., and Nenni, J. P., "Tests of an Improved Rotating Stall Control System on a J-85 Turbojet Engine," *ASME Paper 80-GT-17*, presented at the Gas Turbine Conference and Products Show, New Orleans, March 10-13, 1980.
3. Paduano, J.D., Epstein, A.H., Greitzer, E.M., and Valavani, L., "Active Control of Rotating Stall," *ASME Paper 91-GT-88*, Proceedings, ASME International Gas Turbine Conference, Orlando, June 1991 (to be published in *Journal of Turbomachinery*).
4. Day, I. J., "Active Suppression of Rotating Stall and Surge in Axial Compressors," presented at the 1991 ASME International Gas Turbine Institute Conference, Orlando, June 1991.
5. Moore, F. K., "A Theory of Rotating Stall of Multistage Compressors, Parts I-III," *ASME Journal of Engineering for Power*, Vol. 106, 1984, pp. 313-336.

6. Moore, F. K. and Greitzer, E. M., "A Theory of Post-Stall Transients in Axial Compression Systems, Part I - Development of Equations, and Part II - Application," *ASME Journal of Engineering for Gas Turbines and Power*, Vol. 108, 1986, pp. 68-97.
7. Greitzer, E. M., "Surge and Rotating Stall in Axial Flow Compressors, Part I: Theoretical Compression System Model, and Part II: Experimental Results and Comparison with Theory," *ASME Journal of Engineering for Power*, April, 1976, pp. 190-216.
8. Pinsley, J. E., Guenette, G. R., Epstein, A. H., and Greitzer, E. M., "Active Stabilization of Centrifugal Compressor Surge," *Proceedings, ASME International Gas Turbine Institute Conference*, Brussels, June 1990.
9. Gysling, D. L., Dugundji, J., Greitzer, E. M., and Epstein, A. H., "Dynamic Control of Compressor Surge using Tailored Structures," *Proceedings, ASME International Gas Turbine Institute Conference*, Brussels, June 1990.
10. Paduano, J. D., "Active Control of Rotating Stall," Ph.D. Thesis, MIT Department of Aeronautics and Astronautics, February 1992.
11. Haynes, J., "Active Control of Rotating Stall in a Three-Stage Axial Compressor," S.M. Thesis, MIT Department of Aeronautics and Astronautics, September, 1992.
12. Liaw, D. C., Adomaitis, R. A., and Abed, E. H., "Two-Parameter Bifurcation Analysis of Axial Flow Compressor Dynamics," *American Control Conference*, Boston, June 1991.
13. Simon, J. S., and Valavani, L., "A Lyapunov Based Nonlinear Control Scheme for Stabilizing a Basic Compression System Using a Close-Coupled Valve," *American Control Conference*, Boston, June 1991.
14. Fink, D. A., "Surge, Dynamics and Unsteady Flow Phenomena in Centrifugal Compressors," Ph.D. Thesis, MIT Department of Aeronautics and Astronautics, June, 1988.
15. Lavrich, P. L., "Time Resolved Measurements of Rotating Stall in Axial Flow Compressors," Ph. D. Thesis, MIT Department of Aeronautics and Astronautics, August, 1988.
16. Hynes, T. P. and Greitzer, E. M., "A Method of Assessing Effects of Circumferential Flow Distortion on Compressor Stability," *ASME Journal of Engineering for Gas Turbines and Power*, Vol. 109, 1986 pp. 371-379.

17. McCaughan, F. E., and Hong, X. X, "Stability of Fully Developed Rotating Stall," Presented at the International Gas Turbine and Aeroengine Congress and Exposition, Cincinnati, Ohio June 1-4 1992.
18. Hendricks, G., Haynes, J., and Epstein, A. H., "The Effect of Unsteady Compressor Response on Stall Inception," to be presented at the International Gas Turbine and Aeroengine Congress and Exposition, Cincinnati, Ohio, June 1993.
19. Day, I. J., "Stall Inception in Axial Flow Compressors," presented at the 1991 ASME International Gas Turbine Institute Conference, Orlando, June 1991.
20. Chue, R., Hynes, T. P., Greitzer, E. M., Tan, C. S., Longley, J. P., "Calculations of Inlet Distortion Induced Compressor Flow Field Instability," *International Journal of Heat and Fluid Flow*, Vol. 10, 1989, pp. 211-223.
21. Hanson, K. E., Jorgenson, P., and Larsen, P. S., "Experimental and Theoretical Study of Surge in a Small Centrifugal Compressor," *Journal of Fluids Engineering*, Vol. 103, pp. 391-395 September 1981.

Table I - Compressor Model Parameters

	<u>C1</u>	<u>C2</u>	<u>C3</u>
U (speed at mean wheel radius)	73 m/s	72 m/s	36 m/s
R (wheel radius)	0.259 m	0.287 m	0.686 m
$\bar{\phi}$ at stall inception	0.433, 0.445	0.467	0.433
K_T at stall inception	8.1, 8.6	9.38	6.25
l_c	8.0	6.66	4.75
B	0.1	0.1	0.1
m	2	2	2
μ	0.65	1.29	0.42
λ	0.18	0.68	0.25
λ_{eff} (see [20], adjusted to match frequencies)	0.48	0.95	0.4
measurement position	$\eta = -0.5$	$\eta = -0.2$	$\eta = 0$
nondim. convection time (used for unsteady loss approximation)	0.3	0.3	0.3

Table II - Compressor Characteristics

C1:

$$\psi_C(\phi) = \begin{cases} 1.9753\cdot\phi^2 - 0.098765\cdot\phi + 0.051235 & ; \phi \leq 0.025 \\ -12.776\cdot\phi^3 + 6.3946\cdot\phi^2 - 0.29577\cdot\phi + 0.053597 & ; 0.025 < \phi \leq 0.30 \\ -5.5363\cdot\phi^4 + 7.7202\cdot\phi^3 - 4.2045\cdot\phi^2 + 1.1276\cdot\phi + 0.071953 & ; \phi > 0.30 \end{cases}$$

C2:

$$\psi_C(\phi) = \begin{cases} 12.117\cdot\phi^2 - 2.4235\cdot\phi + 0.22117 & ; \phi \leq 0.1 \\ -49.624\cdot\phi^3 + 39.509\cdot\phi^2 - 6.4130\cdot\phi + 0.39584 & ; 0.1 < \phi \leq 0.40 \\ -10.0695\cdot\phi^2 + 9.4301\cdot\phi - 1.1848 & ; \phi > 0.40 \end{cases}$$

C3:

$$\psi_C(\phi) = \begin{cases} 4\phi^2 - 2\phi + 0.5 & ; \phi \leq 0.25 \\ -143.14\cdot\phi^3 + 143.04\cdot\phi^2 - 44.683\cdot\phi + 4.7172 & ; 0.25 < \phi \leq 0.405 \\ -13.365\cdot\phi^2 + 11.574\cdot\phi - 1.9206 & ; 0.405 < \phi \leq 0.4638 \\ -5.4283\cdot\phi^2 + 4.2112\cdot\phi - 0.21325 & ; \phi > 0.4638 \end{cases}$$

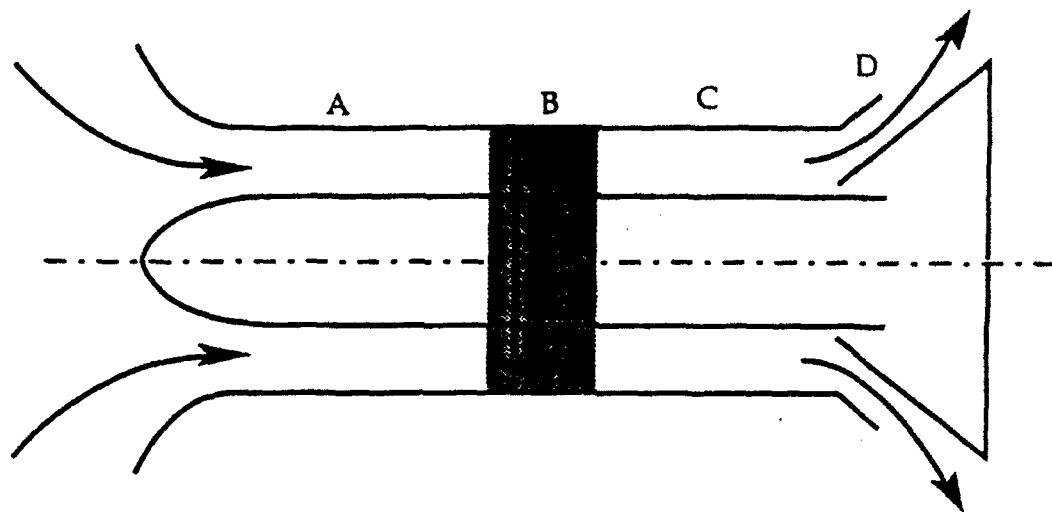


Figure 1 - Compression system components: A - inlet duct, B - compressor, C - downstream duct, D - throttle.

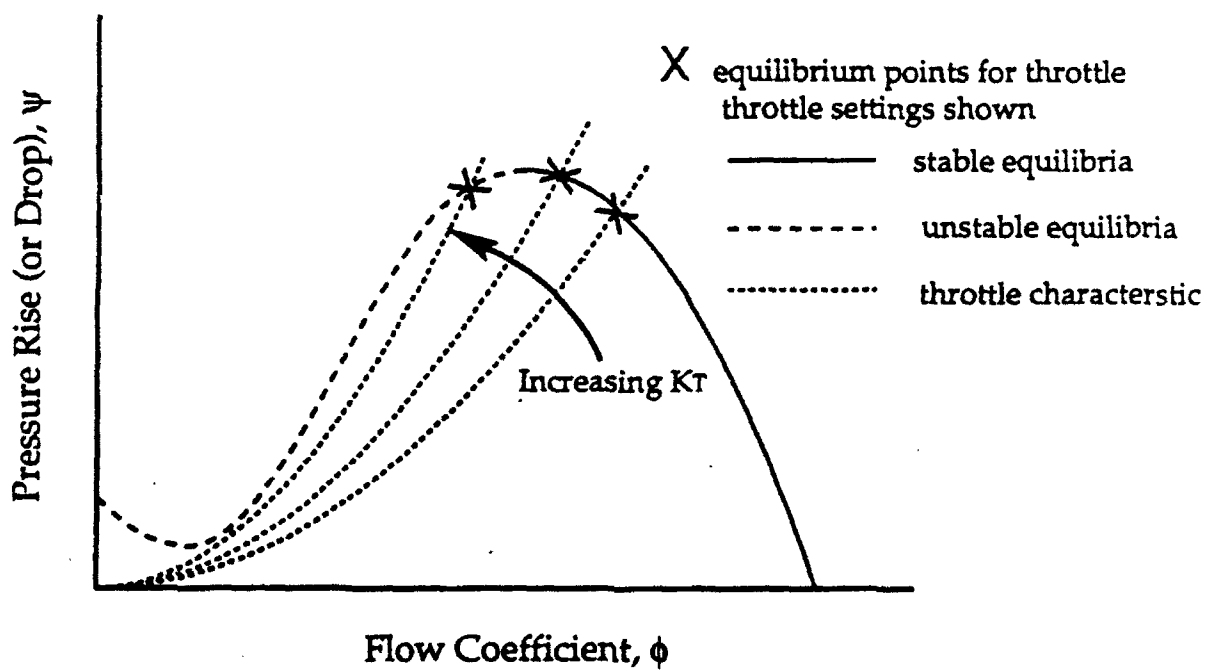
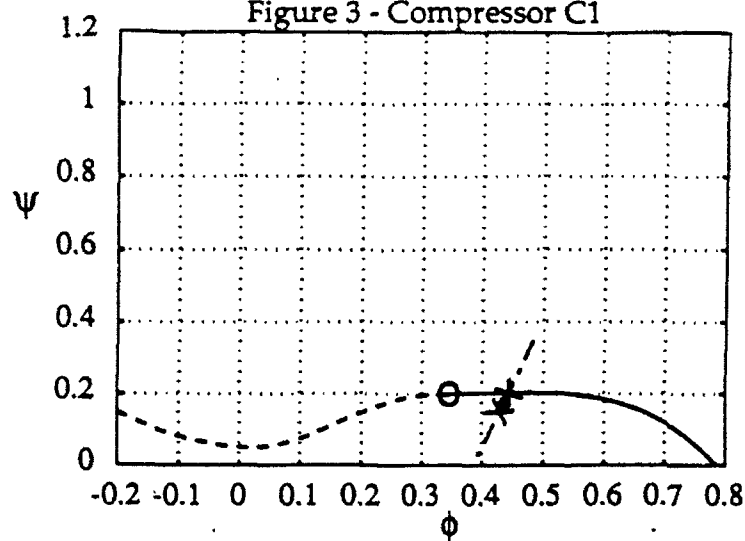


Figure 2 - Compressor and throttle behavior during a typical experimental test.

Figure 3 - Compressor C1



Legend

Known part of compressor characteristic

Estimate of unknown part of compressor characteristic (based on simulation tests)

Transient into rotating stall

Throttle Characteristic

+

Beginning and ending points for the transient into rotating stall

○

Lowest value at which compressor characteristic has been measured

Figure 4 - Compressor C2

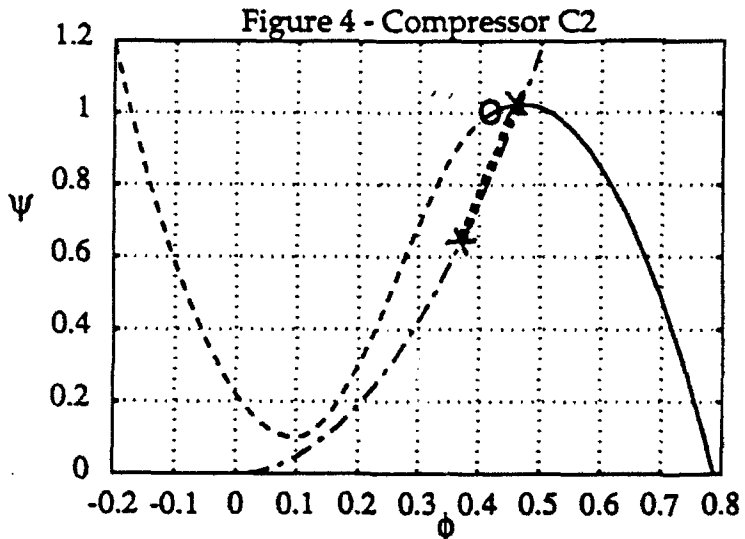
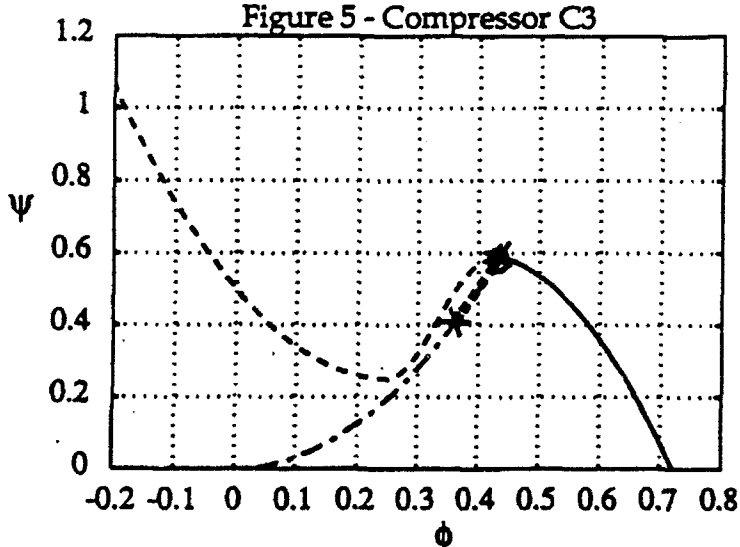
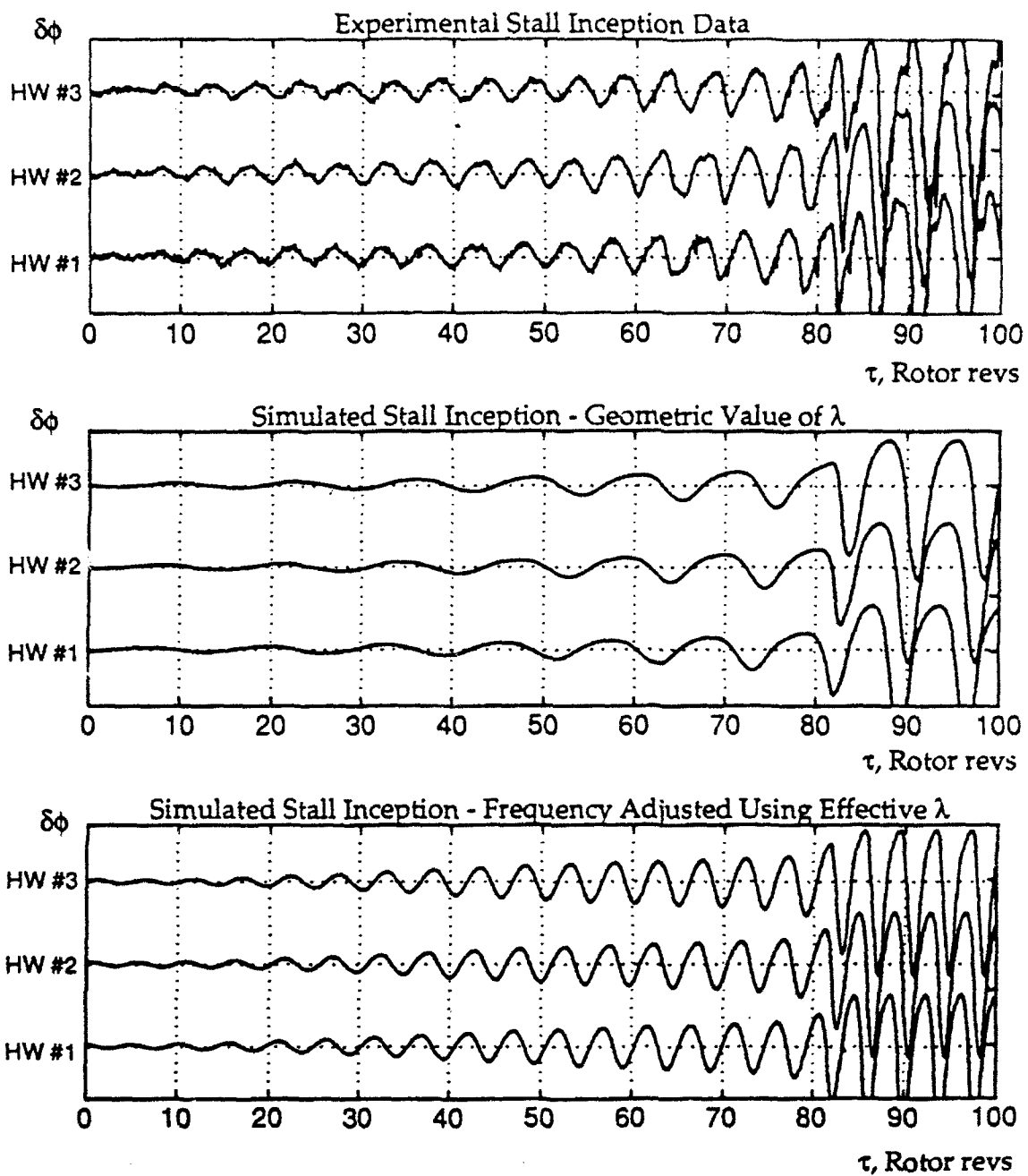


Figure 5 - Compressor C3



Figures 3-5 - Compressor and throttle characteristics used to simulate rotating stall inception in compressors C1, C2, and C3. Transients of annulus average (a.a.) pressure vs. flow during stall inception are also shown.



SCALE:

$$\delta\phi = 0.2$$

SENSOR LOCATIONS:

$$\eta = -0.5$$

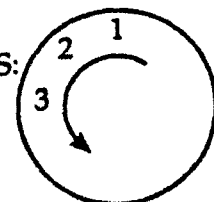


Figure 6 - Comparison of Experimental and Simulated Stall Inception for Compressor C1.

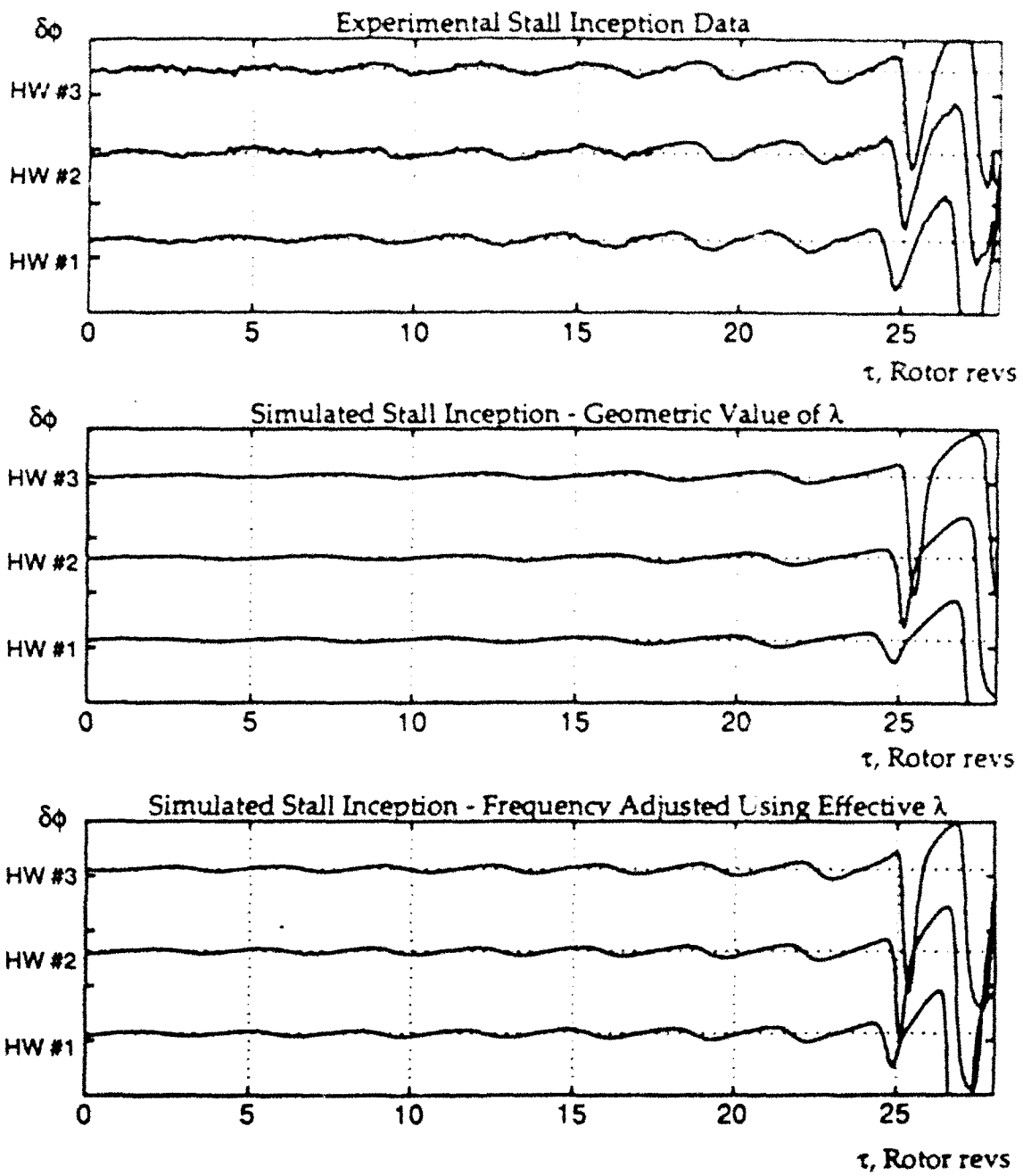
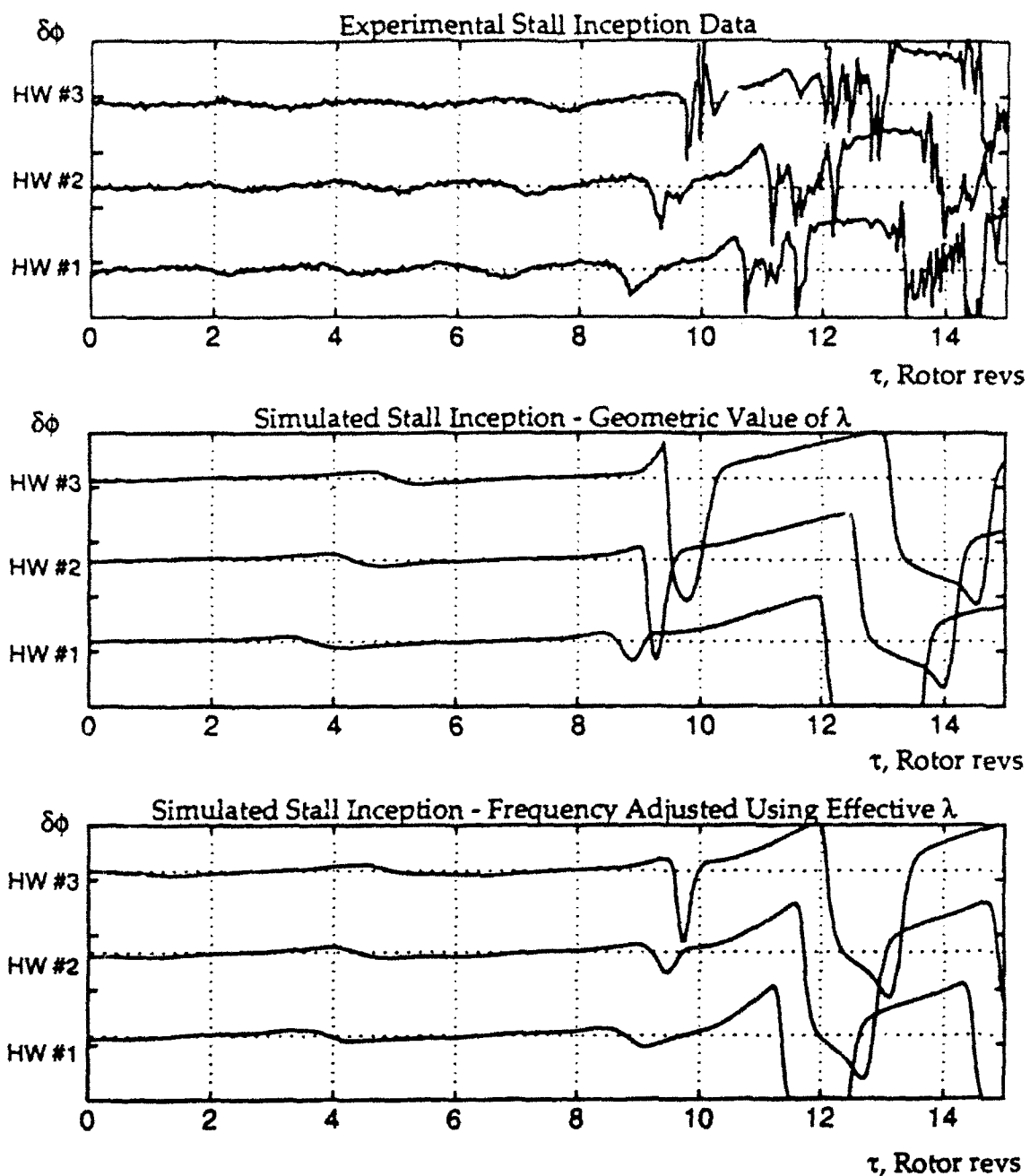


Figure 7 - Comparison of Experimental and Simulated Stall Inception for Compressor C2.



SCALE:
 $\delta\phi = 0.2$

SENSOR LOCATIONS:
 $\eta \approx 0$

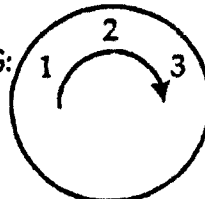


Figure 8 - Comparison of Experimental and Simulated Stall Inception for Compressor C3.

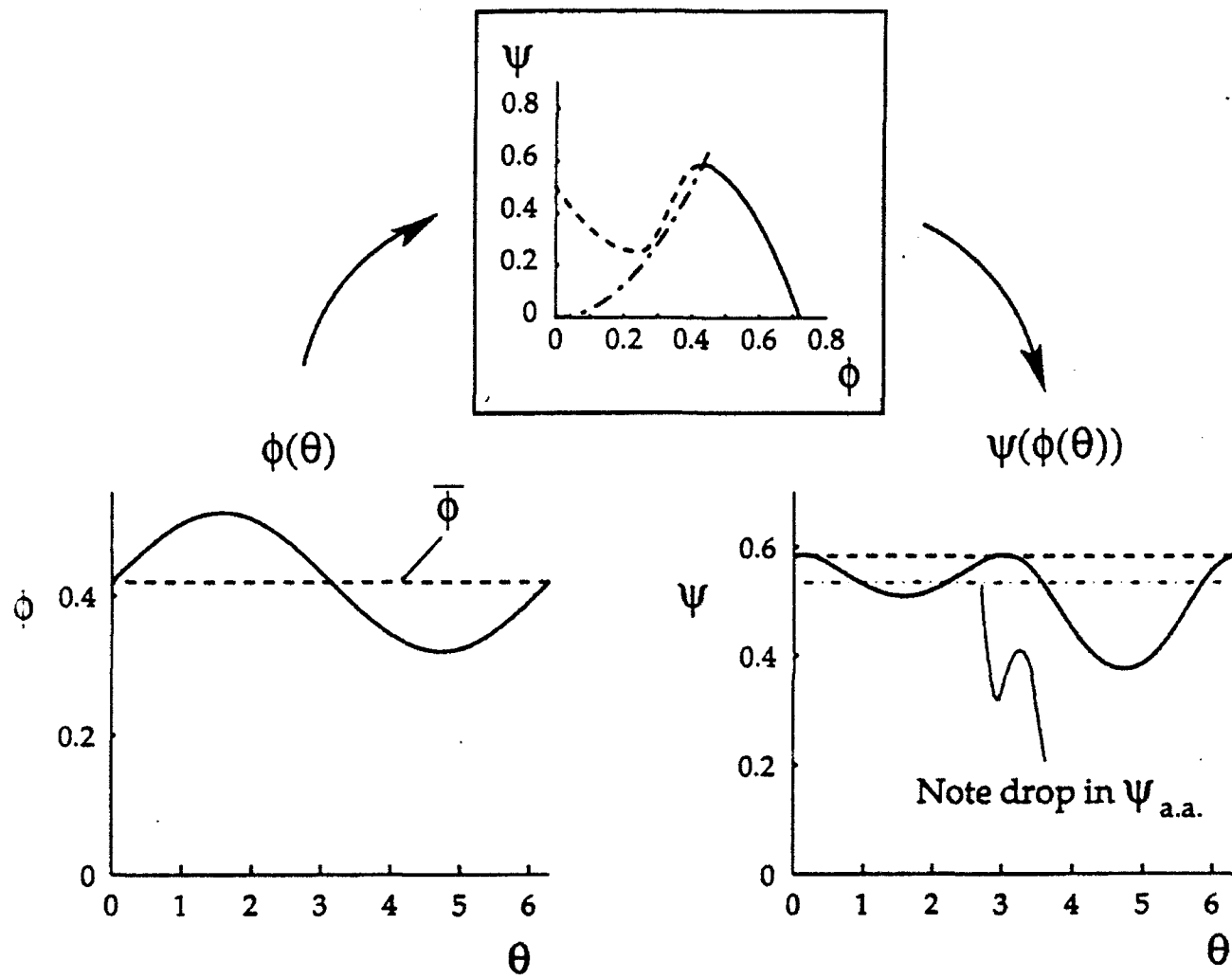


Figure 9 - Effect of nonlinear characteristic on pressure forces which act to accelerate a velocity perturbation. Pressure forces (on right) below the mean value act to decelerate the flow. Note the significant crossfeed between the first harmonic and the zeroth and second harmonics.

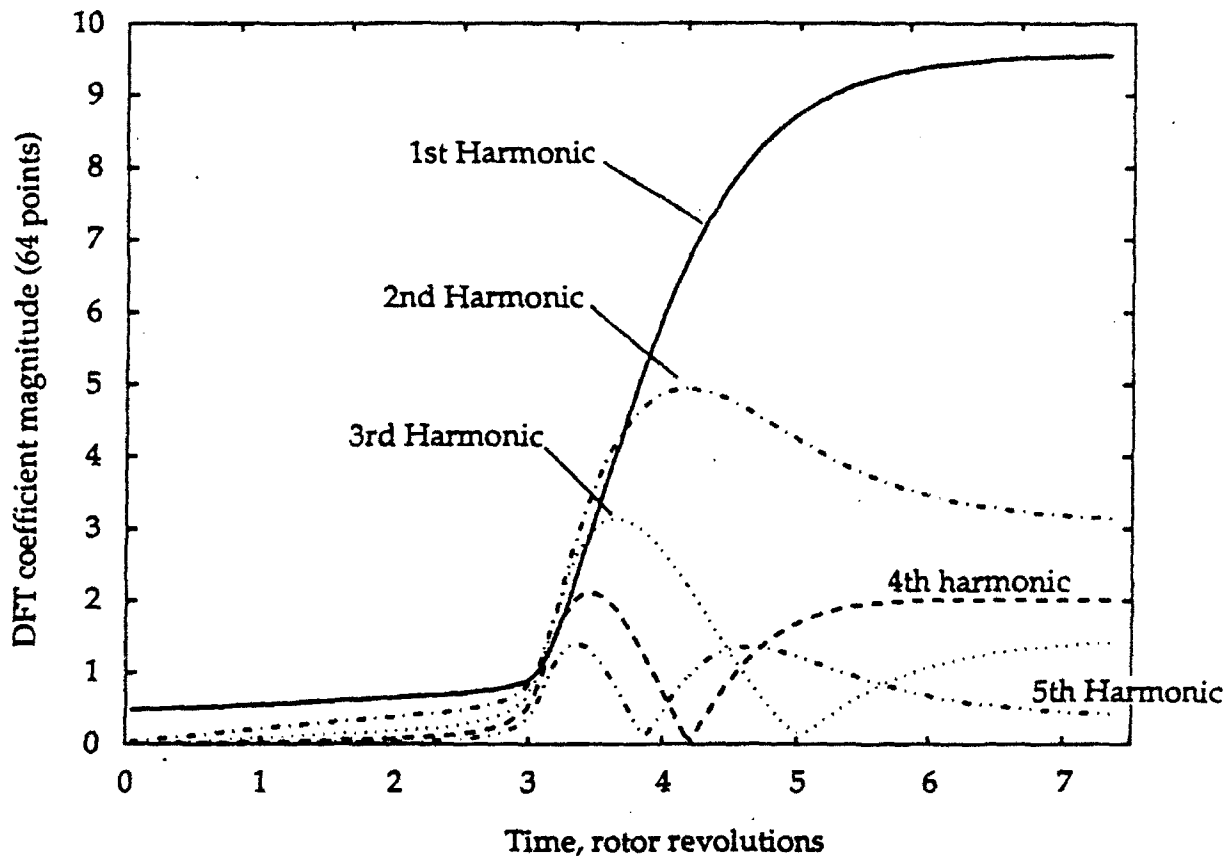


Figure 10 - Participation of 1st 5 Fourier harmonics in stall inception. Note that harmonics 2 and 3 temporarily become larger than the 1st harmonic during stall inception. Simulation results are for compressor C3 (same as Fig. 8).

III. ACTIVE CONTROL OF ROTATING STALL EXPERIMENTS



Active Control of Rotating Stall in a Low Speed Axial Compressor

J. PADUANO, A. H. EPSTEIN, L. VALAVANI, J. P. LONGLEY*, E. M. GREITZER, G. R. GUENETTE

Gas Turbine Laboratory
Massachusetts Institute of Technology
Cambridge, MA 02139

ABSTRACT

The onset of rotating stall has been delayed in a low speed, single-stage, axial research compressor using active feedback control. Control was implemented using a circumferential array of hot wires to sense rotating waves of axial velocity upstream of the compressor. Circumferentially travelling waves were then generated with appropriate phase and amplitude by "wiggling" inlet guide vanes driven by individual actuators. The control scheme considered the wave pattern in terms of the individual spatial Fourier components. A simple proportional control law was implemented for each harmonic. Control of the first spatial harmonic yielded an 11% decrease in the stalling mass flow, while control of the first and second harmonics together reduced the stalling mass flow by 20%. The control system was also used to measure the sine wave response of the compressor, which behaved as would be expected for a second order system.

NOMENCLATURE

C_n	complex spatial Fourier coefficient (Eq. (5))
IGV	inlet guide vane
n	mode number
P	static pressure
P_T	total pressure
R_n	controller gain ($R_n = Z_n $)
r	mean compressor radius
\tilde{t}	non-dimensional time ($= Ut/r$)
U	mean compressor blade speed
V_k	axial velocity measurement (Eq. (5))
Z_n	controller complex gain and phase
β_n	controller phase for n 'th mode ($\beta_n = Z_n $)
γ	IGV stagger angle
$\delta(\cdot)$	perturbed quantity
θ	circumferential coordinate
λ	rotor inertia parameter
μ	rotor + stator inertia parameter

* Current Address: Whittle Laboratory, Cambridge University, Cambridge, England

μ_{IGV}	IGV inertia parameter
ρ	density
ϕ	local flow coefficient (axial velocity/U)
$\bar{\phi}$	area averaged flow coefficient
ψ	compressor pressure rise ($P - P_T$) / (ρU^2)

Subscripts

n	n 'th circumferential Fourier mode
R	real part of complex quantity
I	imaginary part of complex quantity

INTRODUCTION

Axial compressors are subject to two distinct aerodynamic instabilities, rotating stall and surge, which can severely limit compressor performance. Rotating stall is characterized by a wave travelling about the circumference of the machine, surge by a basically one-dimensional fluctuation in mass flow through the machine. Whether these phenomena are viewed as distinct (rotating stall is local to the blade rows and dependent only on the compressor, while surge involves the entire pumping system -- compressor, ducting, plenums, and throttle) or as related (both are natural modes of the compression system with surge corresponding to the zeroth order mode), they generally cannot be tolerated during compressor operation. Both rotating stall and surge reduce the pressure rise in the machine, cause rapid heating of the blades, and can induce severe mechanical distress.

The traditional approach to the problem of compressor flow field instabilities has been to incorporate various features in the aerodynamic design of the compressor to increase the stable operating range. Balanced stage loading and casing treatment are examples of design features that fall into this category. More recently, techniques have been developed that are based on moving the operating point close to the surge line when surge does not threaten, and then quickly increasing the margin when required, either in an open or closed loop manner. The open loop techniques are based on observation, supported by many years of experience, that compressor stability is strongly influenced by inlet distortions and by pressure transients caused by augmentor ignition and, in turn, that inlet distortion can be correlated with aircraft angle of attack and yaw angle. Thus, significant gains have been realized by coupling

the aircraft flight control and engine fuel control so that engine operating point is continually adjusted to yield the minimum stall margin required at each instantaneous flight condition (Yonke et al., 1987).

Closed loop stall avoidance has also been investigated. In these studies, sensors in the compressor were used to determine the onset of rotating stall by measuring the level of unsteadiness. When stall onset was detected, the control system moved the operating point to higher mass flow, away from the stall line (Ludwig and Nenni, 1980). While showing some effectiveness at low operating speeds, this effort was constrained by limited warning time from the sensors and limited control authority available to move the compressor operating point.

This paper presents the initial results of an alternative and fundamentally different means for attacking the problem posed by rotating stall. Here, we *increase* the stable flow range of an axial compressor by using closed loop control to damp the unsteady perturbations which lead to rotating stall. In contrast to previous work, this dynamic stabilization concept increases the stable operating range of the compressor by moving the stall point to lower mass flows, as illustrated conceptually in Fig. 1. There appear to be at least two advantages of this new technique. One is that engine power always remains high with dynamic stabilization while power must be cut back with stall avoidance (often at critical points in the flight envelope). A second advantage is that the gain in operating range can be potentially greater. In the following sections, we briefly describe those elements in the theory of compressor stability that are relevant to active stability enhancement, discuss the design of the experimental apparatus, and present the experimental results.

Conceptual View of Compressor Stability and Active Stall Control

We consider rotating stall to be one of the class of natural instabilities of the compression system, as analyzed for example by Moore and Greitzer (1986) for low-speed machines of high hub-to-tip radius ratio. Their model predicts that the stability of the compressor is tied to the growth of an (initially small amplitude) wave of axial velocity which travels about the circumference of the

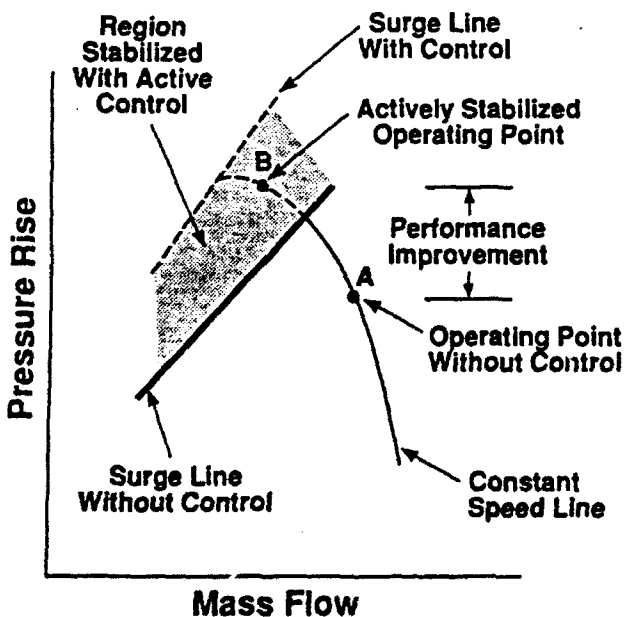


Fig. 1: The intent of active compressor stabilization is to move the surge line to lower mass flow

compressor. If the wave decays (i.e. its damping is greater than zero), then the flow in the compressor is stable. If the wave grows (wave damping negative), the flow in the compressor is unstable. Thus, wave growth and compressor flow stability are equivalent in this view.

One prediction of this model that is useful for present purposes is that rotating waves should be present at low amplitude prior to stall. McDougall (1988, 1989) has identified these waves in a low speed, single-stage compressor, and Garnier, et al (1990) observed them in both a single and a three-stage low speed compressor, and in a three-stage high speed compressor. The waves were often evident long (ten to one hundred rotor revolutions) before stall. It was found that the waves grew smoothly into rotating stall, without large discontinuities in phase or amplitude, and that the wave growth rate agreed with the theory of Moore and Greitzer (1986). Further, the measurements showed how the wave damping, and thus the instantaneous compressor stability, could be extracted from real time measurements of the rotating waves.

In 1989, Epstein, Ffowcs Williams, and Greitzer suggested that active control could be used to artificially damp these rotating waves when at low amplitude. If, as the theory implies, rotating stall can be viewed as the mature form of the rotating disturbance, damping of the waves would prevent rotating stall from developing, thus moving the point of instability onset as in Fig. 1. It was proposed that the compressor stability could be augmented by creating a travelling disturbance with phase and amplitude based on real time measurement of the incipient instability waves. This paper presents an experimental investigation of this idea.

The basic concept is to measure the wave pattern in a compressor and generate a circumferentially propagating disturbance based on those measurements so as to damp the growth of the naturally occurring waves. In the particular implementation described herein, shown schematically in Fig. 2, individual vanes in an upstream blade row are "wiggled" to create the travelling wave velocity disturbance. The flow which the upstream sensors and the downstream blade rows see is a combination of both the naturally occurring instability waves and the imposed control disturbances. As such, the combination of compressor and controller is a different machine than the original compressor - with different dynamic behavior and different stability.

At this point, it is appropriate to present the rotating stall model and connect it with the idea of control. Here, it is the structure of the model that is most important rather than the fluid mechanic details. Since the structure provides a framework for design of the control system, the quantitative details can be derived by fitting experimental data to the model.

The existing models for rotating stall inception in multi-row

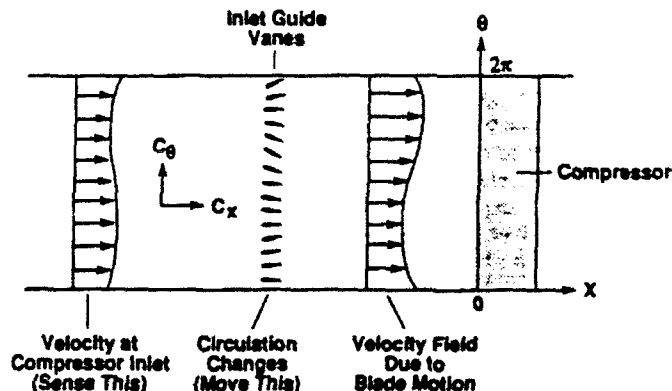


Fig. 2: Conceptual control scheme using "wiggly" inlet guide vanes to generate circumferential travelling waves

axial compressors are typified by an equation for the velocity and pressure perturbations of the form

$$\frac{\delta P_{\text{compressor}} - \delta P_{\text{compressor}}}{\rho U^2} = \frac{\delta \phi}{\delta \theta} - \lambda \frac{\partial \delta \phi}{\partial \theta} - \mu \frac{\partial \delta \phi}{\partial t} \quad (1)$$

Here, δP and δP_T are the static and total pressure perturbations respectively, $\delta \phi$ is the non-dimensional axial velocity perturbation, λ and μ are non-dimensional parameters reflecting the fluid inertia in stator and rotor passages respectively, $(d\psi/d\phi)$ is the slope of the non-dimensional compressor characteristic, and t is a non-dimensional time, $t = tU/r$. Equation (1) has been shown in several publications (e.g. Hynes and Greitzer, 1987; Longley, 1988) and we will not present its development here. The equation is an expression of the matching conditions (across the compressor) for flowfields upstream and downstream of the compressor and, as such, upstream and downstream flow field descriptions are needed to be able to find a solution.

Using these, Longley (1990) has shown that one can put Eq. (1) in a wave operator form. For the n th spatial Fourier coefficient, this is

$$\left(\left(\frac{2}{|n|} + \mu \right) \frac{\partial}{\partial t} + \lambda \frac{\partial}{\partial \theta} \right) \delta \phi = \left(\frac{d\psi}{d\phi} \right) \delta \phi \quad (2)$$

The left-hand side of Eq. (2) is a convective operator corresponding to circumferential propagation with velocity $\lambda/(2/|n| + \mu)$ · (rotor speed). In addition, the growth rate of the wave is dependent on the slope of the compressor characteristic. If $(d\psi/d\phi)$ is positive the waves grow; if negative they decay. Neutral stability (wave travelling with constant amplitude) occurs at $(d\psi/d\phi) = 0$.

We can cast Eq. (2) in a form that is more useful for control by considering a purely propagating disturbance. The first Fourier mode will be of the form $e^{i\theta}$, so Eq. (2) can be written as

$$(2 + \mu) \frac{\partial \delta \phi}{\partial t} + \left[i\lambda - \left(\frac{d\psi}{d\phi} \right) \right] \delta \phi = 0 \quad (3)$$

Thus far, the equations presented have been for flow associated with uncontrolled compressor dynamics. If, in addition, we model the control as due to perturbations in IGV stagger, δy , we obtain the following equation for the first Fourier mode:

$$(2 + \mu) \frac{\partial \delta \phi}{\partial t} + \left[i\lambda - \left(\frac{d\psi}{d\phi} \right) \right] \delta \phi + \left[i\bar{\phi}\mu_{IGV} \left(\frac{\partial \psi}{\partial \phi} \right) - \left(\frac{\partial \psi}{\partial y} - \bar{\phi}\mu_{IGV} \lambda \right) \right] \delta \gamma - i\bar{\phi}\mu_{IGV} \left(1 + \mu - \frac{\mu_{IGV}}{2} \right) \frac{\partial \delta \gamma}{\partial t} = 0 \quad (4)$$

where $\bar{\phi}$ is the axisymmetric (annulus averaged) flow coefficient, μ_{IGV} is the fluid inertia parameter for the IGV's, and $(\partial \psi / \partial y)$ represents the incremental pressure rise obtainable from a change in IGV stagger, γ .

This is formally a first order equation for $\delta \phi$, however it must be remembered that the quantity of interest is the real part of $\delta \phi$. If we express $\delta \phi$ in terms of its real and imaginary parts, $\delta \phi = \delta \phi_R + i\delta \phi_I$, then Eq. (4), which is a coupled pair of first order equations for $\delta \phi_R$ and $i\delta \phi_I$, becomes mathematically equivalent to a second order equation for $\delta \phi_R$. The form thus used in the system identification discussed below is thus second order. Another way to state this is that a first order equation with a complex (or pure imaginary) pole is equivalent to a second order system in the

appropriate real valued states.

The second order model of compressor behavior is useful for two reasons. First, it can be tested experimentally in a straightforward manner. Second, it provides both a conceptual qualitative framework about which to design a control system (i.e. the stabilization of a second order system) and, given the results of the experimental test, the quantitative inputs required to do the control system design.

EXPERIMENTAL APPARATUS

A 0.52 meter diameter, single-stage low speed research compressor was selected as a test vehicle due to its relative simplicity. The general mechanical construction of the machine was described by Lee and Greitzer (1988), and the geometry of the build studied here is given in Table 1. The apparatus can be considered to consist of four sections: the compressor (described above), instrumentation for wave sensing, actuators for wave launching, and a signal processor (controller). The design of the last three components is discussed below.

TABLE 1
SINGLE-STAGE COMPRESSOR GEOMETRY

Tip Diameter	0.597 m		
Hub-to-Tip Ratio	0.75		
Axial Mach No.	0.10		
Operating Speed	2700 RPM		
	IGV	Rotor	Stator
Mean Line Stagger	0	35°	22.5°
Chamber Angle	0	25°	25°
Solidity	0.6	1	1
Aspect Ratio	0.9	2.0	1.9

The sensors used in the present investigation are eight hot wires evenly spaced about the circumference of the compressor, 0.5 compressor radii upstream of the rotor leading edge. The wires were positioned at midspan and oriented so as to measure axial velocity. Hot wires were chosen because their high sensitivity and frequency response are well suited to low speed compressors. The sensors were positioned relatively far upstream so that the higher harmonic components of the disturbances generated by the compressor would be filtered (the decay rate is like $e^{-n\pi k/r}$, where n is the harmonic number). This reduced the likelihood of spatial aliasing of the signal. With eight sensors, the phase and amplitude of the first three disturbance harmonics may be obtained. The outputs of the anemometers were filtered with four pole Bessel filters with a cutoff frequency of 22 times rotor rotation. The axial location of the sensors is important in determining the signal to noise ratio (SNR) of the rotating wave measurements; this question was studied by Garnier et al. (1990), who showed the SNR to be greatest upstream of the stage.

There are many ways to generate the required travelling waves in an axial compressor. Techniques involving oscillating the inlet guide vanes (IGV's), vanes with oscillating flaps, jet flaps, peripheral arrays of jets or suction ports, tip bleed above the rotor, whirling the entire rotor, and acoustic arrays were all considered on the basis of effectiveness, complexity, cost, and technical risk. For this initial demonstration in a low speed compressor, oscillating the IGV's was chosen on the basis of minimum technical risk.

Considerable care was taken in design of the actuation system to maximize effectiveness and minimize complexity and cost. An unsteady singularity method calculation of the potential flow about a cascade was carried out first to evaluate tradeoffs between blade angle of attack and flow turning angles versus cascade solidity, fraction of the cascade actuated, and airfoil aspect ratio (Sikowski).

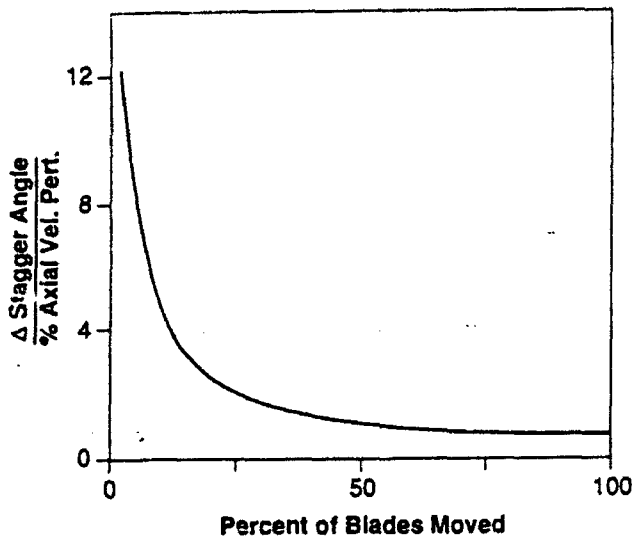


Fig. 3: Calculated blade stagger angle change required to generate a given first harmonic axial velocity perturbation as a function of the fraction of the blade row actuated

1990). The unsteady flow was examined since, although the reduced frequency of the IGV airfoil relative to rotating stall is about 0.3 for the first harmonic, several harmonics may be of interest. Calculations were also performed to evaluate the relative effectiveness of bang-bang actuation versus continuous airfoil positioning. As an example of these actuation studies, the tradeoff between the peak airfoil angle of attack excursion and the fraction of the cascade actuated is shown in Fig. 3. As the fraction of the airfoils which is actuated is increased, the angle of attack requirements on individual blades are reduced.

The limits to blade motion are set by both mechanical constraints (i.e., actuator torque limits) and airfoil boundary layer separation at large angles of attack. A NACA 65-0009 airfoil section was chosen due to its good off-angle performance and relatively low moment. The airfoils were cast from low density epoxy to reduce their moment of inertia. A coupled steady inviscid-viscous solution of the flow over the blades indicated that the boundary layers would stay attached at angles of attack up to fifteen degrees (Drela, 1988).

In this experiment, blade actuation torque requirements are set by the airfoil inertia since the aerodynamic forces are small. Both hydraulic and electric actuators are commercially available with sufficient torque and frequency response. Hollow core D.C. servo motors were selected because they were considerably less expensive than the equivalent hydraulic servos. The blades and motors have roughly equal moments of inertia.

For a given IGV solidity, the number of actuators required can be reduced by increasing the blade chord, but this is constrained by actuator torque and geometric packaging. The final IGV design consists of twelve untwisted oscillating airfoils with an aspect ratio of 0.9 and a solidity of 0.6 (Fig. 4). The complete actuation system has a frequency response of 80 Hz (approximately eight times the fundamental rotating stall frequency) at plus or minus ten degrees of airfoil yaw. The flow angle distribution measured at the rotor leading edge station (with the rotor removed) for a stationary ten degree cosine stagger pattern of the IGV's is compared in Fig. 5 to a prediction of the same flow made by Salkowski (1990).

The control law implemented for the tests described here is a simple proportionality; at each instant in time, the n^{th} spatial mode of the IGV stagger angle perturbation is set to be directly proportional to the n^{th} mode of the measured local velocity perturbation. The

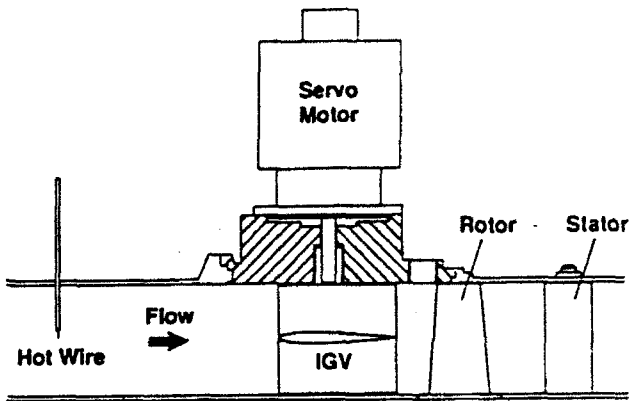


Fig. 4: Compressor flow path

complete control loop consisted of the following steps. First, the sensor signals are digitized. Then, a discrete Fourier transform is taken of the eight sensor readings. The first and/or second discrete Fourier coefficients are then multiplied by the (predetermined) complex feedback gains for that mode. Next, an inverse Fourier transform is taken which converts the modal feedback signals into individual blade commands. These, in turn, are then sent to the individual digital motor controllers. Additional housekeeping is also performed to store information for post-test analysis, limit the motor currents and excursions (for mechanical protection), and correct for any accumulated digital errors.

The controller hardware selection is set by CPU speed requirements (main rotating stall control loop and individual blade position control loops), I/O bandwidth (sensor signals in, blade positions out, storage for post-test analysis), operating system overhead, and cost. The final selection was a commercial 20 MHz 80386 PC with co-processor. A multiplexed, twelve bit analog to digital converter digitized the filtered hot wire outputs. The D.C. servo motors were controlled individually by commercial digital motion control boards. Using position feedback from optical encoders on the motors, each motor controller consisted of a digital proportional, integral, derivative (PID) controller operating at 2000 Hz. The entire control loop was run at a 500 Hz repetition rate. Motor power was provided by 350-watt D.C. servo amplifiers. The complete hardware arrangement is shown in Fig. 6.

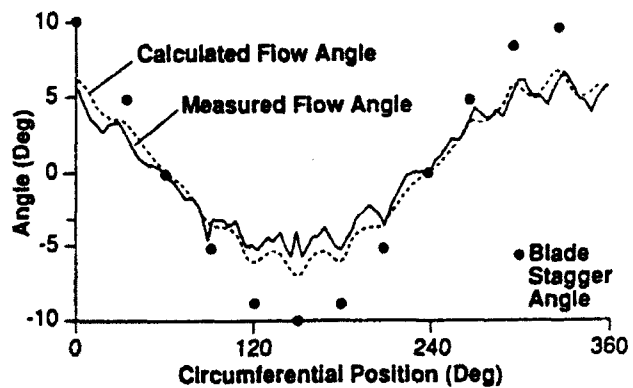


Fig. 5: A comparison of the measured and calculated flow angle generated 0.3 chords downstream by a 10 degree cosine stagger pattern distribution of 12 inlet guide vanes

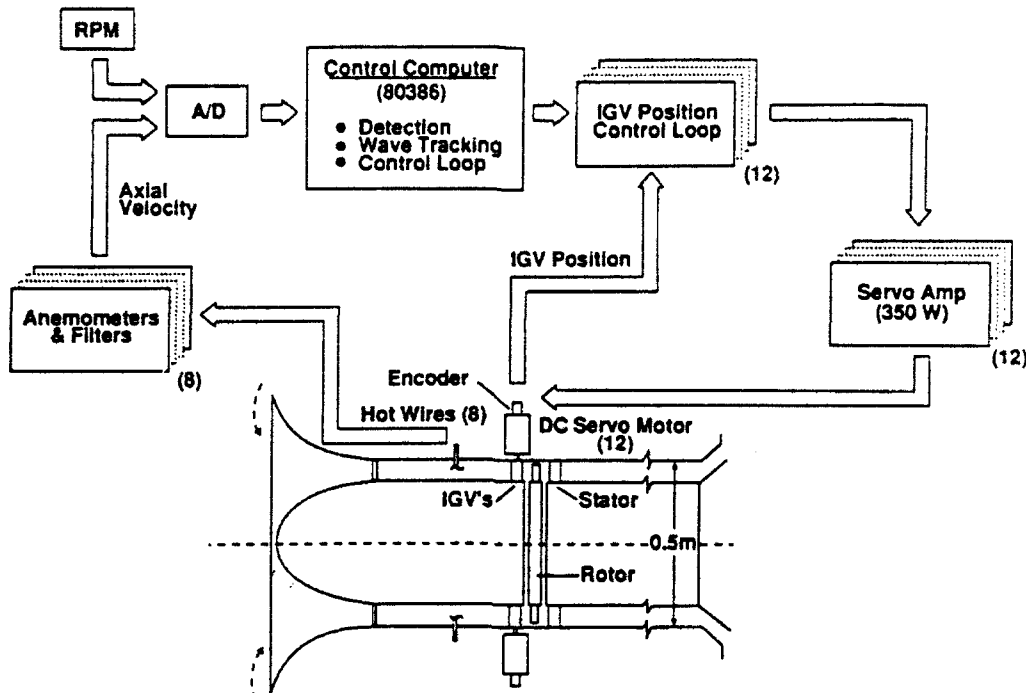


Fig. 6: Hardware component of actively stabilized axial flow compressor

OPEN LOOP COMPRESSOR RESPONSE

The inputs and outputs that characterize the fluid system of interest (the compressor and associated flow in the annular region) are the inlet guide vane angles (inputs) and the axial velocity distribution (outputs). In the present configuration this consists of twelve inputs (twelve inlet guide vanes) and eight outputs (eight hot wires) so that the system is multiple input-multiple output. Because the disturbances of interest are of small amplitude, the system behavior can be taken as linear and we can thus express the spatial distribution of the input and output perturbations (or indeed of any other of the flow perturbations) as a sum of spatial Fourier components, each with its own phase velocity and damping. This representation, which is consistent with Eq. (2), allows us to treat the disturbances on a harmonic-by-harmonic basis, and reduces the the input-output relationship to single input-single output terms, an enormous practical simplification.

The complex spatial Fourier coefficient for each mode n is given by

$$C_n = \frac{1}{K} \sum_{k=0}^{K-1} V_k \exp\left[-\frac{2i\pi k n}{K}\right] \quad (5)$$

where K is the number of sensors about the circumference (8 in this case), and V_k is the axial velocity measured at angular position k . The magnitude of C_1 is thus the amplitude of the first harmonic at any time and its phase is the instantaneous angular position of the spatial wave Fourier component.

An important concept in the present approach is the connection between rotating stall and travelling wave type of disturbances in the compressor annulus. In this view, the wave damping and the compressor damping are equivalent and determine whether the flow is stable. At the neutral stability point, the damping of disturbances is zero, and close to this point, the damping should be small. (The measurements given by Garnier, et al. (1990) show

this.) Thus, for a compressor operating point near stall, the flow in the annulus should behave like a lightly damped system, i.e., should exhibit a resonance peak when driven by an external disturbance. As with any second order system, the width of the peak is a measure of the damping.

The present apparatus is well suited to establishing the forced response of the compressor since the individual inlet guide vanes can be actuated independently to generate variable frequency travelling waves. The sine wave response of the compressor was measured by rotating the ± 10 degree sinusoidal IGV angle distribution shown in Fig. 5 about the circumference at speeds ranging from 0.05 to 1.75 of rotor rotational speed. Figure 7 shows the magnitude of the first spatial Fourier coefficient, as a percentage of the mean flow coefficient, as a function of input wave rotation frequency, i.e. the transfer function for the first spatial mode.

The peak response to the forcing sine wave is seen in Fig. 7 to be at 23% of the rotor rotation frequency. This is close to the frequency observed for the small amplitude waves without forcing (20%) and for the fully developed rotating stall (19%). This behavior supports the view stated previously that the compressor behaves as a second order system.

CLOSED LOOP EXPERIMENTS - ROTATING STALL STABILIZATION OF THE FIRST FOURIER MODE

While the open loop experiments described above are of interest in elucidating the basic structure of the disturbance field in the compressor annulus, this work is principally aimed at suppressing rotating stall using closed loop control. To assess this, experiments were performed using a control scheme of the form

$$[\delta\eta_{IGV}]_{n^{\text{th}} \text{ mode}} = Z_n C_n \quad (6)$$

where

$$Z_n = R_n e^{i\beta_n} \quad (7)$$

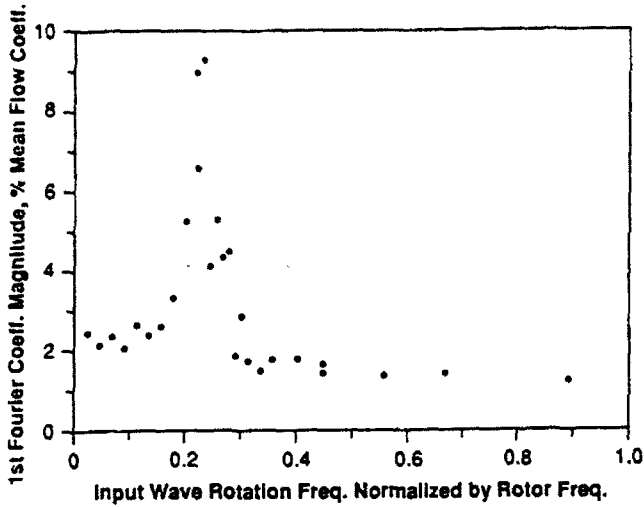


Fig. 7: Measured open loop response of the first spatial mode of the compressor to a 10° IGV stagger rotating sine wave excitation

In Eqs. (6) and (7), $\delta\gamma_{IGV}$ is the change in inlet guide vane stagger angle. The quantity Z_n is the complex feedback gain for the n th Fourier mode (n 'th spatial harmonic component of the disturbance), with R_n the amplitude and β_n the phase angle between the measured axial velocity spatial harmonic (0.5 radii upstream of the rotor) and the input inlet guide vane angular position spatial harmonic. The influence of feedback amplitude (R_n) and phase (β_n) were established with a set of parametric experiments carried on at a flow coefficient (ϕ) close to stall, in a region of marginal flow stability.

Data is shown in Fig. 8 in the form of the power spectral density (PSD) of the first spatial mode axial velocity disturbance (C_1) at two control phase angles (β_1), 0° and 45°. The operating point is fixed at a normally stable slow coefficient of $\phi = 0.475$ (stall without control occurs at $\phi = 0.430$). For each phase, spectra are shown with feedback control and with no control (vanes stationary at zero flow angle). The rotating disturbance is evident in the strong peaks at 23% of rotor rotation frequency. The height of the peaks is a measure of the strength of the rotating waves. The scales are dimensional but all plots are to the same scale so they can be compared directly. The difference between the peak heights with no control in the two cases is due to finite sampling time, i.e., to differences in the ambient disturbance levels during the sampling period.

At 0° phase angle, the peak at 0.23 frequency is higher with active control than with fixed vanes, implying that the feedback control at this phase is amplifying the rotating disturbance waves (i.e. making them less stable). At 45° phase angle, however, the peak with control is lower than that with fixed vanes, implying that control is attenuating the waves in this case. Thus, the ratio of the height of the peak in the PSD with and without control (i.e. the wave amplification) is a measure of the effectiveness of the feedback in influencing the travelling wave's stability. The influence of controller phase (β_1) at fixed gain on the wave amplitude ratio was experimentally evaluated for phase shifts between 0° and 360°, as shown in Fig. 9. For phases between 0° and 150°, the waves are attenuated, while the waves are amplified for phase angles between 160° and 350°. The maximum attenuation found was roughly 30 at $\beta_1 = 75^\circ$, and the maximum amplification of a factor of 1,300 occurs at $\beta_1 = 275^\circ$. Between $\beta_1 = 290$ and $\beta_1 = 345$, the system is unstable (i.e. goes into rotating stall).

If wave stability is equivalent to compressor stability, then compressor stability should be enhanced for control phases at which

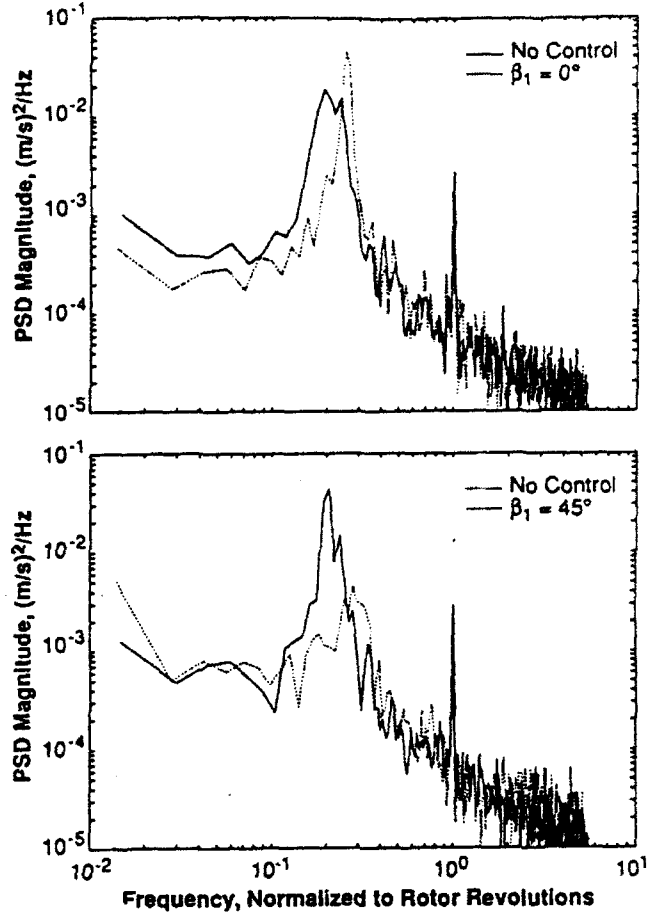


Fig. 8: The influence of proportional feedback control on the power spectral density (PSD) of the first spatial mode of the compressor at two feedback phase angles (β_1) versus the behavior with fixed IGV's

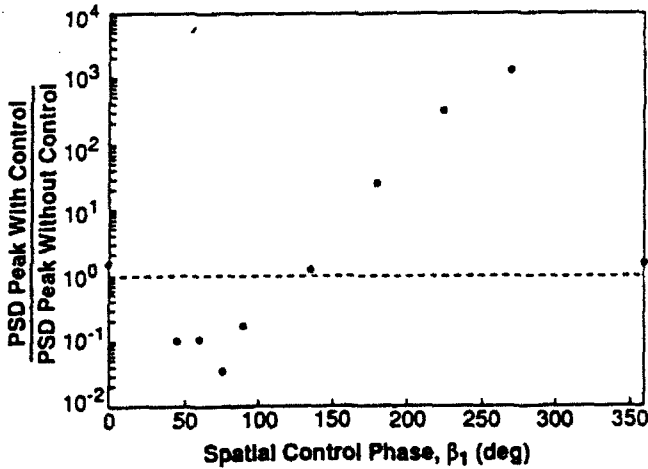


Fig. 9: Influence of feedback control phase angle (β_1) on the strength of the first spatial mode of the flow in the compressor at $\phi = 0.475$

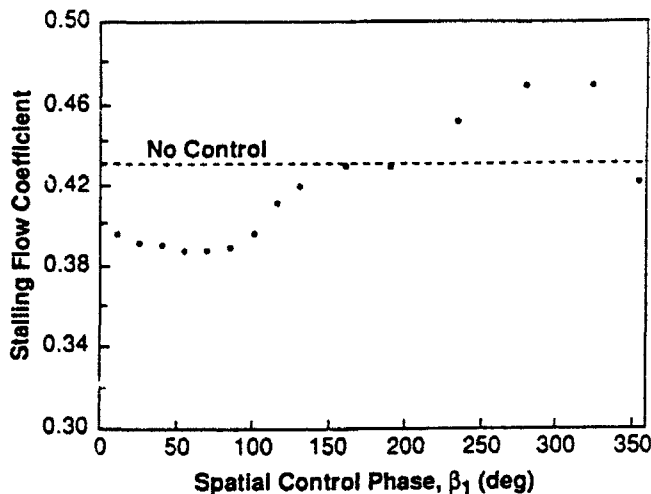


Fig. 10: Influence of feedback control phase angle (β_1) on the flow coefficient at which the compressor goes into rotating stall

the waves are attenuated and should be decreased when the waves are amplified. This is indeed the case as illustrated in Fig. 10. Here, the flow coefficient (ϕ) at which the compressor goes into rotating stall as the compressor throttle is very slowly closed ($d\phi/dt = 2 \times 10^{-5}$ /rotor revolution) is shown as a function of controller phase angle (β_1). Depending upon the phase, the control changes the stalling flow coefficient by as much as $\pm 11\%$. Comparison of Figs. 9 and 10 makes clear the connection between wave damping and rotating stall. Rotating stall is suppressed when the waves are damped and is promoted when the waves are amplified.

Figure 11 shows the influence of control of the first spatial harmonic wave in a more familiar form of non-dimensional pressure rise (ψ) versus non-dimensional mass flow (flow coefficient, ϕ) at constant corrected compressor speed. With fixed inlet guide vanes (no control), the compressor stalls at $\phi = 0.43$. With feedback control

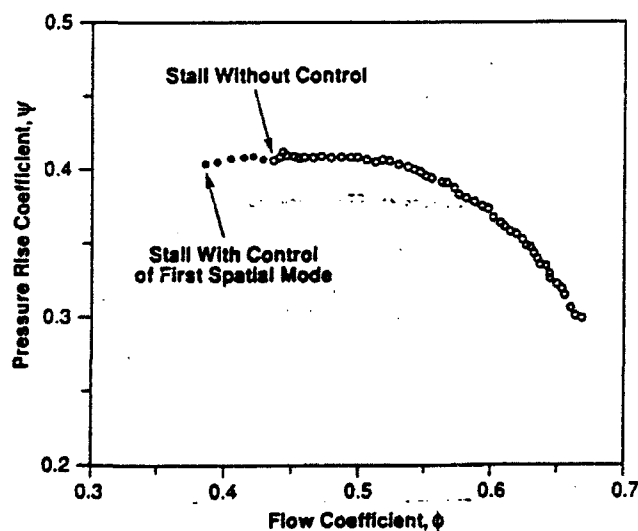


Fig. 11: Non-dimensional pressure rise (ψ) versus mass flow (ϕ) characteristic showing the measured influence of feedback control of the first spatial mode on compressor operating range

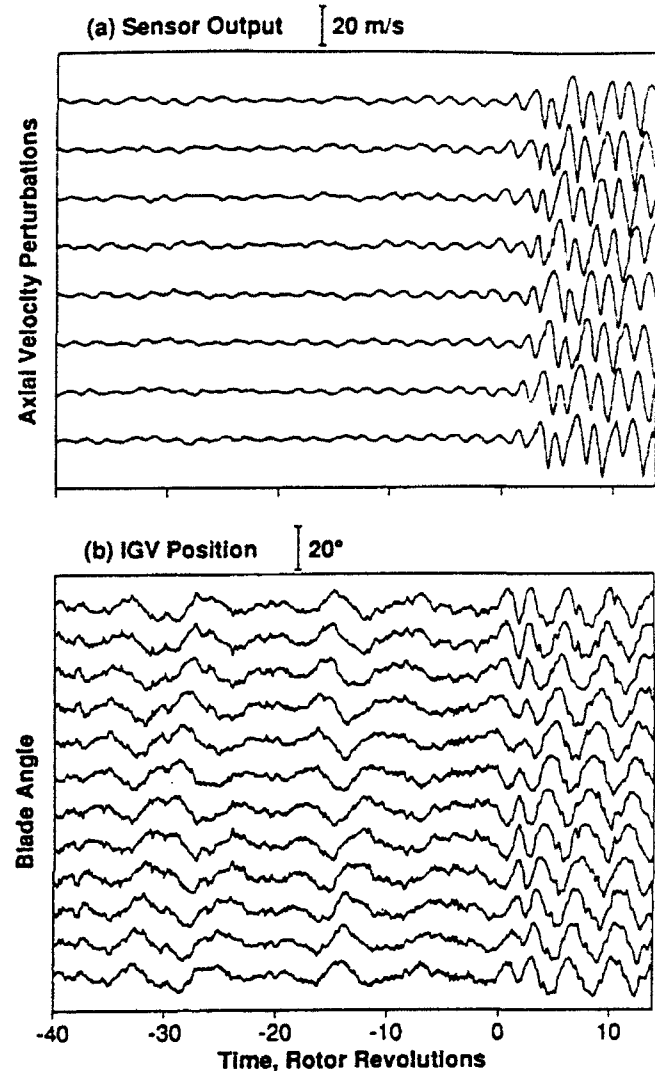


Fig. 12: Time history of compressor sensor output (a) and actuator response (b) with first spatial mode control as the throttle is very slowly closed. Rotating stall onset is at a time of 0.

at the most effective phase found ($\beta_1 = 60^\circ$), the stalling flow coefficient is $\phi = 0.375$, 11% lower. At the phase producing the most wave amplification ($\beta_1 = 275^\circ$), the stalling flow coefficient is 0.475.

Time Resolved System Behavior

Much can be learned from examining the time resolved behavior of the controlled compressor as the throttle is very slowly closed at a controller phase (β_1) of 60° . The overall system behavior is shown in Fig. 12. Here, the onset of stall occurs at a non-dimensional time of 0. Prior to that time, the sensor output is small relative to the rotating stall amplitude. The actuators, however, are clearly producing a travelling wave. (The actuator response to the rotating stall after stall onset is due to the light damping of the blade servos.)

The time evolution measured by a single sensor is shown in Fig. 13. For this compressor with no control (Fig. 13a), the rotating stall grows quite slowly. With control of the first spatial mode (Fig. 13b), the growth is much faster. (Note that this occurs at a lower

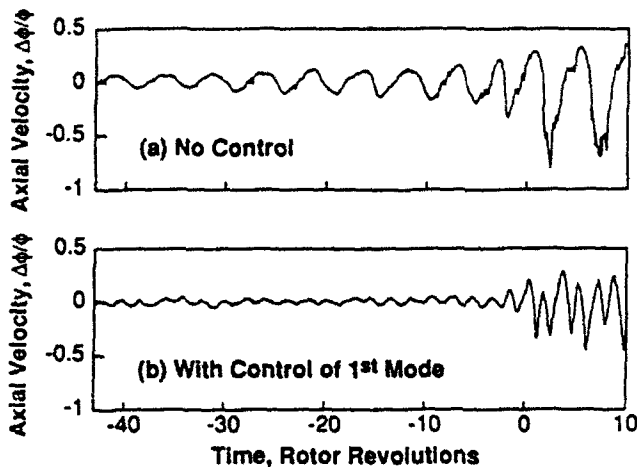


Fig. 13: The influence of control on the time history of a single sensor as the throttle is slowly closed to stall the compressor

flow coefficient than Fig. 13a.) Further, the disturbances with control have twice the frequency as in the no control case. This is due to the primary disturbance now being a two-cell rotating stall, i.e. the second spatial mode.

The influence of first mode control on the disturbance modal structure is illustrated in Figs. 14 and 15, which show disturbance phase and amplitude versus time. A linear variation of phase with time indicates that the disturbance is propagating at constant speed. Without control (Fig. 14), both the first and second spatial modes are evident in both magnitude and phase for 40 rotor revolutions before stall. The first mode is clearly the strongest everywhere and the fully developed stall is an admixture of both modes. When the first spatial mode is controlled (Fig. 15), it is the second which is stronger prior to stall, and predominates in the fully developed rotating stall.

Control of the Second Spatial Mode

Since the second spatial mode appears predominant when the first mode is under control, it makes sense to control the second mode as well. The effect of simultaneous control of the first two spatial

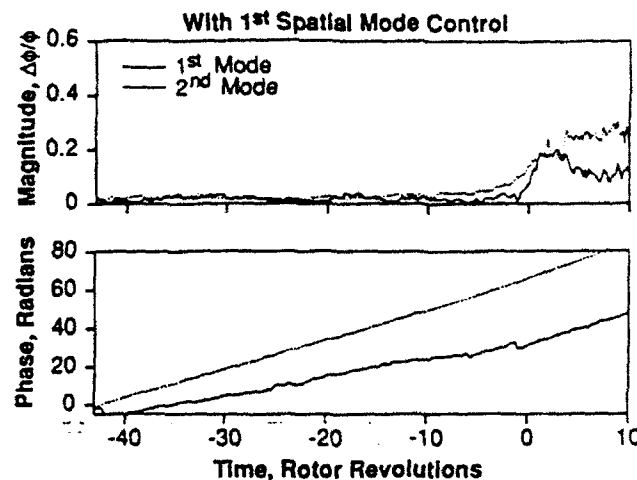


Fig. 15: Same as Fig. 14, but with control of the first spatial mode

modes on compressor stalling pressure rise is shown in Fig. 16. With both modes under the control, the compressor does not stall until a flow coefficient of $\phi = 0.35$, a 20% increase in operating range over the no control case. Examination of the time behavior of the Fourier coefficients, as the compressor throttle is slowly closed (Fig. 17), shows that, prior to stall, the first and second modes are of about equal strength. At the stall point, the second mode growth is initially more rapid but fully developed stall is predominantly the first mode. This suggests that (nonlinear) mode coupling is important as the wave matures. The measured third spatial mode is relatively weak.

SYSTEM IDENTIFICATION

The measurements presented have been for a compressor with a simple proportional control law, one whose rationale is based on a linear theory as summarized by Eq. (4). There are many analytical tools now available to design more sophisticated control schemes with, hopefully, improved performance. The success of the

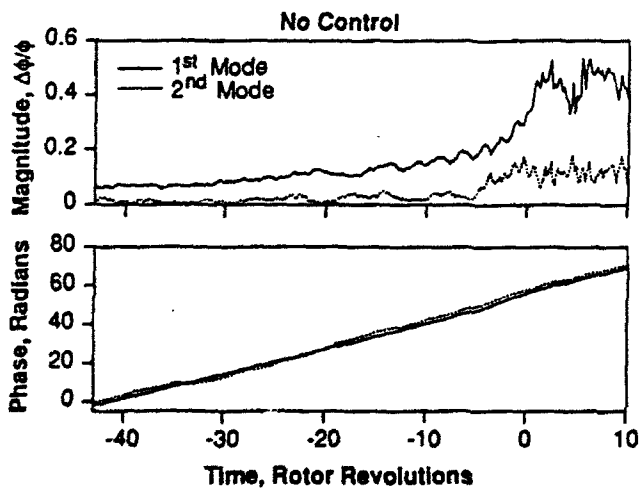


Fig. 14: Time history without control of the first two Fourier coefficients as the throttle is slowly closed to stall the compressor at $t = 0$ revs

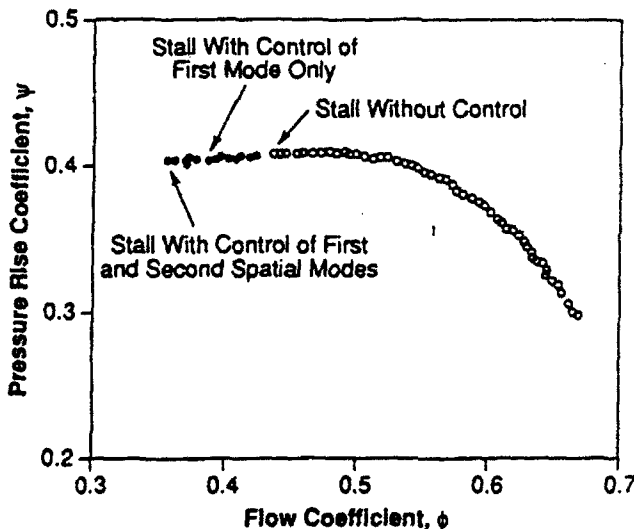


Fig. 16: Compressor characteristic as in Fig. 11, but with active control of first and second spatial modes

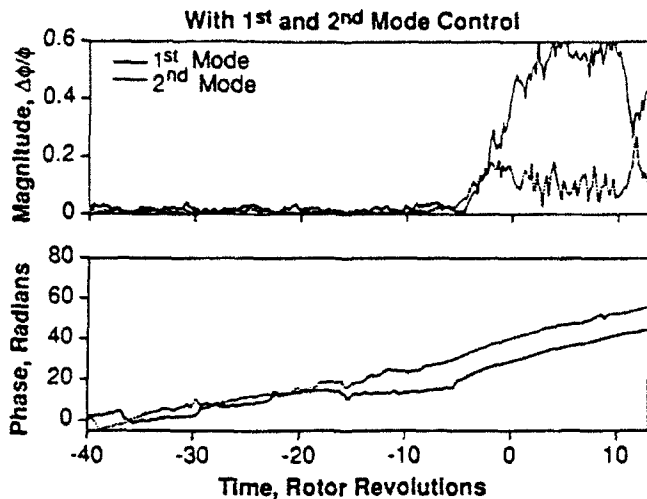


Fig. 17: Same as Figs. 14 and 15, but with control of the first and second spatial modes

control design, however, will be based in no small part on the fidelity of the system model assumed for the compressor. Also, we are interested in understanding more about the compressor fluid mechanics. The apparatus assembled for the active control experiment is well suited to quantitatively establishing the dynamic response of the compressor by directly measuring its transfer function.

The magnitude behavior of the compressor response to IGV motion was given in Fig. 7. This behavior can be put into a more complete form, and compared to at least the structure of the fluid dynamic model, by plotting the phase and magnitude (Bode diagram) of the transfer function between the first Fourier coefficient of IGV motion and the first Fourier coefficient of the resulting axial velocity perturbations. This transfer function has both a magnitude and a phase, which results from both spatial and time lags between the input and output. We expect the behavior of this system based on the modelling described earlier to be that of a second order system. This should be easily identifiable from experiments such as a rotating sine wave response, for example.

We can express the fluid model of Eq. (4) in more convenient transfer function form as

$$\frac{\delta \Phi}{\delta \gamma} (s) = K \frac{s + (A + Bi)}{s + (C + Di)} \quad (8)$$

where s is the Laplace transform variable. The complex form of this transfer function gives rise to second-order behavior in the measured variables, as mentioned previously. The advantage of this form is that it uses the minimum number of parameters to completely specify the transfer characteristics of the system. A linear regression type fit (Lamaire, 1987) can be done for the parameters K, A, B, C , and D . This gives rise to the results shown in Fig. 18, where it can be seen that the response characteristics in the experiment are mimicked by the model. We have obtained this type of fit using various types of IGV inputs: rotating waves, stationary waves with oscillating amplitudes, and stationary waves with random amplitudes. As would be expected in a linear system, the input-output behavior is unaffected by such variations in the character of the input. More details on this system identification can be found in Paduano et al. (1990). Overall, the fit of the second order model to the measurements is very good.

In summary, the fidelity of the model fit to the data in Fig. 18

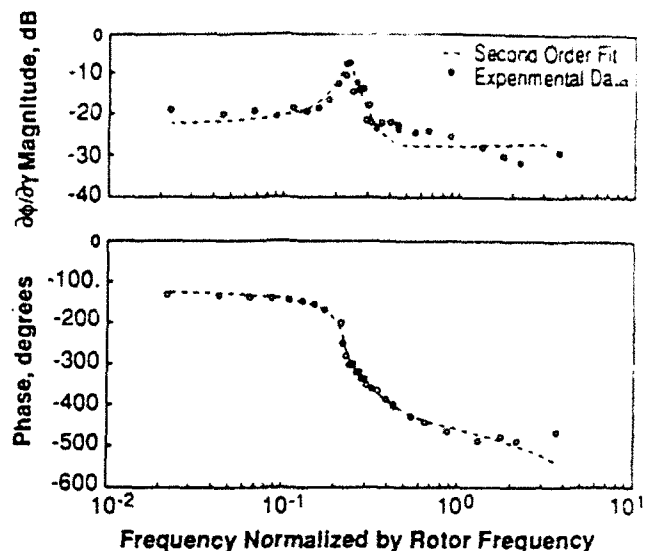


Fig. 18: Bode plot showing response of the compressor to a sine wave forcing excitation at $\phi = 0.475$

indicates that structure of the fluid model of Eq. (4) is appropriate for this compressor at the flow conditions examined. We have yet to make the quantitative prediction of the Bode plot from the compressor geometry.

DISCUSSION

The most important point of this paper is that these experiments demonstrate that it is physically possible to actively control rotating stall in an axial flow compressor and, by doing so, obtain a useful extension in compressor operating range. A second point is that these experiments more firmly establish a clear link between low amplitude circumferentially propagating disturbances prior to stall and fully developed rotating stall -- when the disturbances are suppressed, rotating stall is prevented. This initial attempt to control rotating stall is encouraging. As is often the case, however, these results raise many more questions than they answer. These questions thus suggest future research directions.

The control law used in the experiments reported herein is quite simple. Considerable effort is being spent on the design of more sophisticated, and hopefully more effective, controllers. The controllers can be useful in two ways -- first, in extending compressor performance and, second, in elucidating the details of the dynamic behavior of the compression system.

At the moment, we do not have a quantitative explanation for the experimentally observed limit to control effectiveness on this compressor (i.e. why is there a 20% flow range improvement rather than a 10% or 30% improvement). Preliminary investigations show that, insofar as the linear system analysis exemplified by Eq. (8) is concerned, the bandwidth and actuator authority limits of the current system have not yet been reached. Another possibility is that higher order modes may drive the instability. Measurements to date have not shown that the third spatial mode is strong (the highest mode which can be resolved with the present instrumentation). Various other nonlinearities can be important. Also, at some flow coefficients, the assumptions which underlie the wave model (Eq. (4)) and the actuation scheme chosen may cease to be valid (i.e. two-dimensional flow). Work is ongoing to address these questions.

There are also more general issues raised that go beyond the behavior of this particular compressor. We have no basis on which

to quantitatively extrapolate rotating stall control beyond the machine tested. We note, however, that the wave behavior exploited in this control scheme has been observed on other low and high speed compressors by McDougall and Garnier. Thus, we might expect that those machines could be controlled in a similar fashion to a greater or lesser degree. This question can only be addressed in substance by experimental investigation of other builds of this compressor and of other compressors. A second approach is to quantitatively reconcile the system behavior such as observed experimentally in Fig. 18 with a first principles fluid mechanic model related to compressor geometry as exemplified by Eq. (4). This would facilitate more accurate predictions of compressor behavior with control. Work is ongoing in both areas.

Another concern is the generality of the rotating stall model. Certainly such assumptions as two-dimensionality and incompressible flow are of limited applicability. These models can and are being made more elaborate as fidelity with experimental data requires. It is important to emphasize here that the concept of active control of compressor instabilities is not dependent on the accuracy of any particular mathematical model or conceptual view of the flow in a compressor. The model is there to provide a framework about which to design a control system. Any model would do (assuming it was an accurate representation of the fluid mechanics), although certainly some formulations are much more tractable for control design than others.

Actuation schemes are also important since they influence both the effectiveness of control and the complexity and difficulty of implementation. The approach adopted here was chosen mainly on the basis of minimum technical risk. Many other techniques can be considered and each must be quantitatively evaluated in terms of control authority and implementation difficulty for a particular installation. Research efforts in this area may be fruitful.

As a final point, we would like to comment on the interdisciplinary nature of this research. The effort to date has been successful due to the work of both compressor and controls engineers and it has been challenging for both specialties. In the past several years, we have spent considerable time learning how to talk with each other and can report that the effort appears so far to be rewarding.

CONCLUSIONS

Rotating stall in a low speed axial compressor has been suppressed using active feedback control. To date, a 20% gain in compressor mass flow range has been achieved. The measured dynamic behavior of the compressor has followed predictions from a two-dimensional compressor stability model. These results reinforce the view that the compressor stability is equivalent to the stability of low amplitude waves which travel about the machine circumferentially.

This is a progress report on an ongoing effort. The results so far indicate that active control of large scale fluid mechanic instabilities such as rotating stall in axial compressors is very promising. Much work still needs to be done to assess the practical applicability of these results.

ACKNOWLEDGEMENTS

The authors wish to acknowledge the contributions of Mr. P. Salkowski in the calculation of the oscillating airfoil fluid mechanics. They thank Dr. I.J. Day for his thought-provoking discussions. This work was supported by the US Air Force Office of Scientific Research, Dr. J. McMichael, Technical Monitor, and by the Office of Naval Research, Dr. R.J. Hansen, Technical Monitor.

REFERENCES

- Drela, M., 1988, Private Communication
- Epstein, A.H., Ffowcs Williams, J.E., Greitzer, E.M., 1989, "Active Suppression of Aerodynamic Instabilities in Turbomachines," *J. of Prop. and Power*, Vol. 5, No. 2, pp. 204-211
- Garnier, V.H., Epstein, A.H., Greitzer, E.M., 1990, "Rotating Stall Anticipation and Inhibition in Axial Compressors," ASME Paper 90-GT-156.
- Hynes, T.P., Greitzer, E.M., 1987, "A Method for Assessing Effects of Inlet Flow Distortion on Compressor Stability," *ASME J. Turbomachinery*, Vol. 109, pp. 371-379.
- Lamantia, R.O., 1987, "Robust Time and Frequency Domain Estimation Methods in Adaptive Control," Ph.D. Thesis, Department of Electrical Engineering and Computer Science, MIT.
- Lee, N.K.W., Greitzer, E.M., 1990, "Effects of Endwall Suction and Blowing on Compressor Stability Enhancement," *ASME J. Turbomachinery*, Vol. 112, pp. 133-144.
- Longley, J.P., 1988, "Inlet Distortion and Compressor Stability", Ph.D. Thesis, Cambridge University Engineering Dept., Cambridge, England.
- Longley, J.P., 1990, Unpublished MIT Gas Turbine Laboratory Technical Note.
- Ludwig, G.R., Nenni, J.P., 1980, "Test of an Improved Rotating Stall Control System on a J-85 Turbojet Engine," ASME Paper 80-GT-17.
- McDougall, N.M., 1988, "Stall Inception in Axial Compressors", Ph.D Thesis, Cambridge University.
- McDougall, N.M., Cumpsty, N.A., Hynes, T.P., 1989, "Stall Inception in Axial Compressors", submitted to 1989 ASME Gas Turbine Conference.
- Moore, F.K., Greitzer, E.M., 1986, "A Theory of Post-Stall Transients in Axial Compressors: Part I - Development of the Equations," *ASME J. of Eng. for Gas Turbines and Power*, Vol. 108, pp. 68-76.
- Paduano, J., Valavani, L., Epstein, A.H., Greitzer, E.M., Guenette, G.R., 1990, "Modelling for Control of Rotating Stall," to be presented at 29th IEEE Conference on Decision and Control, IEEE Control System Society, Honolulu, HI.
- Salkowski, P.D., 1990, "Aerodynamic Design of Moveable Inlet Guide Vanes for Active Control of Rotating Stall," M.S. Thesis, Department of Aeronautics and Astronautics, MIT.
- Yonke, W.A., Landy, R.J., Stewart, J.F., 1987, "HIDEC Adaptive Engine Control System Flight Evaluation Results," ASME Paper 87-GT-257.

- DRAFT -

Submitted for Review for the 1993 ASME Gas Turbine Conference

ACTIVE STABILIZATION OF ROTATING STALL
IN A THREE-STAGE AXIAL COMPRESSOR

by

J.M. Haynes, G.J. Hendricks, and A.H. Epstein

ABSTRACT

A three-stage, low speed axial research compressor has been actively stabilized by damping low amplitude circumferentially travelling waves which can grow into rotating stall. Using a circumferential array of hot wire sensors, and an array of high speed individually positioned control vanes as the actuator, the first and second spatial harmonics of the compressor were stabilized down to a characteristic slope of 0.9, yielding an 8% increase in operating flow range. Stabilization of the third spatial harmonic did not alter the stalling flow coefficient. The actuators were also used open loop to determine the forced response behavior of the compressor. A system identification procedure applied to the forced response data then yielded the compressor transfer function. The Moore-Greitzer, 2-D, stability model was modified as suggested by the measurements to include the effect of blade row time lags on the compressor dynamics. This modified Moore-Greitzer model was then used to predict both the open and closed loop dynamic response of the compressor. The model predictions agreed closely with the experimental results. In particular, the model predicted both the mass flow at stall without control and the design parameters needed by, and the range extension realized from, active control.

NOMENCLATURE

A	Annulus flow area
A_n	Coefficient of n th spatial mode of flow coefficient perturbation
b_x	Axial chord
\bar{b}_x	Non-dimensional axial chord
L	Total pressure loss
L_r	Total pressure loss across rotors
$L_{r,ss}$	Steady total pressure loss across rotors
L_s	Total pressure loss across stators
$L_{s,ss}$	Steady total pressure loss across stators
δL_r	Perturbation in total pressure loss across rotors
δL_s	Perturbation in total pressure loss across stators
$\delta L_{unsteady}$	Unsteady total pressure loss perturbation
$\delta L_{quasi-steady}$	Quasi-steady total pressure loss
n	Spatial harmonic number
P_e	Exit static pressure
P_{ie}	Exit total pressure
P_{in}	Inlet total pressure
δP_e	Exit static pressure perturbation
δP_{ie}	Exit total pressure perturbation
δP_{in}	Inlet total pressure perturbation
r	Compressor annulus mean radius
s_n	$\frac{(\alpha_n - i\omega_n)r}{U}$
t	time
\bar{t}	Non-dimensional time (Eq. (A10))
T	Torque
U	Rotor linear velocity at the mean radius

α	Disturbance growth rate
ϕ	Flow coefficient c_x/U
$\delta \phi$	Flow coefficient perturbation
λ	Inertia parameter for compressor rotors
μ	Inertia parameter for compressor
ν	Circumferential coordinate
ρ	Fluid density
τ_{loss}	Unsteady total pressure loss characteristic time
τ_r	Rotor total pressure loss characteristic time
τ_s	Stator total pressure loss characteristic time
$\bar{\tau}_r$	Non-dimensional rotor total pressure loss characteristic time
$\bar{\tau}_s$	Non-dimensional stator total pressure loss characteristic time
$\bar{\tau}_{convection}$	Non-dimensional blade passage convection time (Eq. (10))
ω	Disturbance rotational frequency
ψ	Total-to-static pressure rise
ψ_i	Ideal total-to-static pressure rise
ψ_{ss}	Steady state total-to-static pressure rise
ψ_t	Torque coefficient $\frac{T}{\rho U^2 Ar}$

INTRODUCTION

Axial flow compressors suffer from inherent hydrodynamic instabilities known as surge and rotating stall. Surge is a one-dimensional mass flow disturbance involving the entire compression system, while rotating stall has a two- or three-dimensional structure rotating about and local to the compressor blading. Both are large amplitude disturbances, disrupting compressor operation and imposing large structural loads, and so are unacceptable in routine compressor operation.

A useful theoretical model of compressor hydrodynamic stability started with Emmons et

al. (1955) and has evolved through Moore and Greitzer (1986). This analysis shows that surge and rotating stall are simply the mature form of the natural oscillatory modes of the compression system. Surge is the lowest (zero) order mode and rotating stall is the higher order modes. This model predicts that these hydrodynamic disturbances start at very small amplitude (during which time the modes may be considered as linear and decoupled) but quickly grow into their large amplitude form, surge and rotating stall (which exhibit nonlinear behavior and whose dynamics are coupled). Thus, the stability of the compressor is equivalent to the stability of these small amplitude waves which exist prior to stall. Garnier et al. (1991), McDougal et al. (1990), and Etchevers (1992) presented experimental data showing the existence of these low amplitude waves and their evolution into stall in several axial compressors. More recently, Paduano and Gysling (1992) have shown that the details of the time evolution of the disturbances, especially the wave form, is quite sensitive to the shape of the compressor pressure rise versus mass flow characteristic.

Epstein, Ffowcs Williams, and Greitzer (1989) first suggested that surge and rotating stall could be prevented by using active feedback control to damp the hydrodynamic disturbances while they are still at small amplitude. Aside from reducing the control authority required, control of the fluid disturbances while they still are at very low amplitude permits incipient surge and rotating stall to be treated and controlled separately (since their behavior will be linear and decoupled). Active suppression of surge was subsequently demonstrated experimentally on centrifugal compressors by Ffowcs Williams and Huang (1989) and Pinsley et al. (1991), and on an axial compressor by Day (1991). Paduano et al. (1991) demonstrated active suppression of rotating stall in a single-stage low speed compressor. By damping the small amplitude travelling waves rotating about the annulus prior to stall, they increased the stable flow range of the compressor by 25%.

The data of Paduano et al. provides strong experimental evidence that at least the quantitative structure of the hydrodynamic stability theory is appropriate for this type of compressor and that, indeed, rotating stall can evolve from small amplitude travelling waves since

damping these waves prevents the formation of rotating stall. In these experiments, the travelling waves were decomposed into separate spatial harmonics with each harmonic controlled individually. This showed that the linear and decoupled behavior predicted by the Moore and Greitzer theory did indeed occur. The theory, however, predicted that all spatial harmonics go unstable at the same mass flow, while the experiment showed that the lower the harmonic, the higher the mass flow at instability. This behavior has an important implication for active control since it means that all spatial harmonics need not be simultaneously controlled in order to realize an increase in compressor operating range, greatly simplifying the physical realization of such a control system.

In the work presented herein, we extend the experimental single-stage work of Paduano by applying the same active control techniques to a three-stage, low speed research compressor. Both open loop forced response and closed loop actively stabilized data are presented. We also extend the two-dimensional, incompressible hydrodynamic stability theory of Moore and Greitzer to include non-ideal effects such as time lags associated with the development of viscous losses and deviations. These modifications have the effect of separating in mass flow the instabilities of individual spatial harmonics as observed by Paduano. We then show that this theory does an excellent job in quantitatively predicting both the open and closed loop dynamic behavior of the three-stage compressor. This includes predicting the natural stall point (inception of rotating stall without control) and predicting both the controller parameters required and the improvement in mass flow range gained from active control. Finally, we make some comments on the utility of an actively stabilized machine for exploration of compressor dynamics.

Experimental Apparatus

A 0.6 meter diameter, three-stage low speed axial research compressor was adapted for use as a test article in these experiments. Work in this rig was previously reported by Gamache (1990), Lavrich (1988), and Garnier et al. (1991). The blading details are given in Table 1. The control scheme adopted was that used by Paduano et al. in which the travelling waves of axial

velocity are detected by a circumferential array of hot wires just upstream of the compressor and individually actuated vanes upstream of the rotor are used to generate the rotating disturbance structure required for control. The test compressor was appropriately modified by moving the inlet guide vanes (IGV's) sufficiently far upstream so that control vanes could be placed between the IGV's and the first rotor. In this arrangement, the inlet guide vanes produce the mean swirl while the unchambered control vanes provide the time and circumferential variations needed to stabilize the compressor. Each of the twelve control vanes consisted of NACA 65-0009 cast epoxy airfoils, cantilevered from a hollow core, high torque to inertia DC servo motor (Fig. 1). Instrumentation included circumferential hot wire, total pressure, and static pressure arrays mounted throughout the compressor (Fig. 2). Additional measurements consisted of rotor speed and torque, average compressor mass flow (from a venturi), and rig housekeeping.

The control system hardware is illustrated in Fig. 3. The signals from the eight hot wire anemometers mounted about the compressor circumference are filtered by four-pole Bessel filters set at 1000 Hz, which is 25 times the shaft frequency, ω_s . The signals are then digitized by a 16-bit A/D system in an 80486 computer, which implements the control laws and outputs the commanded control vane positions to individual vane position control systems. These consist of closed loop, PID position servos, one for each channel, feeding 350 watt servo amplifiers which drive the DC servo motors. Optical encoders mounted on each motor provide a vane position signal to the feedback controllers. The vane servo loops operated at $50 \omega_s$ (2000 Hz), while the entire control loop in the computer was operated at $12.5 \omega_s$ (500 Hz). The control vane dynamic response was determined by driving the vane array with a pseudo-random binary signal with a minimum pulse width of $2.5 \omega_s$ (100 Hz), while the compressor was operated near its stall point. These measurements showed that the transfer function of the flow actuation system could be modelled quite closely by two second order systems in series with a natural frequency of 170 Hz and a damping ratio of 0.35. This yields a frequency response flat to ± 3 dB up to $3 \omega_s$ (120 Hz). The first spatial harmonic of rotating stall is approximately $0.3 \omega_s$ (12.5 Hz) in this compressor.

The computer control algorithms were also similar to those used by Paduano. At each

time step, the anemometer data is digitized and linearized into axial velocity; a discrete spatial Fourier transform is then used to decompose the eight velocity measurements into spatial harmonics (only modes 1, 2, and 3 were examined here); a separate control law is then implemented on each spatial harmonic; and then an inverse discrete Fourier transform on the spatial harmonics is taken to yield individual blade position commands to each of the 12 control vane position control systems.

A simple proportional control law was implemented in these experiments. For each spatial harmonic n , the change in control vane stagger angle, γ , is proportional to the measured change in axial velocity, C .

$$|\delta \gamma_{vane}|_n = Z_n C_n \quad (1)$$

where Z_n is the complex constant of proportionality

$$Z_n \equiv R_n e^{i\beta_n} \quad (2)$$

R_n represents the gain of the controller, while β_n is the phase angle between the measured velocity perturbation and commanded stagger angle change for each harmonic. With this harmonic by harmonic control scheme, β_n is a spatial lead which can account for both lags in the control system and the dynamics of the compressor. The total change in vane stagger angle, $\delta\gamma_{vane}$, is then simply the sum of the deflections calculated for the individual harmonics being studied (1, 2, or 3 in this case). Paduano established the optimum gain and phase for each harmonic empirically. Here, as will be shown later, theory can be used to calculate the optimum feedback gain and phase with results closely matching those found experimentally.

Steady State Compressor Performance

Aside from active stabilization experiments, steady state measurements were taken both to assess the compressor operating characteristics and to establish the aerodynamic parameters needed as input to the analytical modeling and control law design. These included measurements of the speedline shape, the torque efficiency, and the influence of control vane stagger angle (γ) on

the non-dimensional pressure rise coefficient (ψ). Specifically, the $\partial\psi/\partial\gamma$ values required by the theory were derived from measurements of the steady state influence of vane stagger on compressor pressure rise, as illustrated in Fig. 4. The resultant values of $\partial\psi/\partial\gamma$ and $\partial\psi/\partial\phi$ are shown in Fig. 5. Data in the normal unstable low flow area were taken while the compressor was stabilized with feedback control.

Compressor Performance With Active Stabilization

Active feedback stabilization of the first two spatial harmonics was implemented as described above. The results using the optimum feedback gain and phase found are illustrated on the speedline in Fig. 6. Control of the first harmonic yields a range increase of 3%, while control of the first and second harmonics together increase that to 8%. At this point, the speedline slope is 0.9. The compressor torque losses continue to decrease smoothly in the actively stabilized region.

It is useful to examine the time history of the transient into stall as an aid in understanding the instability evolution process. The time history of the axial velocity measured by the eight sensors about the compressor circumference is shown in Fig. 7 for the unstabilized compressor. Here, the smooth growth of the first spatial harmonic wave is quite apparent for the 15 rotor revolutions illustrated before stall (it is highlighted by the parallel dotted lines in the figure). When the first spatial harmonic is actively suppressed (Fig. 8), the stall inception process is different in that it occurs at a lower mass flow and that the low amplitude waves growing prior to stall exhibit twice the frequency, as can be readily seen by comparing Figs. 7 and 8. It is the second spatial harmonic which goes unstable and triggers the rotating stall when the first harmonic is stabilized.

A useful tool for examining the wave growth is a discrete spatial Fourier transform of the axial velocities measured about the compressor annulus at each instant in time. This yields a complex Fourier coefficient for each spatial harmonic, the magnitude of which represents the instantaneous strength of that spatial wave, and the phase of which is a measure of the instantaneous angular position of the wave. Thus, a straight line phase history indicates that the

wave is travelling at constant angular velocity. This behavior can be seen in Fig. 9, which presents the spatial Fourier coefficients calculated from the unstabilized data of Fig. 7. The first harmonic position does change at a constant rate for some 15 revolutions before stall. (Note that the compressor is unwrapped here so that 2π radians represents one revolution of the wave, 4π radians two revolutions, and so on.) Examination of the magnitudes of the first three spatial harmonics in Fig. 9 shows that the first is the strongest and that it grows to large amplitude before the second and third do. This uncontrolled compressor has a single lobed stall (primarily first harmonic) at this mass flow. When the first harmonic is actively stabilized, however, the Fourier coefficient of the second harmonic is strongest prior to stall (Fig. 10). Once stall starts, though, the first harmonic quickly dominates. Indeed, examination of the time history in Fig. 8 shows that once the fully developed rotating stall is established, it is a single lobed stall.

A time history of the compressor under first and second harmonic control is shown in Fig. 11 and the corresponding spatial Fourier coefficients in Fig. 12. Here, the instability appears to grow from both the first and second harmonic, with the third harmonic weaker. Again, the fully developed stall is primarily single lobed. Although the third harmonic does not appear to play a dominant role in Fig. 12, simultaneous stabilization of the first three harmonics was implemented with results shown in Figs. 13 and 14. No increase in stable flow range is achieved over control of only the first and second harmonics. The relative roles played by the three spatial harmonics is not clear from the data in Fig. 14, although the first harmonic does appear to grow first.

We have been discussing the temporal structure of the instability onset; the spatial structure is of interest as well since that can be used to connect the harmonic representation with a detailed compressor aerodynamics view of rotating stall. Axial velocity measurements were taken at three spanwise stations at each of four circumferential positions between each of the three rotor and stator blade rows, as indicated in Fig. 2, in order to elucidate the 3-D structure of the flow field. The axial velocity data was transformed into spatial harmonics and then the power spectral density of each harmonic was calculated over an interval prior to stall as a measure of the wave strength at that time. The axial and spanwise variation in the strength of the first harmonic wave taken prior to

stall of the unstabilized compressor is shown in Fig. 15. Upstream, the first harmonic is strongest at midspan (the same is true for the second and third harmonics when the first is stabilized). Behind the first rotor, the signal is strongest at the tip. The decay in wave strength between the upstream measurement station used for control and the first rotor is consistent for both the first and second harmonics so that the first rotor will be considered the compressor face in the subsequent modelling.

We have now presented experimental data showing that a low speed multistage axial compressor can be actively stabilized and illuminating the stall inception processing in this machine. We will now use this data as an aid in refining an analytical model of instability inception and show both how this model can quantitatively predict many details of stall inception and how the model can be used to design an active control system.

MODELING

The two-dimensional, incompressible theory that has been formulated by Moore and Greitzer to describe rotating stall implies that, at the inception of the instability, small amplitude traveling waves develop in the compressor annulus, grow in magnitude, and eventually develop into rotating stall cells. In this analysis of the instability inception, an arbitrary axial velocity disturbance is decomposed into its Fourier spatial harmonics which can then be analyzed independently, since the equations describing the evolution of the instability are linear. If the compressor is assumed to operate in a quasi-steady manner, i.e. pressure rise is a function of flow coefficient only, this model predicts that all the spatial harmonics of the flow coefficient perturbation become unstable at the operating point where the total-to-static pressure rise characteristic (ψ vs. ϕ) becomes positively sloped. Disturbances are damped where the characteristic is negatively sloped, and amplified where the characteristic is positively sloped, with the growth or decay rate of the perturbation being determined by the magnitude of the slope.

Contrary to the assumptions of the above model, airfoils do not respond instantaneously to changes of incidence, and it has been observed in experiments (Nagano et al., 1971; Mazzawy,

1977) that the pressure rise across a compressor does not respond instantaneously to variations in flow coefficient. As will be shown, this finite response time of the compressor pressure rise has a stabilizing effect on flow perturbations, stabilizing higher harmonics to a greater extent than lower ones. When the quasi-steady assumption in the model is relaxed, and allowance is made for finite blade-passage flow response times, the spatial harmonics become unstable sequentially, with higher harmonics becoming unstable at larger positive slopes of the compressor total-to-static pressure-rise characteristic (i.e. lower flow coefficients). This behavior has been observed in experiments on both the three-stage compressor being considered, and previous experiments on a single-stage compressor (Paduano, 1991; Paduano et al., 1991).

The sequential destabilization of higher spatial harmonics of flow coefficient disturbances has beneficial implications for active control. By controlling only the first spatial harmonic of the disturbance, an increase in stable operating range can be obtained, down to the flow coefficient at which the second spatial harmonic of the disturbance becomes unstable. By controlling both the first and second spatial harmonics beyond this flow coefficient, the stable operating range can then be extended to the operating point where the third spatial harmonic becomes unstable. Using this control approach, the maximum range extension possible as predicted by the model is therefore dependent on the number of spatial harmonics of the disturbance that one is able to control, giving the designer the freedom to trade complexity (number of harmonics controlled) for stable range. Indeed, it is just this behavior that was found in the experiment. In the following sections, the model is extended to include the finite response time and the results are compared to experimental data.

ACCOUNTING FOR BLADE ROW PRESSURE LOSSES, DEVIATION AND BLOCKAGE

The peaked shape (Fig. 6) of a compressor total-to-static pressure rise characteristic, ψ is a consequence of viscous effects – stagnation pressure losses, deviation, and blockage – which increase as the flow coefficient, ϕ is reduced. Lower flow coefficients give rise to larger angles of attack on the compressor blading, which lead to stronger adverse pressure gradients within the

blade passages. These adverse pressure gradients produce undesirable flow fields both in the tip clearance region (e.g. large tip vortices) and within the blade passages (e.g. separated boundary layers). Viscous dissipation and mixing within these flow fields cause the associated high stagnation pressure losses, while the displacement effects give rise to deviation and blockage. When the overall flow within the compressor is unsteady, the blade passage flows do not respond instantaneously to fluctuations in axial velocity and blade inlet angle.

To determine the sensitivity of the compressor unsteady response to various phenomena, it is useful to quantify, where possible, the effect of each on the measured pressure rise. In an ideal compressor in which the effects of losses, deviation and blockage are absent, the pressure rise would increase monotonically with a decrease in flow coefficient. The total-to-static pressure rise of such an ideal compressor is given by the Euler compressor equation,

$$\psi_{ideal} = n - \phi \cdot \sum_{i=1}^n (\tan^2 \alpha_i + \tan^2 \beta_i) - \frac{1}{2} \left(\frac{\phi}{\cos(\alpha_e)} \right)^2 \quad (3)$$

where n is the number of compressor stages, α_i and β_i the stator and rotor exit angles of the i 'th stage, and α_e the exit angle from the last stator. The difference between this ideal characteristic and the measured one (ψ) shown in Fig. 16 can be attributed to the effects of losses, blockage, and deviation outlined above. When this pressure loss becomes greater than the increase in ideal pressure rise, the measured pressure rise characteristic, ψ , peaks over and becomes positively sloped.

When the compressor operates isentropically, all of the shaft work input goes into increasing the stagnation pressure of the working fluid. The isentropic stagnation pressure rise across the compressor can therefore be calculated from the shaft torque as:

$$\psi_{isen} = \frac{(P_e - P_{in})_{isentropic}}{\rho U^2} = \left(\frac{\psi_t}{\phi} - \frac{\phi^2}{2 \cos^2 \alpha_e} \right) \quad (4)$$

where ψ_t is the torque coefficient (measured in this case). The isentropic pressure rise characteristic of this three-stage compressor, ψ_{isen} , is also shown in Fig. 16. The contribution of dissipation to pressure losses is then given by the difference between the isentropic pressure rise

characteristic and the measured one, while the contribution of other effects (deviation and blockage) is given by the difference between the ideal and isentropic characteristics. For the purposes of this study, it is convenient to consider the measured pressure rise as being made up of the difference between the ideal pressure rise and the sum of steady pressure losses due to blockage and deviation, $L_{d,ss}$ (i.e. lack of turning), and losses due to dissipation, $L_{u,ss}$ (i.e. entropy production).

It is apparent from Fig. 16 that, for the three-stage compressor being considered here, total pressure losses (entropy), $L_{u,ss}$, increase significantly with a reduction in flow coefficient, whereas the effects of blockage and deviation, $L_{d,ss}$, vary little over the operating range that we are interested in, i.e. past the peak of the measured pressure rise characteristic. The influence of total pressure losses on compressor transient behavior are easier to model than the other non-ideal phenomena since the effects of total pressure losses are mostly confined to individual blade rows (mainly the pressure rise across the blade row is affected); on the other hand, the influence of deviation is not confined to a single blade row. Rather, the deviation of one blade row alters the angle of attack on the following row, changing the pressure rise it produces. However, since the effects of deviation and blockage appear to vary little with flow coefficient over the flow range of interest (i.e. $L_{d,ss}$ is flat in Fig. 16), these phenomena should not significantly affect the compressor transient response. Although we have not studied the generality of this observation to other compressors, we will exploit it here to simplify the analytical modeling. Thus, only the effects of total pressure losses on compressor transient response will be considered.

MODELING COMPRESSOR TRANSIENT BEHAVIOR

To start, it is useful to consider an instantaneous reduction in flow coefficient through the compressor (Fig. 17). Since the fluid dynamic phenomena (such as boundary layers) causing non-ideal compressor behavior are parabolic in nature, they do not adjust instantaneously to their new structure associated with the increased angle of attack on the compressor blading which occurs when the flow coefficient is reduced. Rather, the change in structure evolves over a period

which is dependent on the convection time of the bulk fluid through the blade passage. Thus, the associated pressure losses will evolve temporally as well. Emmons et al. (1955) suggested modeling the evolution of losses with a first order differential equation:

$$\tau_{loss} \frac{d(\delta L_{transient})}{dt} = \delta L_{quasi-steady} - \delta L_{transient} \quad (5)$$

where τ_{loss} represents the time constant characterizing the evolution. For the step reduction in ϕ considered here, the change in stagnation pressure loss $\delta L_{transient}$ is then given by:

$$\delta L_{transient} = \delta L_{quasi-steady} \left(1 - e^{-(t/\tau_{loss})} \right) \quad (6)$$

Since the stagnation pressure losses reflect the time lags associated with the flow within the compressor blade passages, the compressor pressure rise must as well. To illustrate this point, consider again an instantaneous reduction in flow coefficient when the compressor is operating on a positive sloped portion of the characteristic (Fig. 17). Immediately after the reduction in flow coefficient, the stagnation pressure loss is at its initial value, since a finite time is needed for the loss to evolve to its final value. Since the pressure rise across the compressor is made up of the difference between the isentropic value and the loss, the pressure rise initially follows a curve parallel to the isentropic one as shown in Fig. 17. It then decreases to its final value corresponding to the lower flow coefficient after a finite time characterized by the time constant τ_{loss} . Thus, when the flow in the compressor changes abruptly, the slope of the pressure rise characteristic deviates from its quasi-steady value. In particular, in the operating range of the compressor where the steady characteristic is positively sloped, the effective transient slope can be negative when the time constant associated with the flow unsteadiness is low enough, i.e. if the reduced frequency of the unsteadiness is high. This has important implications for the initiation of rotating stall since the stability of disturbances is dependent on the effective slope of the pressure rise characteristic. Specifically, inclusion of the time lag can increase compressor stability.

COMPRESSOR MODELING

The analytical model used in this study is an extension to the one described in Moore

(1984), Hynes and Greitzer (1987), and Epstein, Ffowcs Williams, and Greitzer (1989). The analysis is two-dimensional, which is appropriate since the machine under consideration has a high hub-to-tip ratio. The inlet flow field is undistorted (uniform inlet total pressure), and the inlet and exit ducts are assumed long, so that end effects, i.e. reflection and scattering of the disturbance wave from the ends, are not important. In addition, the tip speed of the compressor is assumed to be low enough for the flow field to be considered incompressible.

In the analysis an arbitrary flow perturbation, $\delta\phi$ is assumed to be of the form:

$$\delta\phi = \sum_{n=1}^{\infty} A_n e^{s_n \tilde{t}} e^{i n \vartheta}, \quad (7)$$

where

$$s_n = \frac{(\alpha_n - i\omega_n)r}{U}. \quad (8)$$

In the above formulation, $\omega_n r/U$ represents the rotation rate of the n 'th spatial harmonic non-dimensionalized by the rotor rotational speed, and $\alpha_n r/U$ the non-dimensionalized growth rate of the n 'th spatial harmonic. When the above form of the flow coefficient perturbation is substituted into the differential equations describing the dynamics of the fluid in the compression system, the analysis yields an eigenvalue problem in s_n , with the growth and rotation rates of each spatial harmonic determined from the solution to the eigenvalue problem. If the real part of s_n is negative, the spatial harmonic is damped, and the compressor operation is stable; if the real part of s_n is positive, the spatial harmonic grows exponentially, so that the compressor is unstable. Details of the extension of the stability modeling to account for finite compressor response time can be found in Appendix A.

An adaptation of this model to a compressor using control vanes for active control was developed by Paduano et al. in their study of the control of rotating stall in a single stage compressor. The details of the closed loop model extended to allow for finite compressor response times are outlined in Appendix B.

SYSTEM IDENTIFICATION OF COMPRESSOR DYNAMICS

Paduano showed that the response of compressor flow perturbations to control vane deflections can be expressed in transfer function form as,

$$\frac{\delta\phi_1}{\delta y} = \frac{(iG_n s + A_n + iB_n)(a_{n1} + a_{n2}s + a_{n3}s^2 + \dots + a_{nn}s^n)}{(s - C_n - iD_n)(b_{n1} + b_{n2}s + b_{n3}s^2 + \dots + b_{nn}s^n)} \quad (9)$$

where s represents the complex frequency (growth rate and rotation speed) of the forcing function δy , the control vane deflection wave, and ϕ_1 refers to the flow coefficient at the measurement station. The transfer function developed from the compression system model in Appendix B can be written in an equivalent form, hence the model parameters can be related directly to those determined experimentally. In particular, C_n corresponds to the growth rate α_n , and D_n to the rotation rate ω_n of the n 'th spatial harmonic. $(-B_n/G_n)$ and (A_n/G_n) represent the growth rate and frequency of the forced perturbation wave at which the actuation system is ineffective at producing a flow perturbation response. (This is defined as a *zero* of the actuation system.) In addition, G_n represents the effectiveness of the compression system to control vane forcing over the frequency range. The parameters A_n , B_n , C_n , D_n , and G_n therefore completely specify the open loop behavior of the compressor/actuation system. The parameters in Eq. (9) were experimentally determined using a least squares algorithm to fit the form of the transfer function to the measured dynamic response of the compressor. The accuracy of the theoretical model as a quantitative predictive tool could therefore be established by comparing the experimentally determined parameters to those predicted theoretically.

Open Loop Identification Methodology

In the development of the hydrodynamic stability model, it is assumed that the spatial harmonics of disturbance waves are decoupled, so that a linear model could be used. This assumption should be valid for the experimental identification studies so long as both the forcing and response disturbances are small in amplitude. Since the compressor characteristic slope plays an important role in the model, a unique transfer function exists at each steady-state operating point for each spatial harmonic of the disturbance wave. In the experiment, the forced response was

determined with the compressor operating in both the stable and normally unstable range. In the normally unstable operating range, the compressor was operated under closed loop active control. Under these conditions, it is the dynamic response of the combination of the compressor and the control system that is measured, therefore it is necessary to also accurately characterize the dynamics of the control system, so that compressor transfer can be deduced from the overall system measured.

The basic approach is therefore to excite the compressor with a well-characterized disturbance (a small amplitude sine wave deflection on the control vanes travelling about the circumferences at various speeds is a simple example). In this case, on the normally stable portion of the compressor map, a pseudo-random binary excitation signal with a bandwidth 1.25 times the rotor's rotational frequency was used to excite the dynamics of the first three spatial harmonics. Identification studies of harmonics higher than three would have required control vane forcing at a frequency beyond the bandwidth of the actuation system. The transfer function $\frac{\delta\phi_1}{\delta\gamma}$ is then determined from simultaneous discrete-time measurements of the control vane deflections, and flow field velocity perturbations around the compressor annulus, using a spectral method. The transfer function of each spatial harmonic resembled a second order dynamic system, which is equivalent to a first order system with complex coefficients of the form,

$$\frac{\delta\phi_1}{\delta\gamma} = \frac{iG_n s + A_n + iB_n}{s - C_n - iD_n} \quad (10)$$

which indicates that the additional terms in Eq. (9) do not affect the transfer function significantly. From the order of magnitude of the coefficients of the additional terms in the theoretical model, one can deduce that they will not affect the shape of the transfer function significantly over the range of forcing frequencies that was used in the experiment. Figures 18 and 19 show a least squares fit of the transfer function of the form in Eq. (10) to the experimental data. The fidelity of fit indicates that the form of Eq. (10) is quite appropriate for this compressor. The fit parameters which therefore form the dynamic model of this compressor are given in Table 2.

When the spatial harmonic of interest was stabilized by closed-loop control, the transfer function could not be determined directly in the above manner. In this case, the parameters

describing the open-loop performance were calculated using an instrument-variable modeling technique adapted to compressor identification by Paduano (1991). This method required an accurate model of the actuator dynamics, and a quantitative estimate of time delays in the feedback system. The actuator dynamics were determined from measurements of the response of control vane motion to the command signal. The open loop transfer function of the compressor was then measured by superimposing a forcing signal on the vane control signal. The accuracy of the instrument-variable method was checked continually by comparing the vane deflections with those simulated by the actuator dynamic model. The open loop dynamic parameters of the compressor could then be obtained from the commanded forcing perturbation, the actual vane deflections, and measurements of velocity perturbations upstream of the compressor. The details of the procedure are described by Haynes (1992).

COMPARING OPEN LOOP MEASUREMENTS AND PREDICTIONS

The symbols in Fig. 20 show the growth rates and frequencies of the first three spatial harmonics of a disturbance wave determined from the experimental identification studies. Negative values of $\alpha_n r/U$ represent temporal decay of a spatial harmonic while positive values represent exponentially growth. The experimental data shows that the spatial harmonics of the disturbance wave become unstable sequentially as ϕ is decreased, with higher harmonics becoming unstable at lower flow coefficients. The spacing of the neutral stability points ($\alpha_n = 0$) of the spatial harmonics is important for active control of rotating stall in compressors, since it gives an indication of the range extension that could be achieved for each additional spatial harmonic that is controlled.

With no control, the identification data indicates that rotating stall would be triggered by the growth of the first spatial harmonic where $\alpha_1 = 0$ at a flow coefficient of $\phi = 0.46$. The time history of spatial harmonic coefficients shown in Fig. 9 does indeed show that a coherent first harmonic perturbation appears first here and grows in amplitude before the higher harmonics do.

Figure 20 also shows the predictions of the unmodified Moore-Greitzer model (which

does not include the effects of finite compressor time response), that all the spatial harmonics of the disturbance wave become unstable at the same flow coefficient, $\phi = 0.468$, which is the peak of the total-to-static pressure rise characteristic. Also, the model underpredicts the rotational frequencies of the spatial harmonics. The model modified to include finite response times, however, gives much better agreement with the experimental data (Fig. 21). Since the exact values of the compressor blade row time lags needed by the model were not known *a priori*, a parametric study was done to determine the effect of their variation on the resultant theoretical predictions. In Fig. 21, the blade row response times $\bar{\tau}_s$ and $\bar{\tau}_r$ are set equal to 1.5 times the blade passage convection times, which gave the best agreement of the model with the experimental data. It is important to note that the growth and rotation rates of all three harmonic disturbances (6 quantities in total) predicted by the model show good agreement with data when only one constant is adjusted, the blade row time lag. Furthermore, the value required to match the data, 1.5 times the blade passage convection time, is within the range found by Nagano et al. (1971) whose experiments to characterize the response time produced values of between 1 and 1.5. This supports the hypothesis that finite pressure rise response time is the physical mechanism causing the sequential destabilizing of the spatial harmonics of the flow coefficient perturbation.

PREDICTING CLOSED LOOP COMPRESSOR BEHAVIOR

As was discussed above, the modified compressor stability model does a good job of predicting the open loop dynamics of the system, implying that the compressor dynamics are appropriately represented. This model adapted to the closed loop system should then be able to predict both the behavior of the compressor under active control as well as the influence of control system design parameters on that behavior. Details of the closed loop model are given in Appendix B.

Figure 22 shows the boundary between stable and unstable operation of the compressor operating under closed loop active control of the first spatial harmonic, as the phase of the control vane deflection wave is varied relative to that of the measured velocity perturbation wave. The

flow coefficient at which the spatial harmonic becomes unstable with no feedback control (gain, R , = 0) is also shown. The operating range of the compressor is thus extended for those phases for which the closed loop stability boundary is lower than the uncontrolled neutrally stable flow coefficient. The control system has a destabilizing effect on the compressor where the stability boundary is greater. The optimum feedback phase is that which gives the largest range extension and corresponds to the trough of the closed loop stability curve.

The model prediction and the experimental results in Fig. 22 agree closely. The agreement for control of the second spatial harmonic is close as well (Fig. 23), suggesting that the model is indeed an accurate representation of the stabilized compressor dynamics.

DISCUSSION AND SUMMARY

We have presented herein details of the closed loop control of a three-stage low speed research compressor. In addition to being only an end unto itself, the actively stabilized compressor is a powerful research tool for use in the understanding of compressor dynamics. In particular, such a machine facilitates the accurate measurement of the compression system dynamics with a combination of forced response experiments and system identification methodology. We have found the adoption of controls formalization to be a great aid in this area of fluid mechanics research.

Two approaches were taken to establish the compressor dynamics: (1) experimental measurement and identification, and (2) an analytical hydrodynamic 2-D stability model of the flow field. The experimental data was used to determine the relative importance of fluid phenomena included in the modeling. In this case, compressor time lags due to losses proved to be important while those stemming from deviation and blockage were not. The Moore-Greitzer stability model when suitably modified to include these time lags accurately predicted the open loop onset of stall as well as the behavior of the stabilized compressor. This implies that, to the degree to which these results may now be generalized, a tool now exists for predicting the rotating stall point in high hub-to-tip ratio compressors for which compressibility is not important.

The active stabilization of the first and second spatial harmonics increases the operating range of this compressor by about 8%, stabilizing the machine up to a characteristic slope of 0.9. Stabilization of the third harmonic does not alter the compressor behavior. At this time, we do not understand the lack of effectiveness of the control in increasing the operating range when the third harmonic is stabilized. Examination of the actuator motion confirmed that actuator authority and bandwidth limits are not reached before the rotating stall has grown to large amplitude. The influence of effects not included in the linear model have not been examined in detail.

Since control of the first two harmonics confirms quite closely to theory, Hendricks and Gysling (1992) have used this modeling approach to examine the performance of alternate actuators in controlling this compressor. They found that a circumferential array of jets at the compressor inlet in place of the control vanes should be particularly effective, stabilizing the compressor down to a characteristic slope of 4, over four times that achievable with control vanes, with a concomitant increase in stable flow range. Work is proceeding on an experimental verification of this modeling.

Overall, we believe that the good agreement between the experiment and theory presented herein indicates that it is now possible to assess analytically the influence of active compressor stabilization on the dynamics of the type of machine tested. Work is ongoing to extend the modeling and experiment to include low hub-to-tip ratio compressors (a 3-D stability model), to account for the effects of compressibility, and to treat the influence of inlet distortion on actively stabilized compressors.

ACKNOWLEDGEMENTS

The authors wish to thank Professors J.D. Paduano and E.M. Greitzer for much help and thoughtful discussion. This work was supported by the Air Force Office of Scientific Research, Major D. Fant, technical monitor.

REFERENCES

Day, I.J., "Active Suppression of Stall and Surge in Axial Compressors," Proceedings, ASME/IGTI Conference in Orlando, FL, 1991.

Emmons, H.W, Pearson, C.E., and Grant, H.P., "Compressor Surge and Stall Propagation", *ASME Transactions*, Vol. 79, pp.455-469, 1955.

Epstein, A.H., Ffowcs Williams, J.E., Greitzer, E.M., "Active Suppression of Aerodynamic Instabilities in Turbomachines", *Journal of Propulsion and Power*, V.5, No 2, 1989, pp. 204-211.

Gamache, R.N., "Axial Compressor Reversed Flow Performance," Ph.D. Thesis, Department of Aeronautics and Astronautics, MIT, 1985.

Garnier, V.H., Epstein, A.H., Greitzer, E.M., "Rotating Waves as a Stall Inception Indication in Axial Compressors", *Journal of Turbomachinery*, Vol. 113, 1991, pp. 290-301.

Haynes, J., "Active Control of Rotating Stall in a Three-Stage Axial Compressor," M.S. Thesis, Department of Mechanical Engineering, MIT, 1992.

Hendricks, G.J., and Gysling, D.L., "A Theoretical Study of Sensor-Actuator Schemes for Rotating Stall Control", presented at the AIAA/SAE/ASME/ASEE 28th Joint Propulsion Conference and Exhibit, Nashville, TN, 1992.

Hynes, T.P., and Greitzer, E.M., "A Method for Assessing Effects of Circumferential Flow Distortion on Compressor Stability", *Journal of Turbomachinery*, Vol. 109, pp. 371-379, 1987.

Lavrich, P.L., "Time Resolved Measurements of Rotating Stall in Axial Flow Compressors," MIT GTL Report No. 194, 1988.

Mazzawy, R.S., "Multiple Segment Parallel Compressor Model for Circumferential Flow Distortion", *Journal of Engineering for Power*, Vol. 99, No. 2, 1977.

McDougal, N.M., Cumpsty, N.A., Hynes, T.P., "Stall Inception in Axial Compressors", *Journal of Turbomachinery*, Vol. 112, 1990, pp. 116-125.

Moore, F.K., "A Theory of Rotating Stall of Multistage Axial Compressors: Part I - Small Disturbances", *Journal of Engineering for Gas Turbines and Power*, Vol. 106, 1984, pp. 313-320.

Moore, F.K., Greitzer, E.M., "A Theory of Post-Stall Transients in Axial Compressors: Part I - Development of the Equations," *ASME Journal of Engineering for Gas Turbines and Power*, Vol. 108, 1986, pp. 68-76.

Nagano, S., Machida, Y., Takata, H., "Dynamic Performance of Stalled Blade Rows", Japan Society of Mechanical Engineering Paper JSME 11, Presented at the Tokyo Joint International Gas Turbine Conference, Tokyo, Japan, 1971.

Paduano, J. D., "Active Control of Rotating Stall in Axial Compressors", Ph.D Thesis, Department of Aeronautics and Astronautics, MIT, 1991.

Paduano, J., Epstein, A.H., Valavani, L., Longley, J.P., Greitzer, E.M., Guenette, G.R., "Active Control of Rotating Stall in a Low Speed Axial Compressor", ASME paper 91-GT-88, Presented at the International Gas Turbine and Aeroengine Congress and Exposition, Orlando, FL, 1991.

APPENDIX A COMPRESSOR STABILITY MODEL INCLUDING TRANSIENT BEHAVIOR

In this model, the pressure rise across a compressor is modified by the pressure difference required to overcome the inertia of the fluid within the blade channels, when the flow within the compressor is unsteady. If one assumes that the flow within the blade passages is one dimensional, the unsteady pressure rise across the compressor can be written as (Moore, 1984; Hynes and Greitzer, 1987):

$$\frac{P_e - P_{ti}}{\rho U^2} = \psi - \lambda \frac{\partial \phi}{\partial \vartheta} - \frac{\mu r}{U} \frac{\partial \phi}{\partial t} \quad (A1)$$

where:

$$\psi = \psi_{isen} - L_r - L_s \quad (A2)$$

ψ_{isen} is the isentropic stagnation pressure rise across the compressor and L_r and L_s are the rotor and stator stagnation pressure losses. The inertia of the fluid in the rotors and in the compressor are represented by λ and μ respectively. At the initiation of rotating stall, the flow coefficient through the compressor is modified by a small perturbation $\delta\phi$ so that:

$$\begin{aligned} \phi &= \bar{\phi} + \delta\phi & \psi_{isen} &= \bar{\psi}_{isen} + \frac{d\psi_{isen}}{d\phi} \delta\phi \\ P_e &= \bar{P}_e + \delta P_e & L_s &= \bar{L}_s + \delta L_s \\ P_{ti} &= \bar{P}_{ti} + \delta P_{ti} & L_r &= \bar{L}_r + \delta L_r \end{aligned} \quad (A3)$$

The compressor pressure rise perturbation equation is therefore:

$$\frac{\delta P_e - \delta P_{ti}}{\rho U^2} = \frac{d\psi_{isen}}{d\phi} \delta\phi - \delta L_s - \delta L_r - \lambda \frac{\partial(\delta\phi)}{\partial \vartheta} - \frac{\mu r}{U} \frac{\partial(\delta\phi)}{\partial t} \quad (A4)$$

$$\psi_{isen} = \psi_{ss} + L_{r,ss} + L_{s,ss} \quad (A5)$$

where ψ_{ss} is the steady, axisymmetric total-to-static pressure rise including losses, and $L_{s,ss}$ and $L_{r,ss}$ the steady stator and rotor stagnation pressure losses respectively. The stator transient

stagnation pressure loss perturbation, δL_s , is given by the differential equation:

$$\tau_s \frac{\partial(\delta L_s)}{\partial t} = \frac{\partial L_{s,ss}}{\partial \phi} \delta \phi - \delta L_s \quad (A6)$$

The rotor unsteady stagnation pressure loss, δL_r , is calculated in a reference frame rotating with the rotor:

$$\tau_r \left(\frac{\partial(\delta L_r)}{\partial t} + \frac{U}{r} \frac{\partial(\delta L_r)}{\partial \vartheta} \right) = \frac{\partial L_{r,ss}}{\partial \phi} \delta \phi - \delta L_r \quad (A7)$$

In this analysis, a general perturbation in flow coefficient of the form:

$$\delta \phi = \sum_{n=1}^{\infty} A_n e^{(\alpha_n - i\omega_n)t} e^{in\vartheta} \quad (A8)$$

is considered. Each spatial harmonic of the perturbation can be considered separately, so only the n 'th spatial harmonic:

$$\delta \phi = A_n e^{(\alpha_n - i\omega_n)t} e^{in\vartheta} \quad (A9)$$

will therefore be examined.

The variables describing the evolution of the perturbation can be non-dimensionalized as follows:

$$\bar{t} = \frac{tU}{r}, \quad \bar{\tau} = \frac{\tau U}{r}, \quad s_n = \frac{(\alpha_n - i\omega_n)r}{U}, \quad (A10)$$

where U is the rotor speed and r is the average radius of the compressor annulus, so that the equations describing the perturbation become:

$$\frac{\delta P_e - \delta P_{ti}}{\rho U^2} = \frac{d\psi_{isen}}{d\phi} \delta \phi - \delta L_s - \delta L_r - \lambda \frac{\partial(\delta \phi)}{\partial \vartheta} - \mu \frac{\partial(\delta \phi)}{\partial \bar{t}} \quad (A11)$$

$$\bar{\tau}_s \frac{\partial(\delta L_s)}{\partial \bar{t}} = \frac{\partial L_{s,ss}}{\partial \phi} \delta \phi - \delta L_s \quad (A12)$$

$$\bar{\tau}_r \left(\frac{\partial(\delta L_r)}{\partial \bar{t}} + \frac{\partial(\delta L_r)}{\partial \vartheta} \right) = \frac{\partial L_{r,ss}}{\partial \phi} \delta \phi - \delta L_r \quad (A13)$$

$$\delta \phi = A_n e^{s_n \bar{t}} e^{in\vartheta} \quad (A14)$$

The upstream stagnation and downstream static pressure perturbations are given by the expressions (Epstein, Ffowcs Williams, Greitzer, 1989):

$$\frac{\delta P_d}{\rho U^2} = -\frac{1}{|n|} \frac{\partial(\delta\phi)}{\partial \bar{r}}, \quad (A15)$$

and

$$\frac{\delta P_e}{\rho U^2} = \frac{1}{|n|} \frac{\partial(\delta\phi)}{\partial \bar{r}} \quad (A16)$$

Substitution of Eqs. (A15), (A16) and (A14) into Eqs. (A11)-(A13) produces a generalized, complex eigenvalue problem in S_n :

$$(A - S_n B) \delta \bar{x} = 0 \quad (A17)$$

where:

$$A = \begin{pmatrix} \frac{1}{\zeta} \left(\frac{d\psi_{isen}}{d\phi} - in\lambda \right) & -\frac{1}{\zeta} & -\frac{1}{\zeta} \\ \frac{1}{\bar{r}_s} \frac{dL_{s,ss}}{d\phi} & -\frac{1}{\bar{r}_s} & 0 \\ \frac{1}{\bar{r}_r} \frac{dL_{r,ss}}{d\phi} & 0 & -\left(in + \frac{1}{\bar{r}_r} \right) \end{pmatrix} \quad (A18)$$

$$B = \begin{pmatrix} 1 & 0 & 0 \\ 0 & 1 & 0 \\ 0 & 0 & 1 \end{pmatrix} \quad (A19)$$

$$\delta \bar{x} = \begin{pmatrix} \delta\phi \\ \delta L_s \\ \delta L_r \end{pmatrix} \quad (A20)$$

$$\zeta = \left(\frac{2}{|n|} + \mu \right) \quad (A21)$$

and

$$\psi_{isen} = \psi_{ss} + L_{s,ss} + L_{r,ss} \quad (A22)$$

The solution to the eigenvalue problem yields the growth and rotation rates of the

perturbation wave. If the real part of s_n is negative, the disturbance is damped, representing stable operation of the compressor. If the real part of s_n is positive, the disturbance grows exponentially, representing unstable operation. For the uncontrolled compressor the growth rate of the perturbation is determined by the slope of the total-to-static pressure rise characteristic.

We must now fit this model to our data. The steady state compressor slope, $d\psi_{ss}/d\phi$ is determined from a polynomial fit to the measured pressure rise data. The total pressure loss across the compressor is estimated from the difference between the isentropic pressure rise characteristic and the measured one. A polynomial fit to this estimate is then used to determine the slopes of the rotor and stator loss curves, $dL_{r,ss}/d\phi$ and $dL_{s,ss}/d\phi$. For the particular build of the three stage compressor that was considered (75% reaction), it was assumed that 75% of the steady total pressure losses occurred across the rotors, and 25% across the stators. The time constants $\bar{\tau}_s$ and $\bar{\tau}_r$ were related to the convection time of the bulk flow through the blade channels. Since the values of these constants was not measured, a parametric study was done by varying these constants about the blade passage convection time. The best agreement with the experimental data was obtained with the time constants set to 1.5 times the blade passage convection time.

APPENDIX B
COMPRESSOR STABILITY MODEL INCLUDING ACTIVE CONTROL

In an actively controlled compressor, the relation between pressure and velocity perturbations can be manipulated by the actuator. Analysis of the movable inlet guide vane actuator involves determining relations between the actuation and perturbations in velocity and pressure introduced into the flow field. The actuator is modeled using quasi-steady actuator disk theory. A detailed model of the compressor with control vane control is given by Paduano (1991) and Paduano et al. (1991), and is outlined here, with modifications to account for finite compressor response times. With control vanes and quasi-steady compressor response the compressor perturbation equation can be written as:

$$\frac{\delta P_e - \delta P_{i2}}{\rho U^2} = \frac{\partial \psi}{\partial \phi} \delta \phi_2 + \frac{\partial \psi}{\partial \gamma} \delta \gamma - \lambda \frac{\partial(\delta \phi_2)}{\partial \vartheta} - \mu \frac{\partial(\delta \phi_2)}{\partial \bar{t}} \quad (B1)$$

where,

$$\frac{\delta P_e}{\rho U^2} = \frac{1}{|n|} \frac{\partial(\delta \phi_2)}{\partial \bar{t}} \quad (B2)$$

and

$$\frac{\delta P_{i2}}{\rho U^2} = \frac{\delta P_{i1}}{\rho U^2} - \mu_{igv} \frac{\partial}{\partial \bar{t}} \left(\delta \phi_2 + \frac{1}{2} \phi \mu_{igv} \frac{\partial(\delta \gamma)}{\partial \vartheta} \right) \quad (B3)$$

with

$$\delta \phi_2 = \delta \phi_1 - i n \phi \mu_{igv} \delta \gamma \quad (B4)$$

and

$$\frac{\delta P_{i1}}{\rho U^2} = - \frac{1}{|n|} \frac{\partial(\delta \phi_1)}{\partial \bar{t}} \quad (B5)$$

Here $\delta \gamma$ represents an angular displacement of the inlet guide vanes from their mean position. When the quasi-steady assumption is relaxed, and the finite compressor response times are modeled, the compressor perturbation equation can be written as:

$$\frac{\delta P_e - \delta P_{r,2}}{\rho U^2} = \frac{\partial \psi_{isen}}{\partial \phi} \delta \phi_2 + \frac{\partial \psi_{isen}}{\partial \gamma} \delta \gamma - \delta L_s - \delta L_r - \lambda \frac{\partial(\delta \phi_2)}{\partial \delta} - \mu \frac{\partial(\delta \phi_2)}{\partial i} \quad (B6)$$

where the transient losses, δL_s and δL_r are now modeled by the following equations,

$$\bar{\tau}_s \frac{\partial(\delta L_s)}{\partial i} = \frac{\partial L_{s,ss}}{\partial \phi} \delta \phi_2 + \frac{\partial L_{s,ss}}{\partial \gamma} \delta \gamma - \delta L_s \quad (B7)$$

$$\bar{\tau}_r \left(\frac{\partial(\delta L_r)}{\partial i} + \frac{\partial(\delta L_r)}{\partial \delta} \right) = \frac{\partial L_{r,ss}}{\partial \phi} \delta \phi_2 + \frac{\partial L_{r,ss}}{\partial \gamma} \delta \gamma - \delta L_r \quad (B8)$$

The above system of equations can be written as a transfer function between the flow perturbation at the measurement location upstream of the IGV's, \bar{x}_{hw} , and the control vane deflection $\delta \gamma$.

$$\frac{\delta \phi_{1,hw}}{\delta \gamma} = e^{-|n|\bar{x}_{hw}} \left(\frac{1}{\zeta} \left(\frac{\partial \psi_{isen}}{\partial \gamma} - \frac{\partial L_{s,ss}/\partial \gamma}{1+s\bar{\tau}_s} - \frac{\partial L_{r,ss}/\partial \gamma}{1+s\bar{\tau}_r} - in\mu_{igv}\phi s \left(\frac{1}{|n|} + \frac{\mu_{igv}}{2} \right) \right) \right) \quad (B9)$$

$$\frac{s + in\lambda}{\zeta} - \frac{1}{\zeta} \left(\frac{\partial \psi_{isen}}{\partial \phi_2} - \frac{\partial L_{s,ss}/\partial \phi_2}{1+s\bar{\tau}_s} - \frac{\partial L_{r,ss}/\partial \phi_2}{1+s\bar{\tau}_r} \right)$$

Control is implemented by sensing the axial velocity perturbation, $\delta \phi_1$ upstream of the inlet guide vanes. The measured signal is then processed by the controller which commands the control vanes to introduce a suitable perturbation into the flow field. With the proportional feedback scheme that was employed in the experiment, the measured signal is modified in amplitude and shifted spatially in phase. This is implemented analytically as follows:

$$\delta \gamma_c = Z e^{-|n|\bar{x}_{hw}} \delta \phi_1 \quad (B10)$$

$$Z = R e^{-i v_a} \quad (B11)$$

where R is the gain in amplitude of the signal, and v_a is the spatial phase shift of the commanded signal relative to the measured signal. In practice, non-ideal behavior causes the output from the actuator to differ from the command given by the controller. The non-ideal actuator dynamics were determined experimentally by measuring the transfer function of the actuator motion relative to an input command signal, and then fitting an appropriate dynamic model to the transfer function. As a simple example, assume that the dynamics of the actuator can be modeled by a second order differential equation,

$$\frac{\partial^2(\delta\gamma)}{\partial\tilde{t}^2} + 2\zeta_a\omega_a \frac{\partial(\delta\gamma)}{\partial\tilde{t}} = \omega_a^2 (\delta\gamma_c - \delta\gamma) \quad (B12)$$

where ω_a and ζ_a are the resonant frequency and damping ratio of the actuation system. (In the experiment a higher order dynamic model was required to accurately match the measured actuator transfer function.) With axial velocity sensing upstream of the control vanes, the actuator equation then becomes:

$$\frac{\partial^2(\delta\gamma)}{\partial\tilde{t}^2} + 2\zeta_a\omega_a \frac{\partial(\delta\gamma)}{\partial\tilde{t}} = \omega_a^2 (Ze^{-|n|\bar{x}_{hw}} \delta\phi_1 - \delta\gamma)$$

Equations (B2)-(B8) and (B10)-(B12) produce an eigenvalue problem. Parameters in the analysis are the operating flow coefficient (which determines the slope of the pressure rise characteristic), the gain and phase of the feedback control law, and the actuator dynamic parameters. For the control vane actuator with velocity feedback, this system of differential equations reduces to the form given in (A17), where the matrices A , B , and the vector $\delta\bar{x}$ are now:

$$A = \begin{pmatrix} \frac{1}{\zeta} \left(\frac{\partial \psi_{isen}}{\partial \phi} - in\lambda \right) & -\frac{1}{\zeta} & -\frac{1}{\zeta} & \frac{1}{\zeta} \left(\frac{\partial \psi_{isen}}{\partial \gamma} \right) & 0 \\ \frac{1}{\bar{\tau}_s} \frac{\partial L_{s,ss}}{\partial \phi} & -\frac{1}{\bar{\tau}_s} & 0 & \frac{1}{\bar{\tau}_s} \frac{\partial L_{s,ss}}{\partial \gamma} & 0 \\ \frac{1}{\bar{\tau}_r} \frac{\partial L_{r,ss}}{\partial \phi} & 0 & -\left(in + \frac{1}{\bar{\tau}_r} \right) & \frac{1}{\bar{\tau}_r} \frac{\partial L_{r,ss}}{\partial \gamma} & 0 \\ 0 & 0 & 0 & 0 & 1 \\ Ze^{-|n|\bar{x}_{hw}} \omega_a^2 & 0 & 0 & \omega_a^2 (Ze^{-|n|\bar{x}_{hw}} in\phi\mu_{igv} - 1) & -2\zeta_a\omega_a \end{pmatrix} \quad (B13)$$

$$B = \begin{pmatrix} 1 & 0 & 0 & 0 & \frac{in\phi\mu_{igv}}{2} \left(\frac{1}{|n|} + \frac{\mu_{igv}}{2} \right) \\ 0 & 1 & 0 & 0 & 0 \\ 0 & 0 & 1 & 0 & 0 \\ 0 & 0 & 0 & 1 & 0 \\ 0 & 0 & 0 & 0 & 1 \end{pmatrix} \quad (B14)$$

$$\delta\bar{x} = \begin{pmatrix} \delta\phi_2 \\ \delta L_s \\ \delta L_r \\ \delta\gamma \\ \partial(\delta\gamma)/\partial\bar{t} \end{pmatrix} \quad (B15)$$

with:

$$\zeta = \left(\frac{2}{|n|} + \mu \right) \quad (B16)$$

and

$$\psi_{isen} = \psi_{ss} + L_{s,ss} + L_{r,ss} \quad (B17)$$

There are five eigenvalues for each spatial harmonic of the disturbance, and the system is stable when the real part of each of the eigenvalues is negative.

TABLE I
MIT THREE-STAGE AXIAL COMPRESSOR DESIGN PARAMETERS

	No. of Blades	Chord (mm.)	Camber (degrees)	Stagger (degrees)	Tip Clearance* (mm.)	Leading Edge Blade Angle* (degrees)	Trailing Edge Blade Angle* (degrees)
Tip Diameter (mm.)					610.00		
Hub-to-Tip Ratio					0.88		
Design Average Reaction					0.75		
Design Flow Coefficient					0.59		
Pressure Rise Coefficient (@design)					2.03		
Efficiency (@design)					84.3%		
Stalling Flow Coefficient					0.460		
Inlet Guide Vanes	25	20.1	11.0	8.1			
IGV/CV Gap		6.0			0		10.0
Control Vanes	12	81.2	0.0	8.1			8.1
CV/R1 Gap		13.0			8.1		
Rotor 1	54	45.2	17.0	42.8	0.97		
R1/S1 Gap		20.0			50.0		41.0
Stator 1	85	31.4	27.0	11.0	0.81		
S1/R2 Gap		20.0			54.5		36.5
Rotor 2	55	44.8	18.0	43.5	0.94		
R2/S2 Gap		20.0			58.0		38.0
Stator 2	88	31.3	25.0	12.0	0.94		
S2/R3 Gap		20.0			18.0		-1.0
Rotor 3	49	50.7	20.0	44.6	0.89		2.5
R3/S3 Gap		18.0			27.5		
Stator 3	90	31.4	53.0	5.5	0.86		
					36.5		-17.0

*Measured by Gamache
CV = Control Vane
IGV = Inlet Guide Vane

TABLE 2
PARAMETER IDENTIFICATION DATA

<u>1st Harmonic</u>								
ϕ	Percent Difference from ϕ_{stall}	$C_1 = \alpha_1$	$D_1 = \omega_1$	A_1	B_1	G_1	$\text{Re(zero)} =$ $-B_1 / G_1$	$\text{Im(zero)} =$ A_1 / G_1
0.488	6.0	-0.1839	0.329	-0.0709	0.00280	-0.0573	0.0489	1.238
0.462	0.4	-0.0303	0.304	-0.0650	0.00375	-0.0515	0.0728	1.262
0.432	-6.0	0.1320	0.270	-0.0463	0.00943	-0.0329	0.2865	1.406

<u>2nd Harmonic</u>								
ϕ	Percent Difference from ϕ_{stall}	$C_2 = \alpha_2$	$D_2 = \omega_2$	A_2	B_2	G_2	$\text{Re(zero)} =$ $-B_2 / G_2$	$\text{Im(zero)} =$ A_2 / G_2
0.488	6.0	-0.2829	0.790	-0.1119	-0.01525	-0.0872	-0.1749	1.283
0.460	0.0	-0.1223	0.762	-0.1032	-0.00446	-0.0724	-0.0616	1.426
0.432	-6.0	0.0510	0.781	-0.0684	0.00345	-0.0431	0.0799	1.587

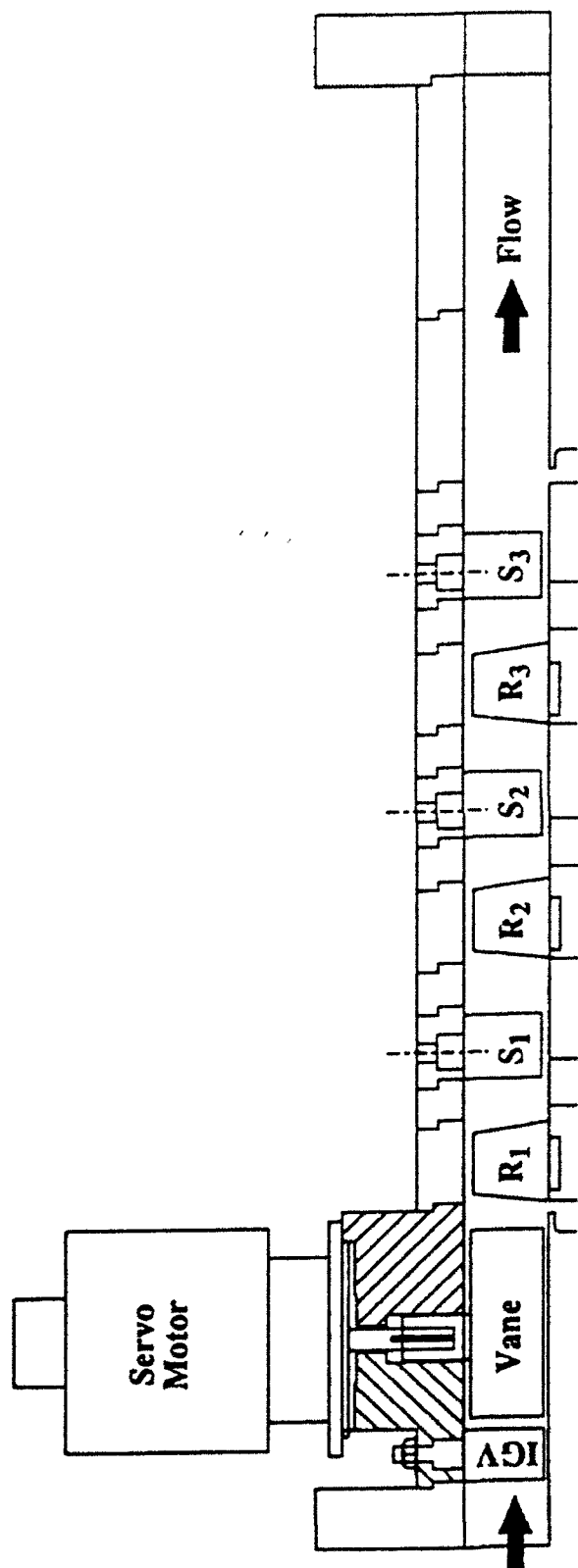
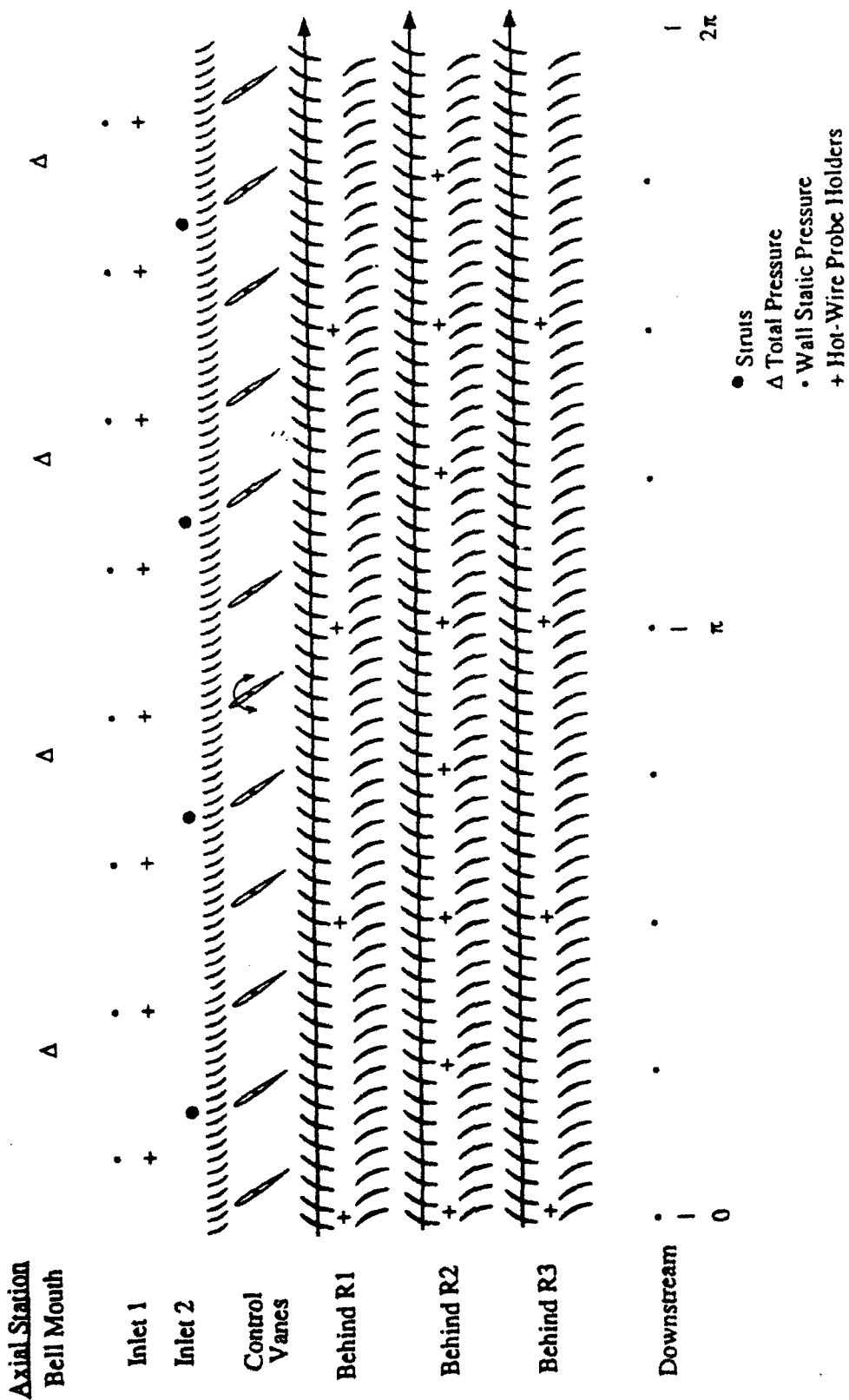


Fig. 1: Three-stage compressor arrangement with individually actuated high speed control vanes



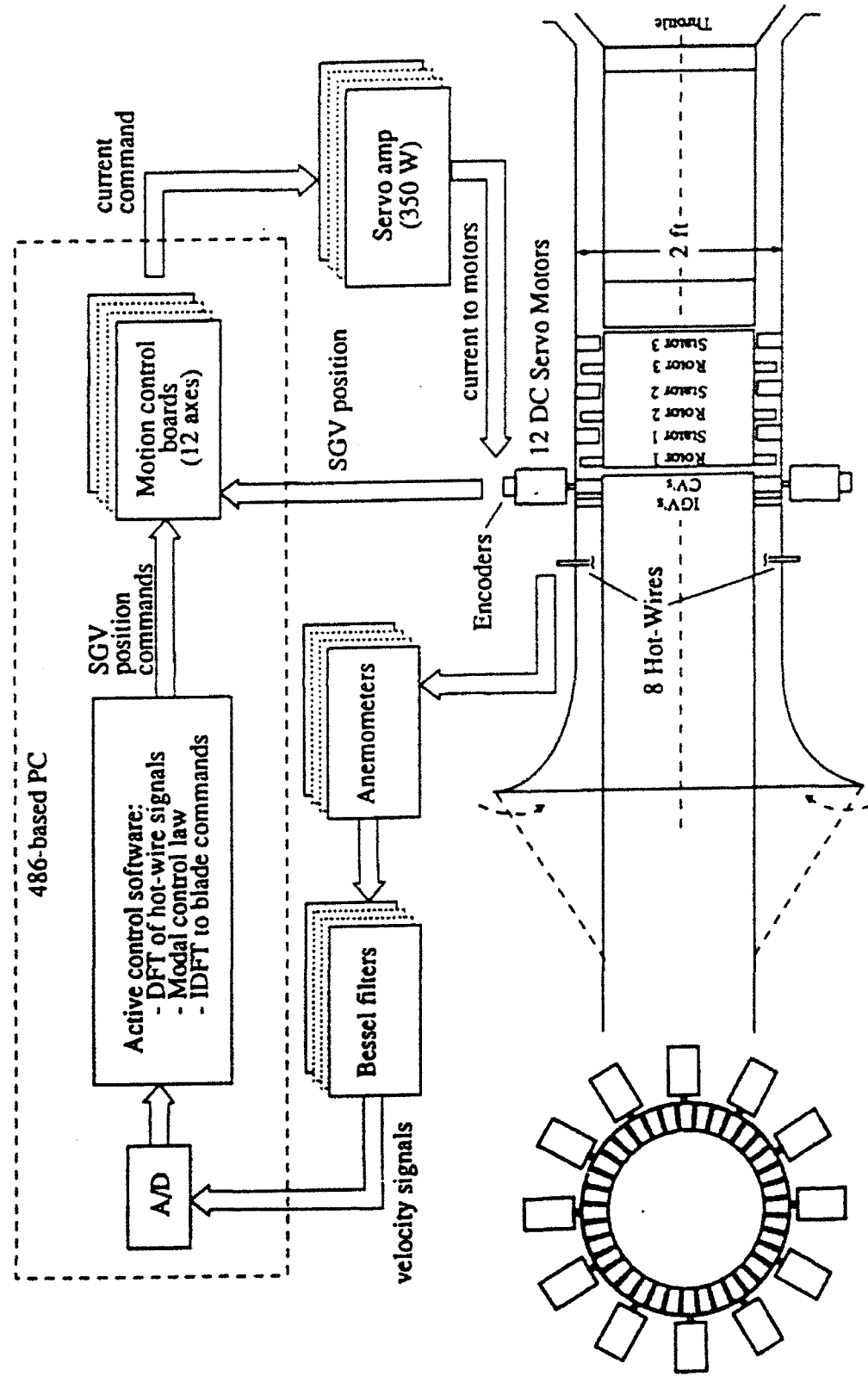


Fig. 3: Closed-loop control feedback path

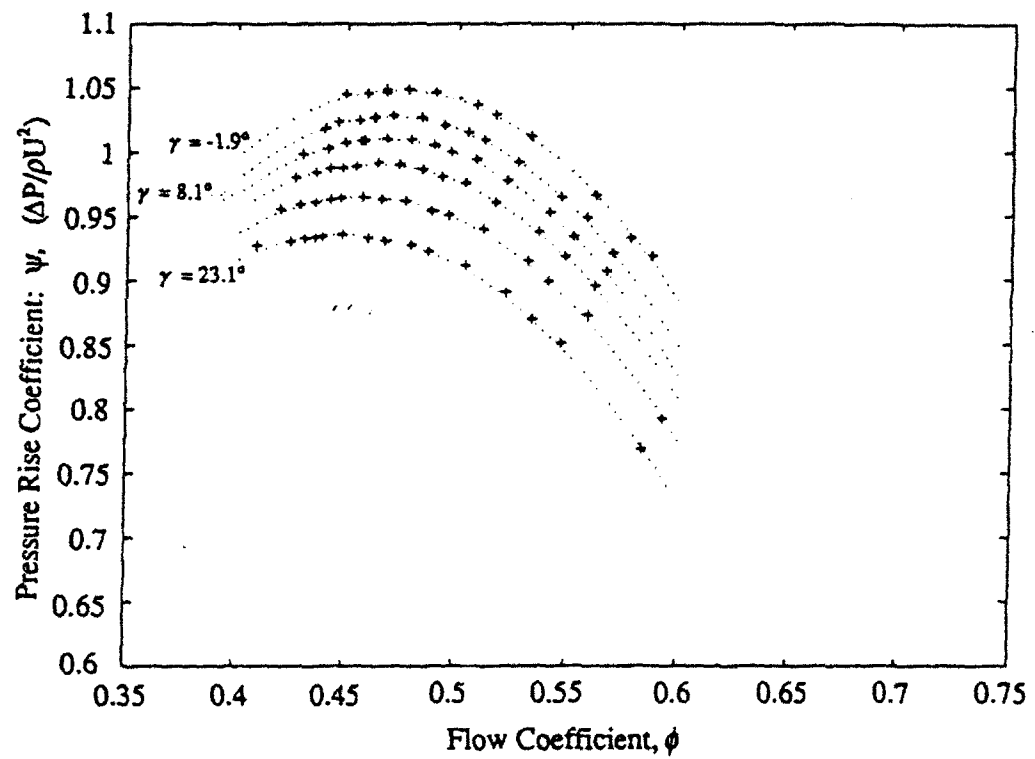


Fig. 4: The influence of uniform control vane stagger angle (γ) on the compressor characteristic at 5° intervals of γ

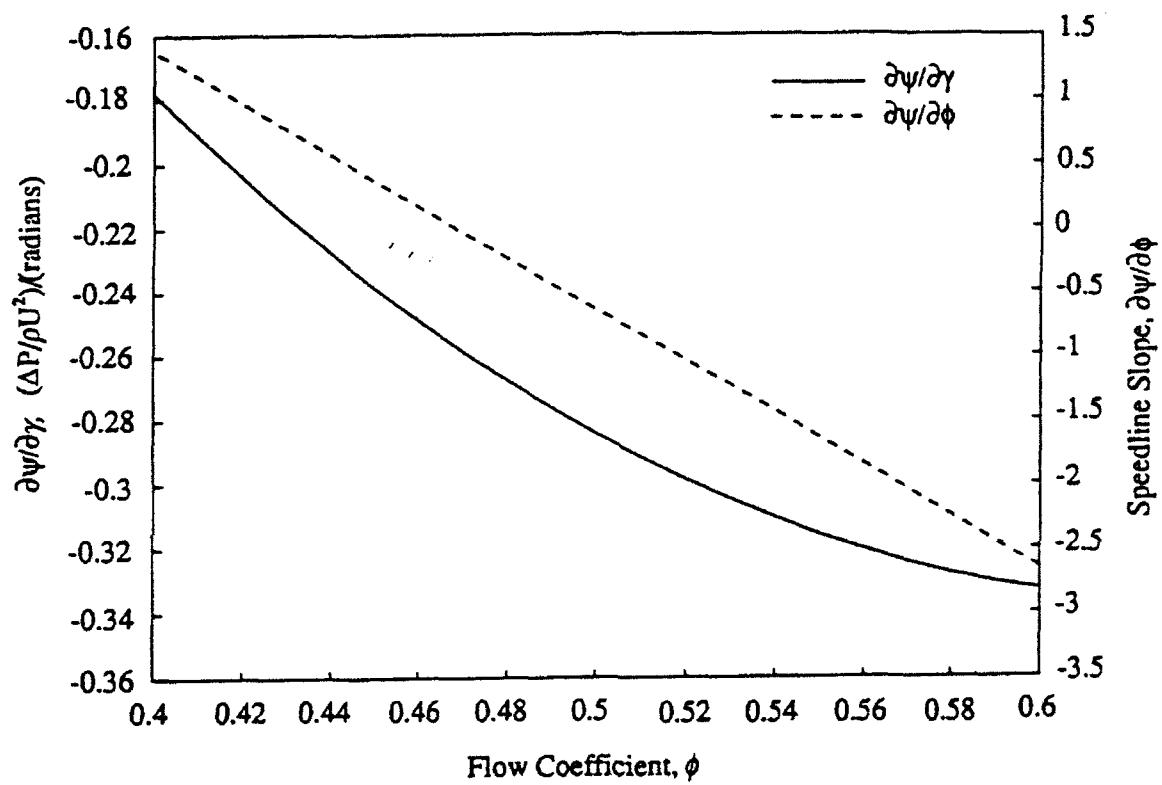


Fig. 5: Variation of speedline slope ($\frac{\partial \psi}{\partial \phi}$) and control vane angle pressure rise influence ($\frac{\partial \psi}{\partial \gamma}$) measured for the three-stage compressor

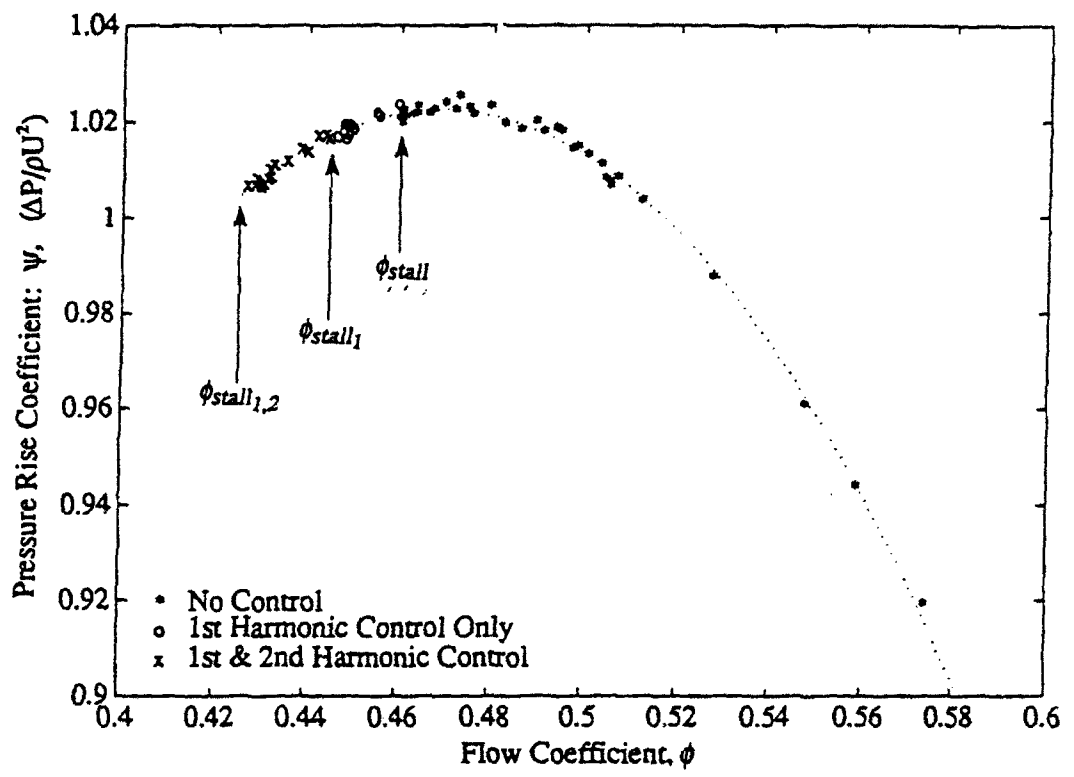


Fig. 6: Active stabilization of the first and second spatial harmonics decreases stalling mass flow by 8%

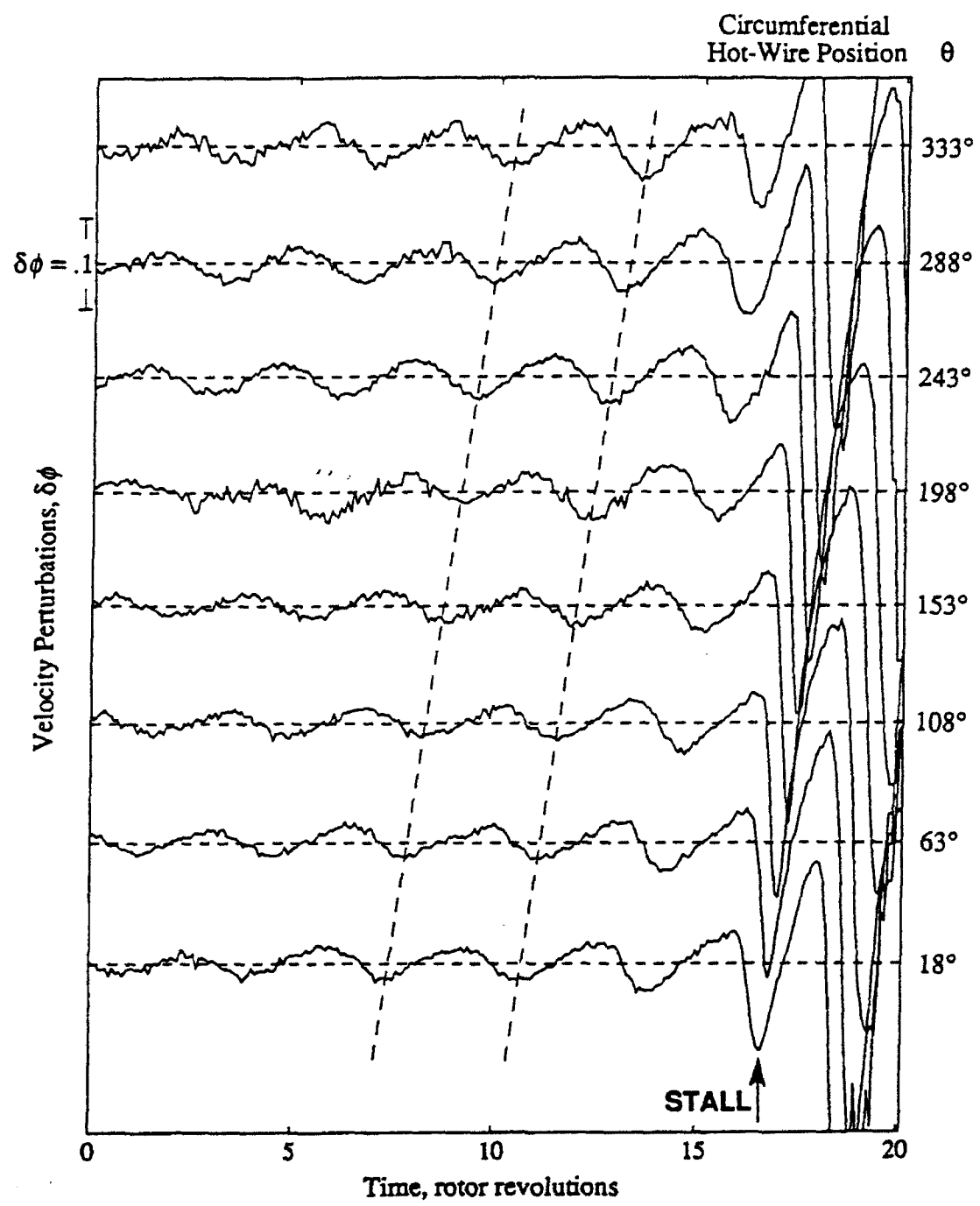


Fig. 7: Stall inception flow field around compressor annulus at midspan measured upstream of the IGV's when $\bar{\phi} = 0.46$, with no control

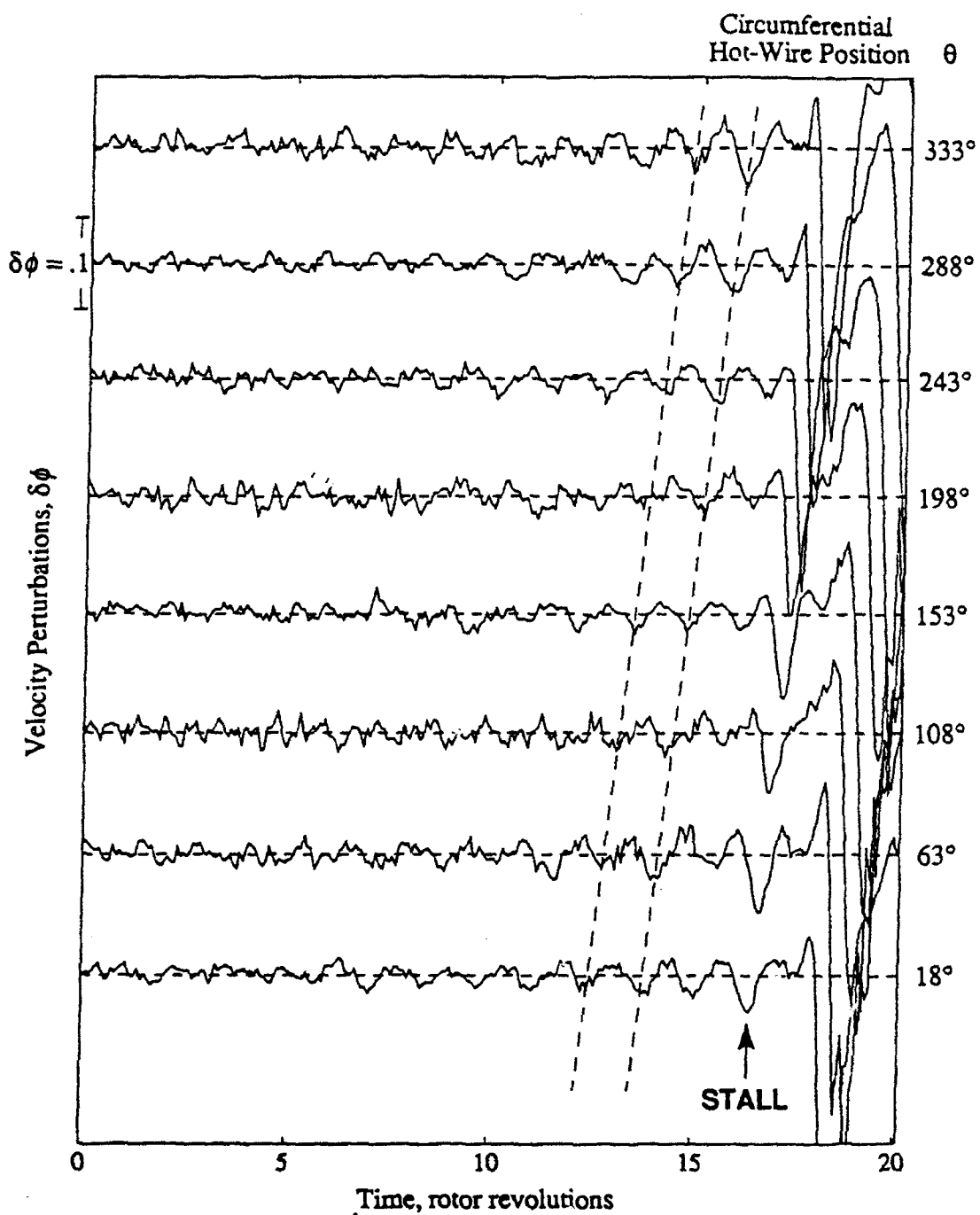


Fig. 8: Stall inception flow field around compressor annulus at midspan during first harmonic control measured upstream of the IGV's when $\bar{\phi} = 0.45$

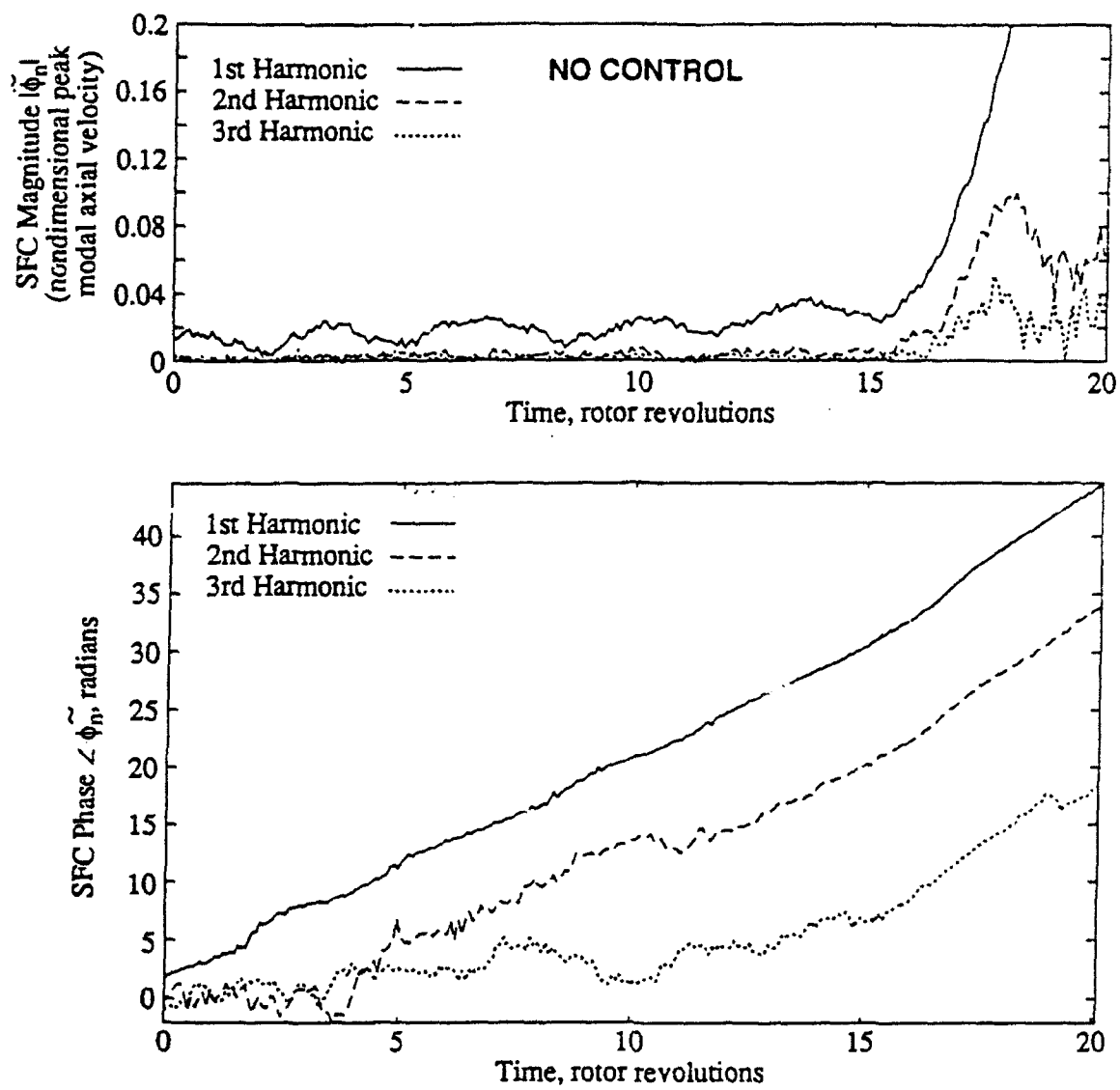


Fig. 9: Magnitude and phases of the first three spatial Fourier coefficients (SFC) calculated from the stall inception flow field at midspan (calculated from the data of Fig. 7)

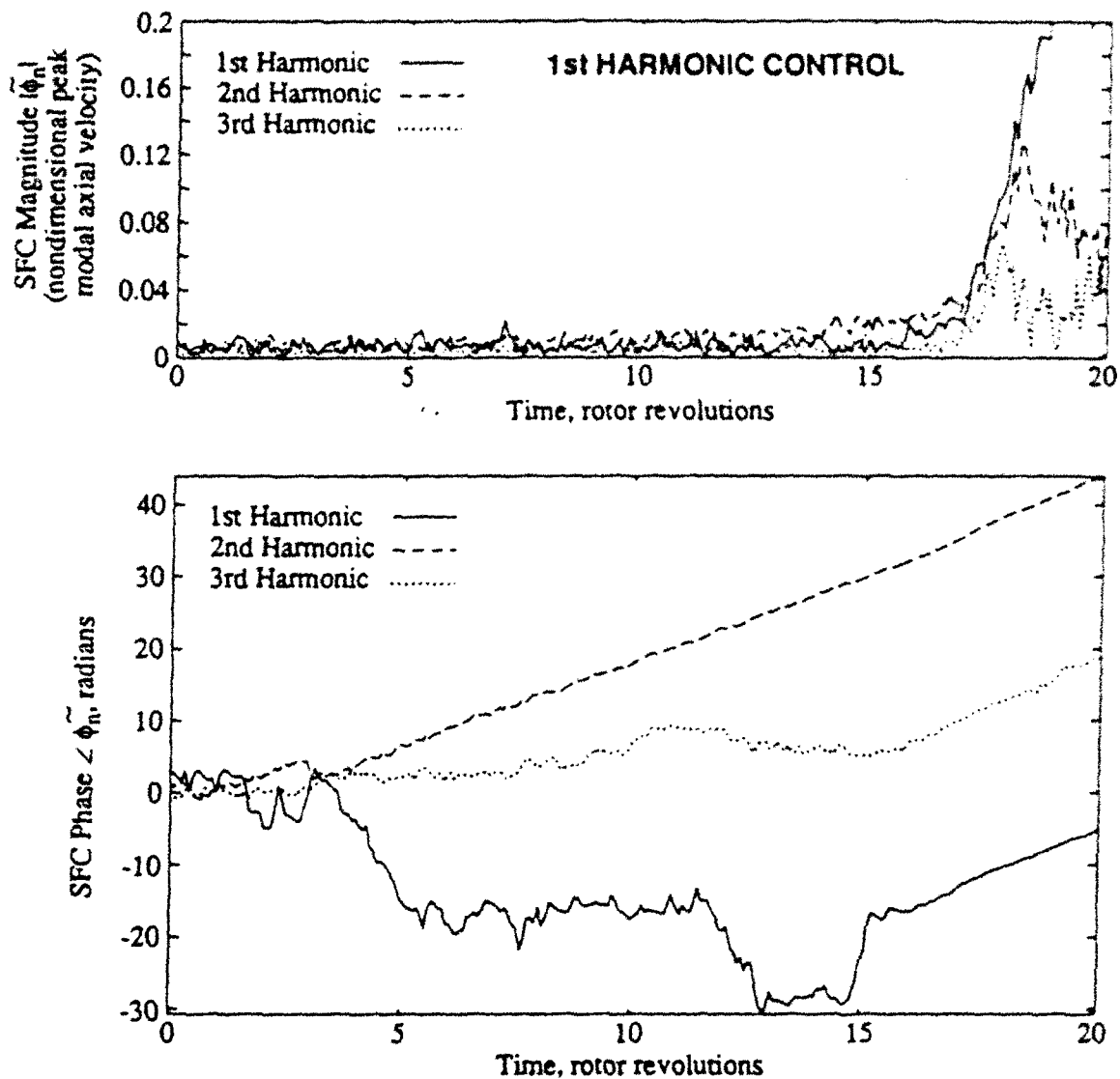


Fig. 10: Magnitude and phases of the first three spatial Fourier coefficients calculated from the stall inception flow field at midspan during first harmonic control (calculated from the data of Fig. 8)

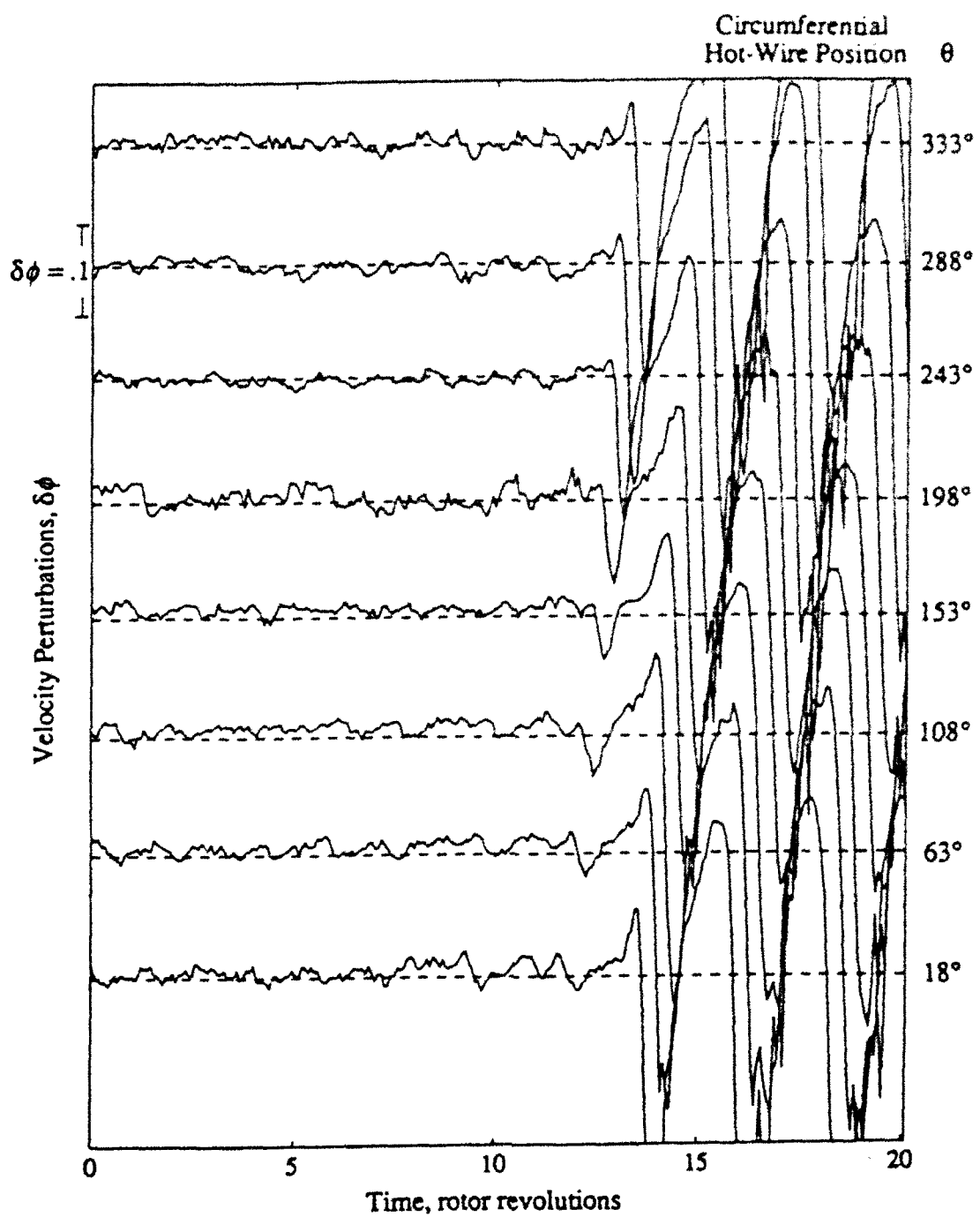


Fig. 11: Stall inception flow field around compressor annulus during optimal 1st and 2nd mode control measured upstream of the IGV's when $\bar{\phi} = 0.43$

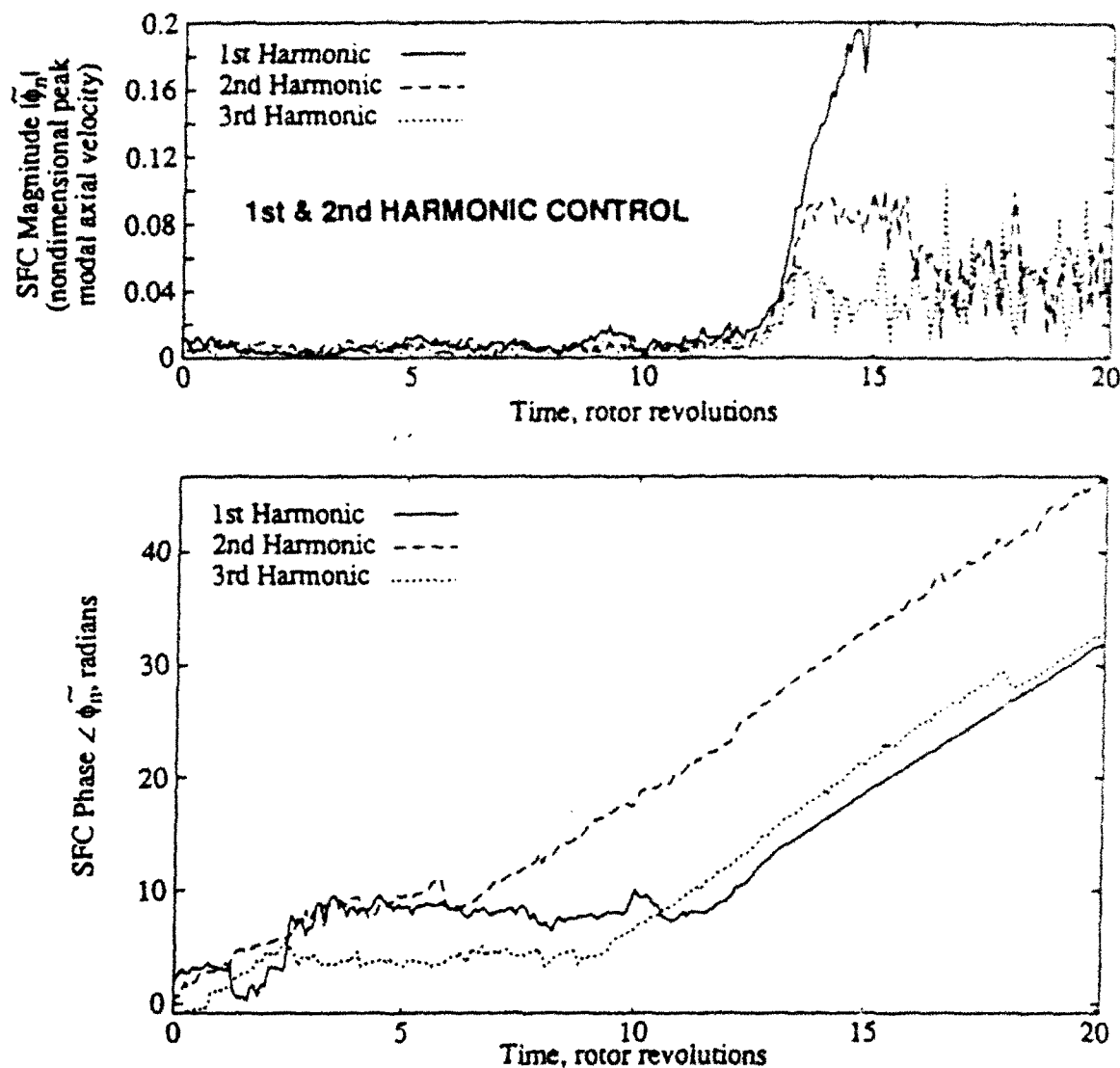


Fig. 12: Magnitude and phases of the first three spatial Fourier coefficients calculated from the stall inception flow field at midspan during optimal first and second harmonic control (calculated from the data of Fig. 11)

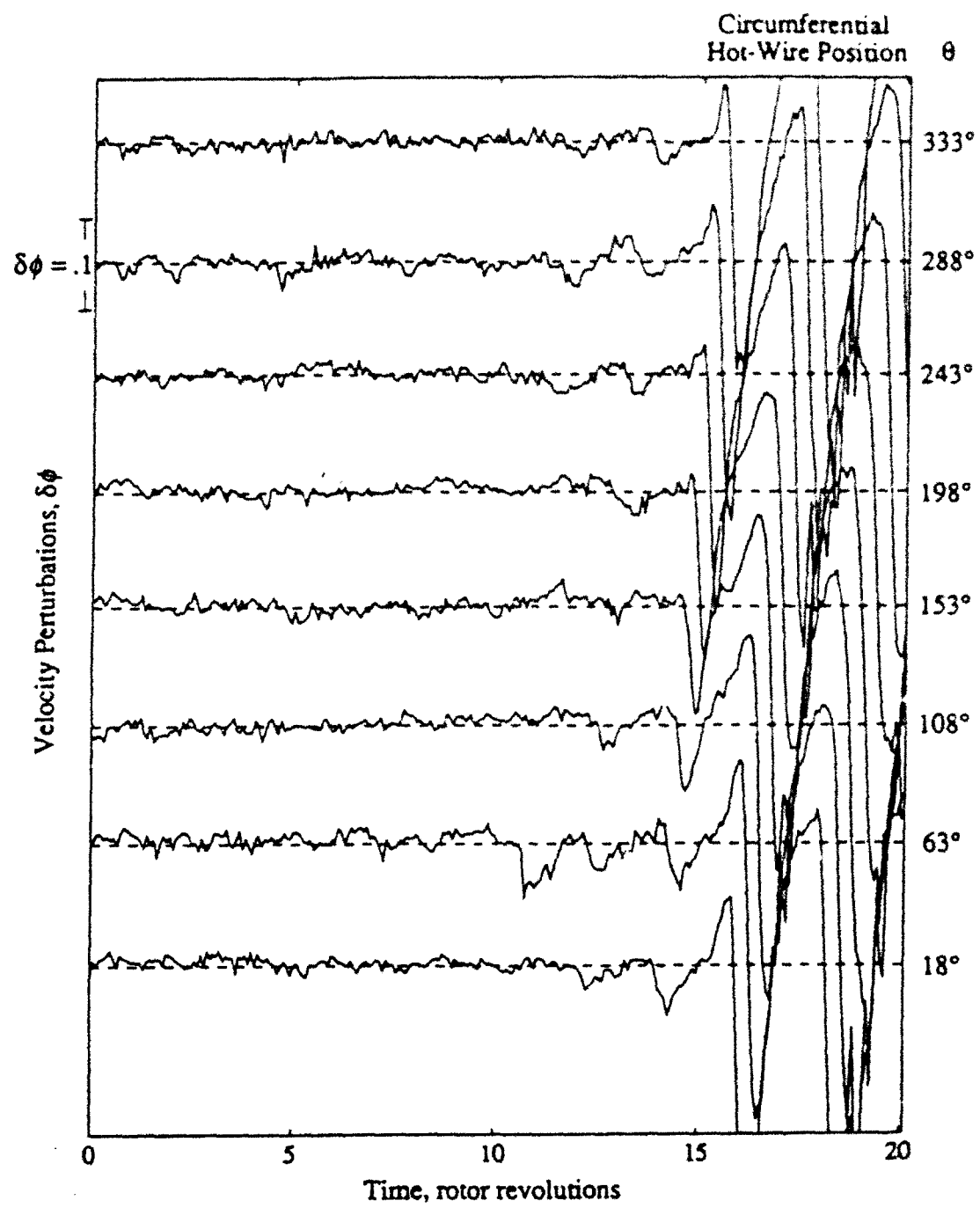


Fig. 13: Stall inception flow field around compressor annulus during optimal 1st, 2nd, and 3rd mode control measured upstream of the IGV's when $\bar{\phi} = 0.43$

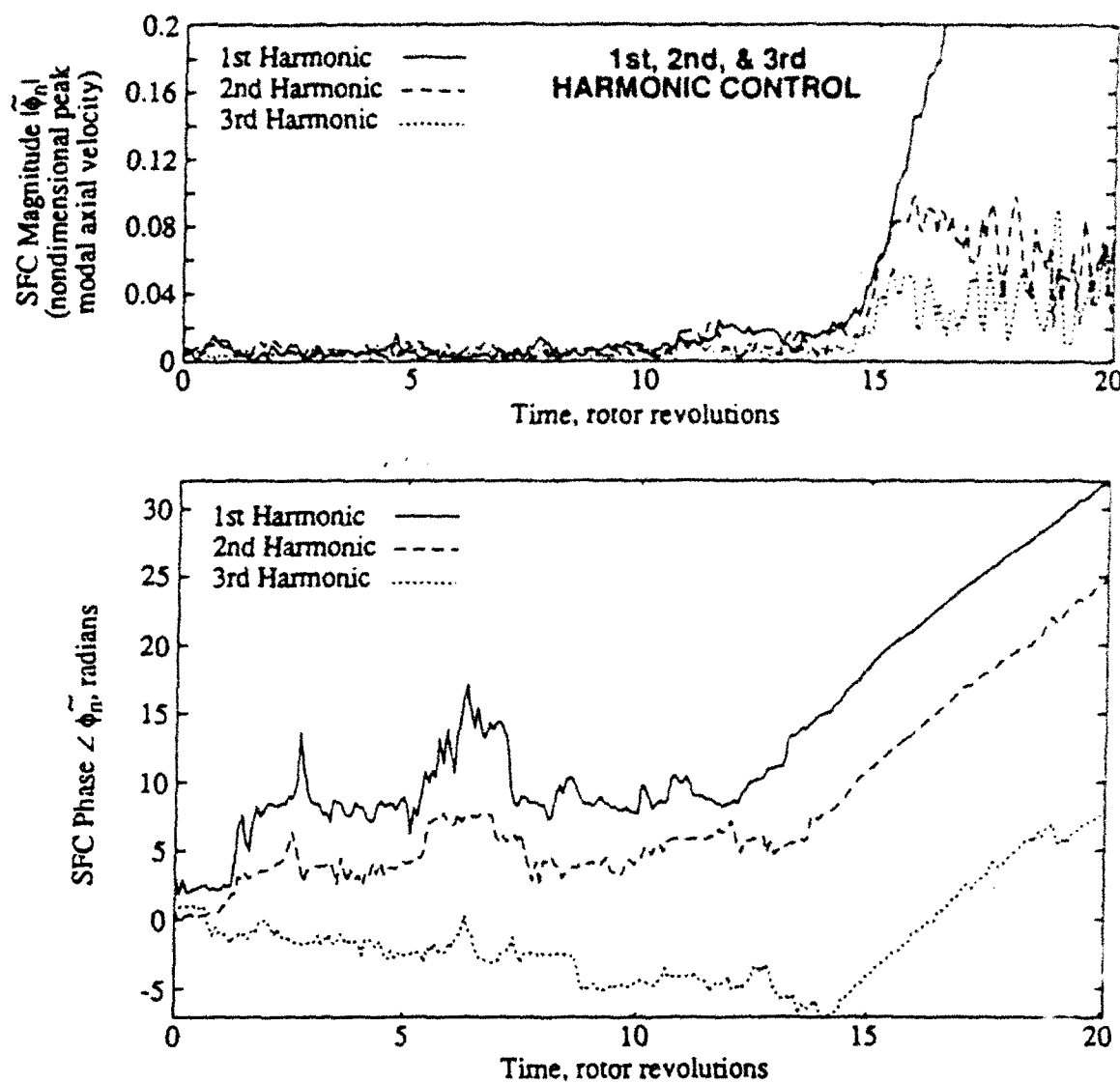


Fig. 14: Magnitude and phases of the first three spatial Fourier coefficients calculated from the stall inception flow field at midspan during optimal first, second, and third harmonic control (calculated from the data of Fig. 13)

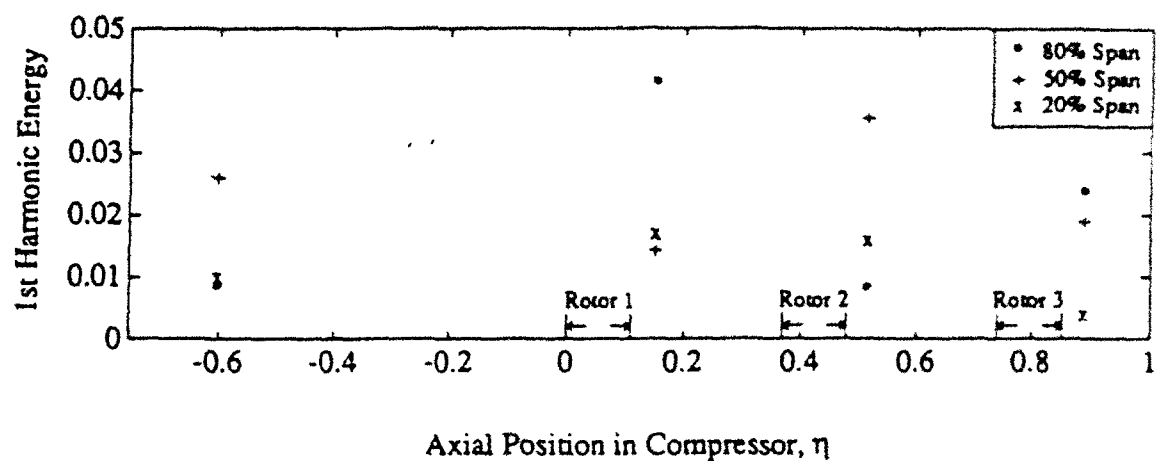


Figure 15: Axial variation in 1st mode strength measured at 3 radial positions

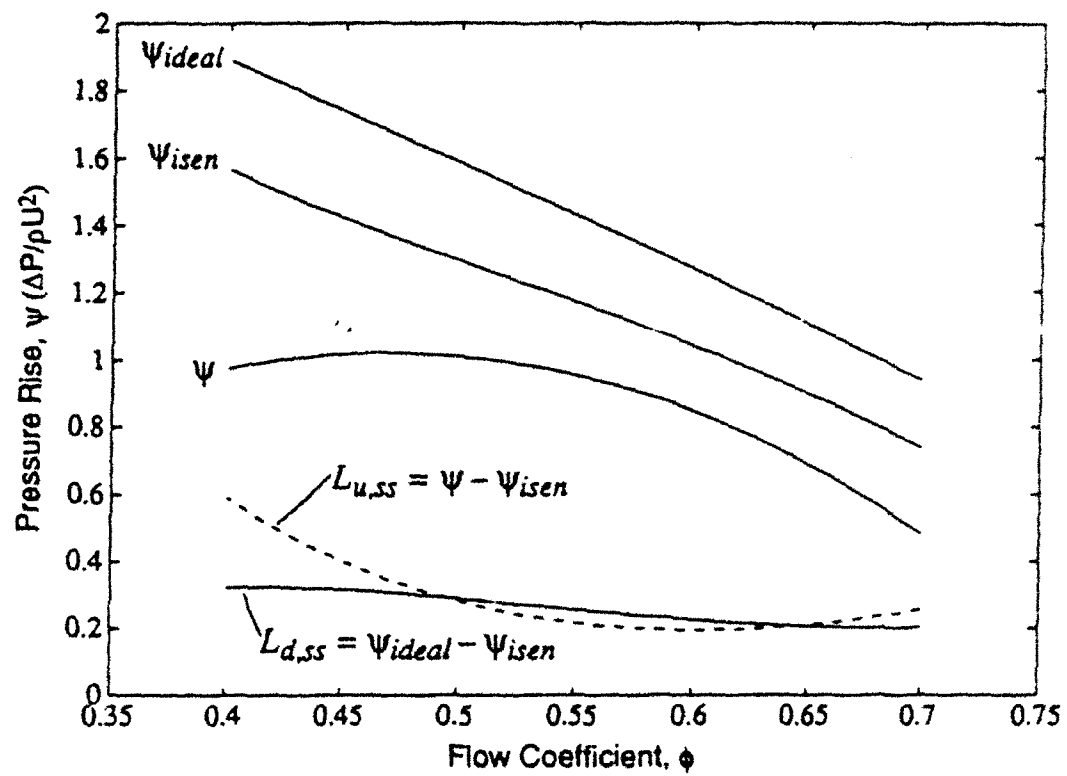


Fig. 16: Comparison of the ideal pressure rise (ψ_{ideal}), the isentropic pressure rise (ψ_{isen}), and the measured pressure rise (ψ). The losses due to deviation, $L_{d,ss}$, and dissipation, $L_{u,ss}$, are also shown.

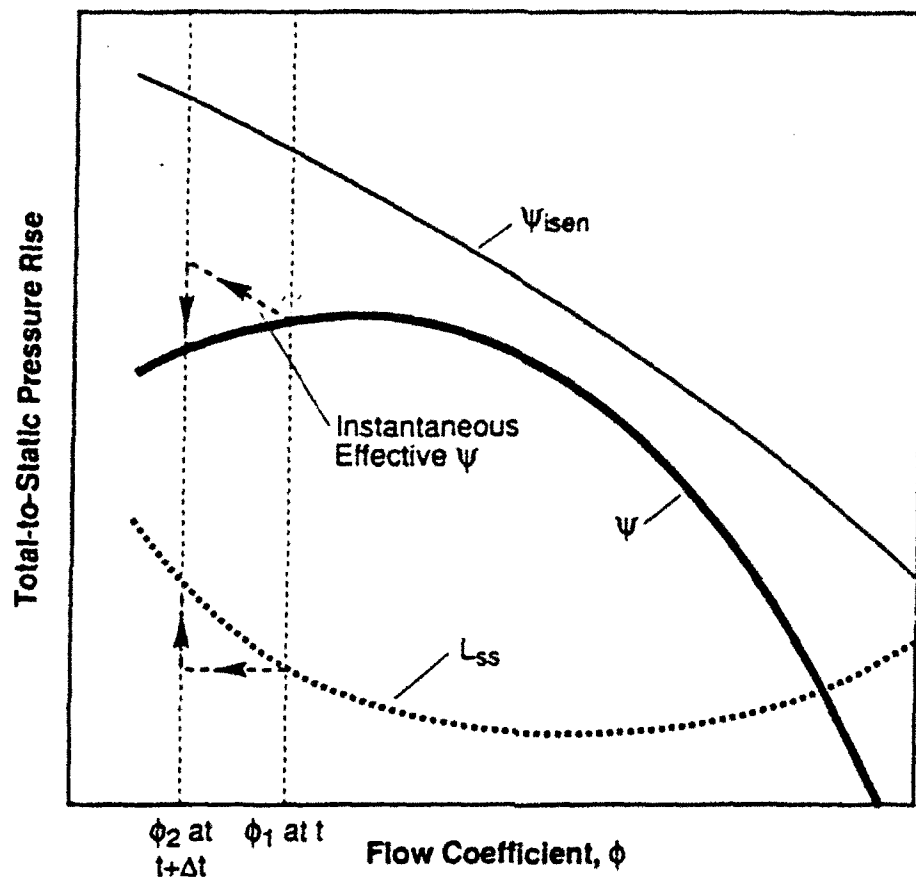


Fig. 17: The effect of the compressor time lag, τ_{loss} , is to temporarily increase the effective slope of the compressor characteristic

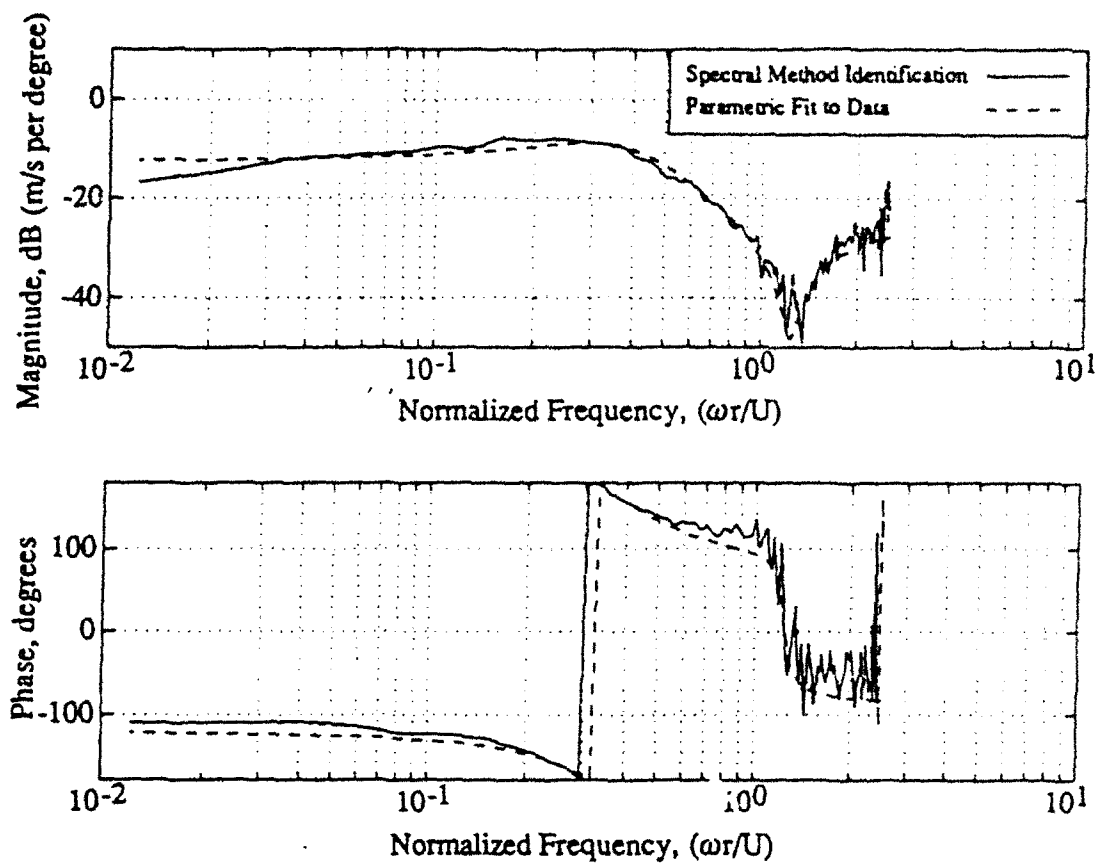


Fig. 18: Estimate of compressor transfer function for first harmonic
at $\phi = 0.49$ (6% above the stalling flow coefficient)

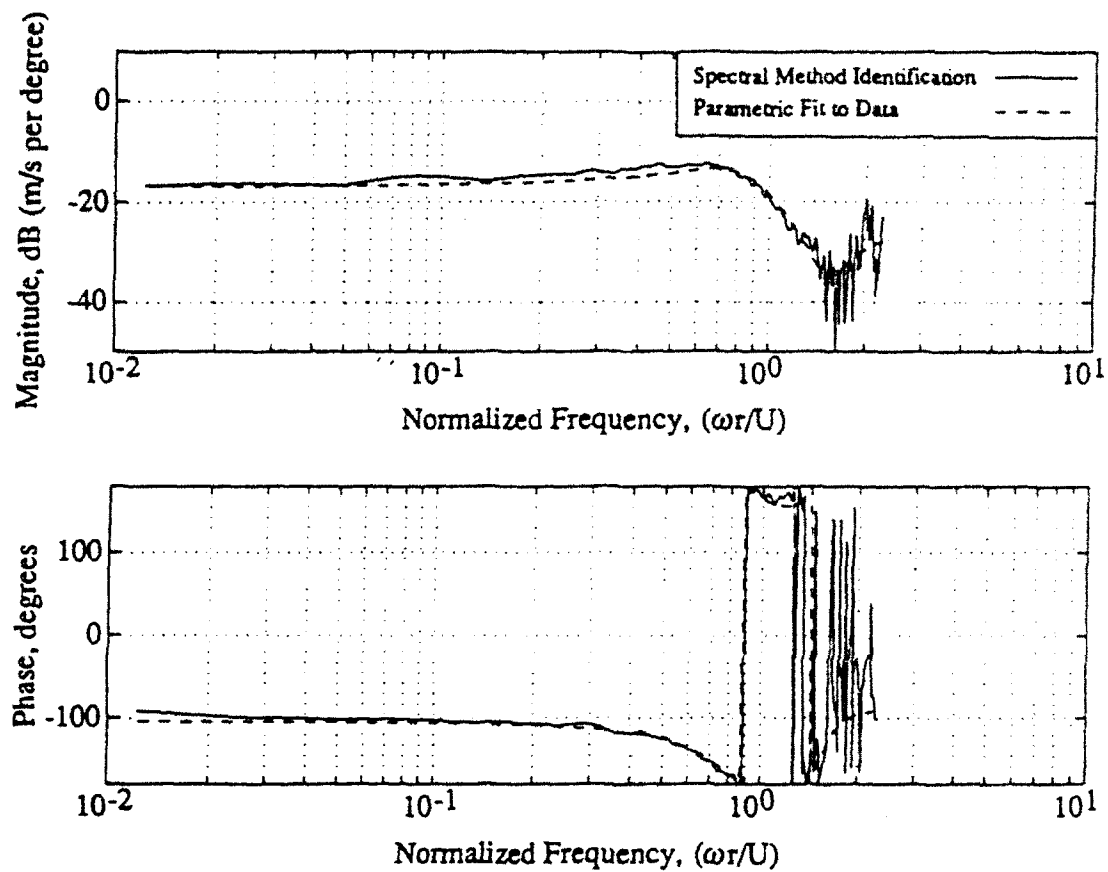


Fig. 19: Estimate of compressor transfer function for second harmonic at $\phi = 0.49$ (6% above the stalling flow coefficient)

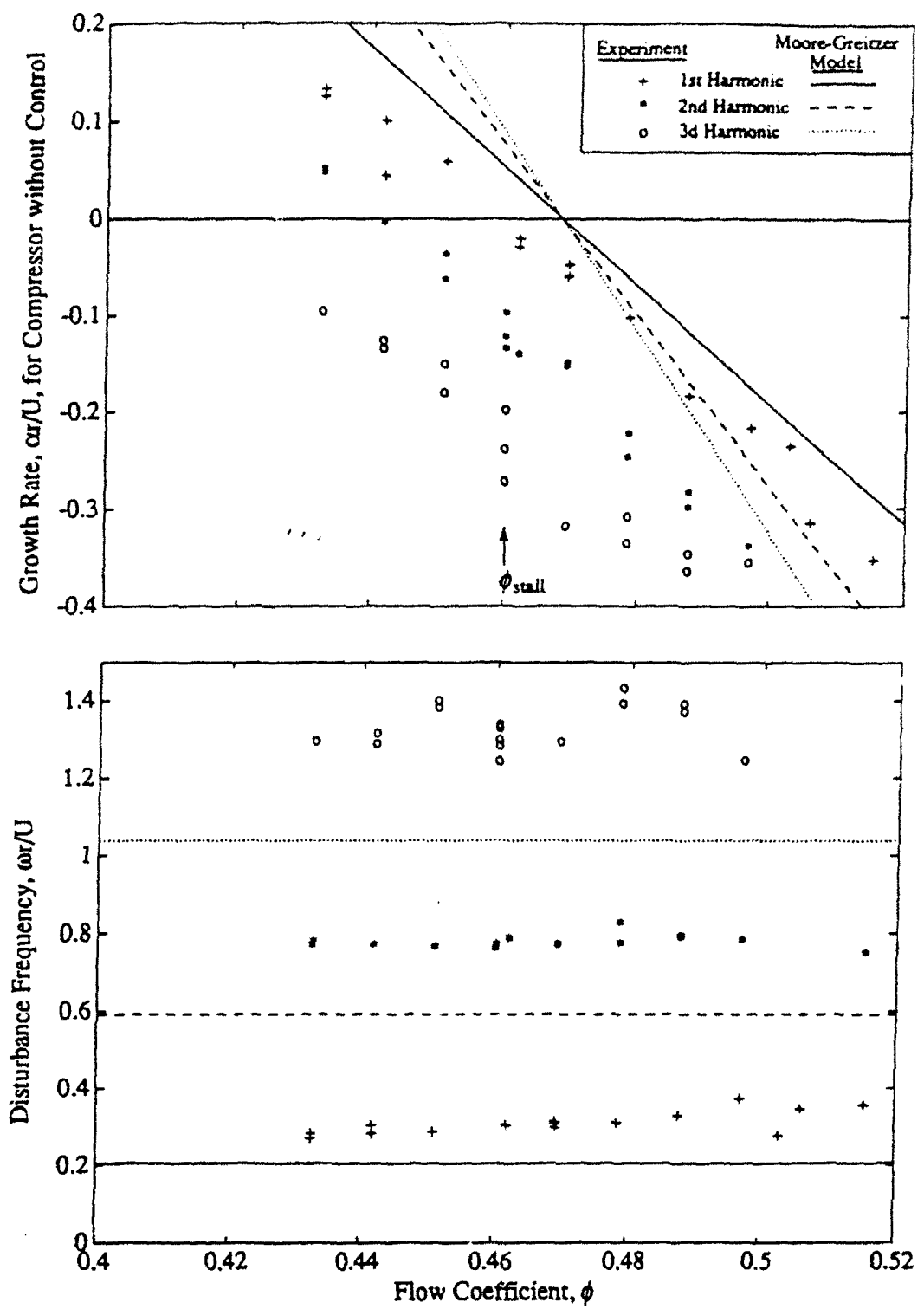


Fig. 20: The wave growth and rotational rates compared with predictions of the unmodified Moore-Greitzer model for the first three spatial harmonics

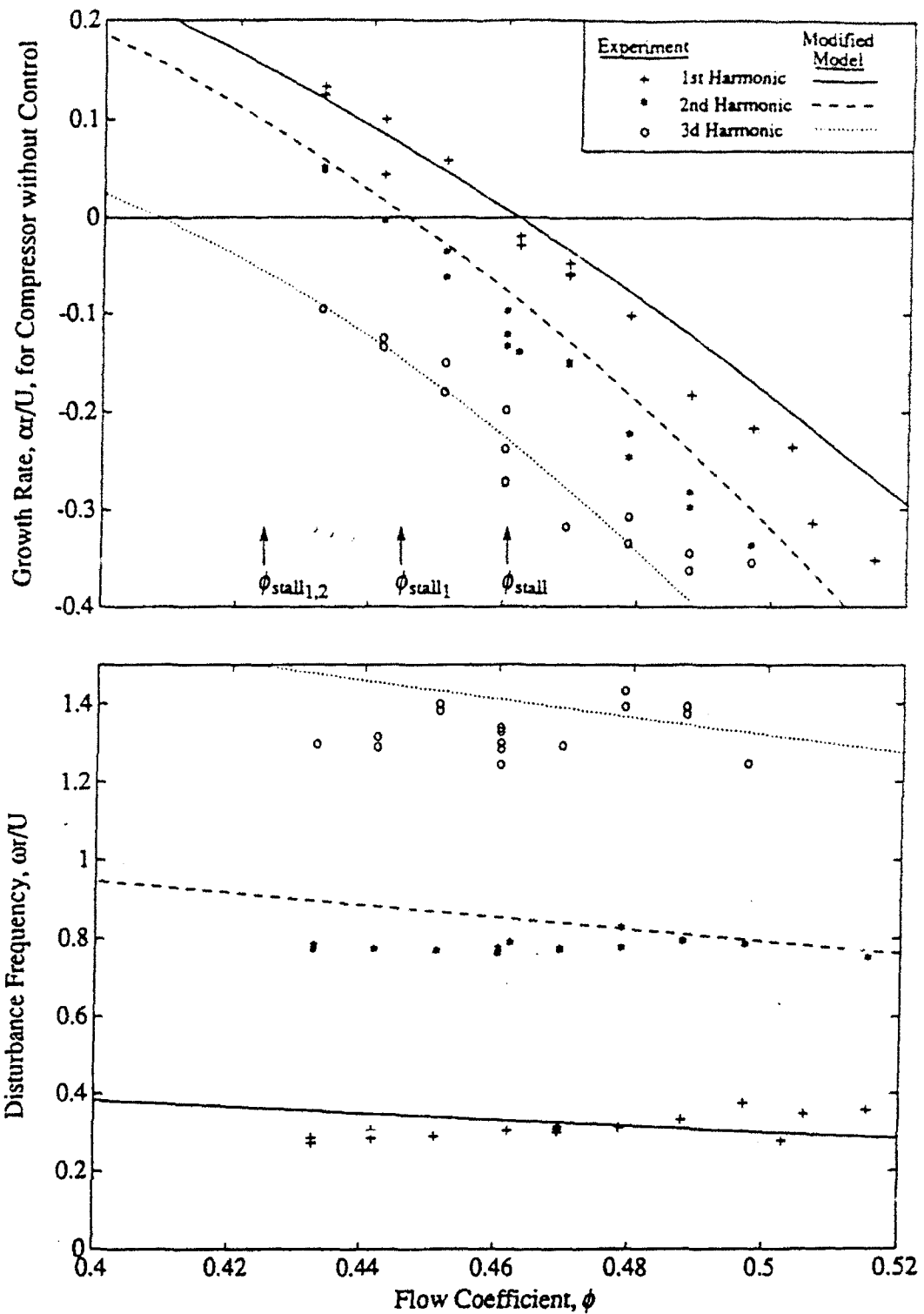


Fig. 21: The wave growth and rotation rates compared with the predictions of the model modified to account for compressor time lags. The arrows denote the experimentally determined rotating stall initiation points.

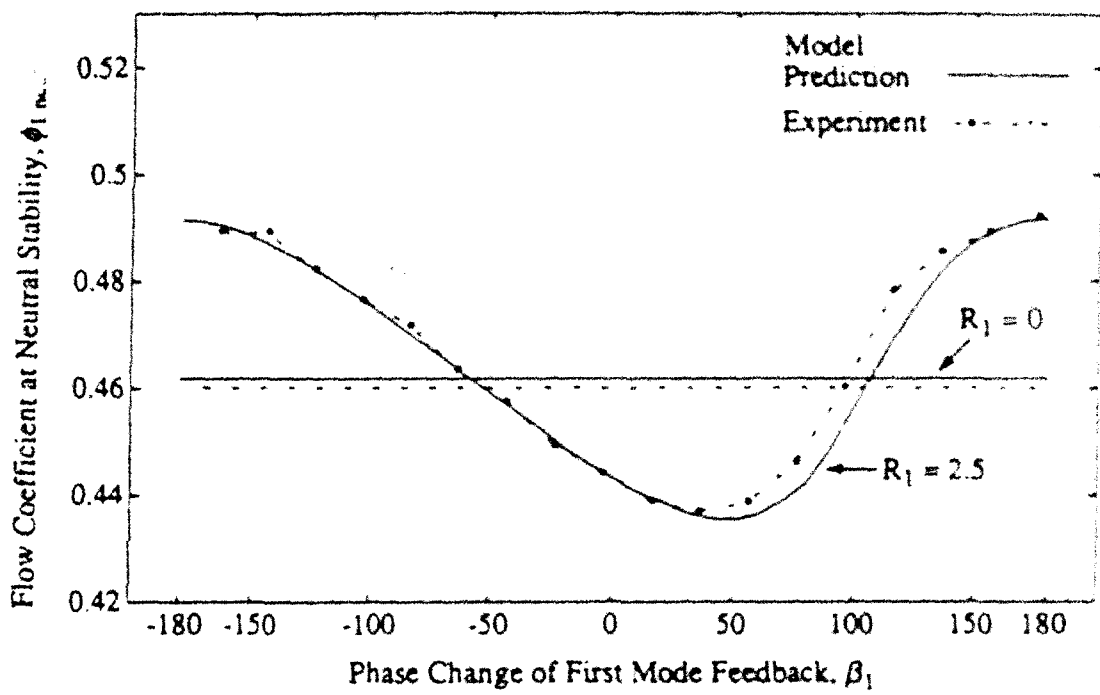


Fig. 22: The influence of the first spatial harmonic controller phase angle, β_1 , on stall flow coefficient as a function of controller gain, R

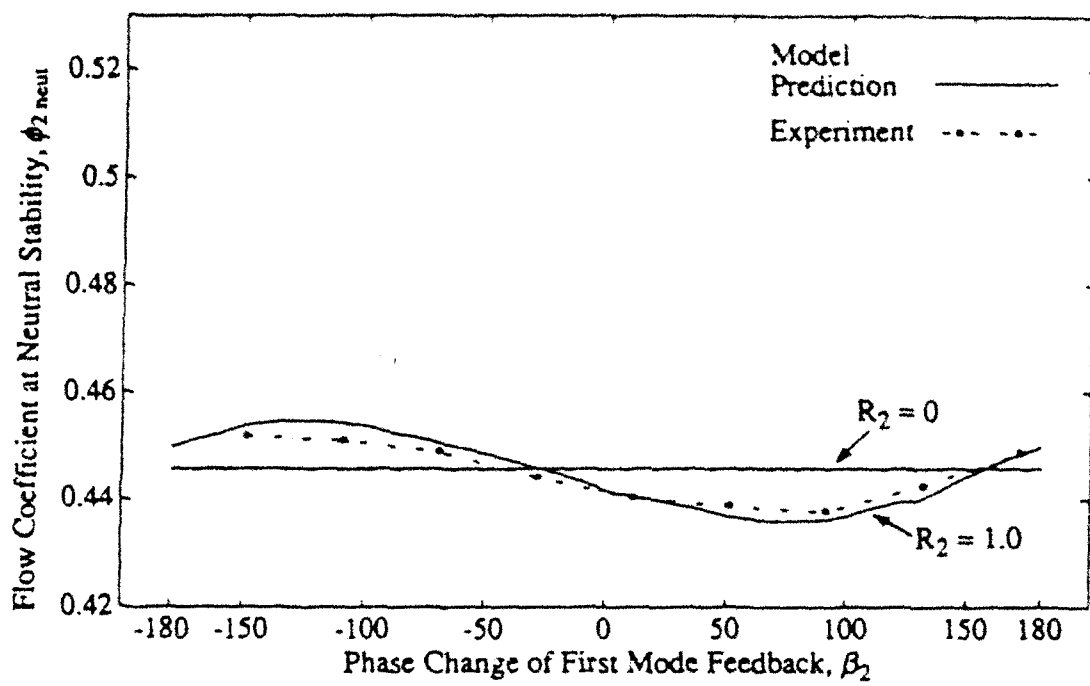


Fig. 23: The influence of the second spatial harmonic controller phase angle, β_1 , on stall flow coefficient as a function of controller gain, R

IV. MODELLING FOR CONTROL AND SYSTEM IDENTIFICATION

MODELING FOR CONTROL OF ROTATING STALL

by

J. Paduano, L. Valavani, A.H. Epstein, E.M. Greitzer and G. Guenette

Department of Aeronautics and Astronautics, Gas Turbine Laboratory

Massachusetts Institute of Technology

Cambridge, Massachusetts 02139

Abstract

An analytical model for control of rotating stall has been obtained from the basic fluid equations describing the process at inception. The model describes rotating stall as a traveling wave packet, sensed -- in spatial components -- via the Fourier synthesis of measurements obtained from a circumferential array of evenly distributed sensors (hot wires) upstream of the compressor. A set of "wiggly" inlet guide vanes (IGV's) equally spaced around the compressor annulus constitute the "forced" part of the model. Control is effected by launching waves at appropriate magnitude and phase, synthesized by spatial Fourier synthesis from individual IGV deflections. The effect of the IGV motion on the unsteady fluid process was quantified via identification experiments carried out on a low speed, single-stage axial research compressor. These experiments served to validate the theoretical model and refine key parameters in it. Further validation of the model was provided by the successful implementation of a simple proportional control law, using a combination of first and second harmonic feedback; this resulted in a 20% reduction of stalling mass flow, at essentially the same pressure rise.

Nomenclature

IGV	inlet guide vane
P_{S2}	exit static pressure
P_{T1}	inlet total pressure evaluated at steady state operating point
ΔP	$P_{S2} - P_{T1}$
φ	flow coefficient C_x / U
C_x	axial velocity
U	wheel speed
λ, μ	fluid inertia parameters inside machine
γ	radius of machine
ρ	fluid density
ψ	pressure rise characteristic $\Delta p / \rho U^2$
$\frac{\partial \bar{\psi}}{\partial \varphi}$	slope of non dimensional pressure rise characteristic
$\bar{P}_{T1n} \stackrel{\Delta}{=} \bar{P}_{T1} e^{j\omega n}$	<i>n</i> th spatial harmonic of corresponding variable
$\bar{\delta}P_{S2} \stackrel{\Delta}{=} \bar{P}_{S2} e^{j\omega n}$	
$\bar{\delta}\varphi \stackrel{\Delta}{=} \bar{\varphi} e^{j\omega n}$	
δ	perturbation quantity
x_{n1}, x_{n2}	<i>n</i> th spatial cosine and sine functions of flow coefficient perturbation
ω_{RS}	rotating stall speed (differs with each spatial harmonic)
θ	circumferential angle ranging from 0 to 2π
$\delta\gamma^{(0,i)}$	circumferential distribution of IGV deflection, degrees
$\delta\gamma_n$	<i>n</i> th spatial harmonic of control action, $-\delta\gamma^{(0,i)}$
γ_{n1}, γ_{n2}	<i>n</i> -spatial cosine and sine components of control action
$G_n(s)$	transfer function between $\bar{\gamma}_n(s)$ and $\bar{\varphi}_n(s)$
$G_{n1}(s)$	transfer function between $u_{n1}(s), x_{n1}(s)$
$G_{n2}(s)$	transfer function between $u_{n2}(s), x_{n2}(s)$
u_{n1}, u_{n2}	<i>n</i> th spatial cosine and sine coefficients of the external input

Introduction

The performance of compression systems can be considerably limited by multi-mode instabilities that variously arise in both axial and centrifugal compressors. These are surge and rotating stall. Surge is essentially a one-dimensional, mass flow disturbance encompassing the entire pumping system -- compressor, ducting, plenum, and throttle. It causes the mass flow through the machine to fluctuate, generally with inevitable flow reversal and performance degradation. Rotating stall is a localized disturbance that starts as small velocity perturbations at a particular sector of the compressor annulus and propagates circumferentially, pervading the entire annulus. In many situations, the velocity perturbations grow exponentially in the initial stages until a nonlinear traveling wave with the speed of rotating stall develops around the annulus (Fig. 1).

These two phenomena can be viewed, in a unified framework, as eigenmodes of the compression system with surge constituting the zeroth order mode and rotating stall representing the higher order modes [1], [2]. This is described in the papers by Moore [7] and by Moore and Greitzer [8] who showed how these two phenomena are linked. Their theoretical work was corroborated later by experimental evidence [10], [11].

Fully developed, surge and rotating stall exhibit their nonlinear nature by causing large amplitude transitions between compressor operating points, from regions of high to extremely low efficiency and, sometimes, unrecoverable conditions. To avoid such events, design engineers have traditionally allowed ample surge margins to keep engine operation away from the unstable region. This, however, can compromise performance since the region near the stability region is of highest achievable performance: high pressure rise/low mass flow operating conditions.

Previous attempts at active control of surge consisted primarily of largely empirical, open loop strategies, with limited success. A systematic feedback approach, even for the one-dimensional surge disturbance, was not reported in the literature until recently. On the other hand, attempts at controlling rotating stall, which is the focus of this paper, have been considerably fewer, in both open-loop [16] and feedback configurations. This can be attributed to the fact that rotating stall is at least two-dimensional in nature, with spatial and time components and, therefore,

considerably more difficult to control. In addition, from the control theoretic point of view, an appropriately defined model for control of rotating stall has not been available, even though more sophisticated fluid model descriptions, along with experimental observations, have existed in the literature [18], [19].

In this paper, which is intended for control audiences, we derive an analytical state-space model for control of rotating stall, validate it, and further refine its key parameters via identification experiments on a low speed, single-stage research compressor. This is the first control theoretic model obtained for rotating stall and is the main focus of the present paper. The derived model structure is further validated by a successful first attempt at feedback control using a simple proportional (state feedback) strategy.

In the following sections, we describe the analytical derivation of the model and the open-loop identification procedures underlying its structure. We also briefly discuss the closed loop control strategy that has resulted in moving the stall point to 20% lower mass flow. A detailed description of the overall experiment, as well as the accompanying implementation/hardware issues, is given in [20], which is aimed for the gas turbine community. [20] focuses on the exposition of experimental and fluid process aspects without any discussion on the dynamic model per se, or any identification and structure model validation details. Such information is deferred to the discussion in the present paper. In a following paper [24], we discuss the complete process identification, with special emphasis on closed-loop algorithms that can accurately identify the process characteristics beyond its natural stability point. In [24], a new closed-loop identification algorithm is proposed, which is tested experimentally, both directly, in terms of identified process characteristics, as well as indirectly, by designing more accurate feedback control laws.

The Fluid Process Model - A Control Theoretic Perspective

In this section we briefly outline the fluid dynamic description of the rotating stall process which we assume to be the mature state of the phenomenon whose linear (perturbation) behavior is described. We start with the basic partial differential equation capturing the physics of the process

and derive from it an analytical, finite dimensional, model amenable to control. Understanding and interpreting the process from a control theoretic perspective is essential in controlling it in a systematic fashion. While, normally, a partial differential equation form would imply an infinite dimensional model for control, in what follows we describe how an accurate ODE model was obtained, based on understanding of the fluid process and judicious utilization of control theoretic and signal processing tools.

The Physical Process Without Control

We start with the basic partial differential equation as derived in [8], which represents the local perturbation in pressure rise across the compressor, at stall inception, and convert it into a canonical wave operator form. The equation is given by:

$$\frac{\delta\Delta p}{\rho U^2} = \left(\overline{\frac{\partial \psi}{\partial \phi}} \right) \delta\phi - \lambda \frac{\partial \delta\phi}{\partial \theta} - \frac{\mu}{U} \frac{\partial \delta\phi}{\partial r} \quad (1)$$

where $(\overline{\partial \psi / \partial \phi})$ is the slope of the non-dimensional compressor pressure rise characteristic $\psi = (\Delta p / \rho U^2)$, where Δp is defined as exit static pressure P_{S2} minus inlet total pressure P_{T1} evaluated at the steady-state operating point, and ϕ is the flow coefficient C_x/U with C_x the axial velocity. Positive numbers λ and μ represent the inertia of the fluid inside the machine that has mean radius r ; U is the wheel speed, ρ is the fluid density.

A general perturbation is represented as a Fourier series and it is convenient to write the functions in equation (1) in terms of their spatial Fourier coefficients:

$$\delta P_{T1} = \sum_n \tilde{P}_{T1n} e^{jn\theta + \left| n \right| x/r} = \sum_n \tilde{P}_{T1n} e^{\left| n \right| x/r}, \quad x < 0 \quad (2a)$$

$$\delta P_{S2} = \sum_n \tilde{P}_{S2n} e^{jn\theta - \left| n \right| x/r} = \sum_n \tilde{P}_{S2n} e^{-\left| n \right| x/r}, \quad x > 0 \quad (2b)$$

$$\delta\phi = \sum_n \frac{1}{\phi e} j n \theta + \left| \frac{1}{n} \right| \frac{x}{r} = \sum_n \frac{1}{\phi_n e} \left| \frac{1}{n} \right| \frac{x}{r}, \quad x < 0 \quad (2c)$$

where x is the distance from compressor face and the definitions of \tilde{P}_{T1n} , \tilde{P}_{S2n} , $\tilde{\phi}_n$, are obvious from equations (2a-2c).

In the upstream region, the axial momentum equation can be written as (an unsteady Bernoulli type) equation of the form:

$$\rho U \frac{\partial (\delta\phi_1)}{\partial t} + \frac{\partial (\delta P_{T1})}{\partial x} = 0 \quad (3)$$

where $\delta\phi_1$ is the upstream flow coefficient. Using equation (2a) in (3), we obtain, for the n th spatial harmonic of the perturbation

$$\tilde{P}_{T1n} = - \frac{\rho U r}{|n|} \frac{\partial \tilde{\phi}_{1n}}{\partial t} \quad (4)$$

Next, using continuity (momentum) and the condition of constant exit angle (axial), the pressure gradient at compressor exit can be related to the velocity perturbations by

$$\frac{\partial (\delta P_{S2})}{\partial x} = - \rho U \frac{\partial (\delta\phi_2)}{\partial t} \quad (5)$$

and $\delta\phi_2$ is the downstream flow coefficient of the perturbation. By continuity at compressor face and given the assumption of incompressibility, $\delta\phi_1 = \delta\phi_2 = \delta\phi$; $\delta\phi$ is as in equations (1) and (2c); also, $x = 0$ at compressor face. Using equation (2b) in (5), we get:

$$\tilde{P}_{S2n} = \frac{\rho U r}{|n|} \frac{d (\tilde{\phi}_{2n})}{dt} = \frac{\rho U r}{|n|} \frac{\partial (\tilde{\phi}_n)}{\partial t} \quad (6)$$

From equations (4) and (6), the LHS of equation (1) becomes, for the n th spatial harmonic:

$$\frac{\delta P_{S2n} - \delta P_{T1n}}{\rho U^2} = \frac{2r}{U|n|} \frac{\partial (\tilde{\phi}_n)}{\partial t} \quad (7)$$

Next, rewriting the RHS of (1) in terms of the spatial Fourier expansion for $\delta\phi$ and taking the n th coefficient we get, in conjunction with equation (7), the following:

$$\beta \frac{\partial (\tilde{\delta\phi}_n)}{\partial t} + \lambda \frac{\partial (\tilde{\delta\phi}_n)}{\partial \theta} = \psi' \tilde{\delta\phi}_n \quad (8)$$

where $\psi' = \overline{(\psi' / d\theta)}$; $\beta = \left[\frac{2r}{U|n|} + \frac{r\mu}{U} \right]$

Equation (8) is the standard form of a partial differential equation of first order in $\tilde{\delta\phi}_n$, with t and θ as the independent variables.

Thus, the complete equation (8) is of the general form:

$$\left[A \frac{\partial}{\partial \theta} + B \frac{\partial}{\partial t} + C \right] \delta\phi = 0 \quad (9)$$

and, consistent with PDE theory in any standard text, its solution can be written as:

$$\delta\phi_n = F(A\theta - Bt) e^{\alpha t} \quad (10)$$

where the functional F represents traveling waves moving in the positive θ direction with velocity $B/A = \lambda/\beta$, and $\alpha = C/B$. Alternatively, the n th spatial Fourier coefficient of rotating stall is indeed a traveling wave, whose amplitude evolves as $e^{\alpha t}$ predicting growth (instability) at positive compressor slopes ψ' ; also, λ/β is the corresponding rotating stall speed, ω_{RS} , in the positive θ direction. Indeed, rotating stall precursors, in the form of traveling waves of increasing amplitude, were identified long before the onset of rotating stall (about 40 rotor revolutions before stall) [18]. A typical representation of the experimental data obtained is shown in Fig. 3.

The Homogeneous State Space Model

The solution we obtained for each spatial Fourier coefficient constituting the rotating stall process, as can be seen in equation (10), represents a general traveling waveform modulated by an exponential. For the application at hand, given the compressor geometry, we seek specific traveling waveforms which are periodic in the argument of F , i.e., θ and time.. Thus, we can write the mass flow perturbation for the n th harmonic as

$$\tilde{\delta\phi}_n = e^{j(n\theta - \omega_{RS}t)} e^{\alpha t} = e^{\alpha t} [\cos(n\theta - \omega_{RS}t) + j \sin(n\theta - \omega_{RS}t)] \quad (11)$$

With this process interpretation, we next take the state variables to be the (complex) Fourier coefficients corresponding to each spatial mode. This is key in the derivation of a state space model for rotating stall. From Eqn. (11) it thus follows that, for each Fourier coefficient, the state variables are given by:

$$\begin{aligned} x_{n1} &\stackrel{\Delta}{=} \operatorname{Re} \tilde{\delta\phi}_n = e^{\alpha t} \cos(n\theta - \omega_{RS} t) \\ x_{n2} &\stackrel{\Delta}{=} \operatorname{Im} \tilde{\delta\phi}_n = e^{\alpha t} \sin(n\theta - \omega_{RS} t) \end{aligned} \quad (12)$$

$\alpha = \psi' / \beta$

$n = 1, 2, \dots$

Taking time derivatives of x_{n1}, x_{n2} in equation (12) and writing the resulting differential equations in matrix form we obtain:

$$\dot{x} \stackrel{\Delta}{=} \begin{bmatrix} \dot{x}_{n1} \\ \dot{x}_{n2} \end{bmatrix} = \begin{bmatrix} \psi' / \beta & \omega_{RS} \\ -\omega_{RS} & \psi' / \beta \end{bmatrix} \begin{bmatrix} x_{n1} \\ x_{n2} \end{bmatrix} = Ax \quad (13)$$

with A the system matrix and x the state vector for each spatial mode.

In conclusion, for each spatial Fourier coefficient we can write a two-dimensional state space model, representing the real and imaginary parts of the solution. This model represents the evolution in time of the amplitude and phase of the corresponding modal traveling wave. As can be seen by inspection of the harmonic form of the A matrix in equation (13), ψ' determines the stability properties of the homogeneous system. In fact, the characteristic equation is given by

$$s^2 - 2 \frac{\psi'}{\beta} s + \frac{\psi'^2}{\beta^2} + \omega_{RS}^2 = 0 \quad (14)$$

and it is Hurwitz (stable) if $\psi' < 0$. For $\psi' > 0$, the characteristic polynomial is unstable and for $\psi' = 0$, the system has zero damping. The eigenvalues - of time evolution of each harmonic - are $\lambda_{1,2} = (\psi' / \beta) \pm j\omega_{RS}$.

Defining the Inputs and Outputs -- The Complete Model

Since the state space consists of traveling wave modes, state (output) measurements will naturally be traveling waves. Also, control of the instability will be effected by traveling wave inputs, consistently designed with the process characteristics.

For sensing, a circumferential array of eight hot wire anemometers was employed, placed midspan upstream of the compressor to measure axial velocity fluctuations. At each hot wire, the obtained signal (measurement) constitutes, at each point in time, a linear combination of the spatial harmonics, as captured by the Discrete Time Spatial Fourier (DTSF) formula:

$$C_{x_i}(t) = \sum_n A_{x_n}(t) e^{jn\theta} \quad (15)$$

θ angle corresponding to location of particular sensor.
 $i=0, \dots, 7$: # of hot wires
 $n=1, 2, \dots, \infty$: spatial harmonics

Thus, at every time t , when a measurement is taken, each harmonic can be synthesized from data of the collection of eight sensors according to the inverse Fourier formula:

$$A_{x_n}(t) = \sum_{k=0}^K C_{x_k}(t) e^{-jn\theta_k} = \sum_{k=0}^K C_{x_k}(t) e^{-jn2\pi k/K} \quad (16)$$

where $\theta_k = \frac{2\pi k}{K}$,
 $k = 1, 2, \dots, K$,
and $K = 7$ in the present context.¹

Equation (16) represents the output equation for the corresponding state space model for each harmonic. Obtaining each spatial Fourier coefficient as a function of time is crucial in the feedback control process; it has also been important in identifying precursor waves to rotating stall [18].

For launching the control (traveling wave inputs), twelve wiggly inlet guide vanes (IGV's) were positioned upstream, each independently actuated by a dc motor, which is controlled for accuracy via an inner loop compensator. With the addition of actuation mechanisms, the partial differential equation describing the (modulated) fluid process now has an additional (exogenous) term, $\frac{\partial \psi}{\partial \gamma} (\delta y_n)$, that reflects the effect of active control on the fluid process.

¹ It is possible for modal content greater than $K/2$ (the spatial Nyquist frequency) to exist in $A_{x_n}(t)$. This information would alias into the computation of the lower modes. However, these modes die away very quickly upstream of the compressor [20, ch. 4.1.2]; in addition, these modes are very well damped at higher flow coefficients as was experimentally observed [20, ch. 5.6]. Thus, placing the hot wires upstream of the compressor, minimizes aliasing from higher spatial modes in Eqn. (16).

$$\beta \frac{\partial}{\partial t} (\delta \tilde{\varphi}_n) + \lambda \frac{\partial}{\partial \theta} (\delta \tilde{\varphi}_n) = \psi' \delta \tilde{\varphi}_n + \frac{\partial \psi}{\partial \gamma} (\delta \gamma_n) \quad (17)$$

where $\partial \psi / \partial \gamma$ is the control input coefficient in the forced equation and $\delta \gamma_n$ is the required control action. Both these terms are as yet unspecified and do not derive from the homogeneous process dynamics. For our specific choice of actuation, control will be effected through deflection of the IGV's. However, the coefficient $\partial \psi / \partial \gamma$ cannot be precisely defined, for control purposes, by a fluids approach alone, either analytically or experimentally. Quantification of the control input gain $\partial \psi / \partial \gamma$ will be through direct system identification.

At each point in time, the individual IGV deflections are determined by spatial Fourier decomposition of the control signal ($\delta \gamma_n$), required to stabilize a particular spatial mode of rotating stall. Thus, if at time t , the required overall control input to Eqn. (17) for mode n is $\delta \gamma_n(t)$, the individual blade deflections will be determined by the inverse spatial Fourier transform:

$$\delta \Gamma_{kn} = \delta \gamma_n e^{-j\theta_k n} = \delta \gamma_n e^{-j2\pi k/12} \quad \theta_k = \frac{2\pi k}{12} \quad (18)$$

$$k = 0, \dots, K, \text{ where } K \text{ is equal to 11 for actuation.}^2$$

Furthermore, if more than one mode is being controlled for rotating stall stabilization, the overall required blade deflections will be, for each blade k at time t :

$$\delta \Gamma_k = \sum_{n=1}^2 \delta \gamma_n(t) e^{-j n \theta_k} \quad \theta_k = \frac{2\pi k}{12} \quad (19)$$

$$k = 0, \dots, K = 11$$

Finally, the overall control action $\delta \gamma_n$ necessary for mode n can be effected as the spatial Fourier synthesis of the individual blade deflections according to:

$$\delta \gamma_n(t) = \sum_{k=0}^{11} \delta \Gamma_{nk} e^{j n \theta_k} \quad (20)$$

² See discussion in footnote on previous page.

Equations (18) - (20) clarify implementation issues but do not determine the required overall control action $\delta\gamma_n$. This should be the outcome of the controller design based on the state space model. Clearly, given the nature of the process and, consequently, of the ensuing control, $\delta\gamma_n$ itself can be represented, in state space form, as a traveling wave that captures the magnitude and phase evolution of the controlling wave. Thus, the nth mode state space model [Eqn. (13)] with control now becomes:

$$\dot{\mathbf{x}} = \begin{bmatrix} \dot{x}_{n1} \\ \dot{x}_{n2} \end{bmatrix} = \begin{bmatrix} \psi'/\beta & \omega_{RS} \\ -\omega_{RS} & \psi'/\beta \end{bmatrix} \begin{bmatrix} x_{n1} \\ x_{n2} \end{bmatrix} + \begin{bmatrix} \left(\frac{\partial\psi}{\partial\gamma}\right)_{n1} & 0 \\ 0 & \left(\frac{\partial\psi}{\partial\gamma}\right)_{n2} \end{bmatrix} \begin{bmatrix} \gamma_{n1} \\ \gamma_{n2} \end{bmatrix} \quad (21)$$

where we have dropped δ from $\delta\gamma_n$ for notational convenience in the linear model. In addition, let $(\partial\psi/\partial\gamma)_{n1} \stackrel{\Delta}{=} \beta_1$, $(\partial\psi/\partial\gamma)_{n2} \stackrel{\Delta}{=} \beta_2$. Since the coefficients $\partial\psi/\partial\gamma$ cannot be accurately defined by fluid considerations alone, identification experiments were designed so that the entries of the control input matrix, as well as those of the transition matrix, could be determined by essentially fitting experimental data to the derived analytical model structure. Also, an additional term to complete the state space description in Eqn. (21) was added to represent a pure phase term corresponding to the need for a spatial lag, in the launched control wave input, that was observed experimentally, due to sensor, actuator, and fluid mechanics considerations. Thus, the complete model is now:

$$\begin{bmatrix} \dot{x}_{n1} \\ \dot{x}_{n2} \end{bmatrix} = \begin{bmatrix} \psi'/\beta & \omega_{RS} \\ -\omega_{RS} & \psi'/\beta \end{bmatrix} \begin{bmatrix} x_{n1} \\ x_{n2} \end{bmatrix} + \begin{bmatrix} \beta_1 & 0 \\ 0 & \beta_2 \end{bmatrix} \begin{bmatrix} \gamma_{n1} \\ \gamma_{n2} \end{bmatrix} + \begin{bmatrix} 0 & -g \\ g & 0 \end{bmatrix} \begin{bmatrix} \dot{\gamma}_{n1} \\ \dot{\gamma}_{n2} \end{bmatrix} \quad (22)$$

According to Eqn. (22), the spatial lag has been converted to an equivalent time lag, whose value needs to be identified. Equation (22) indicates that each mode requires the identification of five parameters. This is undertaken in the next section.

Identification

System identification for the rotating stall process proceeded in two distinct stages. First, nonparametric identification was carried out to determine the transfer functions - for each harmonic

from IGV input to sensor (hot wire) output, without first selecting a possible set of confined models. The procedures employed here determined the transfer functions directly from the experimental data. Next, once the transfer functions were identified - in frequency domain via Bode magnitude and phase plots - we proceeded to parameter identification by assuming a system order consistent with the transfer function forms obtained in the first stage. All experiments were carried out in the open-loop, below the natural stability point, with model structure validation as the primary objective. Our results are described below.

Nonparametric Identification (Transfer Functions)

A schematic representation of the overall experimental setup for identification and control of rotating stall is shown in Fig. 4. This includes the test compressor on the lower part of the figure, as well as the signal processing and control software blocks (left part), along with a control actuation loop that governs the dc servo motors. For more details, the reader is referred to [21]. As noted in the figure, a circumferential array of eight hot wire anemometers (sensors) have been placed midspan upstream of the compressor to measure axial velocity fluctuations. Also upstream, twelve wiggly inlet guide vanes (IGV's) have been positioned, each independently actuated by a dc motor, which is controlled for accuracy via an inner loop compensator. The dc servo actuation bandwidth is 80 Hz, well above the process bandwidth of about 10-14 Hz or, typically, 20%-50% of rotor speed. The IGV's represent just one possible mode of affecting the fluid process, but were chosen over others because they are amenable to modeling and could be actuated with off-the-shelf hardware.

Inputs to the process are the twelve IGV blade deflections - together synthesizing the traveling waves - at the inlet to the compressor. These deflections are represented by twelve numbers, at twelve discrete angular locations around the compressor annulus. Deflections are about the mean IGV angle, which in this case is zero, and can be positive or negative up to about ± 30 degrees; in most experiments it was limited to ± 15 degrees. Even spacing of the blades around the annulus facilitates the decomposition into discrete Fourier coefficients, i.e., the twelve blade positions can be exactly decomposed into discrete Fourier coefficients. These coefficients

are termed the "spatial Fourier coefficients" (SFC's), and are distinct from those in a time Fourier decomposition. The output of the system consists of eight measurements of the local axial air speed, taken by the anemometers around the compressor annulus. The hot wires are at the mean radius of the compressor, approximately .6 compressor radii upstream of the IGV's, with this upstream location chosen so as to reduce the likelihood of spatial aliasing. Since the rotating stall dynamics are non-axisymmetric perturbations to the mean flow of the compressor, all velocity measurements are perturbations about the mean flow. Again, because of even spacing, spatial Fourier coefficients of the measurements are directly obtained.

The model of equation (22) can next be written in transfer function form as follows:

$$\begin{bmatrix} x_{n1}(s) \\ x_{n2}(s) \end{bmatrix} = \begin{bmatrix} G_{n1}(s) & -G_{n2}(s) \\ G_{n2}(s) & G_{n1}(s) \end{bmatrix} \begin{bmatrix} U_{n1}(s) \\ U_{n2}(s) \end{bmatrix} \quad (23)$$

where $u_{n1} = \text{Re } u_n$; $u_{n2} = \text{Im } u_n$; $u_n(t) = A e^{i(n\theta - \omega t)}$ and $U_{n1}(s)$, $U_{n2}(s)$ are the Laplace transforms of U_{n1} , U_{n2} , respectively. The input $u_n(t)$ is realized as a spatial sine wave in the blade deflection angles, of magnitude A , rotating around the annulus at a frequency ω . Thus, for a first mode excitation [$u_1(t)$] there would be only one blade with a deflection of $+A$ degrees at any one time and, at a later time, a different blade around the annulus would have a deflection $+A$.

Equation (23) represents a two-input two-output system. However, it can be straightforwardly shown that a scalar transfer function $G_n(s)$ can be calculated from the transfer matrix elements as follows:

$$G_n(s) = G_{n1}(s) + jG_{n2}(s) \quad (24)$$

Furthermore, $G_{n1}(s)$ and $G_{n2}(s)$ can be excited separately by letting

$$u_{n1}(t) = A \cos(n\theta - \omega t) \quad \text{and} \quad u_{n2}(t) = 0 \quad \text{or} \quad (25a)$$

$$u_{n1}(t) = 0 \quad \text{and} \quad u_{n2}(t) = A \cos(n\theta - \omega t) \quad (25b)$$

and, by directly taking the θ dependence out using spatial Fourier analysis, the inputs to the model in Eqns. (22) and (23) are represented as simple time functions:

$$u_{n1}(t) = A \cos \omega t \text{ and } u_{n2}(t) = 0 \text{ or} \quad (26a)$$

$$u_{n1}(t) = 0 \text{ and } u_{n2}(t) = A \cos \omega t \quad (26b)$$

The above inputs (26a,b) are realized as spatial sine waves whose angular location is stationary.

For example, the input in (26a) represents a sine wave whose peak is at the fourth blade around the compressor while in (26b) a cosine wave is represented whose peak is at the first blade around the compressor. Thus, if the input in (26a) is used, we have:

$$\begin{aligned} x_{n1}(t) &= A |G_{n1}(j\omega)| \cos [\omega t + \angle G_{n1}(j\omega)] \\ x_{n2}(t) &= A |G_{n2}(j\omega)| \cos [\omega t + \angle G_{n2}(j\omega)] \end{aligned} \quad (27)$$

Following the method described in [22, ch. 6], each output sinusoid was correlated with the input sinusoid and its quadrature component. The results of these correlations are then combined to determine the value of the transfer function at the frequency of excitation ω . For example, if the input is $u_{n1}(t) = A \cos \omega t$ and $u_{n2}(t) = 0$, we compute the corresponding correlations $Ic(N)$ and $Is(N)$ as follows:

$$\begin{aligned} \frac{1}{N} \sum_{k=1}^N x_{n1}(kT) \cos (\omega kT) &\xrightarrow[N \rightarrow \infty]{} \frac{A}{2} |G_{n1}(j\omega)| \cos [\angle G_{n1}(j\omega)] \\ Is(N) = \frac{1}{N} \sum_{k=1}^N x_{n1}(kT) \sin (\omega kT) &\xrightarrow[N \rightarrow \infty]{} \frac{A}{2} |G_{n1}(j\omega)| \sin [\angle G_{n1}(j\omega)] \end{aligned} \quad (28)$$

Combining the above results, we find

$$\left| \hat{G}_{n1}(j\omega) \right| = \frac{1}{A/2} \sqrt{Ic^2(N) + Is^2(N)} \quad (29)$$

$$\angle \hat{G}_{n1}(j\omega) = -\arctan[Is(N)/Ic(N)]$$

where $\hat{G}_{n1}(j\omega)$ is the estimated transfer function.

Figures 5-7 show typical results of the frequency analysis by the correlation method for the rotating stall process. Both stationary and rotating sinusoids were used; in the latter case the technique must be somewhat modified but still retains the same properties. In Figure 8, $G_{n1}(s)$ and $G_{n2}(s)$ are combined to form a derived version of $G_n(s)$ for comparison with the experimental version in Figure 7. The good agreement obtained further corroborates the validity of the argument that identification of either $G_{n1}(s)$ or $G_{n2}(s)$ is sufficient, since they are essentially the same transfer functions according to the model of Eqn. (23).

In addition to the correlation methods, spectral analysis methods were used to estimate the same transfer functions $G_{n1}(j\omega)$ or $G_{n2}(j\omega)$. During this sequence of experiments, pseudo-random binary sequences were utilized as inputs. In such cases the input is binary, shifting between two levels u_1 and u_2 in a (pseudo) random fashion, for example:

$$u(t) = \frac{1}{2} (u_1 + u_2) + \frac{1}{2} (u_1 - u_2) \operatorname{sign}[R(q) u(t-1) + w(t)] \quad (30)$$

with $w(t)$ being a computer generated white-noise process and where, by proper choices of the filter $R(q)$, different spectra can be realized. Using the spectral approach [22], the transfer function estimate is the ratio between two spectral estimates as follows:

$$\hat{G}^N(e^{j\omega_0}) = \frac{\hat{\Phi}_{yu}^N(\omega_0)}{\hat{\Phi}_u^N(\omega_0)} \quad (31)$$

with the cross spectrum of the input u with the output y and the spectrum of u given respectively by:

$$\hat{\Phi}_{yu}^N(\omega_0) = \int_{-\pi}^{\pi} W\gamma(\xi - \omega_0) Y_N(\xi) \bar{U}_N(\xi) d\xi \quad (32)$$

$$\hat{\Phi}_u^N(\omega_0) = \int_{-\pi}^{\pi} W\gamma(\xi - \omega_0) |U_N(\xi)|^2 d\xi \quad (33)$$

where $W\gamma(\xi - \omega_0)$ is a frequency window centered at $\xi = \omega_0$, the frequency of interest³ and γ describes the window width, with a large value corresponding to a narrow window. $Y_N(\xi)$, $U_N(\xi)$ correspond to the discrete Fourier transforms of y and u respectively, and $\bar{U}_N(\xi) = |U_N(\xi)|$.

In our experiments, the Blackman-Tukey procedure was applied with a frequency window of the Hamming type (see Appendix). The results of such identification experiments are shown in Figures 9 and 10, where the inputs were chosen to be, respectively:

$$\begin{aligned} U_{n1}(s) &= PRBS & U_{n2}(s) &= 0 \quad \text{and} \\ U_{n1}(s) &= 0 & U_{n2}(s) &= PBRS \end{aligned} \quad (34)$$

The asymptotic mean square error is evaluated by:

$$E \left| \hat{G}_N(e^{j\omega}) - G_0(e^{j\omega}) \right|^2 \sim M^2(\gamma) |R(\omega)|^2 + \frac{1}{N} \bar{W}(\gamma) \frac{\Phi v(\omega)}{\Phi u(\omega)} \quad (35)$$

where $G_0(e^{j\omega})$ is the actual transfer function of the process, Φv is the noise spectrum, and the quantities $M^2(\gamma)$, $\bar{W}(\gamma)$ are as defined in the appendix. For large γ , $M(\gamma)$ decreases while $\bar{W}(\gamma)$ increases; as $N \rightarrow \infty$, the second term on the RHS in equation (35) becomes arbitrarily small. We note that in all figures 5-10, the peak - corresponding to the characteristic rotating stall frequency - is at about 12 Hz, which represents 23% of the rotor rotation frequency in this compressor. In conclusion, our transfer function estimation experiments using the two methods outlined above have shown remarkable consistency and agreement. Furthermore, their shapes suggest second order system dynamics for each mode, consistent with the structure of our analytical model.

System Parameter Identification

Once the frequency domain estimates of the transfer function are available, they can, in turn, be used to find the parameters of the model. We use the structure of the nominal model and a

³ Such "weighting functions" were concentrated around each pole/zero location, as roughly anticipated from available experimental measurements.

type of weighted least-squares fit to the frequency domain estimates $\hat{G}_{nk}^N(\omega)$, $\hat{G}_{n2}^N(\omega)$. There are many ways that one could choose the nominal parameters to fit the frequency-domain estimate. The method that we have employed here follows that in [23] and is computationally efficient, since it only requires the solution of linear equations.

The rotating stall modes are represented by second order proper transfer functions of the form

$$G(z, \theta_0) = \frac{b_0 z^2 + b_1 z + b_2}{z^2 + a_1 z + a_2} \quad (36)$$

where θ_0 is defined as the column vector of parameters $\theta_0 \stackrel{\Delta}{=} [a_1 a_2 b_0 b_1 b_2]^T$

for which we can write:

$$\begin{aligned} z^2 G(z, \theta_0) &= [zG(z, \theta_0) \quad G(z, \theta_0) \quad z^2 \quad z \quad 1] [a_1 \quad a_2 \quad b_0 \quad b_1 \quad b_2]^T \\ &= [zG(z, \theta_0) \quad G(z, \theta_0) \quad z^2 \quad z \quad 1] \theta_0 \end{aligned} \quad (37)$$

Since the parameters are assumed real-valued, we define

$$\begin{aligned} \text{Re} \{z^2 G(z, \theta_0)\} &= [\text{Re} \{zG(z, \theta_0)\} \quad \text{Re} \{G(z, \theta_0)\} \quad \text{Re} \{z^2\} \quad \text{Re} \{z\} \quad 1] \theta_0 \\ \text{Im} \{z^2 G(z, \theta_0)\} &= [\text{Im} \{zG(z, \theta_0)\} \quad \text{Im} \{G(z, \theta_0)\} \quad \text{Im} \{z^2\} \quad \text{Im} \{z\} \quad 1] \theta_0 \end{aligned} \quad (38)$$

Thus, if we know the complex value of $G(z, \theta_0)$ for some unknown z , we can find two linear equations in the parameters. The frequency-domain estimation method in [23] yields an estimate of the plant at frequencies ω_k for $k=0, \dots, N/2$, where N is the number (even) of distinct frequencies over which the Discrete Fourier Transform (DFT) is taken.

Letting $z = e^{j\omega_k T}$ for $k=0, \dots, N/2$, and T the sampling interval, we define an $(N+2) \times 5$ matrix whose elements depend upon the complex values of some discrete function of frequency. We form the matrix $A \{ G(e^{j\omega_k T}, \theta_0) \}$ as follows:

$$\begin{aligned}
A \left\{ G(e^{j\omega_k T}, \theta_0) \right\} = \\
\begin{bmatrix} \text{Re} \{ e^{j\omega_0} G(e^{j\omega_0 T}, \theta_0) \} & \text{Re} \{ G(e^{j\omega_0 T}, \theta_0) \} & \text{Re} \{ e^{2j\omega_0 T} \} & \text{Re} \{ e^{j\omega_0 T} \} & 1 \\ \vdots & \vdots & & & \\ \text{Re} \{ e^{j\omega_{(N/2)}} G(e^{j\omega_{(N/2)} T}, \theta_0) \} & \dots & \dots & \text{Re} \{ e^{j\omega_{(N/2)} T} \} & 1 \end{bmatrix} \\
\begin{bmatrix} \text{Im} \{ e^{j\omega_0 T} G(e^{j\omega_0 T}, \theta_0) \} & \text{Im} \{ G(e^{j\omega_0 T}, \theta_0) \} & \text{Im} \{ e^{2j\omega_0 T} \} & \text{Im} \{ e^{j\omega_0 T} \} & 0 \\ \vdots & \vdots & & & \\ \text{Im} \{ e^{j\omega_{(N/2)} T} G(e^{j\omega_{(N/2)} T}, \theta_0) \} & \dots & \dots & \text{Im} \{ e^{j\omega_{(N/2)} T} \} & 0 \end{bmatrix} \quad (39)
\end{aligned}$$

Similarly, the $(N + 2)$ vector B is formed as

$$B \left\{ G(e^{j\omega_k T}, \theta_0) \right\} = \begin{bmatrix} \text{Re} \{ e^{2j\omega_0 T} G(e^{j\omega_0 T}, \theta_0) \} \\ \vdots \\ \text{Re} \{ e^{2j\omega_{(N/2)} T} G(e^{j\omega_{(N/2)} T}, \theta_0) \} \\ \text{Im} \{ e^{2j\omega_0 T} G(e^{j\omega_0 T}, \theta_0) \} \\ \vdots \\ \text{Im} \{ e^{2j\omega_{(N/2)} T} G(e^{j\omega_{(N/2)} T}, \theta_0) \} \end{bmatrix} \quad (40)$$

Thus, from Eqns. (37)-(40) we can write:

$$A \left\{ G(e^{j\omega_k T}, \theta_0) \right\} \theta_0 = B \left\{ G(e^{j\omega_k T}, \theta_0) \right\} \quad (41)$$

Next, the parameter estimate $\hat{\theta}$ is chosen as the vector that minimizes the frequency weighted norm of the error vector

$$A \left\{ G_N(\omega_k) \right\} \hat{\theta} - B \left\{ G_N(\omega_k) \right\} \quad (42)$$

where the weighting matrix can be a diagonal matrix

$$W = \text{diag} \{ f(\omega_0) \ f(\omega_1) \ \dots \ f(\omega_{(N/2)}) \ f(\omega_0) \ f(\omega_1) \ \dots \ f(\omega_{(N/2)}) \} \quad (43)$$

where $f(\omega)$ is a frequency preference weighting function.

The parameter estimate that minimizes the norm of the error vector $W^T A(G_N(\omega_k))\hat{\theta} - B(G_N(\omega_k))$ is given by the least squares result

$$\hat{\theta} = (A^T W^T W A)^{-1} A^T W^T W B \quad (44)$$

The results of applying the above procedure to rotating stall are shown in Figure 11, where the dotted line represents the five-parameter identified model, and the solid line, the corresponding averaged experimentally obtained transfer function. Similar results were obtained for the second mode, also. For this experiment the values of the five identified parameters are:

$\omega_{RS} = 66.94$, $\sigma_{RS} = \psi' / \beta = -6.58$, $\beta_1 = -5.01$, $\beta_2 = 2.04$, $g_I = -.055$ for the first mode, and $\omega_{RS} = 157.37$, $\sigma_{RS} = -32.46$, $\beta_1 = -11.57$, $\beta_2 = -.54$, $g = -.048$. The mass flow coefficient was .475 for both.

The five parameters were identified for both modes at various mass flow coefficients right before stall, ranging from a mass flow coefficient of .55 down to .475, which is almost at stall; at these extremes, σ_{RS} for the first mode ranged from -36.38 to -6.58 which still represents a stable point on the compressor speed line. ω_{RS} ranged respectively from 50.81 to 71.71. For mode 2 the range was from -93.17 down to -32.46 for σ_{RS} and from 188.60 down to 157.37. The detailed results are shown in Tables 1 and 2 respectively.

Predictably, the mode characteristics become less stable monotonically (σ_{RS}) and more oscillatory (lightly damped) - ω_{RS} - with lower flow coefficients. However, examination of the second mode shows that it is considerably more stable and oscillatory than the first mode. The oscillatory behavior does not, however, exhibit a monotonic trend through various flow coefficients. This is expected, since phase is usually not as accurately observed; in addition, individual mode phase may be more sensitive to the presence of higher modes (spatial aliasing). Although we have not pursued identification of higher order modes, it is expected that these trends will apply to those as well. If this is truly the case, then control can be achieved with just a limited number of modes. Indeed, as will be discussed in the next section, we were able to control rotating stall with only one or two modes.

Another important observation supported by all the phase plots in all the figures is how well the identified model phase agrees with that of the experimentally determined transfer functions. It is remarkable that the parameter g remains essentially constant at about .06 for the majority of flow coefficients in both modes. This further corroborates the model structure and the intended modeling function of the parameter g . Indeed, since this is supposed to capture a spatial phase - turned into time lag - its value should remain relatively unchanged for the range of cases considered here. To summarize, the above described identification experiments validate the model structure, as represented in Eqn. (22), including the pure phase term for the spatial lag.

The preceding identification procedures have been open loop since the operating points were chosen at mass flows at stable -- before stall -- regions of the compressor characteristic. However, model validation notwithstanding, parameter identification is really needed at the unstable post-stall points for which a controller has to be designed. Work has presently been completed [24] on closed-loop parameter identification experiments at stall and beyond, by incrementally advancing to lower mass flow operating points using information from the immediately preceding stabilized ones. With the newly available information, robust compensation can be designed which will reliably control stall well beyond the currently achieved flow coefficient of 0.35. In the process, it is also possible to address a number of interesting issues regarding limits to achievable performance via active control stabilization of rotating stall. The basic question which underlies such considerations at these more extreme conditions is which is the first barrier to further performance improvement using active control: (i) loss of model validity, including the violation of linearity; or (ii) loss of control authority including, apart from the model controllability, limits on actuation bandwidth. Surely, there are also a number of pure fluids issues to be resolved, such as the validity of incompressibility assumption, etc. These are discussed in more detail in [21]. The bottom line is that, with active control, the horizon of such basic investigations is substantially expanded.

Experimental Control of Rotating Stall

The first attempt at controlling rotating stall experimentally utilized a simple proportional control law of the form

$$\gamma_n = -k\delta\tilde{\varphi}_n \quad (45)$$

which, when substituted in equation (24), results in the closed loop system:

$$\begin{bmatrix} \dot{x}_{n1} \\ \dot{x}_{n2} \end{bmatrix} = \begin{bmatrix} \psi'/\beta - kb_1 & \omega_{RS} - kb_2 \\ -\omega_{RS} + kb_2 & \psi'/\beta - gb_1 \end{bmatrix} \begin{bmatrix} x_{n1} \\ x_{n2} \end{bmatrix} \quad (46)$$

Clearly, the system in Eqn. (46) can be stable for appropriate values of k . Since b_1, b_2 were not exactly known at the time this was attempted, a trial and error procedure was employed for values of k that stabilized (46) experimentally. Also, various spatial phases were tried [as indicated in equation (253)] until a combination was found that stabilized the system best. The criterion was damping ratio enhancement measured using the PSD of the closed loop process at a stable but underdamped operating point of the compressor. A gain k of 5 deg/m/s was chosen and a spatial phase of 60 deg was deemed best. Figure 12 shows the overall system damping behavior for various values of phase. (For more details on this experimental procedure, the reader is referred to [21].)

With this simple proportional control law, using only first mode feedback, rotating stall was stabilized and the stable range of compressor operation was extended. The flow coefficient at stall was reduced by 11%, down to 0.375 from the stalling value of 0.43, as shown in Figure 13. Closer study of the transient data indicated that the second spatial Fourier coefficient was actually growing at stall inception when the control was on (Figure 14). This was in good agreement with the linearity of the assumed model at stall inception. When the second mode was also used for feedback, the resulting two-mode proportional control law further extended the stable range of operation of the compressor. Stall flow coefficient was reduced by 20% to 0.35 below the natural stall flow coefficient (Figure 15). This controller used a gain of 5 deg/m/s for both modes with a spatial phase of 53° and 90° for the first and second modes respectively.

The results provide compelling qualitative support for the model structure and for the sensing, feedback and actuation schemes used. It is qualitative because only the qualitative nature of the system behavior - the structure of the model and not its detailed behavior - were used in the control design.

Clearly, a dynamic model with well-defined parameters allows for the systematic design of robust (dynamic) controller structures that could improve performance further and guarantee stability robustness against ambient system disturbances. A rigorously designed control algorithm, with carefully chosen structure and parameter values, can predictably stabilize all modes. For example, if one looks at the exponential term potentially causing the instability, as is also reflected in the solutions of equation (17), it is seen that the system goes unstable when the term ψ' / β becomes positive. Given the definition of

$$\beta = \left[\frac{2r}{U|n|} + \frac{r\mu}{U} \right] \quad (47)$$

together with the compressor fluid inertia parameter μ as defined by

$$\mu = \lambda + \sum_{\text{stators}} \frac{bx_s}{\cos^2(\gamma_s)r} \quad bx_s: \text{stator characteristic parameter} \quad (48)$$

and with λ , the rotor fluid inertia parameter, defined by

$$\lambda = \sum_{\text{rotors}} \frac{bx_r}{\cos^2(\gamma_r)r} \quad bx_r: \text{rotor characteristic parameter} \quad (49)$$

one sees by substituting in Eqn. (47) the expressions of Eqns. (48), (49), that the value of β ranges between an upper and a lower bound, as n varies from 1 to ∞ . With this information, in principle, a robust controller can be designed to stabilize most modes, since an upper bound on the instability rate can be precisely defined. Knowledge of the instability range, together with the precise definition of the five system parameters, is crucial in realizing substantial further performance improvements with predictable overall system robustness properties.

Conclusions

An analytical ODE model for control was developed from the generic fluids partial differential equation describing rotating stall at inception. The model structure was validated by extensive open-loop identification experiments at pre-stall flow conditions. Additionally, key model parameters were identified. Further validation of the derived model structure was provided by the success of a simple, proportional feedback control law, whose parameters were empirically set via successive experimentation.

The modeling approach taken here is quite generic and, therefore, applicable to more complex machines whose unsteady fluid disturbances need to be stabilized for performance enhancement, i.e. operation beyond traditionally set surge lines. In addition, the disturbances (rotating stall) presently studied have been characterized by good identifiability properties, given the quality of the results obtained. This is promising for further investigation and understanding of the basic fluid processes at very low flow coefficients, in conjunction with active stabilization. It is also similarly challenging for the control modeler/theorist.

A number of questions regarding fundamental limits to performance improvement, model and associated assumptions validity, bandwidth and other implementation limitations, have started being addressed. Unquestionably, the horizons for basic research have been considerably expanded pursuant to the present work. The interdisciplinary collaboration between compressor and control engineers has been challenging and rewarding. Our successful experience so far, apart from its potential to effect dramatic changes in the engines industry, has opened new avenues for basic research in both fluids and control - in areas not attempted before, such as large scale PDE processes, in general - which hold significant promise for future technological achievements.

Acknowledgments

This work was supported by the U.S. Air Force Office of Scientific Research, Dr. J.M. McMichael, Technical Monitor, and by the Office of Naval Research, Dr. R.J. Hansen, Technical Monitor. This support is gratefully acknowledged.

References

1. Greitzer, E.M., "Surge and Rotating Stall in Axial Flow Compressors; Part I: Theoretical Compression System Model," Trans. ASME, vol. 98, 1976, pp. 190-198.
2. Greitzer, E.M., "Review -Axial Compressor Stall Phenomena," ASME Journal of Fluids Engineering, vol. 102, 1980, pp. 134-151.
3. Day, I.J., Greitzer, E.M., and Cumpsty, N.A., "Prediction of Compressor Performance in Rotating Stall," ASME Journal of Engineering for Power, vol. 100, Jan. 1978, pp. 1-14.
4. Greitzer, E.M., "The Stability of Pumping Systems - The 1980 ASME Freeman Scholar Lecture," ASME Journal of Fluids Engineering, vol. 103, 1981, pp. 193-243.
5. Cumpsty, N.A. and Greitzer, E.M., "A Simple Model for Compressor Stall-Cell Propagation," ASME Paper 81-CY-73, 1981.
6. Greitzer, E.M., Mazzawy, R.S., and Fulkerson, D.A., "Flow Field Coupling Between Compression System Components in Asymmetric Flow," ASME Journal of Engineering for Power, Vol. 100, Jan. 1978, pp. 66-72.
7. Moore, F.K., "A Theory of Rotating Stall of Multistage Compressors, Parts I-II," ASME Journal of Engineering for Power, Vol. 106, Jan. 1984, pp. 313-336.
8. Moore, F.K. and Greitzer, E.M., "A Theory of Post-Stall Transients in Axial Compression Systems, Part I - Development of Equations, and Part II - Application," Journal of Turbomachinery, Vol. 108, 1986, pp. 68-76 and 231-237.
9. Moore, F.K., "Stall Transients in Axial Compression Systems with Inlet Distortion," Journal of Propulsion, Vol. 2, No. 6, 1986, pp. 552-561.
10. Fink, D., "Surge Dynamics and Unsteady Flow Phenomena in Centrifugal Compressors," Ph.D. Thesis, Department of Aeronautics and Astronautics, Massachusetts Institute of Technology, Cambridge, MA, 1988.
11. Lavrich, P., "Time Resolved Measurements of Rotating Stall in Axial Flow Compressors," Ph.D. Thesis, Department of Aeronautics and Astronautics, Massachusetts Institute of Technology, Cambridge, MA, 1988.
12. Mani, R., Method and Apparatus for Promoting Surge Conditions in a Gas Turbine," U.S. Patent Disclosure 4,449,358, May 1984.
13. Huang, X., "Active Control of Aerodynamic Instabilities," Ph.D. Thesis, Cambridge University, Cambridge, England, 1988.
14. Pinsley, J., "Active Control of Centrifugal Compressor Surge," M.S. Thesis, Department of Aeronautics and Astronautics. Massachusetts Institute of Technology, Cambridge, MA, June 1988.
15. Epstein, A.H., Ffowcs Williams, J.E., and Greitzer, E.M., "Active Suppression of Aerodynamic Instabilities in Turbomachines," Journal of Propulsion and Power, Vol. 5, No. 2, March/April 1989, pp. 204-211.

16. Ludwig, G.R. and Nenni, J.P., "Tests of an Improved Rotating Stall Control System on a J-85 Turbojet Engine," ASME Paper 80-GT-17, 1980.
17. Day, I.J., "Model Perturbations and Stall Inception, Proceedings, ASME International Gas Turbine Conference, Orlando, FL, June 1991.
18. Hynes, T.P. and Greitzer, E.M., "A Method of Assessing Effects of Circumferential Flow Distortion on Compressor Stability," Journal of Gas Turbines and Power, Vol. 109, 1987, pp. 371-380.
19. Garnier, V., "Experimental Investigation of Rotating Waves as a Rotating Inception Indication in Compressors," M.S. Thesis, Department of Aeronautics and Astronautics, Massachusetts Institute of Technology, Cambridge, MA, June 1979.
20. Paduano, J., Epstein, A.H., Valavani, L., Longley, J.P., Greitzer, E.M., Guenette, G.R., "Active Control of Rotating Stall in a Low Speed Axial Compressor," submitted to 1991 ASME Gas Turbine Conference, June 1991.
21. Paduano, J., "Active Control of Rotating Stall," Ph.D. Thesis, Department of Aeronautics and Astronautics, Massachusetts Institute of Technology, Cambridge, MA, in progress.
22. Ljung, L., System Identification: Theory for the User, Prentice-Hall, Englewood Cliffs, NJ, 1987.
23. LaMaire, R.O., Valavani, L., Athans, M. and Stein, G., "Robust Frequency and Time Domain Identification Methods With Guaranteed Error Bounds," to appear, Automatica, January 1991.
24. Paduano, J., Valavani, L., and Epstein, A.H., "Parameter Identification of Compressor Dynamics During Closed-Loop Operation," accepted for publication, ASME Journal of Dynamics, Measurement and Control.

Parameter Identification of Compressor Dynamics During Closed-Loop Operation

J. Paduano, L. Valavani, A.H. Epstein

*Gas Turbine Laboratory, Department of Aeronautics and Astronautics
Massachusetts Institute of Technology
Cambridge, Massachusetts*

Abstract

A low-speed axial research compressor has been fitted with movable inlet guide vanes to allow for feedback stabilization of rotating stall. A model exists whose structure captures the input-output behavior, and stabilization of rotating stall is possible using this model. Quantitative identification of the parameters in the rotating stall model requires the ability to identify MIMO dynamics, which may be unstable, during closed loop operation. The 'instrumental variable' technique is presented as the basic approach to this problem. The necessary extensions to the basic technique are discussed, and the resulting algorithm is applied. Experimental results are presented which verify that the methodology yields useful estimates.

Nomenclature

$B(z)$	numerator, denominator polynomials in discrete SISO model (13)
$A(z)$	
$B_n(z)$	numerator, denominator polynomials in discrete rotating stall model (11)
$A_n(z)$	
$A_u(z)$	polynomial whose roots coincide with the unstable roots of $A(z)$ (32)
$A_s(z)$	polynomial whose roots coincide with the stable roots of $A(z)$ (32)
a_i	denominator coefficients of z^{-1} in discrete models (11,13)
b_i	numerator coefficients of z^{-1} in discrete models (11,13)
b_{r_n}	
b_{i_n}	control power parameters for continuous rotating stall model (8)
g_{i_n}	
$C(z)$	numerator, denominator polynomials in discrete SISO noise model (21)
$D(z)$	
$E(z)$	polynomials in alternate representation of discrete noise model (31)
$F(z)$	
e	prediction error (15)
$G_n(s)$	transfer function between $\tilde{\gamma}_n(s)$ and $\tilde{\phi}_n(s)$, (4)
$G_{r_n}(s)$	transfer function between $u_{1n}(s)$ and $y_{1n}(s)$, (7)
$G_{i_n}(s)$	transfer function between $u_{1n}(s)$ and $y_{2n}(s)$, (7)
$G_c(z)$	dynamics in the feedback path of closed loop system (Figure 4)
$G_s(z)$	dynamics in forward path of closed loop system (Figure 4)
k	time index for discrete systems
L	term to be minimized in the log-likelihood function (30)
n	spatial mode number
t	time, seconds
r	external input for discrete SISO closed-loop system (30, Figure 4)
r_{1n}, r_{2n}	n^{th} spatial cosine and sine coefficients of the external input (Figure 4)
u	input of discrete SISO model (13)
u_{1n}, u_{2n}	n^{th} spatial cosine and sine coefficients of $\delta\gamma$, (5)
y	output of discrete SISO model (13)
y_{1n}, y_{2n}	n^{th} spatial cosine and sine coefficients of $\delta\phi$, (5)
p_i	poles of $A(z)$ whose magnitudes are ≥ 1 (32)
q	
w	dummy signals used in derivation of closed-loop prediction (Section 2.4)

β	vector of instruments in AML method (29)
η	parameter vector in AML method (27)
$\tilde{\gamma}_n$	n^{th} spatial Fourier coefficient of $\delta\gamma$, (3)
δ	perturbation quantity
$\delta\gamma(\theta, t)$	circumferential distribution of IGV deflection, degrees
v	additive (colored) noise random process (13, 21)
$\delta\phi(\theta, t)$	circumferentially non-uniform ϕ perturbation, (2)
ϕ	compressor axial flow coefficient, (1)
$\bar{\phi}$	annulus averaged flow coefficient, (2)
$\tilde{\phi}_n$	n^{th} spatial Fourier coefficient of $\delta\phi$, (3)
Φ	regressors vector (system inputs and outputs) in IV prediction (14)
Φ_n	regressors matrix for rotating stall n^{th} mode (36)
θ	circumferential position, radians
Θ	parameter vector in IV prediction equation (14)
σ_n	stability parameter for n^{th} mode of continuous rotating stall model (8,10)
ω_{rsn}	rotation frequency for n^{th} mode of continuous rotating stall model (8,10)
ξ	white noise random process (21)
ζ	vector of instruments in IV method (16)
ζ_n	matrix of instruments for rotating stall n^{th} mode (37)
φ	regressors vector in AML method (27)
$(\cdot)^\wedge$	prediction or estimation
$(\cdot)^f$	filtered version of argument
$(\cdot)^T$	transpose
$(\cdot)_n$	n^{th} mode version of the argument
$(\cdot)^c$	alternate signal which is highly correlated with the argument
$(\cdot)_i$	i^{th} column of matrix argument, i^{th} element of vector argument
$(\cdot)_{ij}$	(i,j) element of matrix argument
$E\{\cdot\}$	Expected value
$Z\{\cdot\}$	Z-transform
$Z^{-1}\{\cdot\}$	inverse Z-transform
IGV	inlet guide vane
IV	instrumental variable
RIV	refined instrumental variable
AML	approximate maximum likelihood
NF	noise-free
TR	test-repeat
ML	maximum likelihood
ROC	region of convergence
ac	anticausal
snc	stable, noncausal
uc	unstable, causal
'ac	unstable, anticausal

1 Introduction

Rotating stall is a fluid mechanical phenomenon which besets axial compressors at low flow conditions. It is characterized by a severely non-axisymmetric distribution of axial velocity around the annulus of the compressor, taking the form of a wave or 'stall cell', which propagates in the circumferential direction at a fraction of the rotor speed. Because the nonuniformity travels with respect to both the rotor and stator vanes, both are subject to large amplitude unsteady velocities and, thus, loading which can cause vibration, fatigue, and severe heating. Additionally, rotating stall in jet engines reduces the thrust and often leads to surge, an even more severe and debilitating instability involving the entire compression system.

The transition from normal compressor operation into rotating stall is depicted on a typical compressor pressure rise-mass flow characteristic in Figure 1. This plot relates the nondimensionalized flow rate - known as flow coefficient, ϕ - to the nondimensional pressure rise. The lowest flow rate at which the compressor can operate with axisymmetric flow is point A, the peak of the characteristic. At lower flow coefficients, an abrupt transition occurs into rotating stall (point B). This condition will persist until the flow is increased to point C. Thus, there exists a severe 'hysteresis', that is, range of flow coefficients at which two stable operating conditions exist - one of which is undesirable and often unsafe.

Traditionally, stall has been avoided by avoiding operation near point A. This solution necessitates leaving an ample 'stall margin', so that transients in flow rate and ingestion of non-axisymmetric or otherwise disturbing flow will not drive the system to the rotating stall operating condition. A concomitant performance penalty is paid, because the highest pressure rise and, sometimes, the highest efficiency lie at a flow coefficient below the minimum imposed by the stall margin requirement. It is, therefore, of interest to reduce the minimum allowable flow coefficient, without putting

the system in danger of stall and/or surge.

This is the motivation for a number of recent papers, which describe the phenomenology [1,2,3], fluid mechanics [4,5,6] and active control [6,7,8] of rotating stall. In this paper, we will take the results of these papers as a starting point, giving only a brief description of the active control results and the model presented in [7,8]. We will then present techniques for identification of the model parameters.

1.1 Active Control of Rotating Stall

Consider the schematic diagram of an axial compressor in Figure 2. It consists of an upstream annular duct, a set of inlet guide vanes (IGVs), a compressor, a downstream annular duct, and a throttle. Normally, flow through the compressor is circumferentially uniform (axisymmetric), and a single non-dimensional measure of fluid velocity determines the system state. This measure is the flow coefficient, which is axial velocity normalized by rotor speed at the mean radius:

$$\phi = \frac{(\text{axial velocity})}{(\text{rotor speed})}. \quad (1)$$

Under certain conditions, however, the flow through the compressor can become non-axisymmetric - that is, circumferential 'waves' of perturbation flow coefficient, $\delta\phi$, can exist. In this case, the system can be completely characterized by two terms: the annulus averaged flow coefficient, $\bar{\phi}$, and the circumferential perturbation on this average at some axial station:

$$\phi = \bar{\phi} + \delta\phi(\theta, t), \quad (2)$$

where θ is circumferential position and t is time. Velocity waves $\delta\phi$ will tend to propagate around the annulus in the direction of rotor rotation. The time evolution of these waves determines the stability of the system. If they damp out with time, the system is stable and will return to axisymmetric operation. If they grow, the system is unstable and the waves will continue to grow until nonlinear effects take over--this condition is known as rotating stall, and usually consists of one or more 'stall cells'

rotating around the annulus at a fraction of the rotor speed.

Recently [7,8], active control was successfully applied to this problem in a low-speed single-stage research compressor. The experimental setup is shown in Figure 3. Eight hot wire anemometers, arranged around the annulus near the compressor face, measure the velocity perturbations. A digital computer processes these signals and creates a feedback signal to a set of 12 movable inlet guide vanes (IGVs). The IGVs are individually mounted on digitally-controlled high-bandwidth (80 Hz) servomotors. This allows independent control of the IGV incidences, $\delta\gamma_k$. For the wave shapes that are of interest in our experiment, these 12 blade deflections around the circumference can be considered as a continuous 'actuation wave', $\delta\gamma(\theta,t)$. This actuation wave can be commanded in response to the measured wave of perturbation axial velocity - a feedback scheme which allows the compressor to operate axisymmetrically at values of $\bar{\phi}$ which would normally be unstable to flow perturbations $\delta\phi(\theta,t)$.

References [6-8] present a model for the input-output dynamics of this system, which will be reviewed briefly in Section 1.2. Although the *structure* of this model captures the experimentally observed behavior extraordinarily well, quantitative prediction of system dynamics is not as yet possible *a priori*. Instead, experimental searches and parameter identification techniques are used to aid in control system design. Parameter identification using spectral analysis techniques allows open-loop dynamics to be determined [7], but such methods fail during closed-loop operation. In order to extend the operating range, it becomes necessary to identify the unstable dynamics; this identification must necessarily be done during closed-loop operation. Information about unstable compressor dynamics is also of interest from a experimental fluid mechanics point of view; such information has never before been measured.

This paper presents the results of applying an instrumental variable parameter identification procedure to the active control research compressor during closed-loop operation at various values of $\bar{\phi}$ (some of which are unstable). The instrumental

variable (IV) technique [10] was chosen for this study because of its flexibility. For instance, it can be adapted to MIMO or non-standard systems. Also, with proper filtering, the IV estimates can be made to approach the maximum likelihood estimates. Finally, with careful choice of instruments, the problems normally associated with IV identification during closed-loop stabilization can be alleviated. These issues will be presented in Section 2, after a brief description of the system dynamics. In Section 3, experimental results will be shown for the active control research compressor.

1.2 Dynamic System Description

As described above, we assume that the system state can be completely characterized by $\tilde{\phi}$ and the perturbation $\delta\phi(\theta,t)$ at some axial station. $\tilde{\phi}$ can be fixed in an experimental environment by a throttle downstream of the compressor. This defines the system operating point, and 'equilibrium' is defined as axisymmetric flow, i.e. $\delta\phi = 0$. We are interested in the dynamics of $\delta\phi(\theta,t)$ and the stability of the equilibrium point. We are also interested in the *forced* dynamics of this system, that is, the transfer characteristics between $\delta\gamma(\theta,t)$ and $\delta\phi(\theta,t)$.

References [5-7] present a linearized fluid mechanical model for this distributed system. It can be shown that this model has a modal structure which allows the system to be 'diagonalized' as follows: If we represent the functions $\delta\phi$ and $\delta\gamma$ in terms of their spatial Fourier series:

$$\delta\phi(\theta,t) = \sum_{n \neq 0} \tilde{\phi}_n(t) \cdot e^{jn\theta}, \quad (3)$$

$$\delta\gamma(\theta,t) = \sum_{n \neq 0} \tilde{\gamma}_n(t) \cdot e^{jn\theta},$$

then the transfer characteristics between $\tilde{\gamma}_n$ and $\tilde{\phi}_n$ are completely decoupled, i.e.

$$\tilde{\phi}_n(s) = G_n(s) \cdot \tilde{\gamma}_n(s), \text{ for } n = \dots -2, -1, 1, 2, \dots \quad (4)$$

This represents a tremendous simplification of the distributed dynamics and allows standard control techniques to be applied. Furthermore, the system dynamics are dominated by the lower modes; by feeding back only the first few modes ($|n|=1,2,3$), substantial improvement in operating range can be achieved [7,8].

The system diagonalization can also be represented in terms of Fourier sine and cosine coefficients, so that all terms in the equations are real. If we represent the input and output functions as

$$\delta\phi(\theta, t) = \sum_{n>0} y_{1n}(t) \cdot \cos(n\theta) + \sum_{n>0} y_{2n}(t) \cdot \sin(n\theta), \quad (5)$$

$$\delta\gamma(\theta, t) = \sum_{n>0} u_{1n}(t) \cdot \cos(n\theta) + \sum_{n>0} u_{2n}(t) \cdot \sin(n\theta),$$

then the transfer characteristics become

$$\begin{bmatrix} y_{1n} \\ y_{2n} \end{bmatrix} = \begin{bmatrix} T_n(s) \end{bmatrix} \cdot \begin{bmatrix} u_{1n} \\ u_{2n} \end{bmatrix}, \text{ for } n=1,2,\dots \quad (6)$$

where $T_n(s)$ is skew-symmetric because of the symmetry of the annulus:

$$\begin{bmatrix} T_n(s) \end{bmatrix} = \begin{bmatrix} G_{r_n}(s) & -G_{i_n}(s) \\ G_{i_n}(s) & G_{r_n}(s) \end{bmatrix}; \quad (7)$$

$$G_n(s) = G_{r_n}(s) + j \cdot G_{i_n}(s)$$

The structure of $G_n(s)$ is predicted by the fluid mechanical model, and is best expressed by giving the ODE for the system. Again, we can use either the complex Fourier coefficient representation or the real MIMO representation:

$$\dot{\tilde{\phi}}_n = (\sigma + j \cdot \omega_n) \cdot \tilde{\phi}_n + (b_r + j \cdot b_i) \cdot \tilde{\gamma}_n + j \cdot g_i \cdot \tilde{\gamma}_n \quad (8)$$

or, using the identities $\tilde{\phi}_n = \frac{1}{2}(y_{1n} - j y_{2n})$ and $\tilde{\gamma}_n = \frac{1}{2}(u_{1n} - j u_{2n})$:

$$\begin{bmatrix} \dot{y}_{1n} \\ \dot{y}_{2n} \end{bmatrix} = \begin{bmatrix} \sigma & -\omega_{rs} \\ \omega_{rs} & \sigma \end{bmatrix}_n \begin{bmatrix} y_{1n} \\ y_{2n} \end{bmatrix} + \begin{bmatrix} b_r & -b_i \\ b_i & b_r \end{bmatrix}_n \begin{bmatrix} u_{1n} \\ u_{2n} \end{bmatrix} + \begin{bmatrix} 0 & -g_i \\ g_i & 0 \end{bmatrix}_n \begin{bmatrix} \dot{u}_{1n} \\ \dot{u}_{2n} \end{bmatrix}. \quad (9)$$

These two representations each have their advantages: The complex form is compact and contains no redundant parameters. It also automatically satisfies the symmetry conditions in the annulus. The real system, on the other hand, is standard from the point of view of control theory - it has no complex numbers, and the two-state nature of the system is clear ($\tilde{\phi}_n$ consists of a phase and a magnitude, so the system (8) isn't strictly SISO).

The physical significance of σ_n and ω_{rs_n} can be seen by substituting the homogeneous solution to (8) into (3), for some mode n:

$$\delta\phi(\theta, t) = e^{jn\theta} \cdot e^{(\sigma_n + j \cdot \omega_{rs_n})t} = e^{j(n\theta + \omega_{rs_n} \cdot t)} \cdot e^{\sigma_n t} \quad (10)$$

The second equality shows that $\omega_{rs_n} \cdot t$ alters the phase of the wave, causing it to rotate; thus ω_{rs_n} is the 'rotating stall frequency' for the n^{th} mode. It is also clear that $\sigma_n \cdot t$ alters the size of the rotating wave in (10); thus σ_n is the rotating stall stability parameter for the n^{th} mode.

Techniques exist to convert these continuous state-space systems to discrete systems for the purpose of identification using digitally sampled data [9]. In this paper we will convert freely from continuous to discrete-time systems and back without emphasizing the details of such conversion. The discrete-time equivalent system for

the above dynamics can be written as:

$$\begin{bmatrix} y_{1n} \\ y_{2n} \end{bmatrix} = \frac{B_n(z)}{A_n(z)} \begin{bmatrix} u_{1n}(z) \\ u_{2n}(z) \end{bmatrix} + v(z)$$

where

$$A_n(z) = (1 + a_1 z^{-1} + a_2 z^{-2})_n, \quad (11)$$

$$B_n(z) = \begin{bmatrix} (b_1 + b_2 z^{-1})(1 + z^{-1}) & -(b_3 + b_4 z^{-1} + b_5 z^{-2}) \\ (b_3 + b_4 z^{-1} + b_5 z^{-2}) & (b_1 + b_2 z^{-1})(1 + z^{-1}) \end{bmatrix}_n,$$

z is the Z -transform variable and n is the mode number. We have also added $v(z)$ to model disturbances. We will be concerned here with the identification of the parameter set

$$\Theta_n = [a_1 \ a_2 \ b_1 \ b_2 \ b_3 \ b_4 \ b_5]_n^T, \quad n=1, 2, \dots \quad (12)$$

The discrete-time parameters Θ_n can subsequently be converted to the continuous domain, giving σ_{rs} , ω_{rs} , b_r , b_i , and g_i in (8) and (9). We would like to accomplish this identification task for unstable dynamics, during closed-loop stabilization. Section 2 describes our approach to this problem.

2 Instrumental Variable Method

The organization of this section is as follows: Section 2.1 reviews the basic IV method for SISO systems. Section 2.2 outlines Young's Refined IV - Approximate Maximum Likelihood (RIV-AML) method. Modifications to this approach necessary to handle the closed loop case are discussed in Section 2.3, and modifications for unstable plants are discussed in Section 2.4. Finally, a brief discussion of how the MIMO estimation for the rotating stall system is efficiently computed appears in Section 2.5.

2.1 Basic IV Procedure

Consider the system

$$y(z) = \frac{B(z)}{A(z)} \cdot u(z) + v(z) \quad (13)$$

where:

$$A(z) = (1 + a_1 z^{-1} + a_2 z^{-2} + \dots),$$

$$B(z) = (b_1 + b_2 z^{-1} + b_3 z^{-2} + \dots),$$

and $v(k)$ represents the (possibly colored) noise corrupting the measurements. We can build a one-step-ahead predictor for this system:

$$\hat{y}(k) = \Phi^T(k) \cdot \hat{\Theta}, \quad (14)$$

where:

$$\Phi(k) = [-y(k-1) \ -y(k-2) \ \dots \ u(k) \ u(k-2) \ u(k-4) \ \dots]^T,$$

$$\hat{\Theta} = [\hat{a}_1 \ \hat{a}_2 \ \dots \ \hat{b}_1 \ \hat{b}_2 \ \hat{b}_3 \ \dots]^T,$$

and the $(\hat{\cdot})$ indicates prediction or estimation. The prediction error can then be written as

$$e(k) = y(k) - \Phi^T(k) \cdot \hat{\Theta}. \quad (15)$$

The instrumental variable (IV) method [10] finds the value of $\hat{\Theta}$ which will cause the error to be uncorrelated with some chosen set of instruments

$$\zeta(k) = [\zeta_1(k) \ \zeta_2(k) \ \dots]^T. \quad (16)$$

This condition can be written as follows:

$$\hat{\Theta} = \text{sol} \left\{ \frac{1}{N} \sum_{k=1}^N \zeta(k) \cdot e(k) = 0 \right\}, \quad (17)$$

where $\text{sol}\{\cdot\}$ indicates that $\hat{\Theta}$ is the value of Θ for which the equation in brackets is satisfied. Substituting in equation (15):

$$\hat{\Theta} = \text{sol} \left\{ \frac{1}{N} \sum_{k=1}^N \zeta(k) \left(y(k) - \Phi^T(k) \cdot \hat{\Theta} \right) = 0 \right\}. \quad (18)$$

The philosophy of the IV approach is this: if the instruments are chosen to be related to the system inputs and outputs, and $\hat{\Theta}$ does *not* satisfy (17), then there is additional information about the input-output dynamics left in the prediction error. Therefore, a good estimate of Θ should extract this information, making the correlation in (17) disappear.

The solution to (18) is

$$\hat{\Theta} = \left[\frac{1}{N} \sum_{k=1}^N \zeta(k) \Phi^T(k) \right]^{-1} \cdot \left[\frac{1}{N} \sum_{k=1}^N \zeta(k) y(k) \right]. \quad (19)$$

The IV method will have good convergence and consistency properties if the following two conditions are met:

$$\sum_{k=1}^N \zeta(k) \Phi^T(k) \text{ nonsingular} \quad (20a)$$

$$E \left\{ \sum_{k=1}^N \zeta(k) v(k) \right\} = 0 \quad (20b)$$

Condition (20a) guarantees invertibility in (19), and also indicates that ζ is correlated with the system dynamics, which is necessary for equation (17) to yield good estimates. In fact, if $\zeta(k) = \Phi(k)$, then (20a) is satisfied trivially and the estimate becomes the least-squares estimate of Θ .

Condition (20b) specifies that the instruments be uncorrelated with the noise, so that colored noise will not corrupt the estimates. This condition is often not met in the least-squares case ($\zeta(k) = \Phi(k)$), hence the need for a different set of instruments [10]. Pre-filtered versions of the elements of $\Phi(k)$ are usually used in this case. Ljung [10] gives a complete description of the IV method, its convergence and consistency properties, and methods for constructing instruments which are uncorrelated with the noise.

2.2 Young's Refined Instrumental Variable - Approximate Maximum Likelihood (RIV-AML) Technique [11]

Many filtering schemes have been proposed for constructing the instruments $\zeta(k)$ in the IV procedure. Young [11] has developed a particularly attractive set of pre-filters and instruments in the context of maximum likelihood estimation, for the following noise model:

$$v(z) = \frac{C(z)}{D(z)} \cdot \xi(z). \quad (21)$$

In this formulation, both $C(z)$ and $D(z)$ are monic, and $\xi(k)$ is an uncorrelated sequence with Gaussian amplitude distribution over the sample interval:

$$\xi \sim N(0, \Sigma^2 \cdot I) \quad \xi = [\xi(1), \xi(2), \dots, \xi(T)].$$

In Young's approach, the input-output data is first pre-filtered, which introduces a new set of variables:

$$y^f(z) \equiv \frac{D}{A \cdot C} \cdot y(z) ; \quad u^f(z) \equiv \frac{D}{A \cdot C} \cdot u(z) ; \quad \hat{y}^f(z) \equiv \frac{B}{A} \cdot u^f(z) \quad (22)$$

Young shows that, with these definitions, the maximum-likelihood estimate can be stated as the solution of an IV problem:

$$\hat{\Theta} = \left[\frac{1}{N} \sum_{k=1}^N \zeta(k) \Phi_f^T(k) \right]^{-1} \cdot \left[\frac{1}{N} \sum_{k=1}^N \zeta(k) y^f(k) \right] \quad (23)$$

where

$$\zeta(k) = [-\hat{y}^f(k-1) \quad -\hat{y}^f(k-2) \quad \dots \quad u^f(k) \quad u^f(k-1) \quad u^f(k-2) \quad \dots]^T$$

and

$$\Phi_f(k) = [-y^f(k-1) \quad -y^f(k-2) \quad \dots \quad u^f(k) \quad u^f(k-1) \quad u^f(k-2) \quad \dots]^T,$$

In other words, if the above defined variables and instruments are used, then $\hat{\Theta}$ is the maximum likelihood estimate. This is called the refined IV, or RIV, estimate.

Of course, the polynomials $A(z)$, $B(z)$, $C(z)$, and $D(z)$ in equation (22) are not known a priori. Initial estimates of these must be made, and the RIV method applied

iteratively to improve the estimates. The parameters in $\hat{\Theta}$ constitute the updates for \hat{A} and \hat{B} in such a scheme, so iteration on Θ is sufficient as a search on the maximum likelihood estimates of A and B . C and D , on the other hand, are not estimated by the procedure. Therefore, an estimation algorithm for C and D must be added to the iteration.

Young provides an approximate maximum likelihood approach to do exactly that. It provides a way to estimate C and D , based on the current estimates of A , B , C , and D . The basic philosophy is to form an error term based on the current estimates \hat{A} and \hat{B} . This error term is then considered to be the output of a dynamic system driven by white noise, and the dynamics are estimated using a procedure similar to the RIV procedure described above. The specifics of this procedure, called approximate maximum likelihood (AML), are as follows:

We first take the prediction error $e(k)$ in (15) as a measurement of $v(k)$:

$$\begin{aligned} v(z) &= y(z) - \frac{B(z)}{A(z)} \cdot u(z) \\ \Rightarrow \hat{v}(z) &= y(z) - \hat{y}(z) \\ &= e(z). \end{aligned} \quad (24)$$

The dynamics in (21) are then written

$$D(z) \cdot \hat{v}(z) = C(z) \cdot \xi(z). \quad (25)$$

A 'one-step-ahead predictor' for this system is

$$\hat{v}(k) = \phi^T \hat{\eta} \quad (26)$$

where:

$$\begin{aligned} \phi &= [-\hat{v}(k-1) \ -\hat{v}(k-2) \ \cdots \ \xi(k-1) \ \xi(k-2) \ \cdots]^T \\ \eta &= [d_1 \ d_2 \ \cdots \ c_1 \ c_2 \ \cdots]^T \end{aligned} \quad (27)$$

To compute an approximate maximum likelihood estimate of the noise system, prefilter as follows:

$$\begin{aligned}\hat{v}(k) &= \frac{1}{\hat{C}(z)} \cdot \hat{v}(k) \\ \hat{\xi}^f(k) &= \frac{1}{\hat{C}(z)} \cdot \hat{\xi}(k) = \frac{\hat{D}(z)}{\hat{C}(z)} \cdot \hat{v}(k)\end{aligned}\quad (28)$$

The estimate for the noise model is then:

$$\hat{\eta} = \left[\frac{1}{N} \sum_{k=1}^N \beta(k) \varphi^T(k) \right]^{-1} \cdot \left[\frac{1}{N} \sum_{k=1}^N \beta(k) \hat{v}(k) \right]$$

where:

$$\beta(k) = [\hat{v}(k-1) \quad \hat{v}(k-2) \quad \dots \quad \hat{\xi}^f(k-1) \quad \hat{\xi}^f(k-2) \quad \dots]^T$$

The notation here has been made as similar to the IV notation as possible, to show the parallel between this procedure and the RIV procedure described above. Note that we use some set of past estimates \hat{A} , \hat{B} , \hat{C} , and \hat{D} to allow us to best estimate $\hat{\eta}$, which is the updated estimate for C and D. Young gives more detail about the properties of the estimates, and also gives a recursive algorithm for its application.

We now have an estimation procedure for C and D, which can be integrated into the iteration for the maximum likelihood estimates of A and B. The complete RIV-AML recursion algorithm, then, is [11]

1. Begin with initial estimates for $\hat{A}(z)$, $\hat{B}(z)$, $\hat{C}(z)$, and $\hat{D}(z)$.
2. Use the AML procedure (equations (24)-(29)) to update \hat{C} and \hat{D} .
3. Use the RIV procedure (equations (22)-(23)) to update \hat{A} and \hat{B} .
4. Go to 2, repeat with the new values of \hat{A} and \hat{B} .

One purpose of the filters in equations (22) is to eliminate as much as possible the effect of the colored noise on the outputs. Such 'pre-whitening' attempts to insure that $y^f(k)$ is uncorrelated with the disturbances $v(k)$. $y^f(k)$ must be uncorrelated with

$v(k)$ in order to satisfy equation (20b), because $y^f(k)$ is a part of the instruments. The filtered inputs $u^f(k)$, which make up the remainder of the instruments, must also be uncorrelated with $v(k)$ in order to satisfy equation (20b). During open-loop operation, this condition is automatically satisfied, because $\zeta(k)$ in equation (21) is uncorrelated with $u(k)$. During closed-loop operation, however, $v(k)$ and $u(k)$ are correlated (this will be shown in the next section). The above method must, therefore, be modified for closed-loop identification. This is the subject of the following section.

2.3 Choice of Closed-Loop Instruments

Figure 5.3 shows the layout and notation for closed-loop operation. The system dynamics remain as in equation (13). In addition, we introduce the external input signal, $r(k)$, and the following feedback law:

$$u(z) = G_s(z) \cdot [r(z) - G_c \cdot y(z)]. \quad (30)$$

where $G_c(z)$ and $G_s(z)$ are rational transfer functions representing dynamics in the feedback and forward path. For the rotating stall controller, these dynamics are well defined, so here we will assume that they are known. Since $y(k)$ is corrupted by $v(k)$, $u(k)$ will now be correlated with the noise, and equation (20b) will be violated:

$$\begin{aligned} u(z) &= G_s \cdot (r(z) - G_c \cdot (\frac{B}{A} \cdot u(z) + v(z))), \\ &\Rightarrow E \left\{ \sum_{k=1}^N \zeta(k) v(k) \right\} \neq 0, \end{aligned}$$

because $\zeta(k)$ contains $u(k)$. This is a very real problem which does not constitute a mere theoretical technicality. In a high-gain feedback situation such as occurs during stabilization of unstable dynamics, it renders the IV methods described so far useless. Fortunately, these methods regain their applicability if the proper substitutions are made to insure that the instruments fulfill equations (20).

References [12] and [13] discuss in detail the problem of closed-loop estimation,

and the methods they describe will be used here. The idea is to replace $\{ y(k), u(k) \}$ in the computation of the instruments with some $\{ y^c(k), u^c(k) \}$ which are highly correlated with their respective counterparts (condition (5.20a), but which are uncorrelated with the disturbances (condition (5.20b)). The two methods used to accomplish this are described below. In both cases, we assume $r(k)$ is a known external excitation.

Method I: Test-Repeat (TR) Instrumental Variable

This method, introduced in [12], achieves uncorrelated instruments by repeating the experiment twice, with identical $r(k)$ in both cases. The measured inputs and outputs for the two tests are denoted $\{ u(k), y(k) \}$ and $\{ u^c(k), y^c(k) \}$. The procedure is to use one of these input-output pairs to compute the instruments, and the other to compute the estimates. The RIV-AML estimation proceeds exactly as described in Section 2.2, using $\{ u^c(k), y^c(k) \}$ to compute the instruments and $\{ u(k), y(k) \}$ to compute the parameter estimates (The roles of the two input-output pairs can be switched).

Using identical $r(k)$ in the two tests insures high correlation between the instruments and the measurements, and poses no particular difficulty in a digital control environment. Also, because $v(k)$ and $v^c(k)$ are incurred at different times, they are uncorrelated, which means that the instruments (from the first test) will be uncorrelated with the disturbances (from the second test) even if the system is operating closed loop. Reference [12] proves these claims, and discusses the consistency properties of the Test Repeat (TR) method.

Method II: Noise-Free (NF) Instruments

Both [12] and [13] discuss this method, which uses noise-free (NF) simulation of the test to generate the instruments. In this case $\{ u^c(k), y^c(k) \}$ comes from a simulation, using an a priori estimate of the system dynamics (i.e. $\hat{\Theta}$). $v(k)$ will thus

be identically zero. The same input $r(k)$ is then applied to the real system to get $\{u(k), y(k)\}$. The RIV-AML algorithm can now be applied, using $\{u^c(k), y^c(k)\}$ to compute the instruments and $\{u(k), y(k)\}$ as the measurements (in this case the roles of the two input-output pairs cannot be switched).

The same reasoning applies here as in the TR case. The noise-free instruments will naturally be uncorrelated with the noise from the experiment (condition (20a)). The degree of correlation between the instruments and the measurements (condition (20b)) will depend on the accuracy of the a priori estimate of the system dynamics, but (except in trivial cases) some correlation will exist. Closed-loop operation changes none of these observations. [12] and [13] discuss NF estimation more rigorously.

2.4 Modification of the RIV-AML Prefilters for Unstable Plant Dynamics

The test-repeat instrumental variable (TR/IV) and the noise-free instrumental variable (NF/IV) methods allow identification of system dynamics during closed-loop operation, even when the plant is unstable. Experience with these methods has suggested, however, that the covariance of the estimates can be large for standard choices of instruments. Therefore, we have combined the TR and NF methods with the RIV-AML method to obtain more accurate estimates. If the open-loop plant is stable, this presents no problem: the hybrid techniques, termed TR/RIV-AML and NF/RIV-AML, can be synthesized without additional modifications. However, if the open-loop plant is unstable, many of the prefilters required by the RIV-AML procedure (equations (22) and (24)) are also unstable - they contain $\frac{1}{A(z)}$, which is unstable if implemented as a causal filter.

To use the TR/RIV-AML and NF/RIV-AML procedure when the open-loop plant is unstable, we must modify the prefiltering scheme to avoid filters which are unstable. This problem is primarily one of understanding the prefilters in the context of the maximum-likelihood (ML) problem, and applying them properly. To develop the

RIV-AML method, Young [11] first writes the log-likelihood function for the observations $y(k)$, and then reduces the ML problem to the minimization of the following term:

$$L = \left[\frac{D}{C} \left(y - \frac{B}{A} \cdot u \right) \right]^T \left[\frac{D}{C} \left(y - \frac{B}{A} \cdot u \right) \right].$$

The RIV and AML prefilters are then formulated by writing $\partial L / \partial a_i = 0$, $\partial L / \partial b_i = 0$, etc. Thus the prefilters contain $\frac{1}{A}$ because the log-likelihood function contains the prediction error $\left(y - \frac{\hat{B}}{A} \cdot u \right)$.

When the closed-loop system is stabilizing an open-loop unstable plant, we are faced with the following problem: $y(k)$ and $u(k)$ are 'stable' signals; that is, their Z-transforms $y(z)$ and $u(z)$ converge on the unit circle ($|z| = 1$). But $\frac{B(z)}{A(z)}$ is unstable; that is, it is the Z-transform of a causal impulse response, and it contains poles outside the unit circle. Given these conditions, can we compute an estimate of $y(k)$ based on $u(k)$, $A(z)$, and $B(z)$ alone? If we can, then the prediction error can be formulated, and the prefilters necessary for the RIV-AML procedure can be found.

To answer this question, consider our system representation (13.21):

$$y(z) = \frac{B(z)}{A(z)} \cdot u(z) + \frac{C(z)}{D(z)} \cdot \xi(z). \quad (31)$$

We can break $A(z)$ into a polynomial whose roots are stable, times a polynomial whose roots are unstable:

$$A(z) \equiv A_s(z) \cdot A_u(z), \quad (32)$$

where:

$$A_s(z) = \prod_j (1 - v_j \cdot z^{-1}); \quad |v_j| < 1,$$

$$A_u(z) = \prod_i (1 - p_i \cdot z^{-1}); \quad |p_i| \geq 1.$$

This factorization of $A(z)$ allows us to rewrite (31) to reflect the possibility that the

noise dynamics are affected by the unstable poles:

$$y(z) = \frac{B(z)}{A_u(z)A_s(z)} \cdot u(z) + \frac{E(z)}{A_u(z)F(z)} \cdot \xi(z). \quad (33)$$

where $\frac{E}{F}$ is defined such that $\frac{C}{D} = \frac{E}{A_u F}$. Generality is retained in this formulation because $E(z)$ cancels any poles of $A_u(z)$ that are not part of $D(z)$. The transfer function $\frac{E}{F}$ is stable if the system is stabilizable, so we can write:

$$\begin{aligned} y(z) &= \frac{1}{A_u(z)} \cdot \left[\frac{B(z)}{A_s(z)} \cdot u(z) + \frac{E(z)}{F(z)} \cdot \xi(z) \right] \\ &= \frac{1}{A_u(z)} \cdot [q(z)] \end{aligned} \quad (34)$$

where $q(z)$ is bounded for $|z|=1$, because of the our conditions on A_s (stated in (32)), $\frac{E}{F}$ (stated above), $u(k)$ (its Z-transform converges on the unit circle), and $\xi(k)$ (stated after (21) - the important point being that $\xi(k)$ is a finite-duration (windowed) sequence). We have also specified that a feedback system is stabilizing the plant, so that $y(z)$ converges for $|z|=1$. Thus, by studying (34), one concludes that $q(z)$ must contain zeros which cancel the unstable poles of $\frac{1}{A_u}$. We write this condition as follows:

$$q(z) = A_u(z) \cdot w(z) \quad (35)$$

$$\Rightarrow y(z) = \frac{1}{A_u(z)} \cdot [A_u(z) \cdot w(z)].$$

where $w(z)$ also converges for $|z|=1$. The pole-zero cancellation implied by (35) can be derived constructively (although somewhat tediously) by writing the closed-loop transfer function from *any* external signal (such as $r(z)$ or $\xi(z)$) to $y(z)$.

The representation (35) can be used to motivate a filtering scheme as follows:

$\frac{1}{A_u(z)}$ is the (two-sided) Z-transform of at least *two distinct impulse responses* [14]:

1) a causal, unstable impulse response, which we will call h_c , and 2) an anticausal, stable impulse response, which we will call h_{ac} . The Z-transform of h_c converges in the region of convergence (ROC) $|z|>\max(p_i)$, while the Z-transform of h_{ac} converges

in the ROC $|z| < \min(p_i)$ (see Figure 5). The ambiguity of the Z-transform is usually cleared up by invoking causality: because (31) represents a causal dynamics system, we know that the physically meaningful inverse of $\frac{1}{A_u(z)}$ is $h_c(k)$, and that the convolution corresponding to (35) is:

$$y(k) = h_c(k) * [h_A(k) * w(k)], \quad (36)$$

where $*$ indicates convolution and

$$h_c(k) \equiv Z^{-1} \left\{ \frac{1}{A_u(z)} \right\} \quad \text{ROC: } |z| > \max(p_i),$$

$$h_A(k) \equiv Z^{-1} \{ A_u \} \quad \text{ROC: all } z.$$

As we have noted, $h_c(k)$ is causal, but because the poles of $\frac{1}{A_u(z)}$ lie outside the unit circle, $h_c(k)$ grows without bound as $k \rightarrow \infty$. However, it can be shown that the causal, unstable impulse response $h_c(k)$ can be replaced by its anticausal, stable counterpart $h_{ac}(k)$, if a pole-zero cancellation such as (35) occurs. We can write this statement as follows:

$$h_{ac}(k) * [h_A(k) * w(k)] = h_c(k) * [h_A(k) * w(k)] \quad (37)$$

where

$$h_{ac}(k) = Z^{-1} \left\{ \frac{1}{A_u(z)} \right\} \quad \text{ROC: } |z| < \min(p_i).$$

Note here that the ROC overlaps the unit circle. Computing the inverse Z-transform over this ROC results in an impulse response which is bounded for all k [14]. Thus we expect that replacing h_c with h_{ac} will yield a stable (although noncausal) way to predict $y(k)$.

Substituting (37) into (36), we have the following equation for $y(k)$:

$$y(k) = h_{ac}(k) * [h_A(k) * w(k)]. \quad (38)$$

Since all of the sequences in this equation are stable, their Z-transforms exist on the

unit circle, and we can convert back to the Z-domain:

$$\begin{aligned}
 y(z) &= \frac{1}{A_u(z)} \Big|_{ac} \cdot [A_u(z) \cdot w(z)] \\
 &= \frac{B(z)}{A(z)} \Big|_{snc} \cdot u(z) + \frac{C(z)}{D(z)} \Big|_{snc} \xi(z). \\
 \Rightarrow \hat{y}(z) &= \frac{\hat{B}(z)}{\hat{A}(z)} \Big|_{snc} \cdot u(z),
 \end{aligned} \tag{39}$$

where we denote the Z-transform of h_{ac} as $\frac{1}{A_u(z)} \Big|_{ac}$, to distinguish it from the Z-transform of h_c . The operations between transfer functions implied by (39) are valid for the transfer functions and signals we have defined, because they all converge on the unit circle. The subscript 'snc' is used to indicate that we will use a stable, noncausal time-domain implementation of the filter - the anticausal part coming from the unstable poles, and the causal part coming from the stable poles. Figure 5 is an example of the regions of convergence associated with $\frac{1}{A(z)}$, and the corresponding impulse responses.

We have shown how the transfer function between $u(z)$ and $\hat{y}(z)$ must be altered when the open-loop plant is unstable. It can be shown that all of the filtering and prediction described in Sections 2.2 can be similarly altered, without changing the maximum-likelihood results of Young [11]. Thus, our scheme is noncausal when the plant is unstable, and must be implemented off-line, but otherwise it proceeds as described in Sections 2.1-2.3, with $\frac{1}{A(z)}$ replaced by $\frac{1}{A(z)} \Big|_{snc}$.

2.5 Application to the MIMO Rotating Stall System

The rotating stall system described in equation (11) is both multi-modal and MIMO. The multi-modal nature of the system requires dynamics to be identified for each mode number n . This identification can be done mode-by-mode, since the dynamics are decoupled. equation (11) also shows that each mode constitutes a

two-input two-output system. This adds complexity, but otherwise requires no modification to the procedure. Some specifics of the rotating stall analysis will be given, as an illustration and to demonstrate an algorithmic simplification.

The one-step-ahead predictor for the system described in equation (11) is:

$$\begin{bmatrix} \hat{y}_{1n} \\ \hat{y}_{2n} \end{bmatrix}_k = \Phi_n^T(k) \cdot \hat{\Theta}_n$$

where:

(40)

$$\begin{aligned} \Phi_n^T(k) &= \begin{bmatrix} \Phi_{1n}^T \\ \Phi_{2n}^T \end{bmatrix}_k \\ &= \begin{bmatrix} y_1(k-1) & y_1(k-2) & u_1(k)+u_1(k-1) & u_1(k-1)+u_1(k-2) & -u_2(k) & -u_2(k-1) & -u_2(k-2) \\ y_2(k-1) & y_2(k-2) & u_2(k)+u_2(k-1) & u_2(k-1)+u_2(k-2) & u_1(k) & u_1(k-1) & u_1(k-2) \end{bmatrix}_n \\ \hat{\Theta}_n &= [a_1 \ a_2 \ b_1 \ b_2 \ b_3 \ b_4 \ b_5]_n^T \end{aligned}$$

The instruments must match the dimension of the measurement matrix:

$$\zeta_n(k) = \begin{bmatrix} \zeta_{1n}^T \\ \zeta_{2n}^T \end{bmatrix} = \begin{bmatrix} \zeta_{11}(k) & \zeta_{21}(k) & \cdots & \zeta_{71}(k) \\ \zeta_{12}(k) & \zeta_{22}(k) & \cdots & \zeta_{72}(k) \end{bmatrix}_n^T. \quad (41)$$

equations (17) through (28) proceed as before, with the understanding that the summations now contain matrix multiplications rather than scalar and inner products. equation (19) can be made more efficient computationally by breaking up the matrices $\zeta_n(k)$ and $\Phi_n(k)$ into their constituent vectors. The resulting solution to the IV problem is as follows:

$$\hat{\Theta}_n = [\sum \zeta_{1n} \Phi_{1n}^T + \sum \zeta_{2n} \cdot \Phi_{2n}^T]^{-1} \cdot [\sum \zeta_{1n} \cdot x_{1n} + \sum \zeta_{2n} \cdot x_{2n}], \quad (42)$$

where subscripts k have been suppressed.

3 Results and Discussion

The techniques described above were used on data collected from the active control research compressor. The pressure rise - flow coefficient characteristic for this compressor is shown in Figure 6. Points below $\bar{\phi} \equiv 0.45$ are unstable, so these data points are taken with the system operating in closed loop. Data points in the stable regime can also be taken in closed loop. This has been done and the pressure rise of the compressor is essentially unaffected by the controller.

A typical closed-loop IV parameter identification experiment is conducted as follows: First the control system is initialized and closed loop operation begins. Next the downstream throttle is used to manually set the flow coefficient to the value at which the test will be run. This may or may not be an open-loop unstable operating point. The external signal $[r_1(k) \ r_2(k)]_n^T$ is then applied, and measurements are made of $[u_1(k) \ u_2(k)]_n^T$ and $[y_1(k) \ y_2(k)]_n^T$. The test can then be repeated for the TR method. The complete data set is then put through the TR/RIV-AML procedure or the NF/RIV-AML procedure described in Section 2. Estimates of A, B, C, and D are needed to initialize these algorithms. Typically the procedure is to use estimates of A, B, C, and D from a more stable $\bar{\phi}$ as initial guesses for a less stable $\bar{\phi}$.

Numerical results appear in Tables I and II, for operating points between $\bar{\phi} = 0.40$ and $\bar{\phi} = 0.55$, for $n=1$ and 2. Also shown for comparison in these tables are parameter estimates obtained using the spectral estimation techniques described in [7] (during open-loop operation above $\bar{\phi} = 0.45$).

A portion of a typical data set appears in Figure 7, taken at $\bar{\phi} = 0.40$ for a mode number of one ($n=1$). The command is a band-limited pseudo-random binary signal of magnitude 10° on each channel of the input vector $[r_1 \ r_2]_n^T$. The bandwidth of the input is limited to $\omega = 1.1$ (50 Hz), which is about five times the natural frequency (ω_{n1}) of the system. The actual IGV deflections, $[u_1 \ u_2]_n^T$, are responding to both this command

and the feedback signal, as shown in Figure 4 and in equation (29). It is apparent from the differences between $[r_1 \ r_2]_{n=1}^T$ and $[u_1 \ u_2]_{n=1}^T$ that the feedback signal is a major part of the excitation to the system. The outputs $[y_1 \ y_2]_{n=1}^T$ are also shown in Figure 7.

An important step in a parameter identification procedure is model and parameter validation. Here we present several results which indicate that the system structure and identified parameters do in fact model the system well. The first is shown in Figure 7, where a simulation based on the parameter estimates is used to predict the values of u_k and y_k . This is not the output of a one-step-ahead predictor, which would rely on past measurements to make the prediction. Rather, it is a simulation based solely on r_k , the identified parameters for $\bar{\phi} = 0.40$, and the controller and sensor dynamics. The fit is quite good, even though the simulation is noise-free, while the experiment is not: u_k and y_k in the experiment are responding to excitation noise in the compressor. Fits of this quality can be gotten regardless of whether the data to be fit is used to get the estimates. Since the noise free simulation results are used as the instruments in the NF/RIV-AML method, Figure 7 also serves to validate that a high degree of correlation in fact exists between the instruments and the measurements.

The closed-loop IV methods (TR/RIV-AML and NF/RIV-AML) are designed to operate in a regime where the spectral estimation procedure presented in [7] gives poor results - that is, during stabilization of unstable operating points. However, closed-loop data sets can be taken at flow coefficients which are open-loop stable. Such tests can be used to verify that closed-loop IV methods properly account for the loop closure and still provide good estimates. Figure 8 shows the results of such a test. A spectral estimate (based on open-loop data, using the techniques in [7]) is compared to both a TR/RIV-AML and a NF/RIV-AML estimate (based on closed-loop data). Good agreement between the frequency responses is obtained. This agreement is important, because IV-based estimates of $G_n(s)$ not only use the estimated parameters,

but also assume a certain model structure. Since spectral estimates are parameter-free and assume no specific model structure, this comparison verifies both the parameter estimates and the model structure.

Finally, the estimates of the parameters from various methods can be compared graphically, to see if the trends with $\bar{\phi}$ are smooth. Figure 9 shows σ_1 and ω_{rs1} as a function of flow coefficient, plotting spectral, TR/RIV-AML, and NF/RIV-AML results on the same plot. Within reasonable error bands, all of the estimation methods yield the same curves.

The data presented here are a small sample of the data taken, and are intended only to demonstrate the practical applicability of the identification methods. A complete presentation of the data, together with detailed discussion of the physical significance of the parameter estimates, appears in [7], and requires a more complete description of rotating stall modeling. For this discussion, the relevant conclusions of the experiments is that the methods presented here yield consistent, accurate results, with good convergence properties and little sensitivity to the stability of the plant. Established prediction error methods, such as those provided in [10], have similar properties (for the data sets tested). These methods utilize nonlinear search schemes to minimize prediction error, instead of the least-squares type approach utilized by IV methods. Only a thorough comparison of these two approaches would allow one to judge their relative merits. Wellstead [16] also discusses a scheme for *non-parametric* estimation of forward-path transfer functions during closed-loop operation. This method would allow one to deduce the desired plant dynamics (using transfer-function fits to the non-parametric estimates [7]), if sufficient care were taken to model other contributions to the forward-path transfer function. Again, the relative merits of Wellstead's method and the method presented here can only be determined by a thorough comparison.

4 Conclusions

By combining various extensions to the basic instrumental variable approach, a scheme for estimating parameters in an unstable system operating closed-loop has been developed. This scheme was successfully applied to a model for the distributed dynamics of an experimental axial compressor. Thus the usefulness of the procedure and the validity of the model were both verified experimentally.

5 Acknowledgements

This work was supported by U.S. Air Force Office of Scientific Research, Dr. J. M. McMichael, Technical Monitor, and by the Office of Naval Research, Dr. R. J. Hansen, Technical Monitor. This support is gratefully acknowledged.

6 References

1. Kerrebrock, J. L., Aircraft Engines and Gas Turbines, The MIT Press, Cambridge, Massachusetts, 1977, pp. 154-155.
2. Greitzer, E. M., "Review - Axial Compressor Stall Phenomena," ASME J. of Fluids Eng., vol. 102, 1980, pp. 134-151.
3. Greitzer, E. M., "Surge and Rotating Stall in Axial Flow Compressors; Part I: Theoretical Compression System Model," Trans. ASME, vol. 98, 1976, pp. 190-198.
4. Moore, F. K., "A Theory of Rotating Stall of Multistage Compressors," ASME J. of Eng. for Power, vol. 106, 1984, p. 313.
5. Hynes, T. P. and Greitzer, E. M., "A Method for Assessing Effects of Inlet Flow Distortion on Compressor Stability," ASME J. of Turbomachinery, vol. 109, pp. 371-379,
6. Epstein, A. H., Ffowcs-Williams, J. E., and Greitzer, E. M., "Active Suppression of Aerodynamic Instabilities in Turbomachines," J. Propulsion, Vol. 5., No. 2, pp. 204-211.
7. Paduano, J. D., "Active Control of Rotating Stall in Axial Compressors", Ph.D. Thesis, MIT. Dept. of Aeronautics and Astronautics, February, 1992. Also available as MIT Gas Turbine Laboratory Report #208, March 1992.

8. Paduano, J., Epstein, A. H., Valavani, L., Longley, J. P., Greitzer, E. M., and Guennette, G. R., "Active Control of Rotating Stall in A Low Speed Axial Compressor," ASME Paper 91-GT-88, Proceedings, ASME International Gas Turbine Conference, Orlando, June 1991. To be published in ASME Journal of Turbomachinery.
9. Åström, K. J., and Wittenmark, B., Computer Controlled Systems - Theory and Design, Prentice-Hall, New Jersey, 1984.
10. Ljung, L., System Identification - Theory for the User, Prentice-Hall, New Jersey, 1987.
11. Young, P., Recursive Estimation and Time-Series Analysis, Springer-Verlag, 1984.
12. Wang, H., and Cao, D., "Two Instrumental Variable Methods for Closed Loop System Identification," Identification and System Parameter Estimation 1988, Selected Papers from the Eighth IFAC/IFORS Symposium, Beijing, August 1988, p. 543.
13. Söderström, T., Stoica, P., and Trulson, E., "Instrumental Variable Methods for Closed Loop Systems," Automatic Control - World Congress 1987 Selected Papers from the 10th Triennial World Congress of IFAC, Munich, July 1987, pp. 363-368.
14. Oppenheim, A. V., and Schafer, R. W., Discrete-Time Signal Processing, Prentice-Hall, New Jersey, 1989.
15. Wellstead, P. E., "Non-Parametric Methods of System Identification," Automatica, Vol. 17, No. 1, pp 55-69, 1981.

Table I - Parameter Estimates, n=1

Spectral Estimates (from [7])

$\bar{\phi}$	σ	ω_{ts}	b_r	b_i	g_i
0.475	-6.27	67.29	-4.81	2.03	-0.055
0.500	-15.58	71.71	-5.55	2.18	-0.061
0.525	-26.50	65.98	-5.70	1.05	-0.059
0.550	-36.37	50.81	-5.57	-0.84	-0.059

NF/RIV-AML Estimates

$\bar{\phi}$	σ	ω_{ts}	b_r	b_i	g_i
0.400	5.50	52.27	-3.00	1.01	-0.029
0.425	0.61	56.99	-3.10	1.36	-0.033
0.450	-1.62	63.54	-3.56	1.49	-0.039
0.475	-4.96	66.42	-3.91	2.14	-0.044
0.500	-13.50	67.20	-4.75	2.14	-0.050
0.525	-26.27	60.36	-4.90	1.17	-0.051

TR/RIV-AML Estimates

$\bar{\phi}$	σ	ω_{ts}	b_r	b_i	g_i
0.400	4.95	55.15	-3.19	0.90	-0.036
0.425	1.26	59.86	-2.80	0.80	-0.035
0.450	-1.79	63.32	-3.69	1.50	-0.038
0.475	-4.88	68.53	-3.97	2.03	-0.044

Table II - Parameter Estimates, n=2

Spectral Estimates (from [7])

$\bar{\phi}$	σ	ω_{ts}	b_r	b_i	g_i
0.475	-32.46	157.37	-11.57	-0.54	-0.048
0.500	-52.38	168.26	-12.68	-1.28	-0.050
0.525	-77.44	188.59	-15.93	-2.16	-0.060
0.550	-93.17	181.28	-16.36	-3.76	-0.065

NF/RIV-AML Estimates

$\bar{\phi}$	σ	ω_{ts}	b_r	b_i	g_i
0.400	-4.40	137.44	-8.07	0.91	-0.038
0.425	-13.42	144.45	-9.12	0.62	-0.042
0.450	-27.63	152.40	-10.27	0.13	-0.044
0.475	-36.97	157.67	-11.24	0.01	-0.047
0.500	-49.78	159.42	-11.36	-0.22	-0.044
0.525	-75.22	152.07	-11.34	-2.16	-0.041

TR/RIV-AML Estimates

$\bar{\phi}$	σ	ω_{ts}	b_r	b_i	g_i
0.375	0.91	123.16	-7.28	0.63	-0.057
0.400	-3.42	137.27	-7.90	1.01	-0.039
0.425	-13.31	144.14	-8.91	0.60	-0.041
0.450	-24.81	151.65	-9.94	0.17	-0.043
0.475	-37.48	158.56	-11.27	-0.25	-0.047

Figure 1 - Typical pressure rise characteristic for an axial compressor

Figure 2 - Schematic of the active control research compressor. A- inlet duct, B- IGVs, C- compressor, D- exit duct, E- throttle

Figure 3 - Hardware components of the active control research compressor

Figure 4 - Feedback loop layout and notation

Figure 5 - Example of different impulse responses associated with the same transfer function. The inverse Z-transform of $A(z)$ can be computed over any of the three regions of convergence (ROCs) shown (I, II, or III). The impulse response in each case is the sum of the truncated exponentials at right.

Figure 6 - Pressure rise characteristic for the active control research compressor

Figure 7 - Results of a typical identification run. Solid lines are experimental data, dashed lines are predictions based on the parameter estimates (noise-free simulation) $\bar{\phi} = 0.40$.

Figure 8 - Comparison of spectral estimation results [7] and IV parameter identification results. Solid line is an empirical transfer function estimate, dashed line is a transfer function derived from parameters which were identified during closed-loop operation. $\bar{\phi} = 0.475$.

Figure 9 - Parameter variations with flow coefficient. o--Open-loop parameter estimates (from [7]); *--TR/RIV-AML results; x--NF/RIV-AML results.

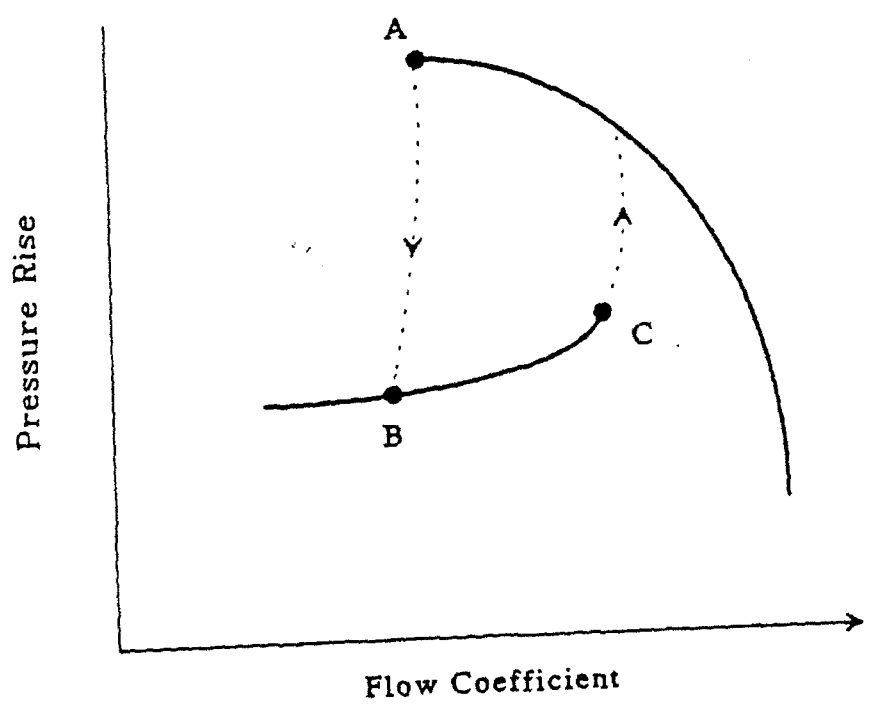


Figure 1

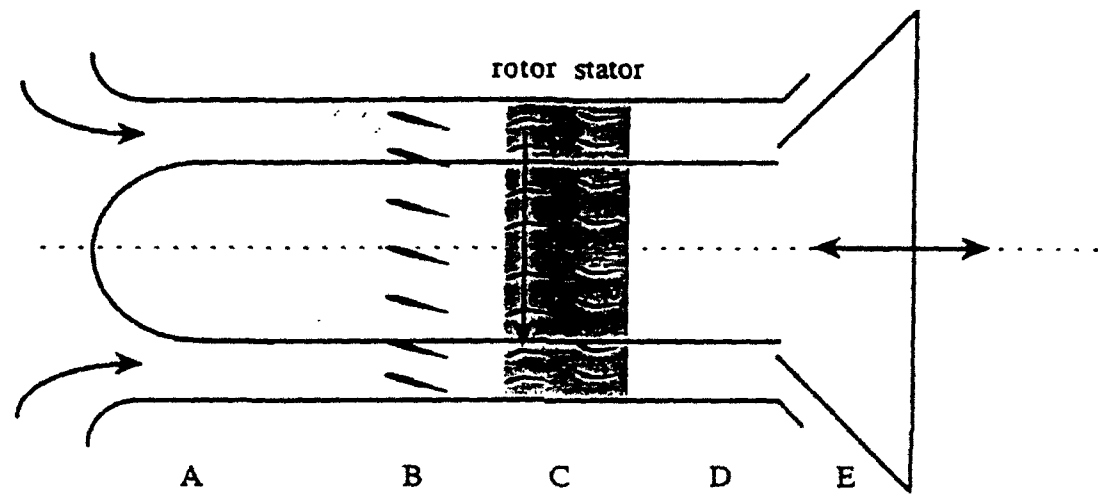


Figure 2

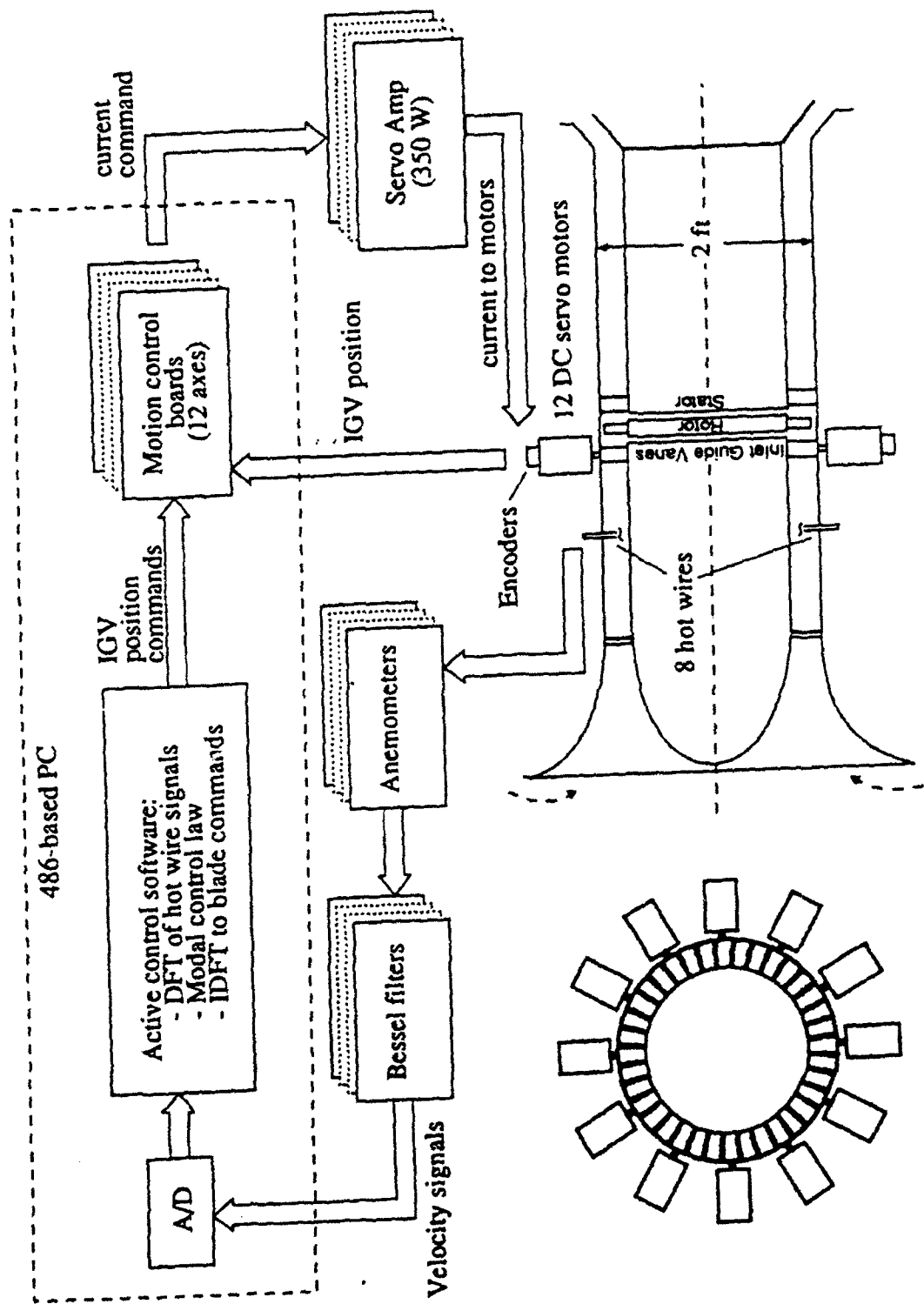


Figure 3

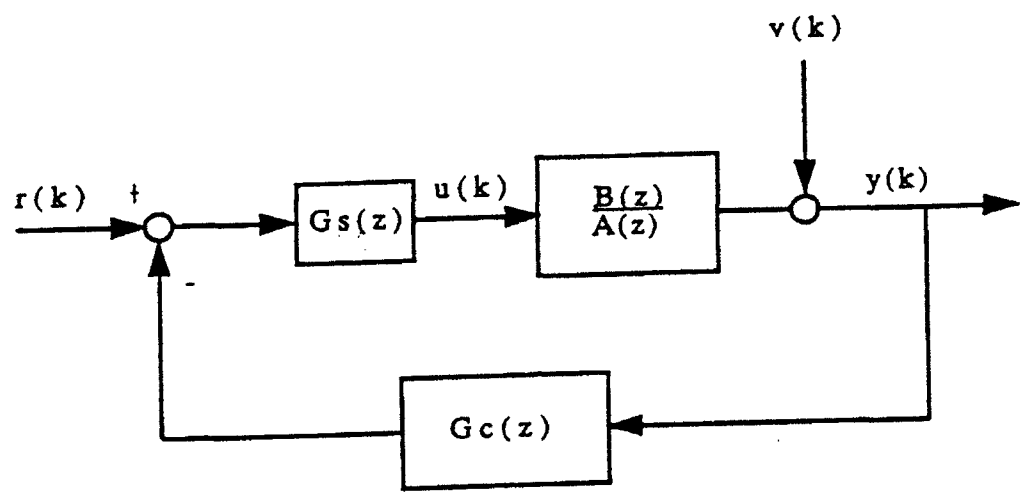


Figure 4

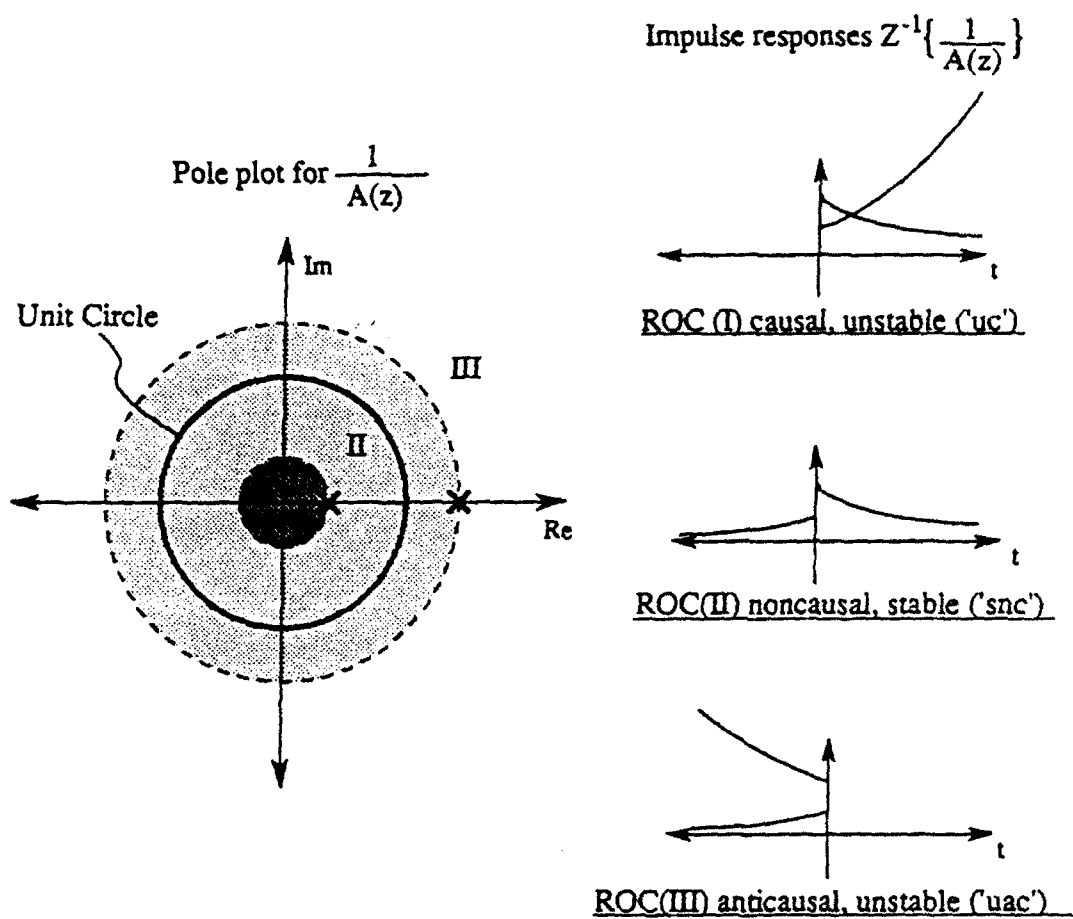


Figure 5 - Example of different impulse responses associated with the same transfer function. The inverse Z-transform of $A(z)$ can be computed over any of the three regions of convergence (ROCs) shown (I, II, or III). The impulse response in each case is the sum of the truncated exponentials shown at right.

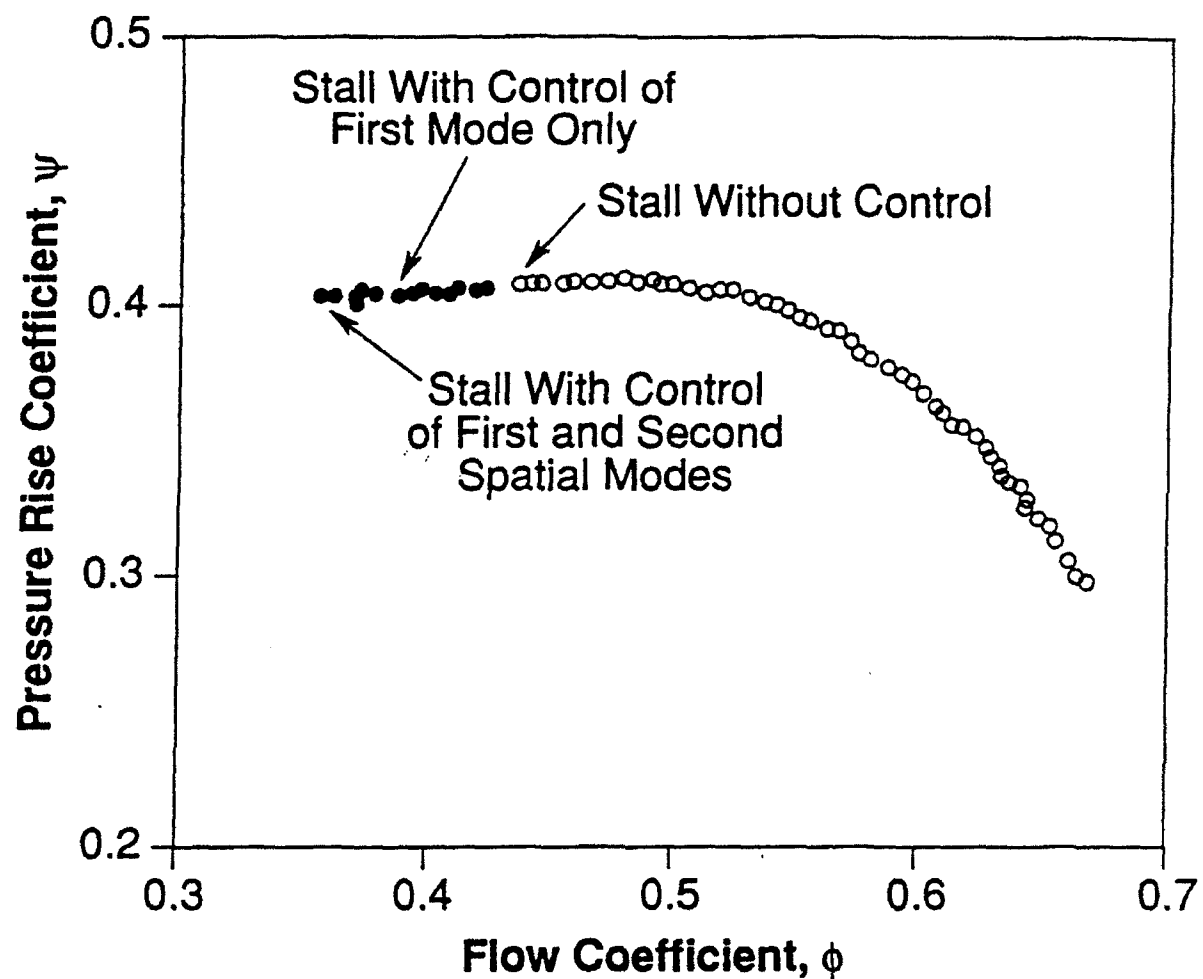


Figure 6

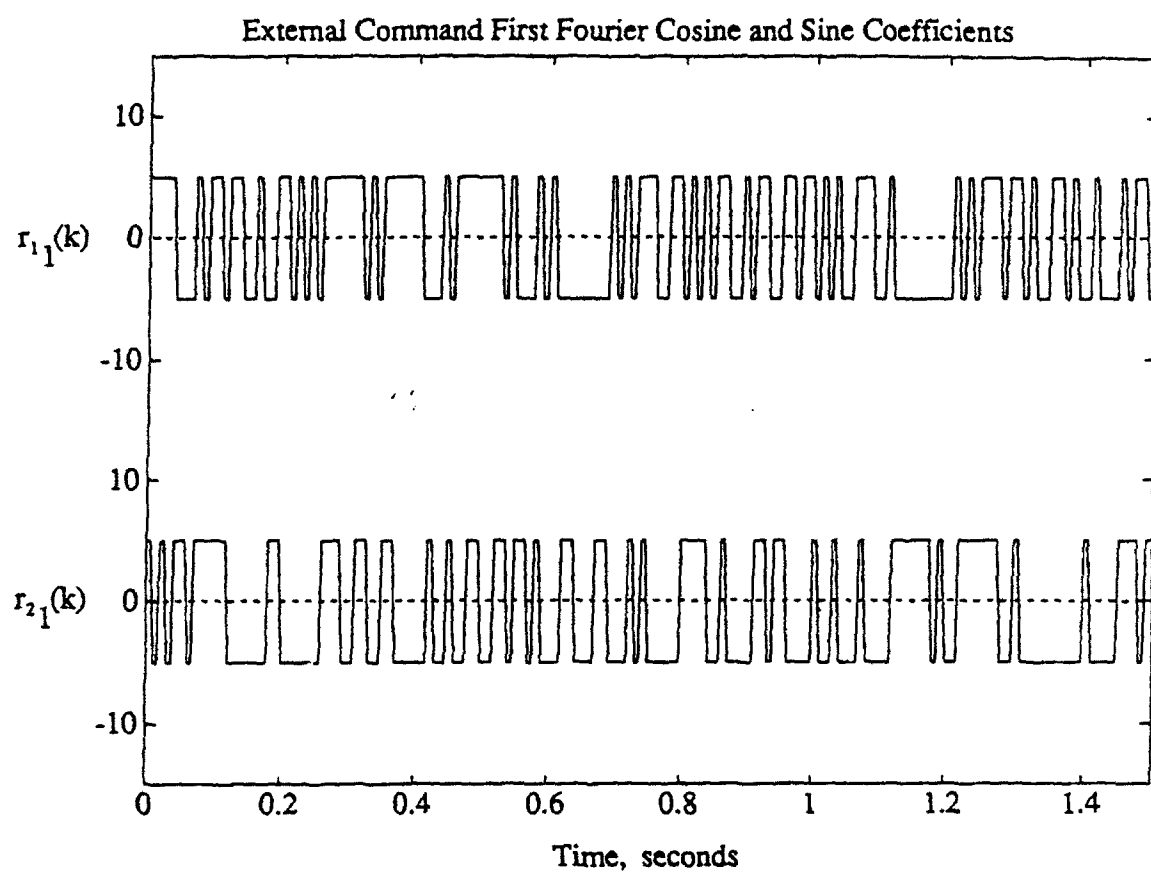
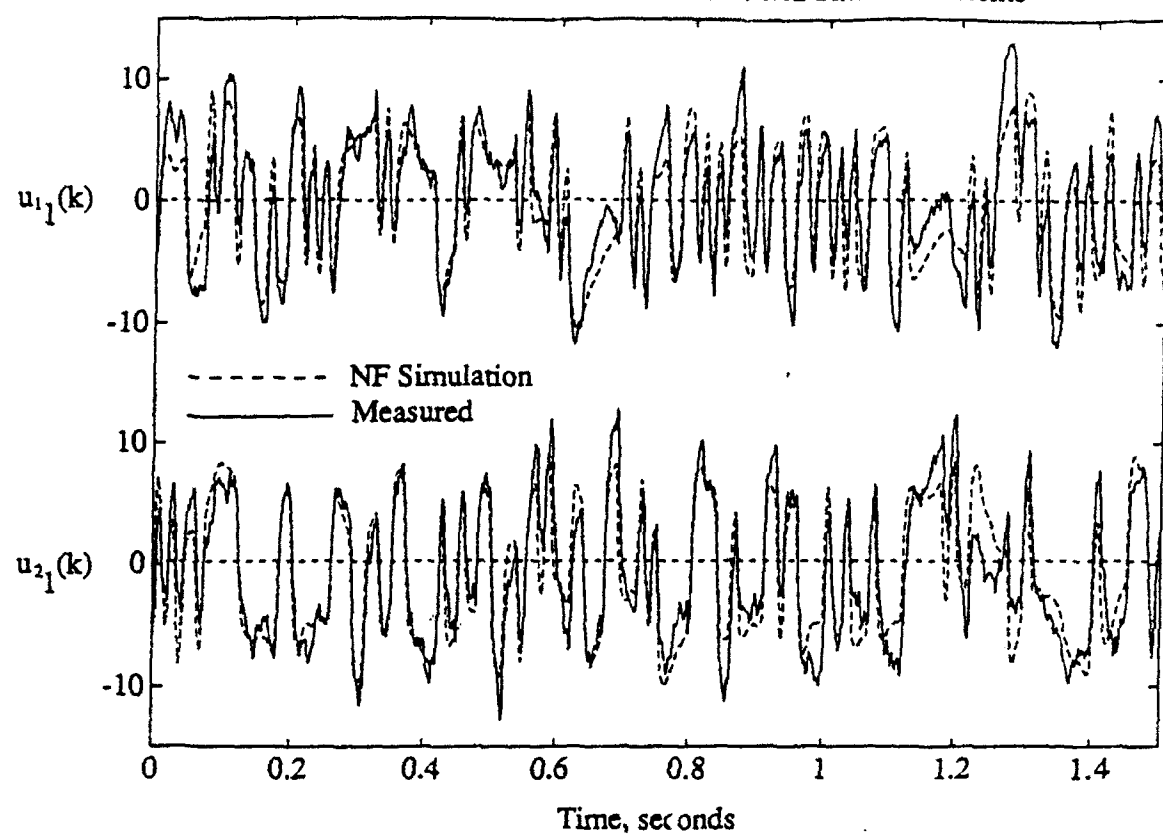


Figure 7 (first part of 3 parts)

IGV Deflection First Fourier Cosine and Sine Coefficients



Velocity Perturbation First Fourier Cosine and Sine Coefficients

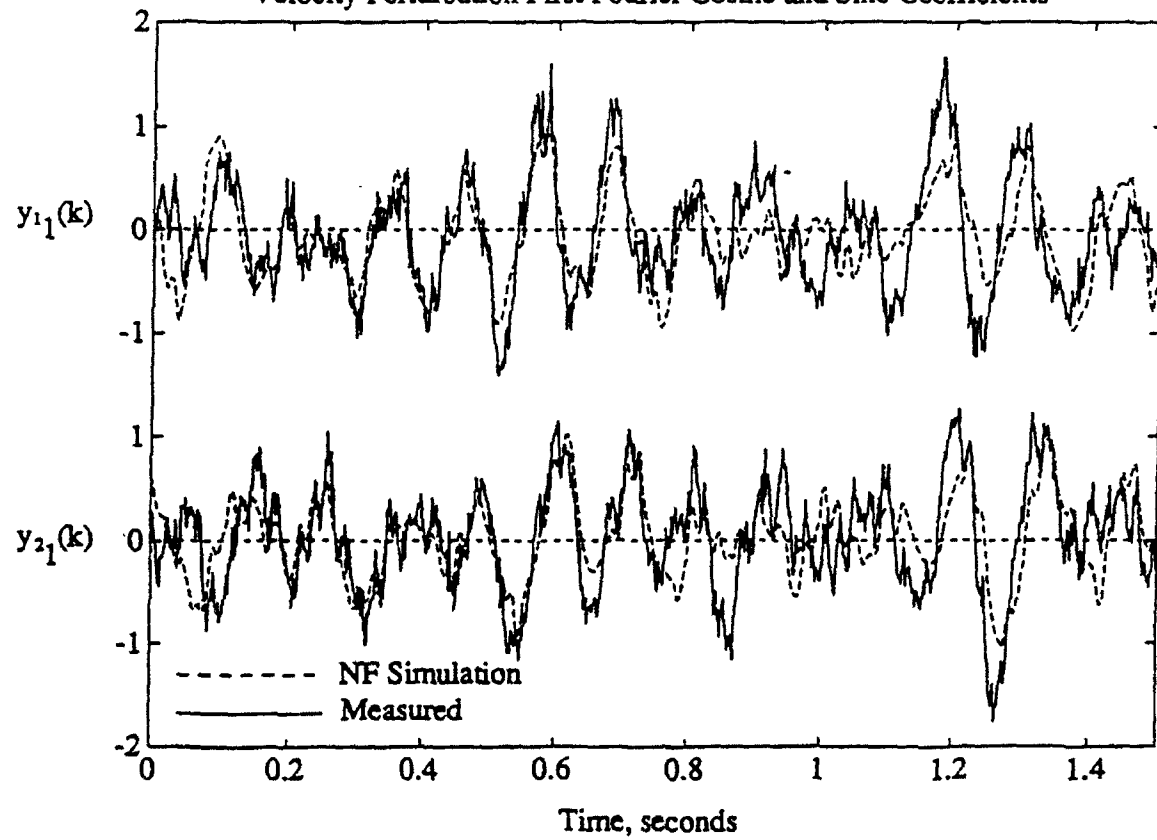


Figure 7 (second and third part of 3 parts)

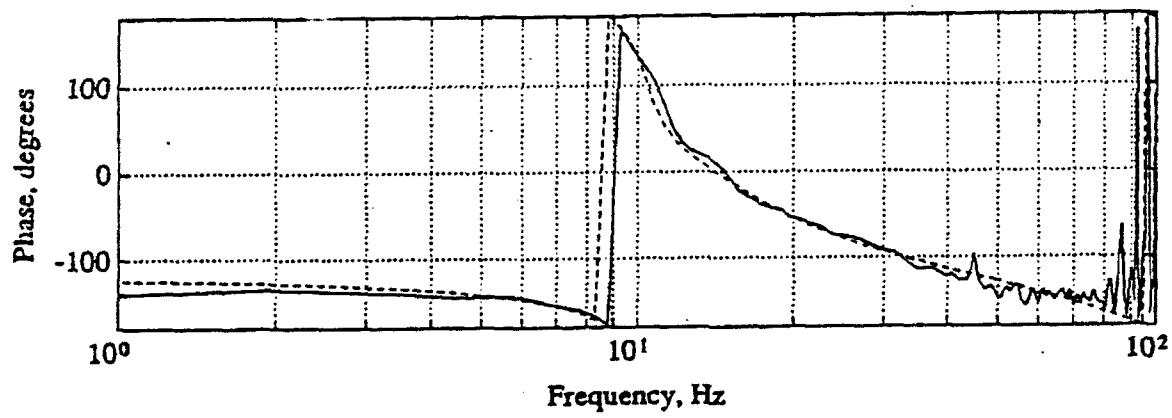
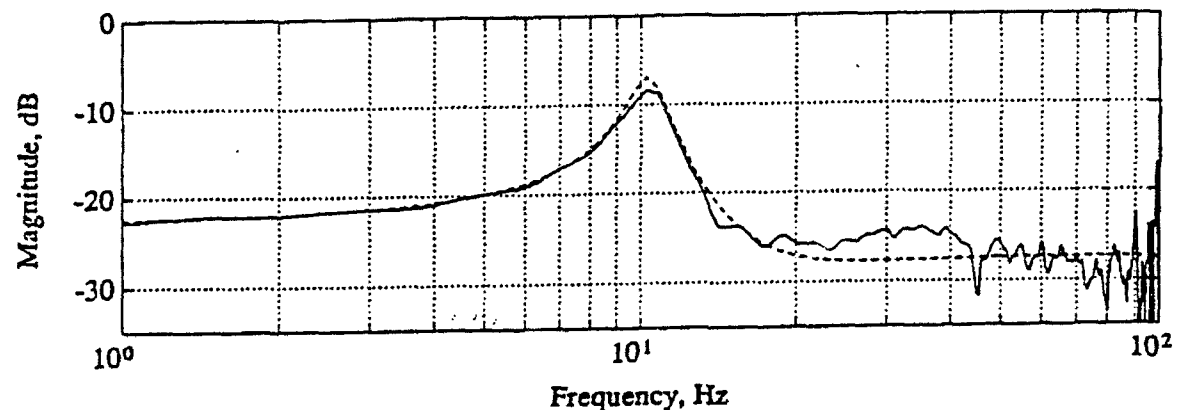


Figure 8

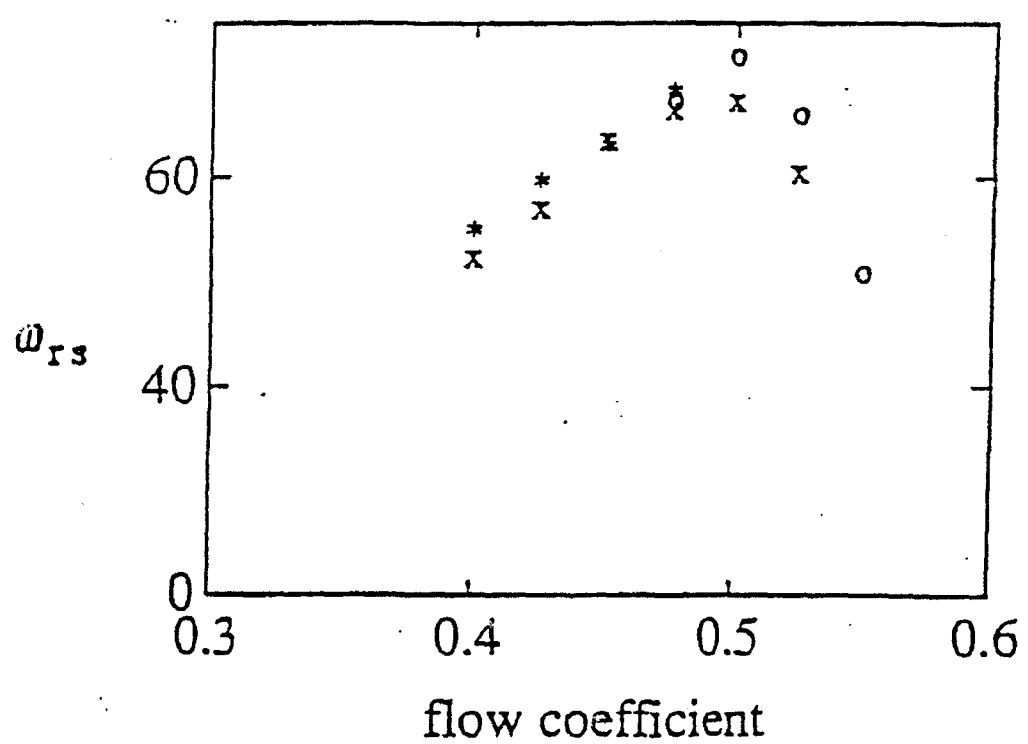
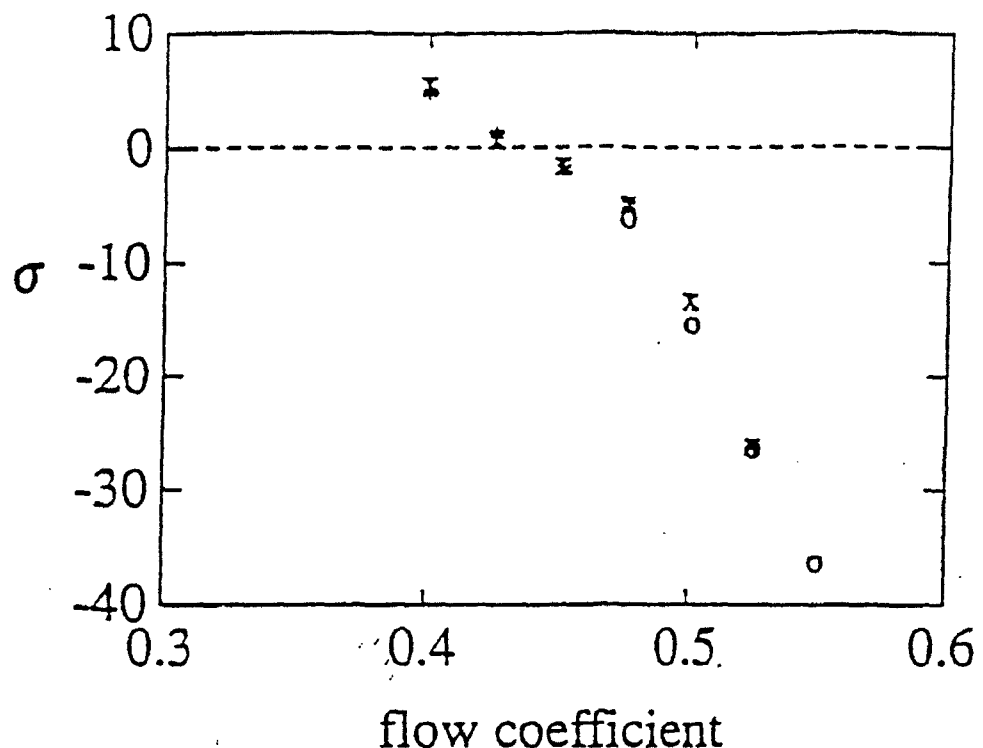


Figure 9

Appendix

Frequency windows typically used in spectral analysis identification procedures are characterized by the following:

$$\int_{-\pi}^{\pi} W\gamma(\xi) d\xi = 1 \quad ; \quad \int_{-\pi}^{\pi} \xi W\gamma(\xi) d\xi = 0 \quad ; \quad \int_{-\pi}^{\pi} \xi^2 W\gamma(\xi) d\xi = M(\gamma)$$

$$\int_{-\pi}^{\pi} |\xi|^3 W\gamma(\xi) d\xi = C_3(\gamma) \quad ; \quad \int_{-\pi}^{\pi} W^2\gamma(\xi) d\xi = \frac{1}{2\pi} \bar{W}(\gamma)$$

A Hamming window is defined as follows:

$$2\pi W\gamma(\omega) = \frac{1}{2} D\gamma(\omega) + \frac{1}{4} D\gamma\left(\omega - \frac{\pi}{\gamma}\right) + \frac{1}{4} D\gamma\left(\omega + \frac{\pi}{\gamma}\right)$$

where $D\gamma(\omega) = \frac{\sin\left(\gamma + \frac{1}{2}\right)\omega}{\sin \frac{\omega}{2}}$

Note: Large γ gives small bias but high variance for the estimate, while the converse is true for wide windows.

V. EVALUATION OF ALTERNATE CONTROL APPROACHES



The Society shall not be responsible for statements or opinions advanced in papers or in discussion at meetings of the Society or of its Divisions or Sections, or printed in its publications. Discussion is printed only if the paper is published in an ASME Journal. Papers are available from ASME for fifteen months after the meeting.

Printed in USA. © 1982 ASME

Evaluation of Approaches to Active Compressor Surge Stabilization

J. S. SIMON, L. VALAVANI, A. H. EPSTEIN and E. M. GREITZER

Gas Turbine Laboratory
Massachusetts Institute of Technology
Cambridge, MA 02139

ABSTRACT

Recent work has shown that compression systems can be actively stabilized against the instability known as surge, thereby realizing a significant gain in system mass flow range. Ideally, this surge stabilization requires only a single sensor and a single actuator connected by a suitable control law. Almost all research to date has been aimed at proof of concept studies of this technique, using various actuators and sensor combinations. In contrast, the work reported herein can be regarded as a step towards developing active control into a practical technique. In this context, the paper presents the first systematic definition of the influence of sensor and actuator selection on increasing the range of stabilized compressor performance. The results show that proper choice of sensor as well as actuator crucially affects the ability to stabilize these systems, and that, overall, those actuators which are most closely coupled to the compressor (as opposed to the plenum or throttle) appear most effective. In addition, the source of the disturbances driving the system (for example, unsteady compressor pressure rise or unsteady combustor heat release) has a strong influence on control effectiveness, as would be expected for a controls problem of this type. This paper both delineates general methodologies for the evaluation of active compressor stabilization strategies and quantifies the performance of several approaches which might be implemented in gas turbine engines.

NOMENCLATURE

a	speed of sound
A_c	compressor flow through area
A_w	area of movable plenum wall
B	compressor stability parameter; $B = (U_T/2a) \sqrt{V/(A_c \bar{V})}$
C_p	specific heat at constant pressure
C_v	specific heat at constant volume
E	energy of gas in plenum
E^*	dimensionless energy of gas in plenum; $E^* = C_v T_p / \rho_a V_p C_v T_a$
K	proportional gain
L	equivalent length; $L = \int_0^x A_c / A(x) dx$
m	mass of gas in plenum

m^*	dimensionless mass of gas in plenum; $m^* = \rho_p V_p / \rho_a \bar{V}$
m_C	dimensionless slope of compressor speed line; $m_C = \partial \Phi_c / \partial \psi$
m_{Ce}	dimensionless slope of equivalent compressor speed line formed by compressor in series with close-coupled valve; $m_{Ce} = \partial / \partial \psi (\Psi_c - \Psi_\infty)$
m_T	dimensionless slope of throttle pressure drop versus flow characteristic; $m_T = 1 / (\partial \Phi_T / \partial \psi)$
m_{Te}	dimensionless slope of equivalent throttle characteristic for parallel combination of throttle and plenum bleed valve; $m_{Te} = 1 / (\partial (\Phi_T + \Phi_b) / \partial \psi)$
M_T	impeller tip Mach number; $M_T = U_T / a$
P	absolute pressure
P_p	plenum pressure ratio; $P_p^* = P_p / P_a$
Q	heat release rate
Q^*	dimensionless heat release rate; $Q^* = Q / P_a U_T A_c C_p T_a$
R	gas constant for ideal gas; $R = C_p - C_v$
s	Laplace transform variable
ΔT_{oc}	total temperature rise across compressor
ΔT_{oc}^*	dimensionless total temperature rise across compressor; $\Delta T_{oc}^* = \Delta T_{oc} / T_a$
t	time
t_w	first order constant for movable plenum wall
t_w^*	dimensionless first order lag time constant for movable plenum wall; $t_w^* = t_w \omega_H$
u	control input signal
U_T	impeller tip speed
V_w	velocity of movable wall
V	slope of valve characteristic; $V = \partial \Phi / \partial \alpha$
V^*	dimensionless plenum volume; $V^* = V / \bar{V}$
V_c	dimensionless commanded rate of change of plenum volume
W	dimensionless term relating changes in plenum volume to plenum pressure; $W = 2P_p / M_T^2 P_a$
x	vector of system states
α_b	bleed valve fraction open
α_{cc}	close-coupled valve fraction open
α_d	desired (commanded) valve fraction open

Presented at the International Gas Turbine and Aeroengine Congress and Exposition
Cologne, Germany June 14, 1982

This paper has been accepted for publication in the Transactions of the ASME
Discussion of it will be accepted at ASME Headquarters until September 30, 1982

γ	ratio of specific heats
ζ	damping ratio
ξ	dimensionless rate of change of plenum volume; $\xi = A_w v_w / U_T A_c$
ρ	density
τ	dimensionless time; $\tau = \omega_H t$
ϕ	flow coefficient; $\phi = \dot{m} / \rho_a U_T A_c$
Φ	function giving dimensionless flow through valve as function of pressure and valve area
ψ	plenum pressure coefficient; $\psi = (p_p - p_a) / (\frac{1}{2} \rho_a U_T^2)$
ψ_{oj}	mass injector supply pressure coefficient; $\psi_{oj} = (p_{oj} - p_a) / (\frac{1}{2} \rho_a U_T^2)$
ψ_{cc}	dimensionless total pressure drop across close-coupled valve. $\psi_{cc}(\phi, \alpha_{cc})$
Ψ_c	dimensionless pressure rise vs. flow characteristic of compressor, $\Psi_c(\phi)$
$\Delta\Psi_d$	downstream injector characteristic, $\Psi_d = \Psi_{d2} - \Psi_{oj}$
$\Delta\Psi_u$	upstream injector characteristic, $\Psi_u = \Psi_{u1} - \Psi_{oj}$
ω_H	Helmholtz frequency;
ω_c	filter cut-off frequency

Superscripts

\wedge	perturbation quantity
$\dot{}$	first derivative with respect to time
$\ddot{}$	second derivative with respect to time
$\bar{}$	time mean quantity

Subscripts

a	ambient
b	bleed valve
c	compressor
cc	close-coupled valve
j	injector jet
p	plenum
T	throttle or impeller tip
1	compressor duct inlet
2	compressor duct downstream of injector
0	total

INTRODUCTION

The stable operating regime of a compressor installed in a jet engine (or any pumping system) is often limited by the onset of large amplitude fluctuations in mass flow and pressure rise known as surge. Due to the loss of performance and thrust, as well as possible mechanical and thermal loads, surge is an important factor in compressor design and operation.

Surge is understood to be the lowest order natural oscillatory mode of the compression system (Greitzer, 1981) and experiments show that small amplitude, linear disturbances can quickly grow into large amplitude, fully developed surge (Fink, 1991). Epstein, Ffowcs Williams, and Greitzer (1989) proposed that surge could be prevented by actively damping these disturbances while their amplitude was low. In this approach, the unsteady perturbations are directly influenced and the mean operating parameters are virtually unaltered. Epstein et al. gave some discussion of the mechanism of this stabilization and commented that various feedback schemes actually differ in how the instability is suppressed.

Active stabilization has now been demonstrated experimentally for centrifugal compressors by several investigators, for example, Ffowcs Williams and Huang (1989) and Pinsley et al. (1991). Gysling et al. (1991) also showed that significant gains in mass flow range can be realized using tailored structure to provide the

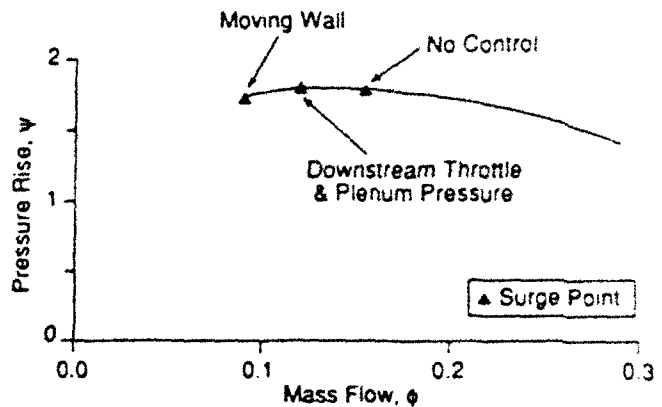


Fig. 1: Centrifugal compressor flow range using different control schemes (data of Pinsley et al. (1991), Gysling et al. (1991), and Simon (1992)).

feedback path. The studies also showed that a lumped parameter model of the pumping system captured the essential dynamics of the surge process in the machines investigated, and this will be the approach taken here.

For example, Fig. 1 shows experimental and analytical results taken from Pinsley et al. (1991) and Gysling et al. (1991), compared to the results for no control. All the results are for a centrifugal turbocharger at a pressure ratio of roughly two. The surge point without control as well as with feedback is also indicated. An active compressor stabilization system conceptually consists of sensors to detect fluid disturbances within the compression system, actuators to introduce desired perturbations, and a suitable control law connecting the two. Theoretically, surge requires only a single sensor and actuator, with many choices available for their type and location. Sensors may measure pressure, mass flow, velocity, or temperature within the compressor duct upstream or downstream of the compressor, in the plenum, or at the throttle. Similarly, there are many methods to introduce unsteady fluid perturbations: varying throttle area, moving a plenum or duct wall, introducing or bleeding off mass flow, varying the heat addition in the plenum (when it is a combustor), as well as introducing a variable throttle between the compressor and plenum, to name a few. A representative list of sensing and actuation options is shown in Table 1.

TABLE 1
SENSING AND ACTUATION OPTIONS CONSIDERED

Actuation	Sensing
Injection in compressor duct	Inlet mass flow
Valve close-coupled to compressor	Plenum pressure
Plenum bleed valve	Compressor face P_{total}
Plenum heat addition	Compressor face P_{static}
Variable plenum volume	Plenum temperature
Variable inlet geometry	
Fast inlet guide vanes	
Tangential inlet injection	
Auxiliary compressor stage	
Plenum mass injection	
Inlet duct bleed	

The central tenet of this paper is to show that selection of sensor and actuator type and location is a critical factor in determining the effectiveness and practicality of an active stabilization system. Because of the practical interest in this question, the paper presents a methodology to compare different implementation alternatives, as well as carries out this comparison for a number of candidate strategies. Describing the performance of such an active compressor surge stabilization system is complex in that there are many sensor-actuator pairs conceivable. When coupled to the compressor, each forms a different physical system, with differing dynamic behavior, physical limitations, and overall performance. The steps included in the comparison of different control strategies are thus as follows:

- Analytical models of specific systems are developed to elucidate the relative performance sensitivities to non-dimensional system parameters.
- Numerical calculations are carried out to quantify the limits to control of various sensor-actuator pairs when connected by a simple proportional control law.
- Optimal control theory is used to evaluate the physical limits to control given perfect measurements of the system state.

It may be useful here to mention two factors that bear on the overall viewpoint and scope of the present work. First, we note that the general problem of actuator/sensor selection has been considered by a number of researchers in other applications (see, for example, Morris and Skelton, 1989; Schmitendorf, 1984; Muller and Weber, 1972). These previous approaches provide comparisons based upon somewhat abstractly defined performance indices. For the present purposes, it was thought useful to obtain quantitative comparisons in a manner which is more closely related to the concepts and thinking of the turbomachinery community. The methodology followed here was developed to this end.

Second, the goals of this work are to make clear the large influence that implementation (sensor-actuator selection) has on the effectiveness of active compressor control and to elucidate physical limitations on active control. We thus do not consider all possible active control systems but select those which may be most readily implemented in various gas turbine systems.

COMPRESSOR SYSTEM MODELLING FOR CONTROL

We use a standard lumped parameter model of compression system dynamics (Greitzer, 1981) following the geometry of Fig. 2a. This model incorporates the following assumptions: one-dimensional, incompressible flow in the compressor duct; compressor considered as a quasi-steady actuator disk; pressure in the plenum is spatially uniform but varying in time and flow velocity is negligible; throttle behavior is quasi-steady. The temporal (τ) behavior of the non-dimensional plenum pressure rise (ψ) and non-dimensional mass flow (or flow coefficient) (ϕ) can then be described as:

$$\frac{d\phi}{d\tau} = B (\Psi_c(\phi) - \psi) \quad (1a)$$

$$\frac{d\psi}{d\tau} = \frac{1}{B} (\phi - \Phi_T(\psi)) \quad (1b)$$

for the system without active control. Equation (1a) expresses a one-dimensional momentum balance in the compressor duct. Equation (1b) represents a mass balance for the plenum. The compressor characteristic, $\Psi_c(\phi)$, gives the non-dimensional compressor pressure rise as a function of the flow coefficient, ϕ , and the throttle characteristic $\Phi_T(\psi)$, represents the throttle pressure drop. The non-dimensional quantity B , defined as $(U_T/2a) \sqrt{V/(A_c L_c)}$, can be regarded as a measure of the ratio of plenum compliance to duct inertia. B will be seen to be of considerable importance in

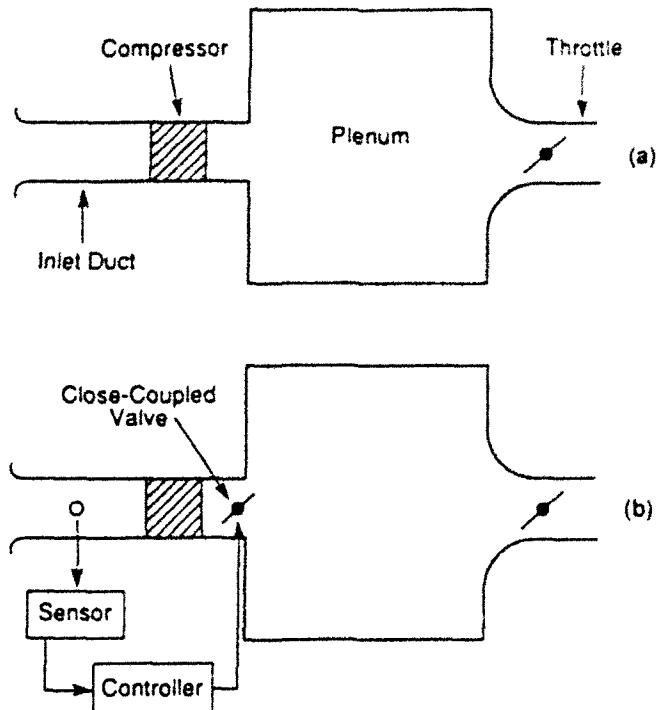


Fig. 2: Lumped parameter compression system: (a) no control; (b) with sensor in inlet and close-coupled valve actuator control system

determining control effectiveness.

To describe actively controlled systems, we must account for the influence of actuators on system performance, represent sensor measurements, and incorporate a feedback law. Each choice of sensor-actuator pair results in a distinct system whose dynamics can differ widely. Because the detailed derivation of the system equations is fairly lengthy, we shall derive the characteristic equations for one particular system in order to illustrate the idea, and then only present results for the other systems.

Suppose a total pressure probe at the compressor inlet is used as the sensor, and a valve which modulates the compressor exit area is selected for the actuator. This actuator will be referred to as the *close-coupled valve* (Fig. 2b). The basic model of Fig. 2a must be modified to include the valve pressure drop in the compressor duct momentum balance. Because the instantaneous mass flow through the compressor is the same as the flow through the close-coupled valve, the equations that describe the system are now:

$$\frac{d\phi}{d\tau} = B (\Psi_c(\phi) - \psi - \Psi_{cc}(\phi, \alpha_{cc})) \quad (2a)$$

$$\frac{d\psi}{d\tau} = \frac{1}{B} (\phi - \Phi_T(\psi)) \quad (2b)$$

Comparison with Eqs. (1) shows that the original system has been modified by the introduction of a *control term*, $\Psi_{cc}(\phi, \alpha_{cc})$, which represents the pressure drop through the close-coupled valve as a function of flow through the valve, ϕ , and valve fraction open, α_{cc} . To include the sensor measurement in the model, the following *output equation* is formed:

$$\psi_{02} = \Psi_{cc}(\phi, \alpha_{cc}) - \Psi_c(\phi) + \psi.$$

TABLE 2
OPEN LOOP TRANSFER FUNCTIONS

(Numerator shown in Table; Denominator, D(s), given below)

Actuator Sensor	Close-Coupled Valve	Plenum Bleed Valve	Moveable Wall
Compressor Mass Flow	$\frac{BT \left(s + \frac{1}{Bm_{Te}} \right)}{D(s)}$	$\frac{V}{D(s)}$	$\frac{WB}{D(s)}$
Plenum Pressure	$\frac{T}{D(s)}$	$\frac{-V (s - Bm_{Ce})}{B D(s)}$	$\frac{-W (s - Bm_{Ce})}{D(s)}$
Compressor Face Total Pressure	$\frac{-Ts \left(s + \frac{1}{Bm_{Te}} \right)}{D(s)}$	$\frac{-Vs}{B D(s)}$	$\frac{-Ws}{D(s)}$
Compressor Face Static Pressure	$\frac{-T \left(s^2 + \left(2\phi B + \frac{1}{Bm_{Te}} \right) s + \frac{2\phi}{m_{Te}} \right)}{D(s)}$	$\frac{-Vs}{B D(s)}$	$\frac{-Ws}{D(s)}$

$$D(s) = s^2 + \left(\frac{1}{Bm_{Te}} - Bm_{Ce} \right) s + \left(1 - \frac{m_{Ce}}{m_{Te}} \right)$$

which expresses the total pressure, ψ_{02} , at the compressor face, as a function of the state variables, ϕ , V , and the input variable α_{cc} .

For small perturbations from equilibrium which we denote as $\hat{\phi}$ and \hat{V} , the system dynamics and measurement equation can be approximated by the linear system

$$\frac{d}{dt} \begin{bmatrix} \hat{\phi} \\ \hat{V} \end{bmatrix} = \begin{bmatrix} B \left(\frac{\partial \psi_{02}}{\partial \phi} - \frac{\partial \psi_{02}}{\partial \hat{\phi}} \right) & -B \\ \frac{1}{B} & -\frac{1}{B} \left(\frac{\partial \phi_T}{\partial V} + \frac{\partial \phi_B}{\partial V} \right) \end{bmatrix} \begin{bmatrix} \hat{\phi} \\ \hat{V} \end{bmatrix} + \begin{bmatrix} B \frac{\partial \psi_{02}}{\partial \alpha_{cc}} \\ 0 \end{bmatrix} \hat{\alpha}_{cc} \quad (3a)$$

$$\hat{\psi}_{02} = \left[\left(\frac{\partial \psi_{02}}{\partial \phi} - \frac{\partial \psi_{02}}{\partial \hat{\phi}} \right) - 1 \right] \begin{bmatrix} \hat{\phi} \\ \hat{V} \end{bmatrix} + \begin{bmatrix} \frac{\partial \psi_{02}}{\partial \alpha_{cc}} \end{bmatrix} \hat{\alpha}_{cc} \quad (3b)$$

which results from retaining only first order terms in a standard Taylor series expansion about equilibrium. In a similar fashion, linear time domain models may be obtained for other sensor-actuator pairs.

The behaviors of systems with different sensor-actuator pairing are most clearly revealed from their *transfer functions*, which are defined as the ratio of the Laplace transformed system output (sensor signal, ψ_{02}) to input (actuator motion, α_{cc}). For the present example, the transfer function, $G(s)$, is

$$G(s) \triangleq \frac{\psi_{02}(s)}{\alpha_{cc}(s)} = \frac{m_{Ce} BT \left(s + \frac{1}{Bm_T} \right)}{s^2 + \left(\frac{1}{Bm_T} - Bm_{Ce} \right) s + \left(1 - \frac{m_{Ce}}{m_T} \right)} \quad (4)$$

In Eq. (4), s is the Laplace transform variable, $m_{Ce} = \partial(\psi_c - \psi_{cc})/\partial\phi$ is defined as the equivalent compressor slope for the combined valve and compressor; $m_T = 1/(\partial\phi_T/\partial V)$ is the slope of the throttle pressure

drop versus flow characteristic, and $T = -\partial\psi_{cc}/\partial\alpha_{cc}$ relates changes in valve area to valve pressure drop.

Open loop transfer functions for the different actuators and four different sensors illustrated in Fig. 3 are presented in Table 2. The transfer functions for all the sensor-actuator pairs in Table 2 have the same denominator polynomial (denoted as $D(s)$ and given below the table), but the numerator polynomials differ so that the inherent differences are captured by the latter. For generality, the expressions given in Table 2 use the equivalent throttle slope m_{Te} of a throttle in parallel with a bleed valve. If no bleed valve is used, $m_T = m_{Te}$.

Feedback Stabilization

For feedback stabilization, one measures the system output, compares it with some desired reference level, determines the error and computes an input signal (command to the actuator) based upon this error to drive the error towards zero. If this can be successfully accomplished, the system output will be maintained close to the desired value, which normally implies that the system is stable*. The relationship between the system error signal and the actuator command is called the *control law*, and may be dynamic (involving differential equations) or static (using only algebraic relationships). In this section, we will use the simplest control law, a proportional relationship between input and output, to elucidate effects of actuator and sensor selection, but in a subsequent section, we will examine the impact of the form of the control law.

* It is possible, in special cases, for a system to have an instability which cannot be seen in a particular sensor's output. However, if a system is *detectable* (Kwakernaak and Sivan, 1972) as is almost invariably the case, this type of pathological behavior cannot occur.

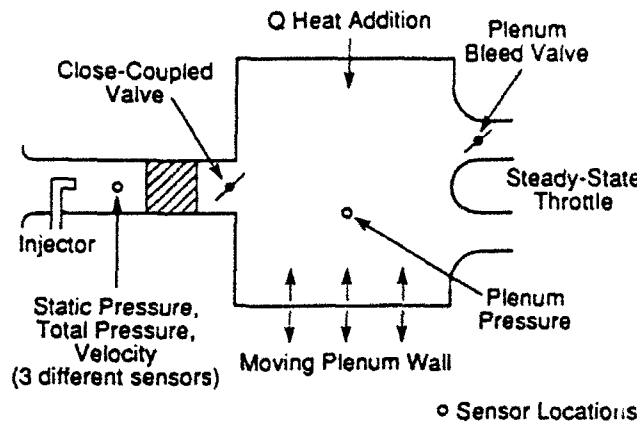


Fig. 3: Actuators and sensors selected for evaluation

Stability Modification Using Proportional Control

System stability under the influence of a proportional control law is determined from the roots of the *closed loop characteristic equation* (this is derived in many texts; see, for example, Ogata, 1970; Di Stefano, 1990; Van de Verte, 1990):

$$G_D(s) + KG_N(s) = 0 \quad (5)$$

In Eq. (5), $G_N(s)$ and $G_D(s)$ are the numerator and denominator polynomials, respectively, of the transfer function given in Table 2 and the gain, K , is a real constant of proportionality in the control law. The system will be stable if and only if all the roots of the characteristic equation have strictly negative real parts. For the present case, where the characteristic equation is a second order polynomial, this is equivalent to requiring all the coefficients in the equation to be strictly positive.

Equation (5) is the sum of two terms, $G_D(s)$ and $KG_N(s)$. When the control is off (K set to zero), stability is determined from the roots of $G_D(s)$ only, and thus is the same whatever the actuator-sensor pair. As the gain K is increased from zero, system stability becomes increasingly modified by the $KG_N(s)$ term, and because the various actuator-sensor pairs have different numerator polynomials, $G_N(s)$, the effect of feedback also varies. This is best illustrated by several specific examples. The first two examples will show the effect of sensor type, whereas comparison between behavior in the second and third illustrate the impact of the actuator.

Example 1: Close-Coupled Control Valve With Mass Flow Measurement

Using the appropriate transfer function from Table 2, substituting into the characteristic Eq. (5), and rearranging results in a characteristic equation of the form

$$s^2 + \left(\frac{1}{Bm_{Te}} - Bm_{Ce} + KBT \right) s + \left(1 - \frac{m_{Ce}}{m_{Te}} + \frac{KT}{m_{Te}} \right) = 0 \quad (6)$$

For stability we require

$$\left(\frac{1}{Bm_{Te}} - Bm_{Ce} + KBT \right) > 0 \quad (7a)$$

and

$$\left(1 - \frac{m_{Ce}}{m_{Te}} + \frac{KT}{m_{Te}} \right) > 0. \quad (7b)$$

All the parameters in these two inequalities are positive numbers except for the compressor slope, m_{Ce} . If $m_{Ce} < 0$, as it typically is for high flow rates, the system will be stable with no feedback, that is with K set equal to zero. As the flow rate becomes lower, m_{Ce} will become less negative, reaching zero at the peak of the compressor characteristic, and then moving to a large enough positive value so that the system will be unstable without feedback. For sufficiently large values of the gain K , however, both the inequalities expressed in Eqs. (7a) and (7b) can be simultaneously satisfied and the system can always be stabilized.

Example 2: Close-Coupled Valve With Plenum Pressure Measurement

In this case, as given in Table 2, the numerator polynomial of the transfer function contains only a constant term. The characteristic equation is:

$$0 = s^2 + \left(\frac{1}{Bm_{Te}} - Bm_{Ce} \right) s + \left(1 - \frac{m_{Ce}}{m_{Te}} + KT \right). \quad (8)$$

The system can now only be stabilized if the equivalent compressor slope is small enough so that the term $(1/Bm_{Te} - Bm_{Ce})$ is positive; in other words, the equivalent compressor slope obeys the inequality $m_{Ce} < 1/B^2 m_{Te}$. The ability of proportional feedback to stabilize this system is thus limited to a certain range of parameters. For many applications, B is unity or larger and the throttle slope, m_{Te} , is on the order of ten to one hundred, so the useful range can be quite small.

Example 3: Plenum Bleed Valve With Measurement of Plenum Pressure

From Table 2, the numerator polynomial for this case is

$$G_N(s) = -\frac{V}{B} (s - Bm_{Ce}) \quad (9)$$

and the characteristic equation is given by

$$0 = s^2 + \left(\frac{1}{Bm_{Te}} - Bm_{Ce} - \frac{KV}{B} \right) s + \left(1 - \frac{m_{Ce}}{m_{Te}} + KVm_{Ce} \right) \quad (10)$$

Whether the gain K is chosen to be positive or negative, it will have the desired effect on only one of the two coefficients of the characteristic equation. As a result, stabilization is limited to cases where $m_{Ce} < 1/B$. The limitation is associated with the sign change between the leading and the constant coefficient of $G_N(s)$ (Eq. (9)), which implies that $G_N(s)$ has a zero in the right half of the complex plane. Systems whose transfer functions have numerators with zeros in the right half of the complex plane are called non-minimum phase systems. The ability to control non-minimum phase systems is known to be subject to certain fundamental limitations (see Freudenberg and Looze, 1985) and this is just one manifestation of the generally poor behavior encountered in such systems.

The remaining actuator-sensor pairs whose transfer functions appear in Table 2 have also been analyzed, and the results are summarized in Tables 3 and 4. Table 3 gives the characteristic equation (the roots of which define the stability of the closed loop system) for all the sensor-actuator pairs. For stability, all coefficients in the characteristic equation must be positive; from this requirement, the capability of each scheme to extend the flow range to high values of compressor slope can be determined.

TABLE 3
CLOSED LOOP CHARACTERISTIC EQUATIONS WITH PROPORTIONAL GAIN K

Actuator Sensor	Close-Coupled Valve	Plenum Bleed Valve	Moveable Wall
Compressor Mass Flow	$s^2 + \left(\frac{1}{Bm_{Te}} - Bm_{Ce} + KBT \right) s + \left(1 - \frac{m_{Ce}}{m_{Te}} + \frac{KT}{m_{Te}} \right)$	$s^2 + \left(\frac{1}{Bm_{Te}} - Bm_{Ce} \right) s + \left(1 - \frac{m_{Ce}}{m_{Te}} + KV \right)$	$s^2 + \left(\frac{1}{Bm_{Te}} - Bm_{Ce} \right) s + \left(1 - \frac{m_{Ce}}{m_{Te}} + KWB \right)$
Plenum Pressure	$s^2 + \left(\frac{1}{Bm_{Te}} - Bm_{Ce} \right) s + \left(1 - \frac{m_{Ce}}{m_{Te}} + KT \right)$	$s^2 + \left(\frac{1}{Bm_{Te}} - Bm_{Ce} + \frac{KV}{B} \right) s + \left(1 - \frac{m_{Ce}}{m_{Te}} - Km_{Ce}V \right)$	$s^2 + \left(\frac{1}{Bm_{Te}} - Bm_{Ce} + KW \right) s + \left(1 - \frac{m_{Ce}}{m_{Te}} - KWBm_{Ce} \right)$
Compressor Face Total Pressure	$(1+KT)s^2 + \left(-Bm_{Ce} + \frac{1}{Bm_{Te}} + \frac{KT}{Bm_{Te}} \right) s + \left(1 - \frac{m_{Ce}}{m_{Te}} \right)$	$s^2 + \left(\frac{1}{Bm_{Te}} - Bm_{Ce} + \frac{KV}{B} \right) s + \left(1 - \frac{m_{Ce}}{m_{Te}} \right)$	$s^2 + \left(\frac{1}{Bm_{Te}} - Bm_{Ce} - KW \right) s + \left(1 - \frac{m_{Ce}}{m_{Te}} \right)$
Compressor Face Static Pressure	$(1+KT)s^2 + \left(-Bm_{Ce} + \frac{1}{Bm_{Te}} + KT2\phi B + \frac{KT}{Bm_{Te}} \right) s + \left(1 - \frac{m_{Ce}}{m_{Te}} + \frac{KT2\phi}{m_{Te}} \right)$	$s^2 + \left(\frac{1}{Bm_{Te}} - Bm_{Ce} + \frac{KV}{B} \right) s + \left(1 - \frac{m_{Ce}}{m_{Te}} + 2KV\phi \right)$	$s^2 + \left(\frac{1}{Bm_{Te}} - Bm_{Ce} + KW \right) s + \left(1 - \frac{m_{Ce}}{m_{Te}} + 2KW\phi B \right)$

TABLE 4
LIMITATIONS ON COMPRESSOR FLOW RANGE INCREASE WITH PROPORTIONAL CONTROL

Actuator Sensor	Close-Coupled Valve	Plenum Bleed Valve	Moveable Wall
Compressor Mass Flow	Unlimited Range Increase $K - \frac{m_{Ce}}{T}$ as $m_{Ce} \rightarrow \infty$ $K - \frac{m_{Ce}}{T}$ as $B \rightarrow \infty$	Limited Range Increase $m_{Ce} < \frac{1}{B^2 m_{Te}}$	Limited Range Increase $m_{Ce} < \frac{1}{B^2 m_{Te}}$
Plenum Pressure	Limited Range Increase $m_{Ce} < \frac{1}{B^2 m_{Te}}$	Limited Range Increase $m_{Ce} < \frac{1}{B}$	Limited Range Increase $m_{Ce} < \frac{1}{B}$
Compressor Face Total Pressure	Limited Range Increase $m_{Ce} < m_{Te}$	Limited Range Increase $m_{Ce} < m_{Te}$	Limited Range Increase $m_{Ce} < m_{Te}$
Compressor Face Static Pressure	Unlimited Range Increase $K - \frac{m_{Ce}}{2T\phi}$ as $m_{Ce} \rightarrow \infty$ $K - \frac{m_{Ce}}{2T\phi}$ as $B \rightarrow \infty$	Unlimited Range increase $K - \begin{cases} \frac{m_{Ce}B^2}{V} & \text{when } \frac{1}{2\phi B^2 m_{Te}} < 1 \\ \frac{m_{Ce}}{2V\phi m_{Te}} & \text{otherwise as } m_{Ce} \rightarrow \infty \end{cases}$ $K - \frac{B^2 m_{Ce}}{V}$ as $B \rightarrow \infty$	Unlimited Range Increase $K - \begin{cases} \frac{m_{Ce}B}{W} & \text{when } \frac{1}{2\phi B^2 m_{Te}} < 1 \\ \frac{m_{Ce}}{2m_{Te}W\phi B} & \text{otherwise as } m_{Ce} \rightarrow \infty \end{cases}$ $K - \frac{Bm_{Ce}}{W}$ as $B \rightarrow \infty$

The behavior of the different pairs is shown more explicitly in Table 4, which summarizes the limitations of each pair. In some instances, for example sensing compressor mass flow and actuating with a close-coupled valve, the range of parameters over which stabilization may be achieved is unlimited, although large values of gain may be required with a large compressor slope or large value of the B parameter. In these cases, therefore, the asymptotic behavior of the required gain is given for large B and compressor slope, in order to show the trends to be expected in these regimes. As will be discussed in more detail subsequently, excessive gain must be avoided in practical situations; however, as shown in Table 4, the gain increases either linearly or quadratically with compressor slope and B. Thus, there will be a practical limitation on maximum slope or maximum B at which the system can be stabilized.

An additional point to note is that the limitations on stability can, in some cases, be relaxed or removed by using a dynamic control law. Thus, the limitations expressed in this section reflect the combined properties of actuator, sensor, and control law taken together, and not necessarily the individual elements. Within the restriction to a fixed control law maintained here, however, the comparison of different sensor-actuator pairs is both valid and useful.

PRACTICAL LIMITS TO CONTROL

The analytical results so far indicate that the ability to stabilize the system with proportional control depends strongly on proper pairing of actuator and sensor, as well as on the values of the system parameters, particularly the compressor slope (m_C) and B.

In the above examples, however, we have considered ideal, linear systems in which only the dynamics of the pumping system are modelled. To address the issue of implementation, it is also necessary to include bandwidth limitations and actuator constraints (for example, servo dynamics and stops) which are encountered in any physical realization. As a matter of definition, by actuator we refer here to the entire actuation system including the flow train element (e.g. the valve), the motor that drives it, and any included feedback elements.

The bandwidth limitations may be imposed by the sensors, processor, actuator, or some combination of the three. System bandwidth may also need to be constrained to maintain stability if unmodelled dynamics are present. Unless the bandwidth of the actuator is much greater than that of the compression system, there is a non-negligible time lag between the command output of the control law and the response of the flow train element. The lags introduced by the actuator generally result in reduced control effectiveness, although to some degree, they can be compensated for by use of a control law more sophisticated than proportional control.

Another constraint on control effectiveness is introduced by bounds on actuator influence. For example, valve areas can only be modulated between 0 and 100% (i.e. the valve must be somewhere between full open and full closed).

Sensor and Actuator Pairs and Fluid Model

In this section, we numerically examine the limitations imposed by effects such as those described in the preceding. Five actuators and four sensors are studied as representative of a diverse set of implementation options. The selected actuators were:

- 1) injection in the compressor duct;
- 2) close-coupled control valve;
- 3) plenum bleed valve;
- 4) plenum heat addition; and
- 5) a movable plenum wall.

The selected sensors were:

- 1) compressor duct mass flow;
- 2) plenum pressure;
- 3) compressor face static pressure; and
- 4) compressor face total pressure.

These actuators and sensors are shown schematically in Fig. 3. At the level of idealization used here, the close-coupled valve could be either at compressor inlet or exit without changing the results.

The linear lumped parameter models of the previous section were extended as required, because the various actuators imply additional system states. The following assumptions were made in modelling the actuator behavior:

- 1) the injector flow is incompressible and fully mixed out;
- 2) the injector is quasi-steady, inertial effects are lumped into upstream and downstream ducts;
- 3) the close-coupled valve flow is incompressible and quasi-steady;
- 4) the plenum is well mixed, has uniform pressure, temperature, negligible velocities, and follows ideal gas laws with constant specific heat;
- 5) the mass of fuel is neglected and heat release is instantaneous; and
- 6) the throttle and bleed valve are quasi-steady.

The differential equations that describe the system dynamics are obtained by performing balances on momentum in the ducts and mass and energy in the plenum (Simon, 1992). They are:

$$\frac{d\phi_1}{dt} = \frac{-B}{(L_1/L_C)} (\Delta\Psi_u + \Psi_{oj}) \quad (11a)$$

$$\frac{d\phi_2}{dt} = \frac{B}{(L_2/L_C)} ((\Delta\Psi_d + \Psi_{oj}) + \Psi_c - \Psi_{cc} - \Psi) \quad (11b)$$

$$\frac{dm^*}{dt} = \frac{M_1^2}{2BT_p} (\phi_2 - (\Phi_T + \Phi_b)) \quad (11c)$$

$$\frac{dE^*}{dt} = \frac{M_1^2 \gamma}{2BT_p} \left(\phi_2 (1 + \Delta T_{oc}^*) - (\Phi_T + \Phi_b) T_p^* + Q^* - P_p^* \left(\frac{\gamma-1}{\gamma} \right) \xi \right) \quad (11d)$$

$$\frac{dV^*}{dt} = - \frac{1}{t_w} V^* + \dot{V}_c^* \quad (11e)$$

There are five states needed. The mass flow rates in the portion of the duct upstream and downstream of the injector are given by ϕ_1 and ϕ_2 , the non-dimensional mass and energy of the gas in the plenum are given by m^* and E^* , and the non-dimensional plenum volume is given by V^* . The effects of the various actuators are given by the functions, $\Delta\Psi_u$ and $\Delta\Psi_d$, representing the injector, Ψ_{oc} , representing the close-coupled valve, Φ_b , representing the plenum bleed, Q^* , representing the plenum heat addition and ξ , representing the plenum wall motion.

The general description is nonlinear, but it is small perturbations which are of primary interest here, and Eqs. (11) can be linearized to yield an equation set of the form:

$$\dot{x} = Ax + Bu \quad (12)$$

with the output vector y defined as

$$y = Cx + Du \quad (13)$$

In Eqs. (12) and (13), the linearized state variables x , the inputs u , and the outputs y , are perturbations from the corresponding equilibrium values, and A , B , C , and D are appropriately dimensioned constant matrices. The state variables have been normalized as detailed in Table 5, so that unity magnitude for any of these perturbation variables has roughly the same physical significance.

TABLE 5
NORMALIZATION FACTORS

Perturbation Variable	Normalized By
Flow	Time mean flow through compressor
Pressure	Time mean compressor pressure rise
Thermal input	Mean compressor work
Moving wall work input	Mean compressor work
Plenum bleed valve area	Area to fully close valve
Close-coupled valve area	Area to fully open or close (whichever is smaller)

All twenty pairings of the five actuators and four sensors have been evaluated with a proportional control law. Such a comparison provides two useful results. One is the identification of actuator-sensor pairs which may be stabilized over a significant range of system parameters using the simplest possible control law. In addition, for those pairs with significant stabilization, the required gain gives a measure of the combined effectiveness of this choice of sensing and actuating locations.

As was discussed, it is useful to weed out those systems which could mathematically be stabilized but stand little chance of succeeding in an actual implementation. To this end, two constraints were imposed. First, the allowable magnitude of the normalized proportional gain was limited to be not more than twenty. For example, at the maximum allowable gain, a five percent change in compressor mass flow would yield a one hundred percent change in plenum bleed valve area; that is, the valve would be fully closed. Second, the bandwidth of the feedback loop was limited by modeling a two-pole, low pass Butterworth filter in the feedback path. This filter can be given various physical interpretations such as probe dynamics, amplifier dynamics, actuator dynamics or unmodelled dynamics in the compression system itself. Whatever the interpretation, the insertion of the filter insures that the feedback path has finite bandwidth, a constraint which will always exist in practice. The study was carried out with the cutoff frequency of this filter maintained at ten times the Helmholtz frequency of the system formed by the plenum and compressor ducts. Sensitivity to this assumption will be examined subsequently.

The figure of merit used to assess the actuator-sensor pairs was to examine the stability boundaries in a compressor slope versus B parameter plane. Preliminary studies showed that these two parameters have a dominant effect on system stability. It is thus more relevant, for example, to quantify the amount of stabilization that can be achieved in terms of the compressor slope which enters into the stability in an explicit manner, rather than the change in mass flow at stall. The relative extent of the stabilized region in this compressor slope B -parameter plane thus provides an appropriate and useful basis for comparison. The boundaries were computed by first performing an incremental search over the three-dimensional (slope, B parameter gain) parameter space. For each fixed B , the value of gain which maximized the slope at instability, as well as the corresponding slope, was then found, again using an incremental search. The stability boundaries in the B parameter versus slope plane thus represent the maximum slope which could be stabilized using any gain less than twenty.

RESULTS OF THE CONTROL SCHEME EVALUATIONS

The results of the calculations are summarized in Fig. 4, which shows the stability boundaries for the twenty actuator-sensor pairs. The figure is broken into four plots, one for each sensor. Within each plot, the five curves indicate the different actuators. The region below and to the left of any given line is the region in which stabilization can be achieved. In the upper left hand plot, for example, all the region to the left of the dash-dot line represents the range of compressor slope and B in which the combination of compressor mass flow sensor and close-coupled valve is capable of suppressing the instability.

Several general conclusions can be drawn from the results in

Fig. 4.

1. The overall trend is that control becomes more difficult as the compressor slope and B parameter increase, with the maximum stable slope decreasing with increasing B .
2. Only the actuators located in the compressor duct, which act upon the compressor duct momentum (injector and close-coupled control valve), are capable of stabilization at steep slopes over the full range of B .
3. Plenum heat addition gives little or no stability.
4. In general, there is no best sensor independent of the actuator.

For reference, the range of B parameters that might be associated with large axial gas turbine engines is roughly 0.2 to 0.4, with that for small centrifugal machines approximately 1 to 4.

A more specific conclusion is given by the comparison of the results with the mass flow sensor to the other sensor locations. As B reaches a value of roughly unity, the ability of all the pairs to stabilize the system becomes quite small, except for the close-coupled valve and the injector which use mass flow sensing. This points out clearly that not only is actuator position important, but sensor position is as well.

The conclusion about the effect of actuator position is one that is in general accord with intuitive ideas of system behavior, but that having to do with sensors is somewhat less familiar. It is therefore worthwhile to give some physical motivation for the impact of sensor position.

The different dynamics brought about by the various sensors can be understood with reference to the non-dimensional characteristic equation for the unsteady system behavior with no feedback:

$$s^2 + \left(\frac{1}{Bm_{Te}} - Bm_{Ce} \right) s + \left(1 - \frac{m_{Ce}}{m_{Te}} \right) = 0 \quad (14)$$

For stability the coefficients of the second and third terms must be positive, so that

$$m_{Ce} < \frac{1}{B^2 m_{Te}} \quad (15a)$$

$$m_{Ce} < m_{Te} \quad (15b)$$

As described by Greitzer (1981) the mechanism of instability can either be static, corresponding to the inequality in Eq. (15b) being violated or dynamic, corresponding to the violation of that in Eq. (15a). Whichever of these events occurs (it is the second that is generally more important), the cause for this is a positive slope of the compressor pressure rise characteristic. Therefore, let us examine how the destabilizing effect of positive slope is ameliorated when different sensing schemes are used. As a case of high practical interest, we consider the close-coupled valve with two different sensors, one measuring compressor mass flow and the other measuring the total pressure at the compressor inlet face.

In the first of these, the valve position, and hence the valve pressure drop, is proportional to the sensed perturbations in

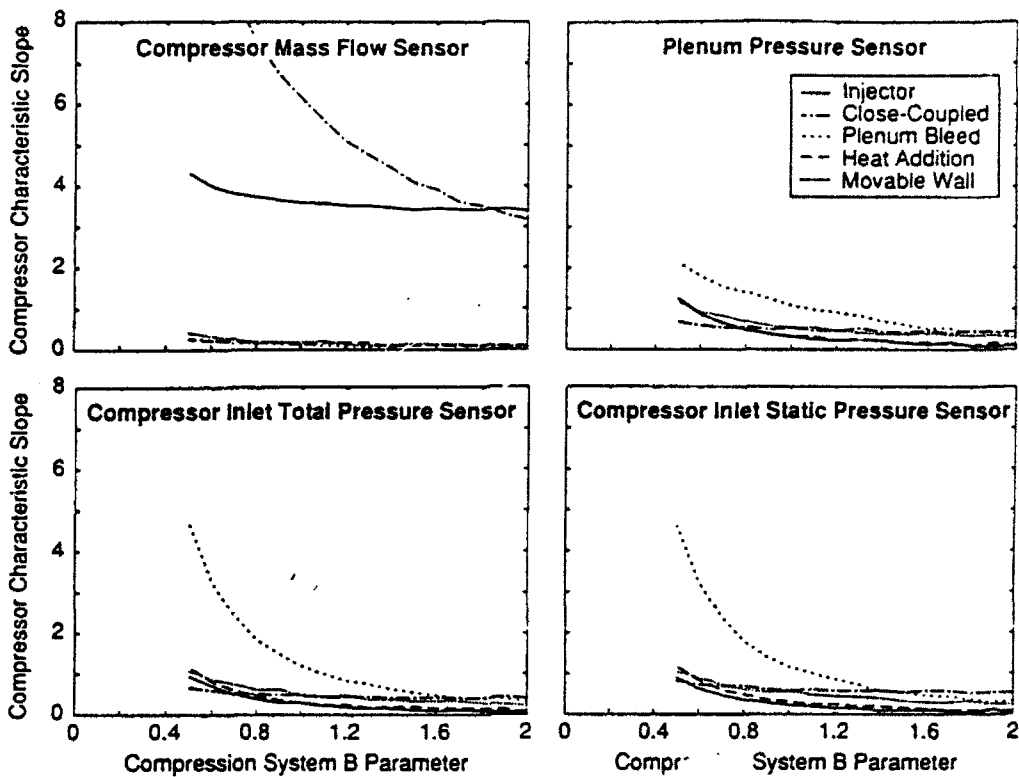


Fig. 4: Influence of sensor and actuator selection on maximum stabilized compressor characteristic slope for a bandwidth and gain-limited system

compressor mass flow. The pressure perturbations across the compressor and the across valve are both proportional to the mass flow perturbations. Because the valve is just downstream of the compressor, the two act in series, creating an effective compressor slope which is the sum of the (positive) slope across the compressor and the (negative) slope across the valve. It is this combined characteristic which the system "sees".

Suppose the constant of proportionality between sensed mass flow and valve opening angle is K , and the rate of change of valve pressure drop per increment in opening angle is T . For a given mass flow perturbation, the effective slope of the compressor will change from m_{C_e} , with no feedback, to $m_{C_e} - KT$ when feedback is applied. Sensing the compressor mass flow and feeding the signal back to the valve actuator thus works directly on the cause of the instability, the positive compressor slope. (Insertion of the slope $m_{C_e} - KT$ in Eq. (14) in fact gives just the characteristic equation in Table 3.)

A different situation prevails for the inlet total pressure sensor. The inlet total pressure perturbation is related to the derivative of the inlet mass flow, i.e., the fluid acceleration in the compressor duct, through the unsteady Bernoulli Equation

$$P_{t_0} - P_{t_1} = \rho \int_0^1 \frac{\partial C_x}{\partial t} dx$$

Non-dimensionalizing and linearizing gives

$$-\delta\psi_{t_1} = \frac{1}{B} \frac{d\phi}{dt}$$

where $\delta\psi_{t_1}$ is the total pressure perturbation at the compressor face in non-dimensional form. If the valve angle perturbation is proportional to the compressor inlet total pressure, the result is to create a pressure change across the valve proportional to the *acceleration*, which is the derivative of the state variable ϕ . In other words the effect of feedback in this case is to alter the overall pressure difference from duct inlet to exit for a given fluid acceleration rate. As far as the system is concerned, this is seen as a change in compressor duct length, since the longer the duct, the larger will be the instantaneous pressure change that results from a given fluid acceleration.

An increase in effective length of the duct does several things to the system. It drops the natural frequency, which scales as $1/\sqrt{L_c}$. More importantly, it changes the effective value of the B-parameter, which also scales as $1/\sqrt{L_c}$. Both these changes can be seen in the characteristic equation in Table 3, in which the critical value of B for instability is increased by $\sqrt{1 + KT}$, $1 + KT$ being just the factor by which the effective length is increased. In the case of total pressure sensing, however, only the dynamic instability is influenced, because the increase in effective mass does nothing to alter the static stability. The instability limit is thus still $m_{C_e} \geq m_{T_e}$.

Somewhat similar arguments can be made for other sensor-actuator pairs, but the main point is that the use of different sensors for the feedback gives the system quite different properties. For the feedback on mass flow, one of the resistive elements in the system is altered directly, whereas for the feedback on inlet total pressure, it is the effective inertia that is changed, and different dynamical behavior thus results.

Effect of Control System Bandwidth

As mentioned previously, the study of the sensor-actuator pairs was carried out using a value of control system bandwidth (ω_c) ten times the compression system Helmholtz frequency (ω_H). We can also examine the influence of this parameter, in other words, of controller bandwidth, on the stabilization process. Figure 5 thus shows the changes in instability onset that occur with different controller bandwidths for conditions corresponding to the close-coupled control valve, with feedback on mass flow, and a B-parameter of 2. In the figure, the horizontal axis is the controller gain, and the vertical axis is the compressor characteristic slope at instability. Curves are shown for values of ω_c/ω_H from 1.0 to 100, representing extremes of this ratio, and it is evident that controller bandwidth strongly influences the range of stabilization that can be achieved.

Several trends are exhibited in Fig. 5. First, for a controller bandwidth such that $\omega_c/\omega_H = 1$, use of the control actually degrades the stability – the more gain the less steep the compressor slope that can be achieved. In this regime, control system effectiveness is adversely affected by the system dynamics and the influence of modelling inaccuracies becomes more pronounced. Second, when ω_c/ω_H becomes considerably larger, increasing the controller bandwidth increases the compressor slope that can be attained. Third, for a given level of bandwidth, increasing gain increases stability only up to a point; beyond this point the stabilization decreases as gain increases. The value of gain for maximum stabilization increases with bandwidth.

The necessity to go to higher bandwidth at higher slope arises because, as the slope increases, the system dynamics become faster relative to the undamped natural frequency (Helmholtz frequency). There can thus be coupling between oscillations in the controller and in the aerodynamic system that lead to instabilities, so actuator dynamics play a role in setting the range of stability (as they clearly do at $\omega_c/\omega_H = 1$). In fact, the analysis so far of the close-coupled valve configuration tested experimentally indicates that the degree of stabilization is theoretically limited by a high frequency instability involving the actuator dynamics. This point is an important one since, in many cases, it is difficult to engineer actuators with bandwidths

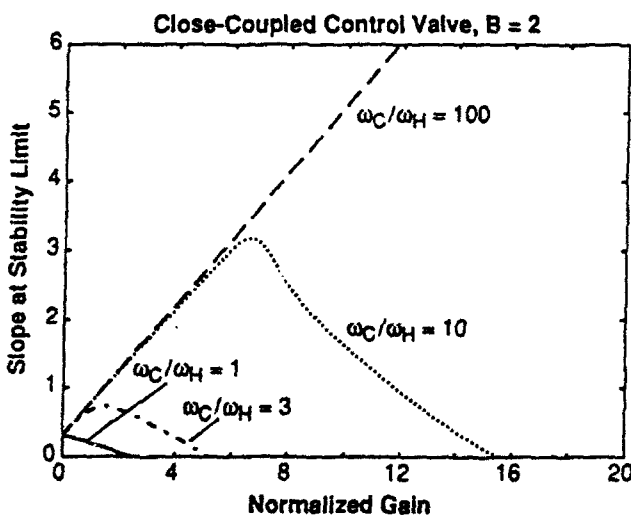


Fig. 5: Influence of normalized control system bandwidth (ω_c/ω_H) on the feedback gain required and flow coefficient at instability onset; close-coupled control valve

many times that of the Helmholtz frequency. The analysis suggests that actuator bandwidth will be a prime determinant of practical system performance and that research and development on this topic is useful to pursue.

LIMITS TO CONTROL WITH AN IDEAL CONTROLLER

With the four sensors studied, and proportional control, the close-coupled valve and injector emerge as the most promising actuators. A further question to address, however, is whether the type of compensation or choice of sensors would affect this conclusion. In this section, optimal control theory is used to provide a definite answer to this question. To motivate the approach taken, some basic aspects of linear dynamic system stabilization are first presented. For small disturbances, the compression system, actuators and disturbances are described by the linear differential equation set:

$$\dot{x} = Ax + Bu + Lw$$

where x is a five-dimensional vector of system states, u is a scalar representing a particular actuated variable, w is a p -dimensional vector of external disturbances, and A , B , and L are constant matrices of appropriate dimensions. This is just Eq. (12) modified to include the effect of external disturbances. It is known (see, for example, Kwakernaak and Sivan, 1972) that systems of this type can be stabilized for all conditions using the control law $u = -Kx$, where K is now a one-by-five constant gain matrix, provided only that the pair A, B is *controllable*. Such a control law is known as *full state feedback* and requires that the state of the system, x , be known perfectly. For a system with n states, this would require n properly placed sensors. For the situation of interest here, over the range of parameters which have been analyzed, the requirement of controllability is met. Thus, with enough properly placed sensors, stabilization of any idealized linear system is not a problem.

All actuators are not equally suitable for this; some have excessive amplitude requirements. In the analysis, therefore, the actuators are compared based upon their minimal required RMS (root mean square) response to a persistent broadband disturbance, while maintaining system stability. This comparison is independent of choice of sensor, because it is assumed that the state of the system is known at all times. Further, the comparison is based upon the minimal possible RMS amplitude, and hence there is no question as to whether a particular actuator would perform better if another control law were used. In this sense, the comparison is also independent of the control law.

Specific details of the computations performed are included in Simon (1992), and a more general treatment can be found in Kwakernaak and Sivan (1972). The central concept to be used is that, if the disturbance can be described as a stationary, Gaussian, white noise process, a particular gain matrix K can be found which will minimize the root mean square value of the actuated variable u . The gain matrix K and the RMS value of u will depend upon the matrix L which determines how the disturbance enters the system and upon the statistical properties of the disturbance.

For this analysis, the disturbances driving the system must be

* A linear time invariant system $\dot{x} = Ax + Bu$ is controllable if and only if there exists a piecewise continuous function $u(t)$ which will transfer the system from any initial state $x_0(t_0)$ to a final state $x_1(t_1)$ in a finite time interval $t_1 - t_0$ (see Kwakernaak and Sivan, 1972).

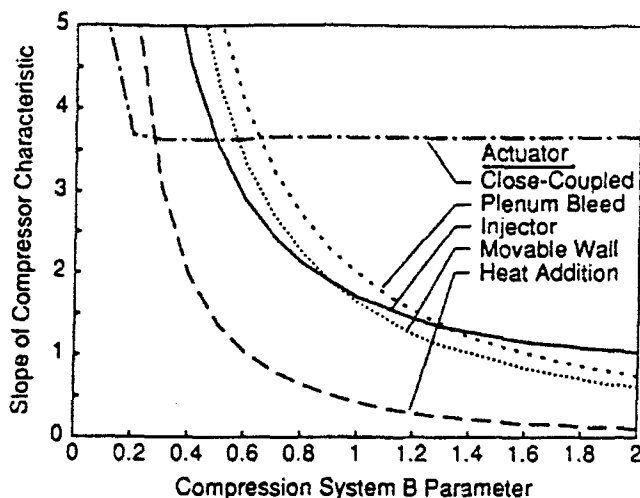


Fig. 6: Maximum slope at which the RMS actuation will be no greater than 25% of the maximum actuator authority; ideal controller and perfect knowledge of the system state

chosen. Three disturbances were studied: 1) a compressor with an unsteady pressure rise; 2) an unsteady heat release in the plenum chamber; and 3) an unsteady outflow through the throttle. In each case, the input disturbance amplitude (white noise intensity) was normalized to that required to produce a one percent RMS fluctuation in compressor mass flow at a fixed, stable operating point.

The results of this analysis are illustrated in Fig. 6. In the figure, the maximum allowable slope at which the system can be stabilized is plotted as a function of B for five different actuators, based on the restriction that the normalized RMS actuation is no greater than 0.25 for the most deleterious type of disturbance. The choice of this level of maximum RMS actuation is somewhat arbitrary, but it is taken to be one that can be achieved in practice. In addition, computations have been carried out at other levels, and the results show similar trends.

For all the actuators, the maximum stable slope that can be attained decreases as the B-parameter increases. However, the sensitivity of the slope to B varies markedly between different actuators. As with the proportional control, those actuators which are most closely coupled to the compressor (the injection and the close-coupled valve) are the most effective. The figure shows that, for B greater than unity, the maximum compressor slope at which the system can be stabilized is quite limited. (For reference, the characteristic of the turbocharger used in the experiments described previously has a maximum slope of approximately six, i. e., $m_c \geq 6$). In addition, except for the close coupled valve, whose performance becomes independent of B, the maximum stable slope decreases monotonically with B parameter. In particular, heat addition, which might seem attractive because of ease of implementation through fuel injection, shows little potential for stabilization at values of B larger than unity.

Another result is that the behavior of the plenum bleed, the injector, and the moving wall are roughly comparable, although the injector has some advantage for larger values of B (greater than two, say). At these high values of B parameter, however, the close coupled valve has a clear advantage over all of the other schemes examined, in stabilizing the system.

EFFECT OF DISTURBANCE TYPE ON SYSTEM BEHAVIOR

The influence of the disturbance type on controlled compressor performance is shown in Fig. 7 for the close coupled valve, the actuator shown to be most effective in enhancing flow range for large values of B. The horizontal axis is the slope of the compressor characteristic, and the vertical axis is the normalized RMS actuation level. The difference between the three curves indicates the impact of disturbance type on the ability to control the system. Compressor pressure rise disturbances, such as might arise from local unsteady flow in the impeller or diffuser, create a situation that is more difficult to control than disturbances due to combustor heat release or throttle mass flow fluctuation.

The implication of Fig. 7 is that the nature of the disturbances driving the system is an important factor in setting the requirements for stabilization. There is little known at present about the detailed disturbance structure within turbomachinery and engines. It thus appears that characterization of these unsteady phenomena is a research item of considerable practical concern.

SUMMARY AND CONCLUSIONS

An evaluation of strategies for the active control of compression system surge has been carried out, as a first step towards developing rational design procedures for active surge stabilization. A basic result is that actuators and sensors which measure and act upon the momentum of the fluid in the compressor duct are the most effective for geometries and compressor slopes of interest for gas turbine applications. Although this result was qualitatively known, the analysis has quantified the severity of these trends, showing them to be extremely important over the parameter range of interest. The following specific conclusions can be made:

- Proper choice of actuator and sensor is an important part of the overall design of a surge stabilization system.
- Mass flow measurement with either a close-coupled valve or an injector for actuation are the most promising approaches of those evaluated.

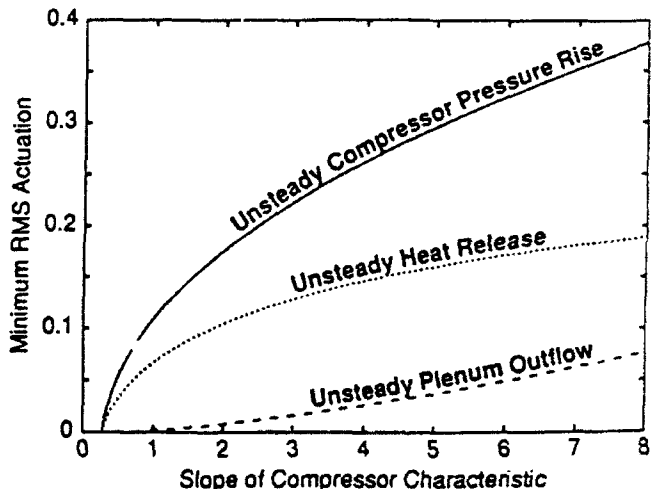


Fig. 7: Influence of compression system disturbance type on actuator motion required to stabilize the system; close-coupled valve actuator, $B = 2$

- Fuel modulation is not a promising candidate for practical ranges of system parameters.
- Characterization of compression system disturbance sources is important for determining the requirements for active control schemes.
- Steep slopes and large B parameters make control more difficult.
- Actuator bandwidth can be an important constraint in many practical implementations.

ACKNOWLEDGEMENTS

The authors would like to thank Dr. J. Paduano, Dr. G.R. Guenette, and Mr. D.L. Gysling for many useful discussions, and Ms. D.I. Park for her forbearance during preparation of this manuscript. This work was supported by the US Arm. Propulsion Directorate, Aviation Research and Technology Activity, Aviation Systems Command, Dr. L.F. Schurmann, Technical Monitor, and the Air Force Office of Scientific Research, Major D. Fant, Technical Monitor.

REFERENCES

Di Stefano, J.J., Stubberud, A.R., Williams, I.J., 1989, *Feedback and Control Systems*, 2nd Edition, Schaum's Outline Series, McGraw-Hill, Inc.

Epstein, A.H., Ffowcs Williams, J.E., Greitzer, E.M., 1989, "Active Suppression of Compressor Instabilities," *Journal of Propulsion and Power*, Vol. 5, pp. 204-211.

Ffowcs Williams, F.E., Huang, X., 1989, "Active Stabilization of Compressor Surge," *Journal of Fluid Mech.*, Vol. 204, pp. 245-262.

Fink, D.A., Cumpsty, N.A., Greitzer, E.M., 1991, "Surge Dynamics in a Free-Spool Centrifugal Compressor System," ASME Paper 91-GT-31.

Freudenberg, J.S., Looze, D.P., 1985, "Right Half Plane Poles and Zeros and Design Tradeoffs in Feedback Systems," *IEEE Transactions on Automatic Control*, AC-30, pp. 555-565.

Greitzer, E.M., "The Stability of Pumping Systems - The 1980 Freeman Scholar Lecture", 1981, *ASME Journal of Fluids Engineering*, Vol. 103, pp. 193-242.

Gysling, D.L., Dugundji, J., Greitzer, E.M., Epstein, A.H., 1991, "Dynamic Control of Centrifugal Compressor Surge Using Tailored Structures," *Journal of Turbomachinery*, Vol. 113, No. 4, pp. 710-722.

Kwakernaak, H., Sivan, R., 1972, *Linear Optimal Control Systems*, John Wiley and Sons Inc.

Muller, F.C., Weber, H.I., 1972, "Analysis and Optimization of Certain Qualities of Controllability and Observability for Linear Dynamical Systems," *Automatica*, Vol. 8, No. 3, pp. 237-246.

Norris, G.A., Skelton, R.E., 1989, "Selection of Dynamic Sensors and Actuators in the Control of Linear Systems," *Journal of Dynamic Systems, Measurement and Control*, Vol. III, pp. 389-397.

Ogata, K., 1970, *Modern Control Engineering*, Prentice Hall, Inc.

Pinsley, J.E., Guenette, G.R., Epstein, A.H., Greitzer, E.M., 1991, "Active Stabilization of Centrifugal Compressor Surge," *Journal of Turbomachinery*, Vol. 113, pp. 723-732.

Schmitendorf, W.E., 1984, "An Exact Expression for Computing the Degree of Controllability," *Journal of Guidance*, Vol. 7, No. 4, pp. 502-504.

Simon, J.S., 1992, "Feedback Stabilization of Compression and Pumping Systems," Ph.D. Thesis, Department of Mechanical Engineering, Massachusetts Institute of Technology.

Van de Verte, J., 1990, *Feedback Control Systems*, 2nd Edition, Prentice-Hall, Inc.

A Theoretical Study of Sensor-Actuator Schemes for Rotating Stall Control

G.J. Hendricks* and D.L. Gysling**

Gas Turbine Laboratory, Massachusetts Institute of Technology

Cambridge, MA 02139

ABSTRACT

A theoretical study has been conducted to determine the influence of actuator and sensor choice on active control of rotating stall in axial-flow compressors. The sensors are used to detect the small amplitude traveling waves that have been observed at the initiation of rotating stall on several different compressors. Control is achieved by feeding the sensed quantity back to the actuator with a suitable gain and spatial phase shift relative to the measured wave. Actuators using circumferential patterns of jets, intake ports, and movable inlet guide vanes upstream of the compressor, and valves downstream of the compressor were considered. The effect of axial velocity, static pressure, or total pressure measurement on control effectiveness was investigated. In addition the influence of the actuator bandwidth on the performance of the controlled system was determined. The results of the study indicate that the potential for active control of rotating stall is greater than that achieved thus far with movable inlet guide vanes. Further, axial velocity sensing was most effective. Actuator bandwidth affected the performance of the controlled compressors significantly, but certain actuators were affected less severely than others.

NOMENCLATURE

l	- Compressor annulus height
δl	- Jet valve opening
$L_{r,0}$	- Steady total pressure loss across rotors
$L_{s,0}$	- Steady total pressure loss across stator
δL	- Perturbation in total pressure loss across rotors
δL_s	- Perturbation in total pressure loss across stators
n	- spatial harmonic number
P_i	- Inlet total pressure
δP_e	- Exit static pressure perturbation
δP_i	- Inlet static pressure perturbation
δP_s	- Inlet total pressure perturbation
$\delta P_{e,i}$	- Exit static pressure perturbation
r	- Compressor annulus mean radius
R	- Feedback gain

* Postdoctoral Associate, Member AIAA
** Graduate Student

Copyright © American Institute of Aeronautics and Astronautics, Inc., 1992. All rights reserved.

s	- $(\alpha + i\omega)r/U$
t	- time
τ	- Non-dimensional time tU/r
Z	- Complex feedback gain $R e^{i\phi}$
α	- Disturbance growth rate
η	- Compressor efficiency
ϕ	- Flow coefficient c_e/U
$\delta\phi$	- Flow coefficient perturbation
λ	- Inertia parameter for compressor rotors
μ	- Inertia parameter for compressor
ϑ	- Circumferential coordinate
ϑ_s	- Feedback spatial phase shift
ρ	- Fluid density
τ_a	- Non-dimensional actuator time constant
τ_r	- Non-dimensional rotor total pressure loss characteristic time
τ_s	- Non-dimensional stator total pressure loss characteristic time
ω	- Disturbance rotational frequency
ω_r	- Rotor rotational frequency
γ	- Total-to-static pressure rise
γ_i	- Ideal (isentropic) total-to-static pressure rise
γ_{ss}	- Steady state total-to-static pressure rise

1. INTRODUCTION

Active control of aerodynamic and mechanical instabilities has attracted considerable research interest in the past few years. Work is being conducted at a number of institutions in applications including the control of boundary layer and combustion instabilities. This paper addresses active control of rotating stall, a fluid dynamic instability which limits the operating range of compressors.

Rotating stall, which is characterized by a region of stalled flow rotating about the annulus of a compressor, has a severe effect on the operation of a gas turbine engine. When encountered, the instability causes an abrupt drop in the pressure rise across the compressor, resulting in a significant decrease in the power output of the engine. In addition, engine health is affected adversely by large fluctuating loads that are induced on the compressor blades. Because of this, the compressor of the gas turbine engine is normally operated far enough away from the stall initiation point to ensure that instability is not triggered under any engine operating condition, with the margin of safety known as the stall margin. Because

rotating stall is normally encountered close to the peak of the pressure-rise characteristic of the compressor, the stall margin places a limit on both the performance and operating range of the engine. An actively controlled compressor could operate stably past the peak of the pressure rise characteristic. With the same stall margin as in the uncontrolled case, the peak of the characteristic could then be a safe operating point.

Active control of rotating stall studied here is based on a linear model of its initiation. The model implies that, at the inception of the instability, small amplitude traveling waves develop in the compressor annulus, grow in magnitude and eventually develop into rotating stall cells [1], [2], [3]. Although such small amplitude waves have not been observed in all situations, they are a clear feature of recent tests on several compressors of widely different geometry [4], [5].

The correspondence observed so far between linear fluid dynamic analysis and experimental observations is encouraging since it gives one confidence in using the theory to design devices which can be used to modify the inlet and/or exit flow fields of the compressor in order to suppress the instability. These controlling devices would act in the inception phase of the instability, before it develops to its performance limiting amplitude. The controllers that will be described in this study are therefore designed to prevent the compressor from going into rotating stall when the system is operated within the parameters of the controller.

A schematic diagram of a conceptual controlled system is shown in figure 1. A fluid dynamic variable which gives an indication of the magnitude and form of the instability is sensed by a suitable array of transducers. The signal from the transducer array is processed by the controller which commands the actuator to introduce a suitable control disturbance into the flow field. Initial studies of this problem [3] have considered only simple control strategies, for example actuators which introduce a vortical velocity perturbation at the compressor inlet plane (a model for movable guide vanes far upstream of the compressor). The use of close coupled movable inlet guide vanes for the control of rotating stall has been demonstrated experimentally by Paduano [6,7] and Haynes [8] (the stalling mass flow rate was decreased by 23% in the experiment on a single stage compressor [6,7], and 8% on a three stage unit [8]). The objective of the present study is to examine the potential for increasing the system controllability, in particular to assess the effectiveness of a number of different sensing and actuation devices.

2. ANALYTICAL MODEL

2.1 Overall Considerations

The analytical model used in this study is an extension of that described in [1], [2], and [3]. The analysis is two-dimensional, so only high hub-to-tip ratio machines are considered. The mean inlet flow field is undistorted (uniform inlet total pressure), and the inlet and exit ducts are assumed long, so that end effects, i.e. reflection and scattering of the disturbance wave from the ends, are not important. In addition, the tip speed of the compressor is assumed to be low enough for the flow field to be considered incompressible. In the analysis an arbitrary

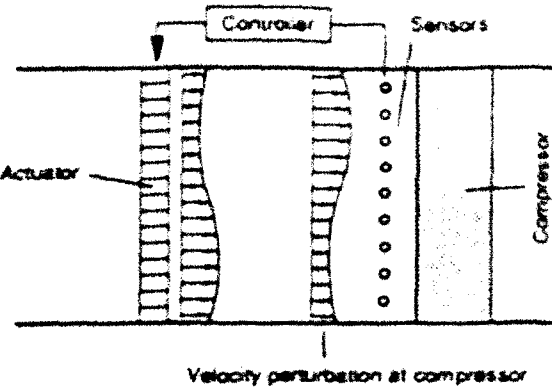


Figure 1: Compressor with actuator and sensors
axial velocity disturbance wave is decomposed into its spatial Fourier harmonics:

$$\delta\phi_r = \sum_{-1}^1 A_r e^{i\theta} e^{i\omega r}, \text{ where } s = \frac{(a + i\omega)r}{U}$$

In the above formulation a/U represents the rotation rate of each spatial harmonic non-dimensionalized by the rotor rotational speed, and $a\omega/U$ the non-dimensionalized growth rate of the disturbance. The spatial harmonics, which are the natural eigenmodes of the system, can then be analyzed independently, since the equations describing the evolution of the instability are linear. When the above form of the flow coefficient perturbation is substituted into the differential equations describing the dynamics of the fluid in the compression system, the analysis yields an eigenvalue problem in s with the growth and rotation rates of each spatial harmonic determined from the solution to the eigenvalue problem. If the real part of s is negative, the disturbance is damped, representing stable operation of the compressor; if the real part of s is positive, the disturbance grows exponentially, representing unstable operation.

If the compressor is assumed to operate in a quasi-steady manner, i.e. pressure rise is a function of flow coefficient only, the model predicts that all the spatial harmonics of the flow coefficient perturbation become unstable at the operating point where the total-to-static pressure-rise characteristic (ψ vs. ϕ) becomes positively sloped. Disturbances are damped where the characteristic is negatively sloped, and amplified when the characteristic is positively sloped, with the growth rate of the perturbation being determined by the magnitude of the positive slope. In the formulation of the model used in the present study the quasi-steady assumption is not made.

2.2 Unsteady Compressor Behavior

It has been observed in experiments [9,10], that the pressure rise across a compressor does not respond instantaneously to variations in flow coefficient. This is thought to be a result of the finite time required for the flow fields within the blade passages to respond to changes in flow coefficient. The finite response time of the compressor pressure-rise to flow perturbations has a stabilizing effect on the perturbations, and higher harmonics are stabilized to a greater extent than lower harmonics. When this effect is included the analysis, the spatial harmonics of the disturbance become unstable

sequentially, with higher harmonic disturbances becoming unstable at larger positive slopes of the compressor total-to-static pressure-rise characteristic (i.e. lower flow coefficients). This behavior has been observed in experiments on both single and three stage low-speed compressors [6,7,8], and the model shows good quantitative agreement with experiments conducted on a three stage compressor [11]. The sequential destabilization of higher spatial harmonics of flow coefficient disturbances has beneficial implications for active control. By controlling only the first spatial harmonic of the disturbance, an increase in stable operating range can be obtained, down to the flow coefficient at which the second spatial harmonic of the disturbance becomes unstable. By controlling both the first and second spatial harmonics beyond this flow coefficient, the stable operating range can then be extended to the operating point where the third spatial harmonic becomes unstable. Using this control approach, the maximum range extension possible is therefore dependent on the number of spatial harmonics of the disturbance that one is able to control.

It has been mentioned earlier that the slope of the compressor pressure rise characteristic $d\psi/d\phi$, is an important parameter governing the growth rate of a disturbance wave. The pressure-rise characteristic shown in figure 2, which has a slope going to an infinite positive value at a flow coefficient of 0.25, is used in the computations described below since it covers all positive slopes that could be encountered in practice.

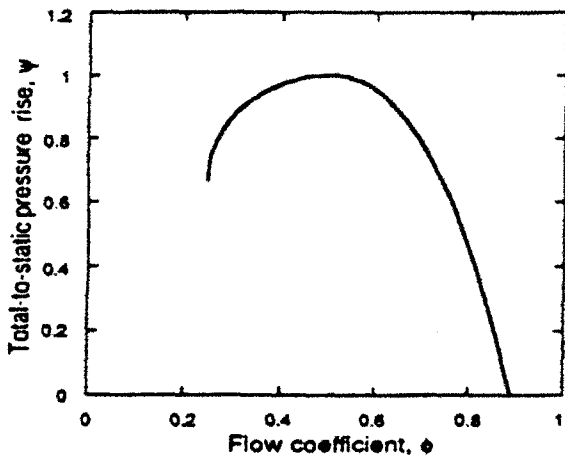


Figure 2: Compressor total-to-static pressure rise characteristic used in the analysis

3. ACTUATORS AND SENSORS

Actuators normally introduce both potential and vortical disturbances into compressor inlet or exit flow fields. Potential disturbances decay with axial distance from the actuator whereas vortical disturbances persist, and are convected with the flow field downstream of the actuator. One of the initial objectives of the study was to determine the type of disturbance (potential or vortical) that would be most effective in controlling rotating stall disturbances.

For an actuator to produce purely vortical control disturbances at the compressor face, it must be located sufficiently far upstream of the compressor for potential

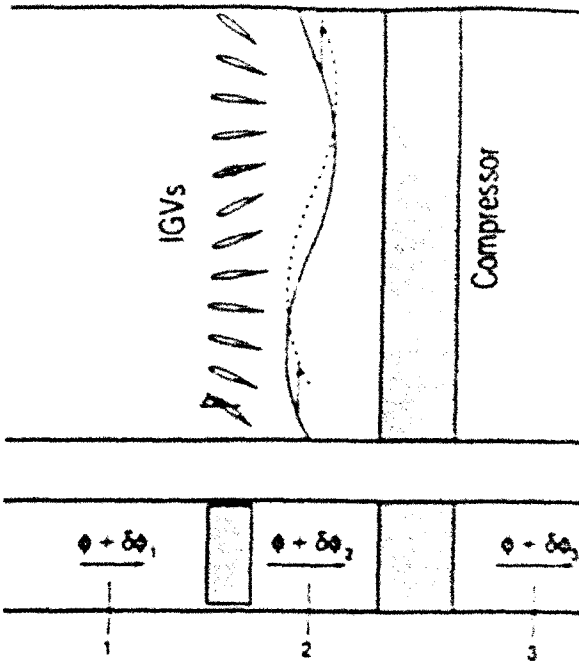


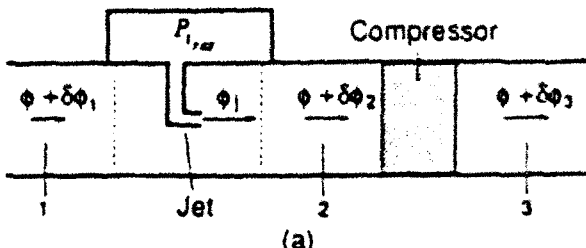
Figure 3: Inlet guide vane actuator

disturbances produced by the actuation to decay to small amplitudes at the compressor face. If so, there is a time delay corresponding to the convection time of the control disturbance from the actuator to the compressor face introduced into the control system. Even at moderate slopes of the compressor pressure-rise characteristic, the time scale associated with the disturbance growth rate is much smaller than this convection delay time. Actuators that produce a purely vortical disturbance at the compressor face are therefore not effective in controlling rotating stall, and in this study only close coupled actuators are considered. Actuators can be considered close coupled if they are positioned a distance much smaller than the compressor radius from the compressor inlet or exit plane.

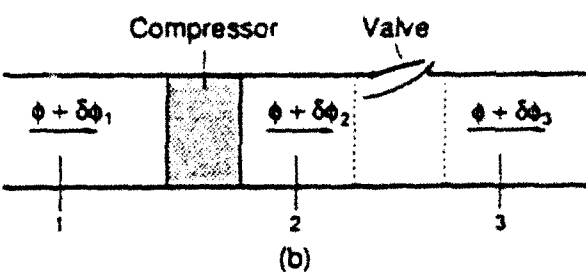
The following actuators are considered:

- 1) jets upstream of the compressor
- 2) intake ports upstream of the compressor
- 3) valves downstream of the compressor
- 4) movable inlet guide vanes upstream of the compressor

This is not a complete list of the actuators that could be used to control rotating stall, but the actuators considered give an indication of the variations in performance that one could expect in selecting an actuator. The actuators are shown schematically in figures 3-4. Although the intake port and jet actuators are similar physically, they differ in the type of disturbance that they introduce into the flow field. The jet actuator is supplied by a high pressure reservoir whereas the intake port actuator is supplied by a reservoir having the same total pressure as the compressor inlet. The consequence is that the intake port actuator introduces only potential disturbances into the flow field whereas the jet actuator introduces both potential and vortical disturbances. (Gysling [12] has identified the jet distribution as an effective actuator in a similar study on control of rotating stall using aeromechanical feedback.). In the study, the reservoir of the jet actuator is supplied by the exit of the compressor.



(a)



(b)

Figure 4: (a) Jet / intake port actuator
 (b) Valve actuator

so the reservoir stagnation pressure is set equal to the exit stagnation pressure at the compressor operating point. The intake port actuator does not require such a high pressure air supply; fluid at the total pressure of the inlet air can be derived from the free stream outside the compressor casing. The movable inlet guide vane actuator has already been implemented experimentally by Paduano [6] and Haynes [8], and is used as a basis for comparison for the other actuators. These experiments have also served as a validation of the modeling technique used in the study.

In the uncontrolled compression system the relation between flow coefficient and pressure perturbations at the compressor inlet and exit planes is determined by the dynamics of the fluid in the compressor, and in the inlet and exit ducts of the compressor. Under active control these relationships can be manipulated by the actuator. In the analysis the actuators are modeled using quasi-steady actuator disk theory. The last aspect of the analysis involves sensing a fluid dynamic variable, and prescribing a feedback law between the sensed variable and the actuation. Only the following proportional feedback law is considered in this paper:

$$\text{Actuation} = Z \times \text{Sensed variable}, \text{ where } Z = R e^{i\phi}.$$

R is the gain in amplitude of the sensed variable, and ϕ , the circumferential spatial phase shift of the actuated wave relative to the sensed wave. In the study the gain and spatial phase of the feedback signal are optimized for various compressor operating conditions.

In practice the output of the actuator will differ from the command given by the controller. To capture this (non-ideal) behavior, the actuator is modeled as a first-order time-lag system:

$$\tau_a \frac{d(\text{actuation})}{dt} = \text{command} - \text{actuation}$$

A time lag τ_a is assumed between the actuation and the command given by the controller. The inverse of this time constant, $1/\tau_a$, represents the bandwidth of the actuator.

When the feedback law and actuator dynamics are coupled to the compressor dynamics, a new eigenvalue problem is generated, with the eigenvalues of the system, i.e. the growth rate and frequency of the disturbance, dependent on the gain and phase of the feedback signal. The effect of non-ideal behavior of the actuator on the system performance can be assessed by varying the time constant associated with the actuation (varying the bandwidth of the actuator). These effects are described in the next section.

Sensors measuring the following flow variables are evaluated:

- 1) axial velocity
- 2) static pressure
- 3) stagnation pressure

A comparative study was done with the sensors positioned at various axial stations in the compression system: upstream of the actuator, between the actuator and the compressor, and downstream of the compressor. The performance of the controlled systems are reported only with the sensors located at the axial stations where they perform most favorably.

A detailed analysis of the compression system coupled with the jet actuator is given in Appendix A and B. Analysis of the inlet guide vane actuator is based on the model developed by Paduano et al, and details can be found in [6] and [7].

4. CALCULATED RESULTS AND DISCUSSION

4.1 Influence of Actuator Type

Figures 5-8 present neutral stability curves for the first harmonic of the disturbance wave. The results for the higher spatial harmonics show trends similar to those for the first harmonic. The figures show the maximum compressor slope ($d\psi/d\phi$) at which stabilization can be achieved, as a function of controller gain for the four actuators considered. The areas below the neutral stability curves represent stable operation of the controlled system. For the jet, intake port and valve actuators, gain is defined as the ratio of the non-dimensionalized mass flow added to, or removed from the flow field, and the sensed variable (velocity, static pressure, or stagnation pressure as indicated in Appendix B). For the movable inlet guide vane actuator, the gain is defined as the ratio of the deflection angle (in radians) of the inlet guide vanes from their zero positions, and the sensed variable.

In each case the performance of the controlled system is shown with the best sensor located at its optimum axial station (in all cases sensing the axial velocity perturbation gave the best results). The horizontal axis in the figures represents the spatial phase shift between the measured disturbance and the actuation, and the vertical axis shows the slope of the compressor total-to-static pressure rise characteristic. Only positive compressor slopes are shown, so the figure represents an operating range that was previously inaccessible to the uncontrolled compressor.

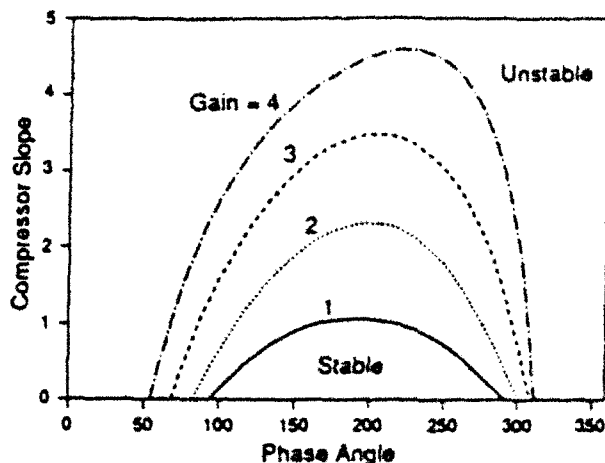


Figure 5: Jet actuator; compressor slope at neutral stability as a function of feedback gain and phase. The system is stable in the area under the curves.

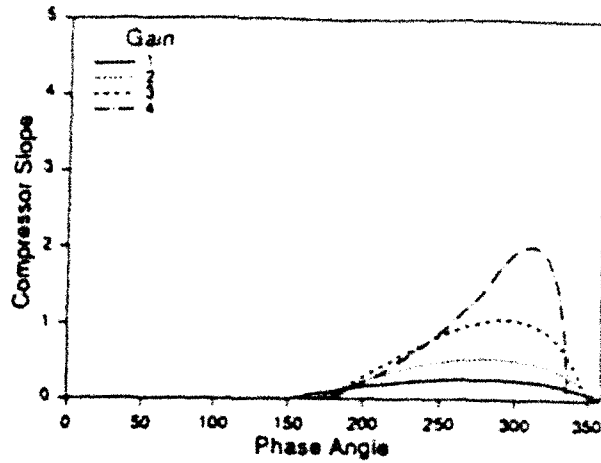


Figure 6: Intake port actuator; compressor slope at neutral stability as a function of feedback gain and phase. The system is stable in the area under the curves.

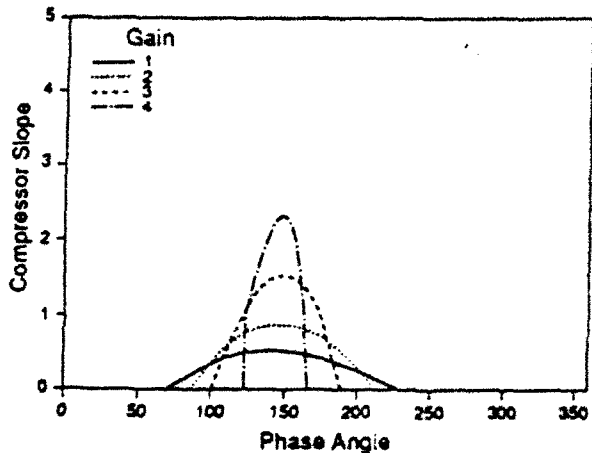


Figure 7: Downstream valve actuator; compressor slope at neutral stability as a function of feedback gain and phase. The system is stable in the area under the curves.

(The analysis was also performed for negative characteristic slopes; this indicated that the control system could destabilize a naturally stable compression system for certain phases of the controller.)

To facilitate comparison, the neutral stability curves for the four actuators operating at a gain of four are plotted on the same axes in figure 9. This gain was used for comparison since all the actuators showed unstable behavior for certain phases above this value. (An experiment on a three stage compressor [8] also showed that the performance of the system was degraded for gains above four.)

It should be noted that the performance of the inlet guide vane actuator is influenced by the "swirl sensitivity" of the compressor, i.e. the rate of change of pressure rise across the compressor with inlet guide vane deflection. The swirl sensitivity of the three stage compressor on which the experiment was performed [8], was used in the analysis since it was thought to be representative of practical compressors. Swirl sensitivity is determined

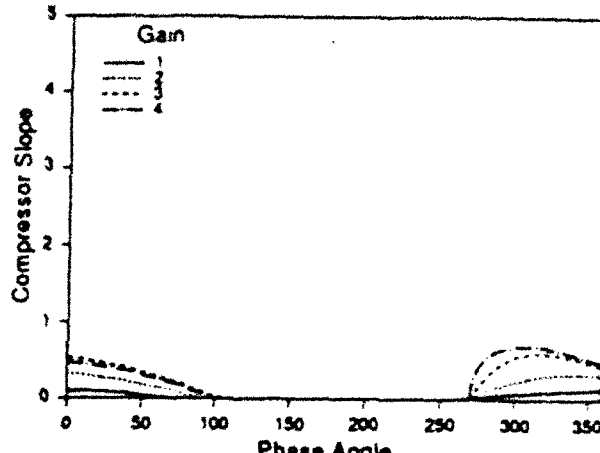


Figure 8: Inlet guide vane actuator; compressor slope at neutral stability as a function of feedback gain and phase. The system is stable in the area under the curves.

primarily by the rate of change of the pressure rise with inlet guide vane deflection in the first stage, since the inlet angles to the rotors of the downstream stages are not affected significantly by inlet guide vane deflection. It is therefore not dependent on the number of stages of the compressor, if the geometric configuration of the first stage is similar.

Three performance parameters that are important in comparing the various actuation systems are:

- 1) the largest positive compressor slope that the controlled system can achieve; this gives a measure of the range extension provided by the actuation system,
- 2) the *phase margin* of the controller, which gives a measure of the range of phases over which the controlled system is stable at a particular operating point, and
- 3) the rotation rate of the controlled perturbation. Under active control both the growth and rotation rates of the

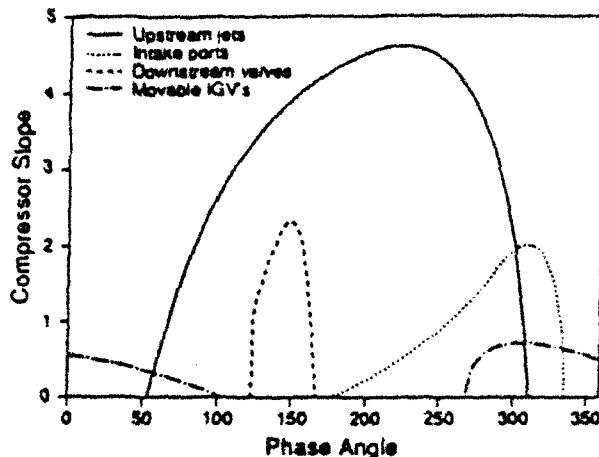


Figure 9: Comparison of actuation schemes; velocity sensing, gain=4.

flow perturbation are modified. The rotation rate of the controlled disturbance is important since it is one of the parameters that determines the bandwidth requirement of the actuator. An actuator that increases the rotation rate of the perturbation is undesirable.

From figure 9 it is apparent that the upstream jet distribution delivers the most favorable performance. In addition to providing the highest degree of range extension, the jet distribution also has the largest phase margin at a fixed operating point. At a compressor slope of 1, for example, the jet distribution stabilizes the compressor over a phase range of 250 degrees, as opposed to 100 degrees for the intake port distribution, and approximately 50 degrees for the downstream valves. The movable inlet guide vanes cannot stabilize the compressor at any phase at this slope.

Figure 10 shows the change in the growth and rotation rates of the first spatial harmonic of a disturbance in the individual controlled systems, at the optimum phase for each, as the feedback gain is increased. The jet distribution again performs most favorably since disturbance rotation rate is reduced as the feedback gain is increased. Note that the rotation rate of the disturbance wave is dependent on the gain and phase of the feedback

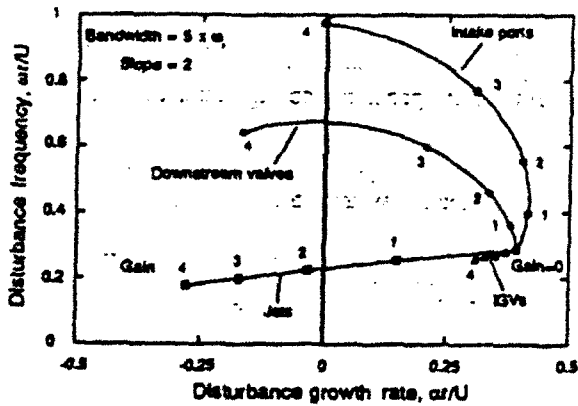


Figure 10: Perturbation growth and rotation rates at the optimum phase for each system

signal, and the dependence of rotation speed on gain shown in the figure holds for the optimum phase based on range extension at the particular operating point that was chosen. For a particular operating point one could also optimize the phase of the actuation to produce the lowest rotation rate for the controlled disturbance. Even if feedback phase is optimized in this way, the trends shown in figure 10 hold, i.e. the jet actuator achieves lower disturbance rotation rates than do the other actuators.

4.2 Influence of Sensor

Sensing schemes are compared using the jet distribution as an actuator, since it appears to be the most effective based on the performance criteria identified above. Figure 11 shows a comparison of the system performance with the various sensing schemes. In this figure the sensors are located at the axial station where they perform best; downstream of the actuator for axial velocity sensing (either upstream or downstream of the compressor), and downstream of the compressor for static and stagnation pressure sensing. From the figure it is apparent that the system performs best when axial velocity is sensed. While axial velocity is readily measured in low speed flows with hot wires, these sensors are not practical in high speed turbomachinery. Here velocity could be synthesized from total and static pressure measurements.

There are indications that the disappointing performance of the pressure sensors could be a result of the simple proportional feedback law that was used. The system performance could possibly be improved if dynamic compensation is used in the feedback loop, but this was not pursued in the study.

4.3 Influence of Actuator Bandwidth

For the results that have been presented thus far, a bandwidth of five times the rotor frequency has been used in order to compare the actuators and sensors operating as close as possible to ideal. This actuator bandwidth might be difficult to achieve in practice and figure 12 shows a comparison of the performance of the jet actuator for various bandwidths, from five times rotor frequency down to 50% of rotor frequency. The major effect of decreasing the bandwidth is narrowing of the phase margin of the actuation system. The range extension

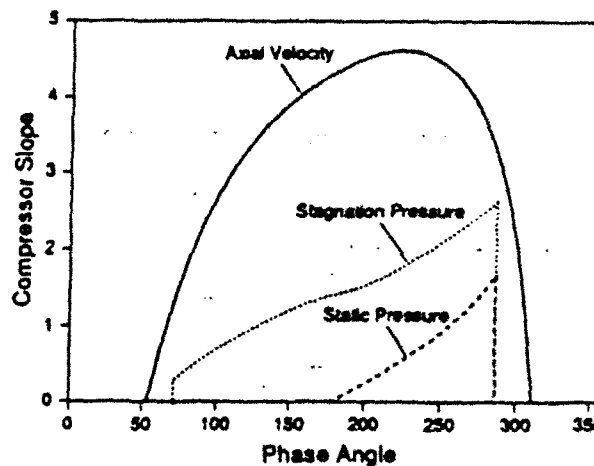


Figure 11: Jet actuator with various sensors; neutral stability at a gain=4.

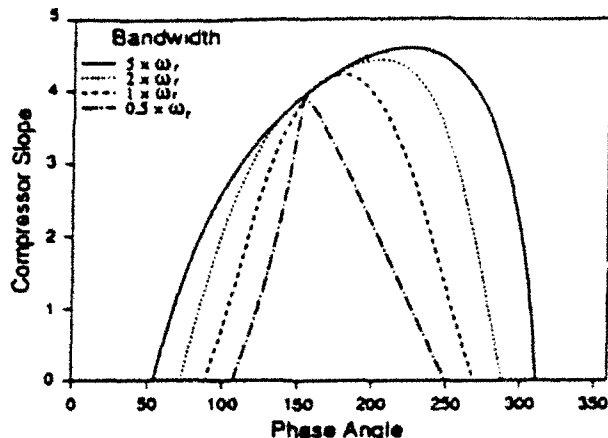


Figure 12: Jet actuator; neutral stability as a function of actuator bandwidth

gained from the actuator is affected less severely by narrower actuator bandwidths.

The other actuators are impacted more severely by a decrease in actuator bandwidth than is the jet actuator, as seen in figure 13. The plot is similar to figure 10, except that the actuator bandwidth has been decreased from five to two times rotor frequency. Because the rotational frequency of the controlled disturbance is small in the case of the jet actuator, the increased time delay corresponds to a small additional spatial phase shift between the sensed and the actuated waves, so the effect on the stability of the wave is relatively small. With the valve and intake port actuators, the frequency of the controlled wave increases significantly as the gain is increased, as seen in figure 10. An increase in actuator time delay therefore increases the spatial phase shift between the sensed and actuated waves significantly. In addition, from figure 9, it is evident that the range of phases over which these controlled systems are stable is significantly smaller than in the case of the jet actuator. The additional spatial phase shift in the actuation which results from the increased time delay moves the system outside the area of previously stable operation. This is clear if one compares figure 13 to figure 10. The effects of time delays can probably be decreased if suitable dynamic compensation is used in the

feedback loop, but this has not been pursued in the present study.

4.4 Practical Implementation Issues

It has been observed in the experiments that have been conducted with the movable inlet guide vane actuator that flow coefficient perturbations of the order of 1% are experienced upstream of the actuator when the compressor is operated under active control [13]. For the jet distribution, the mass injected into the compressor annulus would be approximately 2% of the annulus mass flow for every 1% flow coefficient fluctuation upstream of the actuator when the controller is operated at a gain of four. The control can influence compressor efficiency in two ways. The first would be the effect of the jets on the detailed fluid mechanics in the blade passages. This may have a positive or negative impact on performance depending on the design details. This question is beyond the scope of the present study. The second impact on compressor efficiency is associated with the air supply required to feed the jets. If the injected fluid is supplied from the compressor exit, an efficiency penalty would be incurred since the injected air would then be recycled through the compressor continually. If this were the only source of efficiency loss, the efficiency of the controlled system can be approximated by the expression:

$$\eta_{\text{controlled}} = \frac{\psi + 0.5(1+x)^2\phi^2 + x\phi(\phi_r - \phi)}{(1+x)(\psi + 0.5(1+x)^2\phi^2)} \eta_{\text{uncontrolled}}$$

where x is the mass fraction of fluid recycled through the compressor. The ratio of controlled to uncontrolled efficiency is plotted as a function of mass fraction recirculated in figure 14, for a compressor operating at a total to static pressure rise of 1, at a flow coefficient of 0.5 (these are the operating conditions of the three stage experimental compressor that has been used in the active control program, close to stall [8]). For a recycled mass fraction of 2%, an efficiency penalty of approximately 1% is incurred, which may be acceptable as it need only be incurred in the otherwise unstable portion of the compressor map, since the control system may be deactivated on the stable part of the compressor map. If

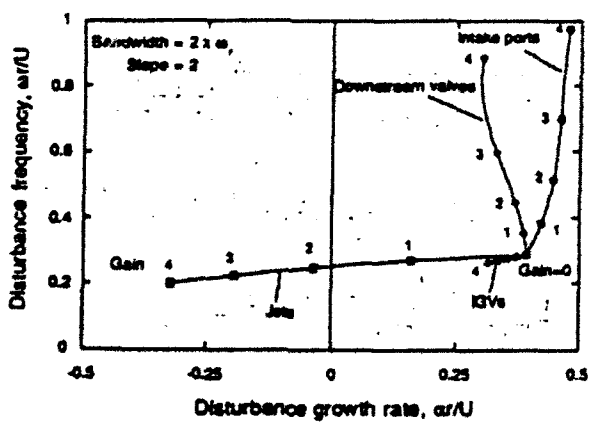


Figure 13: Perturbation growth and rotation rates (bandwidth = 2 x rotor frequency)

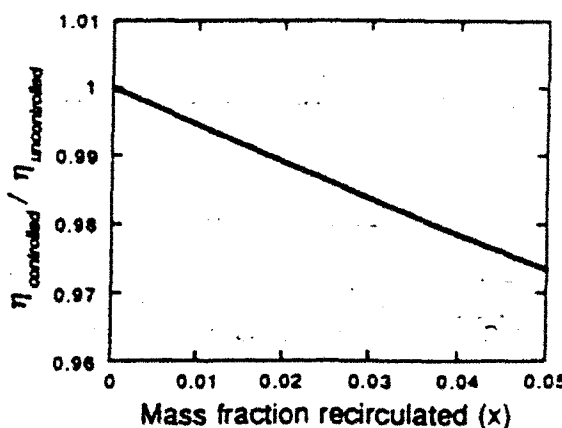


Figure 14: Efficiency loss ratio as a function of mass fraction recirculated for the jet actuator

the efficiency penalty is of concern and only a modest increase in range extension is desired, the other actuation schemes such as the moving inlet guide vane and intake port actuators could be selected, since these do not incur the bleed air penalty.

5. CONCLUSIONS

The model that has been used in this study captures the behavior of the rotating stall disturbance waves that have been observed in experiments. The quantitative agreement of the model with the experiments gives us confidence in using the modeling technique in the analysis of the controlled compressors considered in the study. This theoretical analysis indicates that a circumferential array of jets upstream of the compressor performs significantly better than the other actuators that were considered, in all of the performance criteria that were identified. In addition to providing the maximum range extension, jets also outperform the other actuators that were considered in other areas that would be important in practical applications. The large phase margin associated with jet actuation implies that the system will not be sensitive to errors in disturbance wave measurement. The jet actuator decreases the rotation rate of disturbances and this alleviates the high bandwidth requirement of some of the other actuators. One may however, incur an efficiency penalty when the jet actuator is used, because of the high pressure air supply required. This penalty is incurred only if the compressor is operated in the previously unstable flow range. Whether this efficiency penalty is acceptable or not depends on the design goals of the compressor.

The results of the study also indicate that velocity sensing is more effective than either static or total pressure sensing in controlling rotating stall disturbances, for the proportional control law that was considered. In low speed compressors velocity sensing with hot wire probes is effective, but in high speed compressors the use of hot wires might not be practical. The velocity perturbation could then be synthesized from static and total pressure measurements.

The bandwidth requirement of actuators is important since it has a significant effect on the performance of the controlled system. For the jet actuator the phase margin of the controlled system is degraded as the bandwidth of the actuator is reduced.

Finally, although the movable inlet guide vane actuator performed well in practice, it did not compare favorably with the other actuators that were considered in the theoretical study. The potential for compressor range extension is therefore much greater than that achieved thus far in the laboratory.

6. ACKNOWLEDGMENTS

This work has been supported by the U.S. Air Force Office of Scientific Research, Major D. Fant technical monitor, and the Government Engine and Space Propulsion Division of Pratt & Whitney / United Technologies, Dr. S. Baghadi and Mr. J. Garberoglio technical monitors. Financial support for D.L. Gysling was provided by the Air Force Research in Aero Propulsion Technology (AFRAPT) program. The authors wish to thank Professors E.M. Greitzer, A.H. Epstein, J.D. Padiano, and Messrs. J.S. Simon, and J.M. Haynes for many illuminating discussions.

7. REFERENCES

- 1) Moore F.K., "A Theory of Rotating Stall of Multistage Axial Compressors: Part 1 - Small Disturbances", *Journal of Engineering for Gas Turbines and Power*, Vol. 106, April 1984, pp. 313-320.
- 2) Hynes T.P., Greitzer E.M., "A Method for Assessing Effects of Circumferential Flow Distortion on Compressor Stability", *Journal of Turbomachinery*, Vol. 109, July 1987, pp. 371-379.
- 3) Epstein A.H., Ffowcs Williams J.E., Greitzer E.M., "Active Suppression of Aerodynamic Instabilities in Turbomachines", *Journal of Propulsion and Power*, V.5, No 2, March-April 1989, pp. 204-211.
- 4) Garnier V.H., Epstein A.H., Greitzer E.M., "Rotating Waves as a Stall Inception Indication in Axial Compressors", *Journal of Turbomachinery*, Vol. 113, 1991, pp. 290-301.
- 5) McDougal N.M., Cumpsty N.A., Hynes T.P., "Stall Inception in Axial Compressors", *Journal of Turbomachinery*, Vol. 112, January 1990, pp. 116-125.
- 6) Padiano J. D., "Active Control of Rotating Stall in Axial Compressors", Ph.D. Thesis, Massachusetts Institute of Technology, Department of Aeronautics and Astronautics, November 1991.
- 7) Padiano J., Epstein A.H., Valavani L., Longley J.P., Greitzer E.M., Guenette G.R., "Active Control of Rotating Stall in a Low Speed Axial Compressor", ASME paper 91-GT-88, Presented at the International Gas Turbine and Aeroengine Congress and Exposition, Orlando, Florida, June 3-6, 1991.
- 8) Haynes J.M., "Active Control of Rotating Stall in a Three-Stage Axial Compressor", M.S. Thesis, Department of Mechanical Engineering, Massachusetts Institute of Technology, September, 1992.
- 9) Nagano S., Machida Y., Takata H., "Dynamic Performance of Stalled Blade Rows", Japan Society of Mechanical Engineering Paper JSME 11, Presented at the Tokyo Joint International Gas Turbine Conference, Tokyo, Japan, October 1971.
- 10) Mazzawy R.S., "Multiple Segment Parallel Compressor Model for Circumferential Flow Distortion", *Engineering for Power*, Vol. 99, No. 2, April 1977.
- 11) Greitzer E.M., Epstein A.H., Guenette G.R., Gysling D.L., Haynes J., Hendricks G.J., Padiano J., Simon J.S., Valavani L., "Dynamic Control of Aerodynamic Instabilities in Gas Turbine Engines", Presented at the AGARD Lecture Series on Steady and Transient Performance Prediction of Gas Turbine Engines, Cambridge, USA, May 27-28, 1992.
- 12) Gysling D.L., "Dynamic Control of Rotating Stall in Axial Flow Compressors Using Aeromechanical Feedback", Ph.D. Thesis, Massachusetts Institute of Technology, Department of Aeronautics and Astronautics, To be published.

13) Haynes J.M., Massachusetts Institute of Technology, Private communication.

14) Chue R., Hynes T.P., Greitzer E.M., Tan C.S., Longley J.P., "Calculations of Inlet Distortion Induced Compressor Flow Field Instability", *International Journal of Heat and Fluid Flow*, Vol. 10, No. 3, September 1989.

APPENDIX A: OVERALL FLOW MODEL

The basic derivation of the flow has appeared several times before [1,2,3] and is included for completeness only. In the model the pressure rise across a compressor is modified by the pressure difference required to overcome the inertia of the fluid within the blade channels, when the flow within the compressor is unsteady. If one assumes that the flow within the blade passages is one dimensional, the unsteady pressure rise across the compressor can be written as ([1], [2]):

$$\frac{P_s - P_d}{\rho U^2} = \psi - \lambda \frac{\partial \phi}{\partial \vartheta} - \frac{\mu r}{U} \frac{\partial \phi}{\partial t} \quad (A1)$$

where: $\psi = \psi_i - L_r - L_s$, $(A2)$

ψ_i is the ideal stagnation pressure rise across the compressor and L_r and L_s are the rotor and stator stagnation pressure losses. The inertia of the fluid in the rotors and in the compressor are represented by λ and μ respectively. At the initiation of rotating stall, the flow coefficient through the compressor is modified by a small perturbation $\delta\phi$ so that:

$$\begin{aligned} \phi &= \phi + \delta\phi & \psi_i &= \psi_i + \frac{d\psi_i}{d\phi} \delta\phi \\ P_s &= P_s + \delta P_s & L_r &= L_r + \delta L_r \\ P_d &= P_d + \delta P_d & L_s &= L_s + \delta L_s \end{aligned} \quad (A3)$$

The compressor pressure rise perturbation equation is therefore:

$$\frac{\delta P_s - \delta P_d}{\rho U^2} = \frac{d\psi_i}{d\phi} \delta\phi - \delta L_r - \delta L_s - \lambda \frac{\partial(\delta\phi)}{\partial \vartheta} - \frac{\mu r}{U} \frac{\partial(\delta\phi)}{\partial t} \quad (A4)$$

$$\psi_i = \psi_{i,0} + L_{r,0} + L_{s,0} \quad (A5)$$

where $\psi_{i,0}$ is the steady, axisymmetric total-to-static pressure rise including losses, and $L_{r,0}$ and $L_{s,0}$ the steady stator and rotor stagnation pressure losses respectively. The stator unsteady stagnation pressure loss perturbation, δL_s , is taken to be given by the differential equation:

$$\tau_r \frac{\partial(\delta L_s)}{\partial t} = \frac{\partial L_{s,0}}{\partial \phi} \delta\phi - \delta L_s \quad (A6)$$

The rotor unsteady stagnation pressure loss, δL_r , has to be calculated in a reference frame rotating with the rotor:

$$\tau_r \left(\frac{\partial(\delta L_r)}{\partial t} + \frac{U}{r} \frac{\partial(\delta L_r)}{\partial \vartheta} \right) = \frac{\partial L_{r,0}}{\partial \phi} \delta\phi - \delta L_r \quad (A7)$$

In the analysis, a general perturbation in flow coefficient of the form:

$$\delta\phi = \sum_n A_n e^{(a+i\omega)t} e^{in\vartheta} \quad (A8)$$

is considered. Each spatial harmonic of the perturbation can be considered separately and only the n th spatial harmonic:

$$\delta\phi = A_n e^{(a+i\omega)t} e^{in\vartheta} \quad (A9)$$

will therefore be examined.

The variables describing the evolution of the perturbation can be non-dimensionalized as follows:

$$i = \frac{iU}{r}, \quad \bar{t} = \frac{tU}{r}, \quad s = \frac{(a+i\omega)r}{U}, \quad (A10)$$

where U is the rotor speed and r is the average radius of the compressor annulus, so that the equations describing the perturbation become:

$$\frac{\delta P_s - \delta P_d}{\rho U^2} = \frac{d\psi_i}{d\phi} \delta\phi - \delta L_r - \delta L_s - \lambda \frac{\partial(\delta\phi)}{\partial \vartheta} - \mu \frac{\partial(\delta\phi)}{\partial t} \quad (A11)$$

$$\bar{t} \frac{\partial(\delta L_s)}{\partial \bar{t}} = \frac{\partial L_{s,0}}{\partial \phi} \delta\phi - \delta L_s \quad (A12)$$

$$\bar{t} \left(\frac{\partial(\delta L_r)}{\partial \bar{t}} + \frac{\partial(\delta L_r)}{\partial \bar{\vartheta}} \right) = \frac{\partial L_{r,0}}{\partial \phi} \delta\phi - \delta L_r \quad (A13)$$

$$\delta\phi = A_n e^{is} e^{in\bar{\vartheta}} \quad (A14)$$

The upstream stagnation and downstream static pressure perturbations are given by the expressions [3]:

$$\frac{\delta P_s}{\rho U^2} = - \frac{1}{|\mu|} \frac{\partial(\delta\phi)}{\partial \bar{t}} \quad (A15)$$

, and $\frac{\delta P_d}{\rho U^2} = \frac{1}{|\mu|} \frac{\partial(\delta\phi)}{\partial \bar{t}}$ $(A16)$

Substitution of (A15), (A16) and (A14) into (A11)-(A13) produces a generalized, complex eigenvalue problem in s :

$$(A - sB) \delta\bar{\vartheta} = 0 \quad (A17)$$

where:

$$A = \begin{pmatrix} \frac{1}{\zeta} \left(\frac{d\psi_i}{d\phi} - in\lambda \right) & -\frac{1}{\zeta} & -\frac{1}{\zeta} \\ \frac{1}{\bar{\tau}_i} \frac{dL_{r,ss}}{d\phi} & -\frac{1}{\bar{\tau}_i} & 0 \\ \frac{1}{\bar{\tau}_i} \frac{dL_{s,ss}}{d\phi} & 0 & -\left(in + \frac{1}{\bar{\tau}_i} \right) \end{pmatrix} \quad (A18)$$

$$B = \begin{pmatrix} 1 & 0 & 0 \\ 0 & 1 & 0 \\ 0 & 0 & 1 \end{pmatrix}, \quad \delta\bar{x} = \begin{pmatrix} \delta\phi \\ \delta L_r \\ \delta L_s \end{pmatrix} \quad (A19), (A20)$$

$$\zeta = \left(\frac{2}{|n|} + \mu \right), \text{ and } \psi_i = \psi_{ss} + L_{s,ss} + L_{r,ss}. \quad (A21), (A22)$$

The solution to the eigenvalue problem yields the growth and rotation rates of the perturbation wave. If the real part of s is negative, the disturbance is damped, representing stable operation of the compressor. If the real part of s is positive, the disturbance grows exponentially, representing unstable operation. For the uncontrolled compressor the growth rate of the perturbation is determined by the slope of the total-to-static pressure rise characteristic.

To determine the unsteady response of the compressor to flow perturbations, an isentropic pressure rise characteristic for the compressor has to be assumed. For the analysis it is assumed that the compressor operates at its maximum efficiency at a flow coefficient of 0.6. At this maximum efficiency operating point the slope of the isentropic pressure rise characteristic is close to that of the measured pressure rise characteristic, since the losses are minimum. To simplify the analysis, the isentropic characteristic is assumed to have this slope over the entire operating range of the compressor as shown in figure 15. The steady total pressure loss

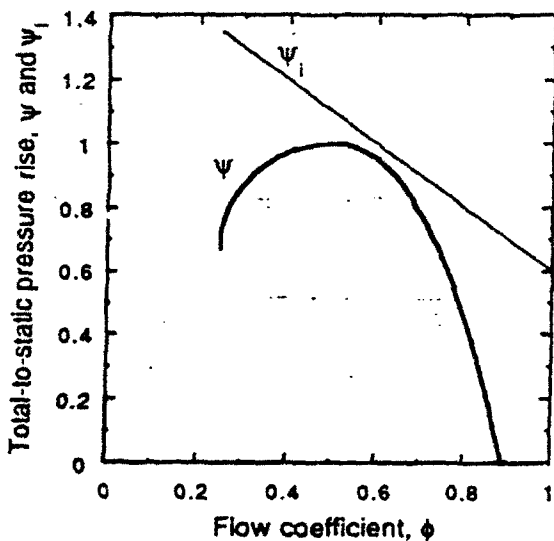


Figure 15 Compressor total-to-static characteristics used in the analysis.

($L_{ss}(\phi) = L_{r,ss}(\phi) + L_{s,ss}(\phi)$) used in equation (A5) is then the difference between the isentropic pressure rise curve and the measured one. In the analysis it is also assumed that steady total pressure losses are equally distributed across the rotors and the stators (i.e. $L_{r,ss} = L_{s,ss}$).

APPENDIX B:

MODIFICATION OF THE FLOW MODEL FOR ACTIVE CONTROL

In an actively controlled compressor, the relationship between pressure and velocity perturbations can be manipulated by the actuator. Analysis of the various actuators involves determining relationships between the actuation and perturbations in velocity and pressure introduced into the flow field. The actuators are modeled using quasi-steady actuator disk theory. Mass and momentum balances across the actuators give relationships between velocity and pressure perturbations upstream and downstream of the actuators, as a function of the actuation. The upstream jet distribution will be used as an example to illustrate the analysis method. A mass balance across the actuator gives:

$$\rho(c_s + \delta c_{s1})l_s + \rho c_{s2} \delta l_j = \rho(c_s + \delta c_{s2})l_s \quad (A23)$$

and non-dimensionalizing the velocities by the rotor speed U yields:

$$\delta\phi_j = \delta\phi_1 + \phi_j \frac{\delta l_j}{l_s} \quad (A24)$$

The non-dimensionalized injection rate $\phi_j(\delta l_j/l_s)$ is a function of the annulus spatial variable ϑ . The non-dimensionalized injection axial velocity ϕ_j , the jet nozzle opening δl_j , and the annulus height l_s are indicated in figure 16.

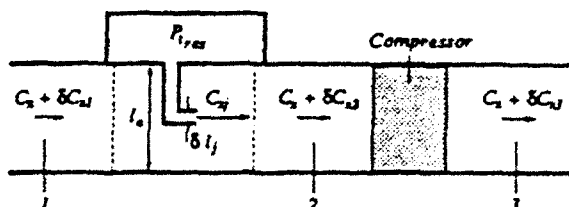


Figure 16 Jet actuator

A momentum balance across the actuator gives:

$$\rho(c_s + \delta c_{s1})^2 l_s + (P + \delta P_1)l_s + \rho c_{s2}^2 \delta l_j = \rho(c_s + \delta c_{s2})^2 l_s + (P + \delta P_2)l_s \quad (A25)$$

If only first order terms are retained, the above expression yields:

$$\frac{\delta P_1}{\rho U^2} = \frac{\delta P_1}{\rho U^2} + (\phi_j - 2\phi) \phi_j \frac{\delta l_j}{l_s} \quad (A26)$$

Equation (A26) can be written in terms of the total pressure perturbation at the compressor face:

$$\frac{\delta P_{12}}{\rho U^2} = \frac{\delta P_{11}}{\rho U^2} + (\phi_1 - \phi) \phi_1 \frac{\delta l_1}{l_a} \quad (A27)$$

The downstream static pressure perturbation is given by expression (A16). It is apparent from (A23) and (A26) that the compressor inlet total pressure and flow coefficient perturbations can be controlled by specifying $\phi_1(\delta l_1/l_a)$, the annular injection rate of jet fluid into the air stream.

Control is accomplished by sensing a fluid dynamic variable describing the perturbation. The measured signal is then processed by the controller which commands the actuator to introduce a suitable perturbation into the flow field. In the simplest controller, the measured signal is modified in amplitude and shifted spatially in phase (proportional feedback). This is implemented analytically as follows; if the flow coefficient perturbation at the compressor face is sensed, the commanded jet injection rate is:

$$\phi_1 \frac{\delta l_1}{l_a} \Big|_e = Z \delta \phi_2, \quad Z = R e^{i\theta}. \quad (A28), (A29)$$

where R is the gain in amplitude of the signal, and θ is the spatial phase shift of the commanded signal relative to the measured signal. In practice, non-ideal behavior will cause the output from the actuator to differ from the command given by the controller. To capture the non-ideal dynamics, the actuator is modeled as a first order system:

$$\bar{\tau}_a \frac{\partial}{\partial t} \left(\phi_1 \frac{\delta l_1}{l_a} \right) = \phi_1 \frac{\delta l_1}{l_a} \Big|_e - \phi_1 \frac{\delta l_1}{l_a} \quad (A30)$$

where $\bar{\tau}_a$ is the time constant associated with the actuator. If the flow coefficient (axial velocity) at the compressor face is sensed, the actuator equation becomes:

$$\bar{\tau}_a \frac{\partial}{\partial t} \left(\phi_1 \frac{\delta l_1}{l_a} \right) = Z \delta \phi_2 - \phi_1 \frac{\delta l_1}{l_a} \quad (A31)$$

Sensing the other fluid dynamic variables give the following actuator commands:

stagnation pressure upstream of the actuator:

$$\phi_1 \frac{\delta l_1}{l_a} \Big|_e = Z \frac{\delta P_{11}}{\rho U^2} = -Z \frac{s}{|n|} \left(\delta \phi_2 - \phi_1 \frac{\delta l_1}{l_a} \right) \quad (A32)$$

static pressure upstream of the actuator:

$$\phi_1 \frac{\delta l_1}{l_a} \Big|_e = Z \frac{\delta P_{11}}{\rho U^2} = -Z \left(\frac{s}{|n|} + \phi \right) \left(\delta \phi_2 - \phi_1 \frac{\delta l_1}{l_a} \right) \quad (A33)$$

exit static pressure:

$$\phi_1 \frac{\delta l_1}{l_a} \Big|_e = Z \frac{\delta P_{11}}{\rho U^2} = Z \frac{s}{|n|} \delta \phi_2 \quad (A34)$$

exit stagnation pressure

$$\phi_1 \frac{\delta l_1}{l_a} \Big|_e = Z \frac{\delta P_{11}}{\rho U^2} = Z \left(\frac{s}{|n|} + \phi \right) \delta \phi_2 \quad (A35)$$

which, when substituted into equation (A30), yield equations similar to equation (A31).

Equations (A11)-(A13) and equation (A30) with the appropriate sensed variable produce an eigenvalue problem. Parameters in the analysis are the operating flow coefficient (which determines the slope of the pressure rise characteristic), the gain and phase of the feedback control law, and the bandwidth of the actuator. For the jet distribution with velocity feedback the system of differential equations reduces to the form given in (A17), where the matrices A , B , and the vector $\delta \bar{x}$ are now:

$$A = \begin{pmatrix} \frac{1}{\zeta} \left(\frac{d\psi_i}{d\phi} - in\lambda \right) & -\frac{1}{\zeta} & -\frac{1}{\zeta} & \frac{1}{\zeta} (\phi_1 - \phi) \\ \frac{1}{\bar{\tau}_a} \frac{dL_{s,u}}{d\phi} & -\frac{1}{\bar{\tau}_a} & 0 & 0 \\ \frac{1}{\bar{\tau}_a} \frac{dL_{r,u}}{d\phi} & 0 & -\left(in + \frac{1}{\bar{\tau}_a} \right) & 0 \\ \frac{1}{\bar{\tau}_a} Z & 0 & 0 & \frac{1}{\bar{\tau}_a} \end{pmatrix} \quad (A37)$$

$$B = \begin{pmatrix} 1 & 0 & 0 & -\frac{1}{|n|\zeta} \\ 0 & 1 & 0 & 0 \\ 0 & 0 & 1 & 0 \\ 0 & 0 & 0 & 1 \end{pmatrix}, \quad \delta \bar{x} = \begin{pmatrix} \delta \phi_2 \\ \delta L_s \\ \delta L_r \\ \phi_1 \frac{\delta l_1}{l_a} \end{pmatrix} \quad (A38), (A39)$$

with:

$$\zeta = \left(\frac{2}{|n|} + \mu \right), \text{ and } \psi_i = \psi_u + L_{s,u} + L_{r,u}. \quad (A40), (A41)$$

There are four eigenvalues for each spatial harmonic of the disturbance.

VI. CONTROL OF SURGE AND STALL WITH STRUCTURAL DYNAMICS

Dynamic Control of Centrifugal Compressor Surge Using Tailored Structures

D. L. Gysling

J. Dugundji

E. M. Greitzer

A. H. Epstein

Gas Turbine Laboratory,
Department of Aeronautics and Astronautics,
Massachusetts Institute of Technology,
Cambridge, MA 02139

A new method for dynamic control of centrifugal compressor surge is presented. The approach taken is to suppress surge by modifying the compression system dynamic behavior using structural feedback. More specifically, one wall of a downstream volume, or plenum, is constructed so as to move in response to small perturbations in pressure. This structural motion provides a means for absorbing the unsteady energy perturbations produced by the compressor, thus extending the static operating range of the compression system. In the paper, a lumped parameter analysis is carried out to define the coupled aerodynamic and structural system behavior and the potential for stabilization. First-of-a-kind experiments are then conducted to examine the conclusions of the analysis. As predicted by the model and demonstrated by experiment, a movable plenum wall lowered the mass flow at which surge occurred in a centrifugal compression system by roughly 25 percent for a range of operating conditions. In addition, because the tailored dynamics of the structure acts to suppress instabilities in their initial stages, this control was achievable with relatively little power being dissipated by the movable wall system, and with no noticeable decrease in steady-state performance. Although designed on the basis of linear system considerations, the structural control is shown to be capable of suppressing existing large-amplitude limit cycle surge oscillations.

Introduction

The operating range of turbomachinery compression systems is very often limited by the onset of fluid dynamic instabilities. Surge is a self-excited, essentially one-dimensional instability, which is characterized by oscillations in area-averaged mass flow and pressure rise, and is generally the most important instability in centrifugal compression systems. Surge can cause reduced performance and efficiency of the turbomachine, and, in some cases, failure due to the large unsteady aerodynamic forces on the blades (Stenning, 1980).

To avoid surge, the compression system is generally operated away from the "surge line," the boundary between stable and unstable operation on the pressure rise versus mass flow performance map. Operating the compressor at some distance from this line, on the negatively sloped part of the compressor speedlines, can ensure stable operation. Doing this, however, may result in a performance penalty since peak performance and efficiency often occur near the surge line (Dean and Young, 1977).

The goal of the research described here is to develop methods to extend the stable operating range by modifying the dynamic behavior of the compression system to suppress surge. This would allow compressor operation in previously unusable, or

even previously unstable, regions of the compressor map. The experimental phase of the current research is focused on centrifugal compression systems, although the analysis applies to axial compression systems as well.

Dynamic Surge Suppression

Surge is the manifestation of a dynamic instability, which occurs when the compressor feeds more mechanical energy into disturbance than the rest of the system can dissipate. The result is an oscillatory disturbance that grows exponentially, until limited by nonlinearity, into a limit cycle (surge cycle). The key to dynamic surge suppression, therefore, lies in increasing the system's ability to dissipate or damp this disturbance energy (Epstein et al., 1989).

There have been several investigations of surge suppression, all in recent years, using closed-loop active control to increase system damping. Ffowcs Williams and Huang (1989) used a movable plenum wall, driven by a signal proportional to the unsteady plenum pressure, to suppress surge in a centrifugal turbocharger. Pinsky et al. (1991) describe active stabilization using a variable area throttle valve, also driven by a signal proportional to the unsteady plenum pressure. Both of these studies demonstrated that surge can be suppressed in the linear regime, before the disturbances grow to large amplitude, by modification of system dynamics through closed-loop control.

There has been little previous work on stabilization using

Contributed by the International Gas Turbine Institute and presented at the 35th International Gas Turbine and Aeroengine Congress and Exposition, Brussels, Belgium, June 11-14, 1990. Manuscript received by the International Gas Turbine Institute January 18, 1990. Paper No. 90-GT-122.

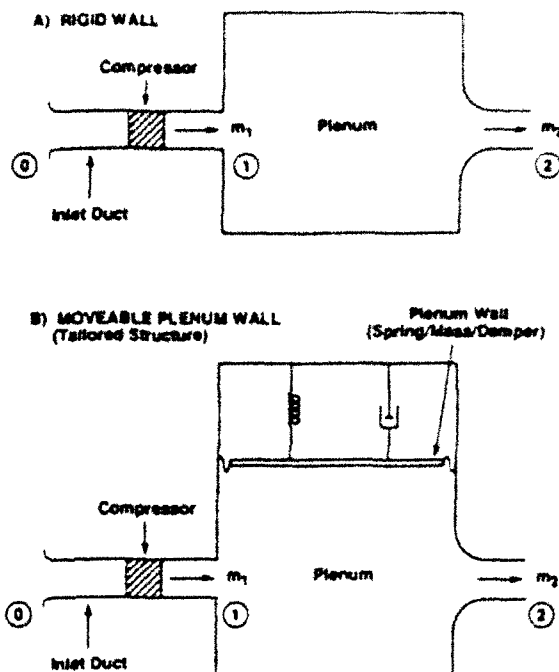


Fig. 1 Schematic of rigid (fixed) wall (a) and movable plenum wall (b) compression systems

structural feedback. In this approach, the dynamic properties of the system are modified so that the compression system becomes inherently stable, without external input. A limited analytical investigation of such a control scheme has been carried out by Chen (1987). He found that a variable area throttle valve, modeled as a mass-spring-damper driven by plenum pressure perturbations, would have a stabilizing effect, but that a flexible plenum wall with no damping would be destabilizing.

Scope of the Present Work

The work reported here is directed at surge suppression in centrifugal compression systems using tailored structural dy-

namics as a feedback mechanism. A movable plenum wall is used as the tailored structure. The movable wall acts as a mass-spring-damper system driven by unsteady pressure perturbations in the plenum, and its motion is thus coupled to the compression system dynamics. A schematic of a generic rigid compression system and a modified compression system having a tailored structure is shown in Figs. 1(a) and 1(b).

It will be demonstrated that an appropriately tailored moving plenum wall can significantly extend the stable operating range of a compression system. The aeroelastic coupling between the wall and the basic compression system allows the damper on the moving wall to dissipate mechanical energy associated with flow disturbances, thereby suppressing surge. The degree of suppression depends on matching the structural dynamics to the system fluid dynamics. A set of nondimensional parameters, which govern the interaction between the compression system and the wall, are thus presented and their influence is developed. Experiments are carried out to evaluate the actual performance of the flexible plenum wall system and the analytical model.

System Modeling

The basic lumped parameter model of the compression system has been used by other authors to investigate surge for a rigid plenum configuration (e.g., Emmons et al., 1955; Greitzer, 1981). In this description, system inertia is represented by the fluid in the inlet ducting, system compliance is due to the compressibility of the fluid in the plenum, and system damping (positive or negative) is due to the compressor and the throttle.

The differential equations describing the compression system with flexible plenum wall are given below.

Inlet duct momentum

$$(P_0 + \Delta P_c - P_s) A_{in} = \frac{d(\rho_0 A_{in} L_c C_s)}{dt} \quad (1)$$

The quantity ΔP_c is the compressor pressure rise, which is a known function of mass flow, m .

Mass conservation in the plenum

$$\dot{m}_1 - \dot{m}_2 = \frac{d(\rho_0 V_p)}{dt} \quad (2)$$

Nomenclature

a	speed of sound	U	impeller exit tip speed	ω_H	Helmholtz frequency = $a\sqrt{A_{in}/V_p L_c}$
A_{in}	compressor inlet area	v	nondimensional wall velocity	ω_s	frequency of wall mass-spring-damper system
A_s	plenum movable wall area	V	volume	$d\psi_c/d\phi$	slope of compressor characteristic
B	stability parameter	W	nondimensional wall aero-elastic coupling parameter		
	$= (U/2a)\sqrt{(V_{plenum}/A_{in}L_c)}$	ζ	nondimensional wall damping ratio parameter		
	$= (U/2\omega_H L_c)$	η	nondimensional wall displacement		
C_x	axial velocity	ρ	density	c	compressor
f	Coulomb friction force	τ	nondimensional time = $\omega_H t$	in	compressor inlet
F	nondimensional Coulomb friction force = $f/(\rho_0 U^2 A_p)$	ϕ	mass flow coefficient = $\dot{m}/(\rho_0 U A_{in})$	p	plenum
I	rotational inertia of turbo-spool	ψ	plenum pressure coefficient = $(P_p - P_0)/0.5\rho_0 U^2$	t	throttle; tip of impeller exit
L	effective length	V_c	compressor pressure rise coefficient = $\Delta P_c/0.5\rho_0 U^2$	0	ambient conditions
m	mass of plenum wall	ψ_t	throttle pressure drop coefficient = $\Delta P_t/0.5\rho_0 U^2$	1	compressor exit
\dot{m}	mass flow			2	plenum exit
P	pressure				
ΔP	pressure difference				
ΔP_c	compressor pressure rise				
ΔP_t	throttle pressure drop				
q	wall displacement				
Q	wall frequency parameter				

Subscripts

c	compressor
in	compressor inlet
p	plenum
t	throttle; tip of impeller exit
0	ambient conditions
1	compressor exit
2	plenum exit

Operators

$\delta(\cdot)$	perturbation quantity in analysis
$\overline{(\cdot)}$	time averaged
$(\cdot)'$	fluctuation in experimentally measured quantity

Throttle pressure drop characteristic

$$P_\phi - \Delta P_t = P_0 \quad (3)$$

The throttle pressure drop ΔP_t is also a known function of mass flow.

Wall dynamics

$$m\ddot{q} + c\dot{q} + kq = (P_\phi - P_{\text{auxiliary plenum}})A_s \quad (4)$$

Linearizing and nondimensionalizing the equations of motion as shown in the appendix yields the following nondimensional equations describing the linear stability of the system:

Inlet duct momentum

$$\frac{d\delta\phi_1}{d\tau} = B \left[\left(\frac{d\psi_c}{d\phi} \right) \delta\phi_1 - \delta\psi \right] \quad (5)$$

Mass conservation in the plenum

$$\frac{d\delta\psi}{d\tau} = \frac{1}{B} [\delta\phi_1 - \delta\phi_2] - \frac{\bar{\rho}_p}{\rho_0} \frac{2}{M^2} \delta u \quad (6)$$

Throttle pressure drop characteristic

$$\delta\psi = \frac{\rho_0}{2\bar{\rho}_p} \frac{\dot{\phi}^2}{\dot{\psi}} \delta\phi_2 \quad (7)$$

Wall dynamics

$$\frac{d\delta u}{d\tau} = (2WB^2)\delta\psi - \left(2\sqrt{\frac{\rho_0\bar{\rho}_p}{\rho_p\rho_0}} \zeta Q \right) \delta u - \left(\frac{\bar{\rho}_p}{\rho_0} Q^2 \right) \delta\eta \quad (8)$$

$$\frac{d\delta\eta}{d\tau} = \delta u \quad (9)$$

In Eqs. (5)–(9), nondimensional pressure rise and mass flow coefficients, ψ and ϕ , are defined as

$$\psi = \frac{\Delta P}{\frac{1}{2} \rho_0 U^2}, \quad \phi = \frac{\dot{m}}{\rho_0 A_{in} U}$$

The nondimensional wall displacement, η , is given as

$$\eta = \frac{A_p q}{V_p}$$

In Eqs. (6)–(9), perturbation variables are denoted by δ (), and steady-state variables are represented by $(\bar{\ })$. Nondimensional time is defined in terms of the Helmholtz frequency, $\tau = \omega_H t$, where the Helmholtz frequency is defined as:

$$\omega_H = \bar{a}_p \sqrt{\frac{A_{in}}{V_p L_c}}$$

Other definitions can be found in the appendix.

The parameter $d\psi_c/d\phi$ is the slope of the nondimensional compressor pressure rise characteristic and is linked directly to the onset of the surge instability. In the regions of the compressor map where this slope is negative, both the throttle and compressor act to damp out flow disturbances. In the positively sloped regions, the compressor adds energy to disturbances while the throttle continues to dissipate unsteady energy. For a rigid wall system, therefore, the flow through the system becomes unstable when the compressor feeds more energy into disturbances than the throttle can extract.

Nondimensional Parameters. The behavior of the system described by Eqs. (5)–(9) has a complex parametric dependence involving the following nondimensional parameters.

The B -parameter has a major influence on the surge dynamics of the compression system (Greitzer, 1981). It is defined as:

$$B = \frac{U}{2\omega_H L_c} = \frac{U}{2\bar{a}_p} \sqrt{\frac{V_p}{A_{in} L_c}}$$

For the fixed wall compression system at a given operating point, the magnitude of the (positive) compressor characteristic slope required for disturbances to grow is set by the B -parameter, which can be viewed as providing a measure of the coupling between mass flow oscillations through the compressor and through the throttle. The larger the B -parameter, the more isolated the throttle is (from the compressor), and the less able to remove energy from flow disturbances. As the B -parameter increases, therefore, surge occurs at a smaller positive compressor slope.

The *tip Mach number* (based on plenum conditions) is defined as:

$$M = \frac{U}{a_p}$$

The tip Mach number enters the system equations as a measure of the effect of wall motion on the mass balance in the plenum. It thus does not appear explicitly for a fixed wall configuration. The tip Mach number affects the coupling of wall motion to compression system dynamics by determining the degree to which plenum pressure responds to wall motion. The pressure and mass flow fluctuations are functions of tip Mach number (they scale as M^2 at low speed), but the wall motion is not. The Mach number is thus a measure of this aerodynamic-structural coupling, rather than a representation of the importance of compressibility in the system dynamic model. The larger the Mach number, the smaller the effect a given non-

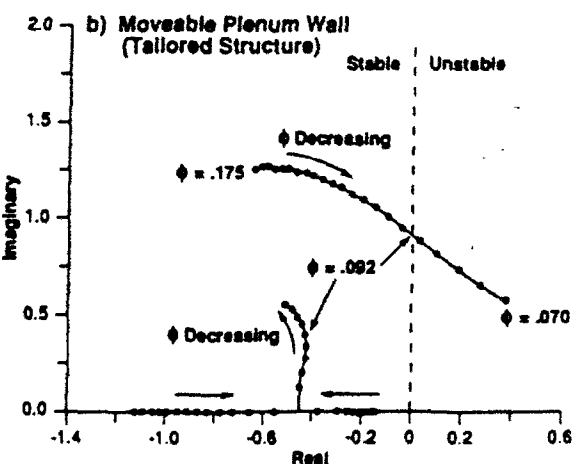
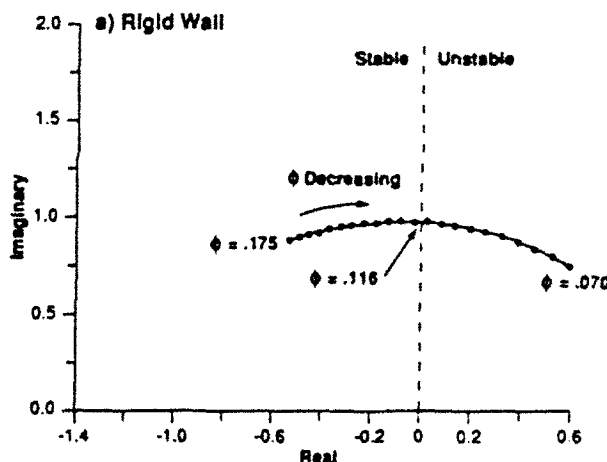


Fig. 2. Root locus plots for rigid wall (a) and movable plenum wall (b) compression systems: $B = 0.5$, $M = 0.4$, $W = 0.11$, $\zeta = 1.5$, $Q = 0.51$ for movable wall system

dimensional wall motion has on nondimensional mass flow and pressure perturbations in the system.

The parameters W , ζ , and Q determine the wall dynamic characteristics relative to the unsteady behavior of the basic (rigid wall) compression system. W is an aeroelastic coupling parameter defined as

$$W = \frac{\rho_0 A_p^2 L^2}{m V_p}$$

This parameter determines the degree to which the wall responds to the pressure fluctuations in the plenum. Increasing the W -parameter implies a greater wall response to perturbations in plenum pressure.

ζ is the critical damping ratio of the plenum wall mass-spring-damper system, corrected to remain independent of compressor operating conditions. Correction is necessary since the aerodynamic spring constant, and hence, the wall natural frequency, varied with plenum pressure. ζ is defined as

$$\zeta = \frac{c}{2m\omega_p} \sqrt{\frac{P_p}{P_0}}$$

Q defines the ratio of natural frequencies for the wall mass-spring-damper system and for the fixed wall compression system (the Helmholtz frequency), also corrected so that it is independent of compressor operating point.

$$Q = \frac{\omega_p}{\omega_H} \sqrt{\frac{P_0}{P_p}}$$

Linear Stability Analysis

Linear analysis of the system stability for a given set of operating conditions leads to the set of equations shown below:

$$\begin{bmatrix} B \left(\frac{d\bar{\psi}_c}{d\phi} \right) - s & -2B \frac{\bar{\psi}}{\phi} & 0 & 0 \\ \frac{\bar{\phi}}{\phi} & -\frac{1}{2B\bar{\psi}} - s & 0 & -\frac{\bar{\rho}_p}{\rho_0} \frac{1}{M^2} \frac{\bar{\phi}}{\bar{\psi}} \\ 0 & 0 & -s & 1 \\ 0 & 2WB^2 \frac{\bar{\psi}}{\phi} & -\frac{\bar{\rho}_p}{\rho_0} Q^2 & -2\zeta Q \sqrt{\frac{P_0 \bar{\rho}_p}{P_p \rho_0}} - s \end{bmatrix} \times \begin{bmatrix} \delta\phi_1 \\ \delta\phi_2 \\ \delta\eta \\ \delta\nu \end{bmatrix} = \begin{bmatrix} 0 \\ 0 \\ 0 \\ 0 \end{bmatrix} \quad (10)$$

Equation (10) constitutes an eigenvalue problem for the (complex) growth rate, s , involving two coupled dynamic systems: the compression system, with variables $\delta\phi_1$ and $\delta\phi_2$, and the moving wall, with variable $\delta\eta$ and $\delta\nu$. The terms associated with the uncoupled fixed wall compression system and the moving plenum wall dynamics are located on the tridiagonal of the stability matrix. The two nonzero terms located off the tridiagonal are the aeroelastic coupling terms.

Solving the eigenvalue problem as a function of B , M , ϕ , W , ζ , and Q and using the experimentally determined compressor characteristics of Pinsley (1988) enables prediction of the instability onset condition for various system and control parameters. The fixed wall behavior is obtained in the limit of either $W = 0$ or $Q = \infty$. Either has the effect of making the wall appear massive and the spring constant stiff, or essentially rigid.

To illustrate the trends obtained from the stability computations, a root locus plot for a fixed wall system with $B =$

0.5 is shown in Fig. 2(a). The compressor pressure rise characteristic used is based on a third-degree polynomial curve fit of Pinsley's (1988) measured 70K speedline as shown in Fig. 3, the measurements being conducted using a close coupled throttle to avoid surge. The abscissa and ordinate of the root locus plots are nondimensionalized by the system Helmholtz resonator frequency. The roots are plotted as a function of nondimensional flow coefficient for flow coefficients ranging from 0.175 to 0.070 in increments of 0.005. As the mass flow decreases and the compressor slope increases, the poles are driven from the left half-plane (stable) to the right half-plane (unstable), with the imaginary axis defining the neutral stability point. The behavior is that of a (positively or negatively) damped second-order system. The neutral stability point for this fixed wall system (at $\phi = 0.116$), as indicated on the compressor characteristic in Fig. 3, occurs near the peak of the characteristic, which is located at $\phi = 0.120$.

The introduction of a movable plenum wall introduces a second mode of oscillation to the compression system. A root locus plot for the two modes is shown in Fig. 2(b), again using the compressor characteristic shown in Fig. 3. One characteristic frequency is somewhat close to the Helmholtz frequency, but there is now another frequency that is associated primarily with the wall motion. More importantly, however, the neutral stability point occurs well past the peak of the characteristic in the positively sloped region at $\phi = 0.92$; this is also indicated in Fig. 3. Away from instability (high mass flow), the moving wall system has one (damped) oscillatory mode and one nonoscillatory (overdamped) mode. Near instability, the two modes exhibit increased fluid-structure coupling and both become oscillatory.

To optimize the moving wall compression system performance, a parametric study was performed. Since the B -parameter and Mach number are not independent quantities (both scale with wheel speed), the relation between these two parameters in this study is based on selecting values for the dimensions of the compression system that were typical of modern compression machines as well as convenient from an experimental view point. The parameter search showed that movable wall performance is optimized, over the range of B -parameters and Mach numbers used, with the following control parameters: $W = 0.11$, $\zeta = 1.5$, and $Q = 0.51$. (These parameters were used in Fig. 2b.)

The steady state mass flow coefficient by itself (i.e., explicitly rather than through the effect on compressor characteristic slope) is not a very useful indication of stability for the optimized moving wall system. Determining the maximum com-

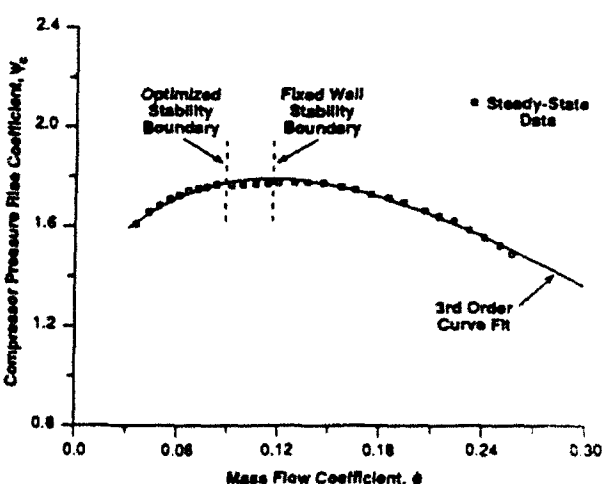


Fig. 3 Compressor pressure rise characteristic used in analysis; data of Pinsley (1988)

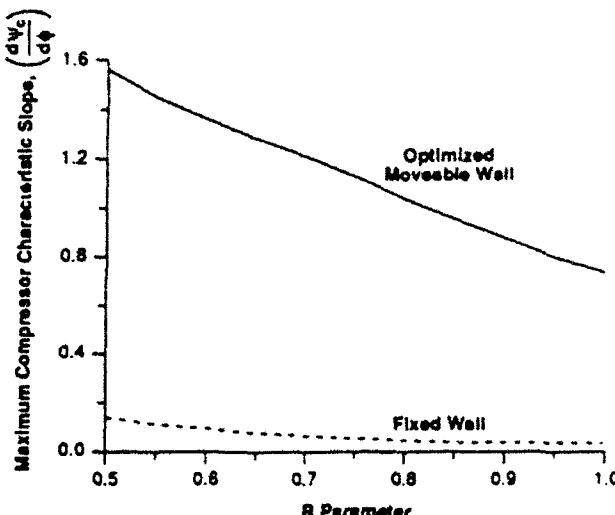


Fig. 4 Maximum achievable compressor characteristic slope for stable compressor operation versus B -parameter

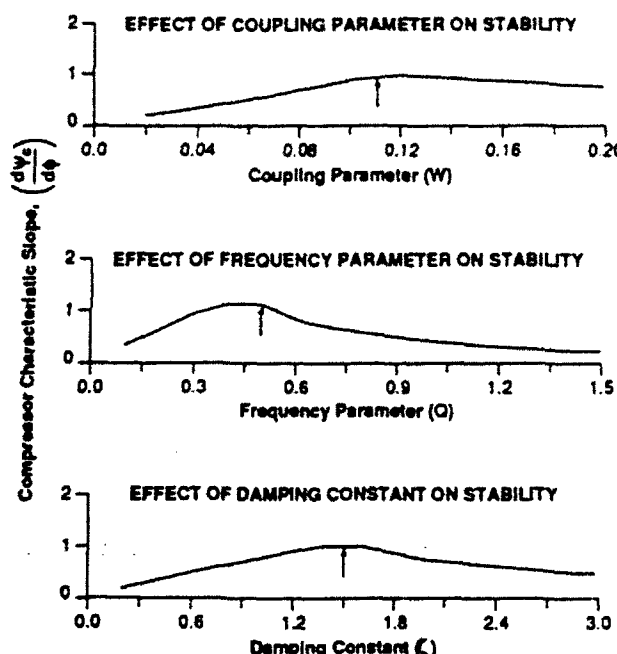


Fig. 5 Effect of tailored structure control parameters on maximum achievable compressor characteristic slope for stable operation. ! indicates optimum value from parameter search.

pressor characteristic slope at which the system was stable versus the B -parameter was found to be a much more useful discriminant for the effectiveness of the control strategy. The maximum stable slope versus B -parameter for the fixed wall system and for the (optimized) moving wall system is shown in Fig. 4; as indicated, the movable wall system is capable of stable operation at a positive compressor slope that can be an order of magnitude larger than that for the fixed wall system.

We can also plot maximum stable slope versus each of the control parameters about the optimized values to see how rapidly one departs from optimum conditions. Figure 5 shows the variations in maximum stable slope versus W , ζ , and Q , respectively. The optimized values are indicated by arrows. Although substantial changes in the structural control parameters away from the optimized configuration will degrade performance, the stabilization is insensitive to small (± 25 percent, say) variations. This implies that the system need not be "re-

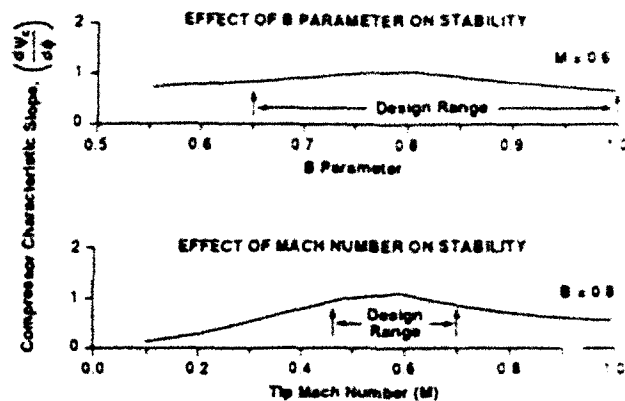


Fig. 6 Independent effects of B -parameter and tip Mach number on maximum achievable compressor characteristic slope for stable operation

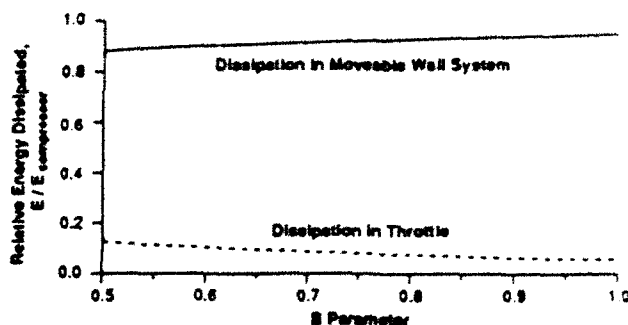


Fig. 7 Comparison of perturbation energy dissipation in throttle and in movable wall system; relative units

tuned" for each compressor operating condition. The independent effects of B -parameter and tip Mach number, for a system with a fixed set of control parameters, are shown in Fig. 6 where one parameter is held constant and the other varied. As discussed, although the tip Mach number does not directly affect the stability of a system with a fixed wall, it is an important parameter for the stability of the moving wall system.

Energy Analysis

To examine the physical mechanism associated with stabilization, it is useful to look at the perturbation energy. From this viewpoint, the system is unstable when more energy is fed into any mode of oscillation over a cycle than is removed; neutral stability corresponds to zero net energy input. Because the modes are orthogonal, it is only necessary to consider one mode at a time. If any mode is unstable, the system is unstable. The analysis is given by Gysling (1989) and we present here only the central result.

Figure 7 shows the relative perturbation energy input and dissipation over a cycle at the neutral stability point, as a function of the B -parameter for the mode that becomes unstable first. Energy dissipation due to the wall motion is dominant, being more than ten times that for the throttle over a large range of B -parameters. The stabilization due to the wall is thus direct dissipation through plenum wall motion, rather than modification of the system dynamics to promote increased dissipation in the throttle, as was the case in the throttle control experiments reported by Pinsley et al. (1990).

Time-Domain Analysis and Nonlinear Aspects

The linear analysis yielded a set of optimized, nondimensional control parameters, which gave large increases in the

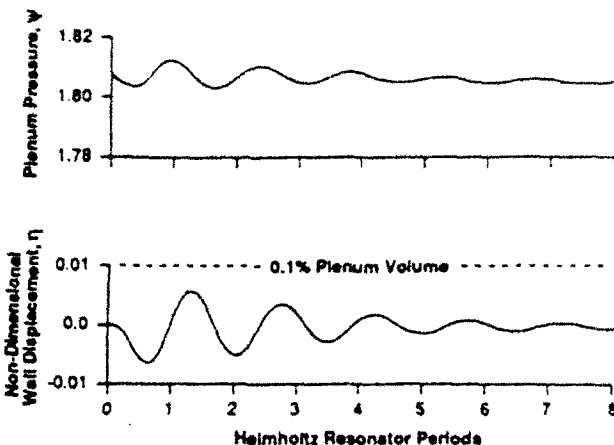


Fig. 8 Wall motion and plenum response to impulse of $0.01 \text{ in units of } 1/\text{s}$, optimized system parameters

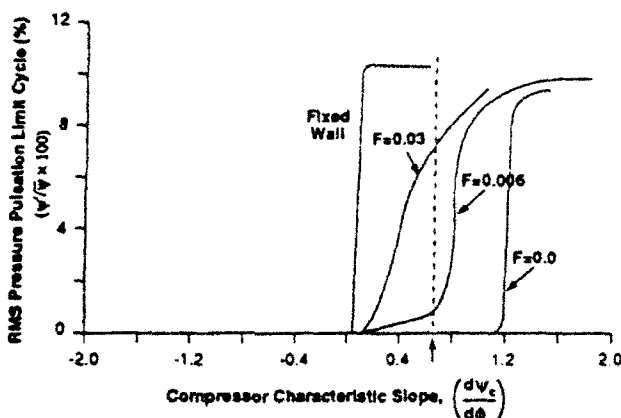


Fig. 9 Effect of Coulomb friction on limit cycle amplitude; optimized system parameters

stable flow regime. The response beyond the initial instability, i.e., the nonlinear system behavior, is also of interest. Nonlinear computations were thus performed to assess the effects of finite amplitude disturbances and of nonlinearities in the wall dynamics. The equations of motion were integrated using the Newmark time-averaged acceleration method (Bathe and Wilson, 1976). As in the linear analysis, the compressor characteristic shown in Fig. 3 was used.

As an example of the results, Fig. 8 shows the time response of the optimized system to a small impulsive disturbance at the inlet operating near the linearly predicted stability line ($\phi = 0.096$). Wall motion and pressure perturbations exhibit essentially damped harmonic motion. A more interesting point, to be discussed further in connection with the experiments, is that the nonlinear computations showed that introducing wall motion into a fixed wall system undergoing deep surge cycles could suppress the surge. In other words, even though the control scheme was designed based on linear analysis, it was useful for oscillations that were strongly nonlinear.

An important use of the nonlinear analysis was to examine the effect of Coulomb friction in the wall dynamics. The presence of Coulomb friction, in a strict sense, invalidates the linearity assumption. However, the degree to which the accuracy of the linear model is affected is a function of the ratio of the Coulomb friction forces compared to the other, essentially linear, forces in the system (Halfman, 1962). To assess this, computations were carried out with a constant magnitude friction force imposed on the wall in the direction opposite to

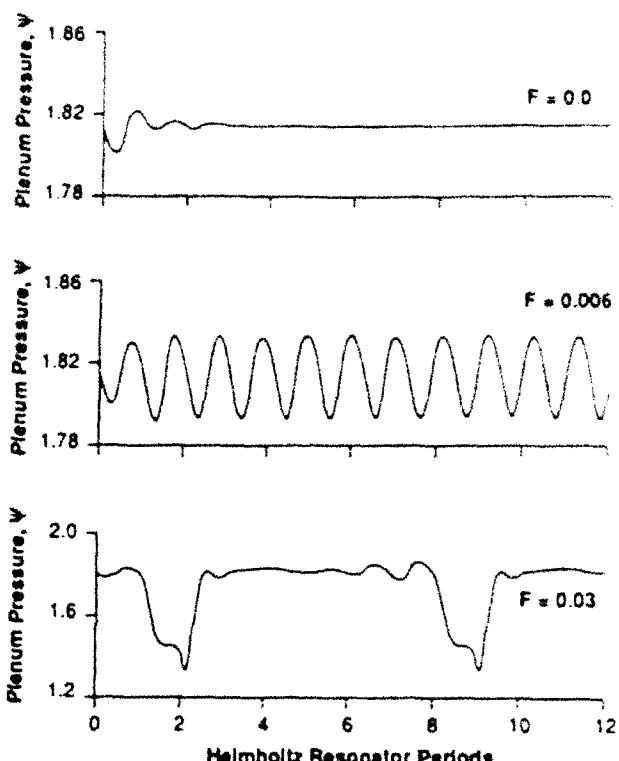


Fig. 10 Effect of Coulomb friction on transient system response; compressor characteristic slope $(d\Psi_c/d\phi) = 0.66$ (dashed line on Fig. 9)

its motion, to model the sliding friction present in an actual design.

One important result of the Coulomb friction is that it prevents the wall from responding to disturbances below a threshold level, i.e., disturbances must grow to a critical amplitude before the wall can respond. Therefore, in a strict sense, operating points to the left of the natural surge line remain linearly unstable for the actual (nonideal) tailored structure system. The linear instability that results from the presence of Coulomb friction grows into a limit cycle, whose amplitude (for a given compression system and set of control parameters) is a function of the nondimensional friction force, F , defined as

$$F = \frac{f}{\rho_0 U^2 A_p}$$

and the slope of the compressor characteristic.

The effect of Coulomb friction on surge suppression is demonstrated in Fig. 9 where the root mean square of the calculated limit cycle pressure fluctuations, divided by the steady-state pressure rise, is plotted versus the local compressor characteristic slope, for various nondimensional friction levels. The vertical dashed line denotes the value of slope corresponding to the results in Fig. 10, discussed below. The maximum value of the slope prior to deep surge (large amplitude oscillation) decreases with increasing friction levels. The deep surge boundary for the nonlinear system with Coulomb friction agrees well with the linear stability boundary in the limit of zero friction. With increasing Coulomb friction levels, however, the performance of the movable plenum wall system approaches that of the fixed wall system. Analysis showed that the movable plenum wall became unable to suppress surge significantly past the rigid wall surge line for nondimensional friction levels greater than $F = 0.02$.

As examples of predicted limit cycles with different levels of Coulomb friction, the time response of systems with various levels of Coulomb friction to a small impulse (0.01 in units of

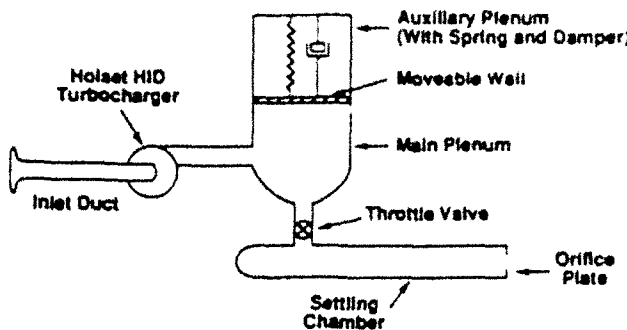


Fig. 11 Schematic of experimental facility

$\bar{\tau}$) is shown in Fig. 10. Parameters are given in the figure caption. The amplitude of each limit cycle is indicated in Fig. 9.

The disturbance decays in the system without Coulomb friction, but grows into a limit cycle in the systems with Coulomb friction. For the system with a small amount of Coulomb friction ($F = 0.006$) the limit cycle is small and approximately sinusoidal (mild surge) with frequency near the predicted Helmholtz frequency. However, for the system with larger Coulomb friction ($F = 0.030$), the limit cycle is no longer sinusoidal and contains regions of reversed flow (deep surge).

Experiment Design

The basic prediction is that a properly designed moving plenum wall can substantially increase the stable flow range of a centrifugal compression system. To investigate this experimentally, a design study was undertaken to match the nondimensional control parameters, while minimizing the effects of nonlinearities, in a physically realistic device.

The conceptual design was based on use of an existing centrifugal compressor facility, constructed to investigate active throttle control of surge. The facility is described in detail by Pinsley (1988); however, the major components will be outlined here. The centrifugal compressor was a Holset model H1D turbocharger. The impeller has an inlet area of 0.00125 m^2 with hub-to-tip radius ratio of 0.37 and exit tip diameter of 0.055 m. The compressor has no inlet guide vanes, six blades, six splitter blades, and a vaneless diffuser. A schematic of the compression system facility is shown in Fig. 11.

Design of Movable Plenum Wall

Several different ways to implement the control scheme mechanically were reviewed. A major constraint was that the wall had to be capable of withstanding large steady-state and transient pressure loading, yet still respond to small amplitude perturbations in plenum pressure. A rigid piston serving as the plenum wall, and an aerodynamic spring, were determined to be practical solutions to these constraints. In particular, a design utilizing a separate, explicit spring, mass, and damper was attractive since it facilitated parametric experimentation. No attempt was made to engineer a "flight weight" system.

To serve as the movable wall, the rigid piston was mounted on a shaft, guided by linear bearings and allowed to float between the main plenum and an auxiliary plenum. The seal between the two plenums was made with a low-friction, convoluted diaphragm. A small-diameter tube connected the two plenums so they were isolated for high-frequency pressure disturbances (i.e., surge oscillations), but steady-state pressures were equalized so that no steady-state load existed on the piston. A mechanical spring was used to maintain a constant equilibrium position for the piston over various operating conditions since at steady state, the plenum wall had no preferred

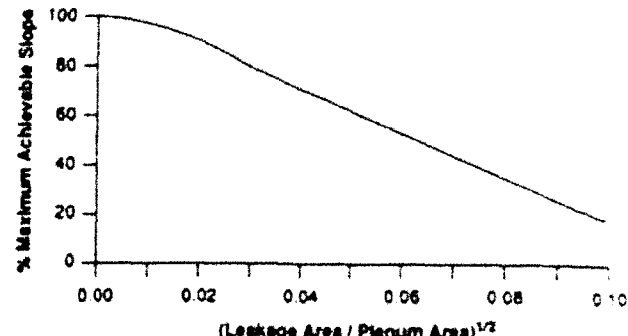


Fig. 12 Effect of leakage on maximum achievable compressor characteristic slope for stable operation with optimized system

Table 1 Design specifications for the flexible plenum wall experimental facility

B Parameter	0.65 to 1.0
Helmholtz Frequency	18.5 Hz to 19.9 Hz
W Parameter	0.11
Q Parameter	0.51
ζ Parameter	1.5 to 3.0
Area of Wall	0.0669 m^2
Mass of Wall	6.2 kg
Volume of Plenum	0.0108 m^3
Inlet Duct Length	1.16 m
Inlet Area	0.00125 m^2
Auxiliary Plenum Volume	0.0388 m^3
Aerodynamic Spring Constant	24,000 N/m to 35,000 N/m
Mechanical Spring Constant	2100 N/m
Damping Coefficient	1000 N s/m to 2000 N s/m
Maximum Wall Motion	$\pm 1.25 \text{ cm}$
Coulomb Friction	10 N

position. The mechanical spring also allowed the steady-state position of the wall to be adjustable.

Because the presence of the steady-state equalization tube could affect the behavior of the aerodynamic spring, computations were carried out to quantify the effect of leakage between the two plenums. The leakage was modeled as flow through an orifice plate. The results are shown in Fig. 12, where the decrease in maximum slope prior to surge is plotted versus nondimensional orifice area for the optimized system at typical operating conditions. Leakage caused small amplitude limit cycles similar to those predicted to occur as a result of Coulomb friction, so it is important that leakage be kept to a minimum.

A viscous dashpot was used for the damping. To minimize Coulomb friction, a low-friction, pneumatic, double acting actuator was modified to serve as a damper. The actuator was filled with 5W-30 oil and the ports on either end were connected through a variable area valve. Testing of various dashpots developed from the same basic design showed that the force-velocity relation for the dashpot was closely linear over the expected range of wall velocities, as well as easily adjustable.

The final rig specifications are given below in Table 1 and a detailed drawing of the movable plenum wall apparatus is shown in Fig. 13.

Experimental Data and Analysis

The compression system was investigated with fixed and flexible wall for three different sets of structural control parameters, at B -parameters ranging from 0.65 to 1.0. Steady-state measurements were used to map the compression system performance and to define the surge line for both fixed and flexible wall systems. Time-resolved measurements were used to evaluate the model assumptions and to determine the per-

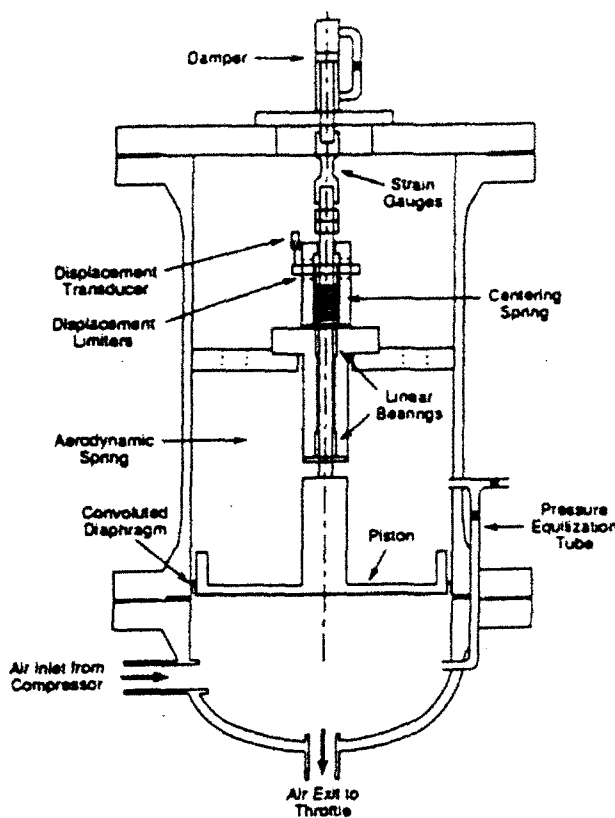


Fig. 13 Movable plenum wall (tailored structure) showing mass-spring-damper system

formance characteristics of components in the compression system and in the flexible wall.

Steady-State Behavior. The experimental compression system could be operated in a fixed wall configuration by shutting the steady-state pressure equalization line and bleeding the auxiliary plenum to atmospheric pressure. Pressure in the main plenum then forced the wall against its upper stops, yielding a fixed wall configuration. Forcing the plenum wall against the upper stop resulted in increasing the plenum volume approximately 5 percent, and, hence, the B -parameter 2.5 percent, which had a slightly destabilizing effect on the fixed wall compression system. Any movement of the surge line to the left due to wall motion will thus slightly overestimate the actual increase in stable flow range, although this difference is small compared to the difference seen between the fixed and flexible wall systems. (We have not tried to correct for this in the data presentation, but it should be noted that our estimates of the shift in surge flow coefficient due to this change in B -parameter are roughly one-half percent of the surge mass flow as a worst case (at low speed), and one or two tenths of a percent at higher speeds. Thus, these changes are, in general, two orders of magnitude less than the difference between the fixed wall and the movable wall surge points.)

The compressor was operated at corrected speeds (referenced to 288 K) ranging from 60,000 rpm to 100,000 rpm, corresponding to a range of B -parameters of 0.65 to 1.0. The steady-state performance is reported in terms of (inlet total to plenum static) pressure ratio and mass flow, given in standard cubic feet per minute (SCFM). Mass flow is also given in some of the figures in terms of nondimensional flow coefficient, an annulus-averaged inlet axial velocity divided by tip speed.

Because it was of interest to operate with the movable plenum wall in the optimized as well as in the nonoptimized configurations, speedlines for the movable wall system were recorded

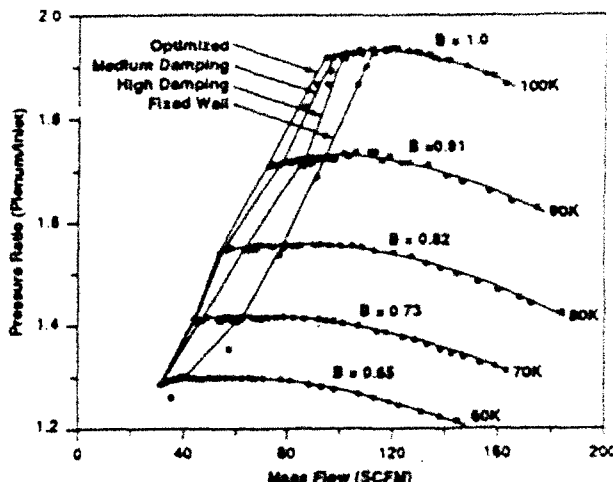


Fig. 14 Compressor map showing increase in stable flow region due to tailored structure for three values of damping; damping values $\zeta = 1.5, 2.25, 3.0$, other parameters at optimized values

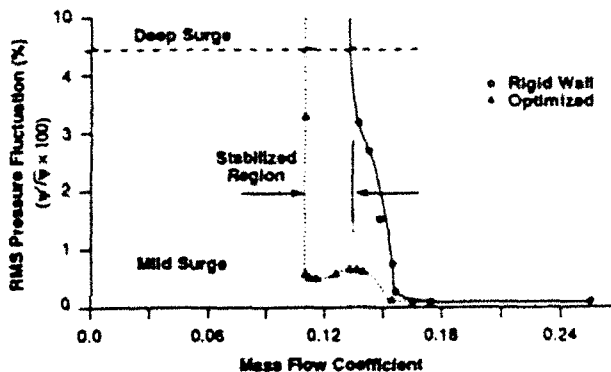


Fig. 15 Limit cycle pressure pulsation amplitude versus mass flow coefficient; 90K speedline, optimized movable wall system

with various levels of wall damping. The wall was operated at the theoretically optimized configuration ($W = 0.11$, $Q = 0.51$, $\zeta = 1.5$) as well as at values of $\zeta = 2.25$ and 3.0 .

The steady-state compressor performance map for the three movable wall configurations and the fixed wall system is shown in Fig. 14. The steady-state pressure ratio is unaffected by the presence of the moving wall in the stable flow range of the fixed wall system, but the surge line is moved to the left substantially. Also, the degree of surge suppression achieved is dependent on the movable wall control parameters, as predicted. The optimized configuration performed the best, with the performance of the other two configurations decreasing as one moved farther from optimum. A surge line recorded for the movable plenum wall system with a lower than optimum damping ratio ($\zeta = 0.75$) confirmed that movement in either direction in parameter space away from the optimal damping ratio was destabilizing.

Figure 15 shows the root-mean-square value of the fluctuations in plenum pressure versus mass flow coefficient for the fixed wall system and the optimized movable plenum wall system at $B = 0.91$ (90K speedline). On the negative sloped region of the speedline (above $\phi = 0.155$), the rms pressure fluctuations for fixed and movable wall systems are the same. However, small-amplitude limit cycles exist in the stabilized region. Based on the results of numerical calculations, these limit cycles can be attributed to Coulomb friction in the wall motion and pressure equalization leakage. Small amplitude

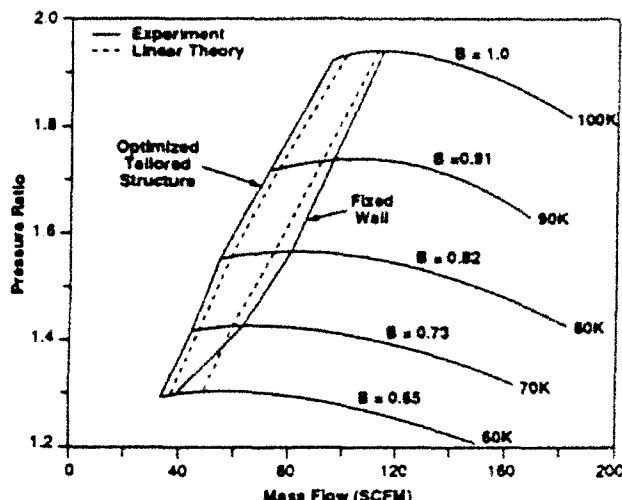


Fig. 16 Predicted and measured stability limits; compressor characteristics approximated by third-order fit

limit cycles also occur over a limited range of mass flow in the fixed wall system prior to deep surge; these, however, appear to be a result of nonlinearities in the compressor and throttle characteristics.

Figure 16 shows predicted and experimentally determined surge lines for the rigid wall and for the optimized system. The predicted surge line is based on the linear instability point as determined by the eigenvalue stability analysis described previously. The experimental surge line is defined as the onset of deep surge (i.e., reverse flow); this also marked the points at which the time-mean pressure ratio dropped sharply. The compressor characteristics used are from a third-degree polynomial curve fit of the speedlines measured by Pinsley (1988).

The experimental results can be compared to the nonlinear calculations by examining the amplitudes of pressure fluctuations in the plenum as a function of mass flow. As inputs to the calculation, the friction force present during wall motion was measured to be approximately 10 N and the leakage was estimated to be equivalent to a 0.003 m diameter orifice plate. The results of the calculation and experiment for the optimized system operating at $B = 0.91$ are shown in Fig. 17, where the amplitude of the small plenum pressure limit cycles before the onset of deep surge are shown versus mass flow coefficient. The linear stability boundary is also shown in the figure for comparison. The linear analysis does not predict the small-amplitude limit cycles in the stabilized region, but it is able to portray accurately the onset point for deep surge. The reason is that the oscillations are the result of nonlinear effects, described above. If the nonlinear effects are small, which is inherent in the experimental design, the linearly predicted stability limit corresponds to the onset of deep surge. The nonlinear analysis shows limit cycles in the stabilized region, although the detailed relationship between mass flow and limit cycle amplitude is not captured.

Transient System Behavior

Time-resolved measurements were recorded for the fixed wall compression system and for the moving wall system at three control parameter configurations. The measurements were made on the 70K and 90K speedlines, corresponding to B-parameters of 0.73 and 0.91. The data shown are from the former, at the points marked on Fig. 18.

As noted previously, the flow through the compression system becomes progressively more unsteady as the system approaches the surge line. To demonstrate this, the time resolved nondimensional mass flow coefficient and the nondimensional

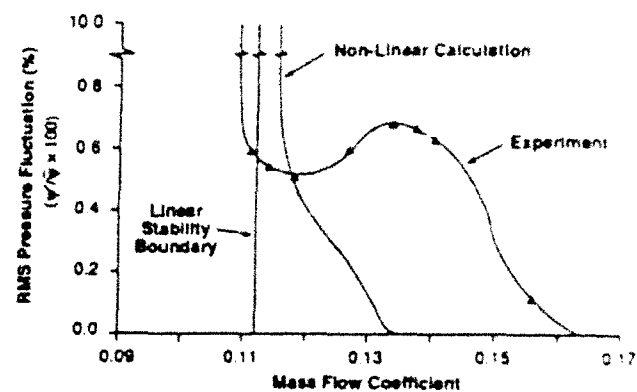


Fig. 17 Amplitude of pressure fluctuations versus mass flow; optimized system (90K speed, $B = 0.91$)

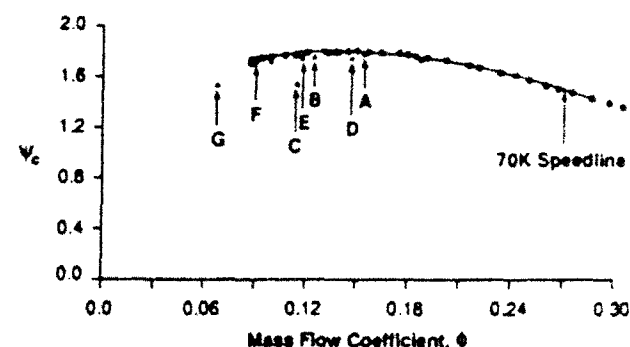


Fig. 18 Compressor characteristic with points at which time-resolved data are shown

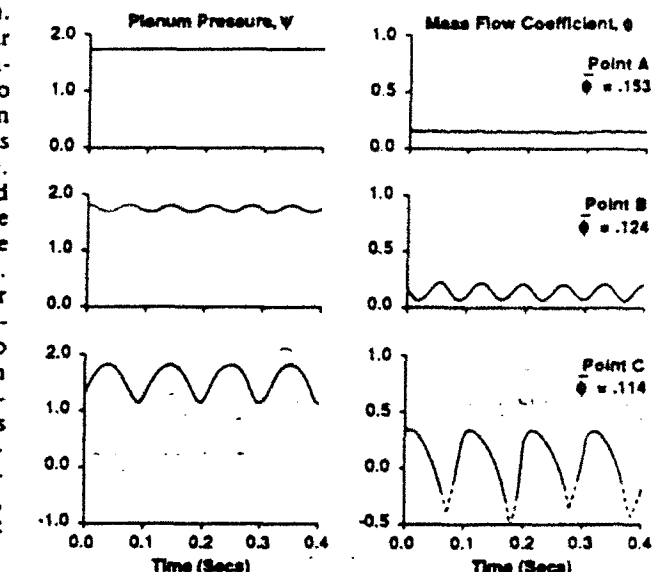


Fig. 19 Measurements of time-resolved plenum pressure and mass flow in fixed wall system (70K speed, $B = 0.73$)

pressure rise for the fixed wall system are shown in Fig. 19 for three operating points (marked A-C in Fig. 18). The transient mass flow measurements (taken in the inlet duct) are based on a linearized hot-wire calibration and the large oscillations in mass flow are presented for qualitative information only. The data shown correspond to points in both stable and unstable operating regions.

For flows near point A, on the negative slope region of the

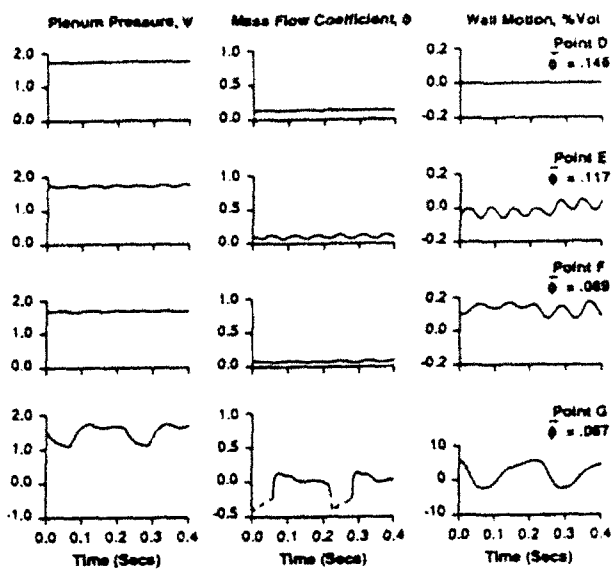


Fig. 20 Measurements of time-resolved plenum pressure, mass flow, and wall motion in optimized movable wall system (70K speed, $B = 0.73$)

compressor characteristic, stable operation with only slight unsteadiness is exhibited.

Point B is slightly to the left of the peak of the compressor characteristic. Small-amplitude limit cycles (mild surge) are seen. The frequency of the mild surge cycle is approximately 14.5 Hz, compared to the predicted Helmholtz frequency of 17.5 Hz.

At mass flows corresponding to points C and below, on the positive slope region of the speedline, the compressor is in deep surge. The time-averaged pressure rise and mass flow are decreased and the frequency of the oscillations has changed to approximately 10 Hz. The hot wire does not distinguish reversed flow, and the reversed flow regions are shown with a dashed line. The decrease in frequency is associated with the time needed for plenum blow-down and repressurization, as described by Fink (1988).

With the moving wall system, small-amplitude limit cycles existed over the stabilized region. Figure 20 shows the non-dimensional mass flow, pressure rise, and corresponding non-dimensional wall motion for the medium damping configuration operating at the 70K speedline for four operating points, D, E, F, and G, shown on the compressor characteristic in Fig. 18.

Point D is in smooth operation on the negatively sloped region of the map. The steady-state and unsteady behavior is similar to point A for the fixed wall configuration. The position of the wall is shown to be stationary, indicating that the disturbances in the stable system are not large enough to overcome the wall friction.

Points E and F are located on the positively sloped, stabilized region of the characteristic and exhibit small amplitude limit cycles. The maximum wall motion required to stabilize the system is approximately 0.1 percent of the plenum volume and the power dissipated is approximately 0.05 percent of the steady power needed to drive the compressor.

At point G, in deep surge, the pressure and mass flow traces are similar in amplitude to those with the fixed wall, although the fluctuations have a much lower natural frequency (4-5 Hz). Also, in deep surge, the wall is shown to be hitting the displacement limiters, as indicated by the flat spots on the time trace of the wall motion.

Introduction of a movable plenum wall can also eliminate deep surge when wall motion is initiated during an existing fixed wall surge cycle. This is demonstrated by the time history

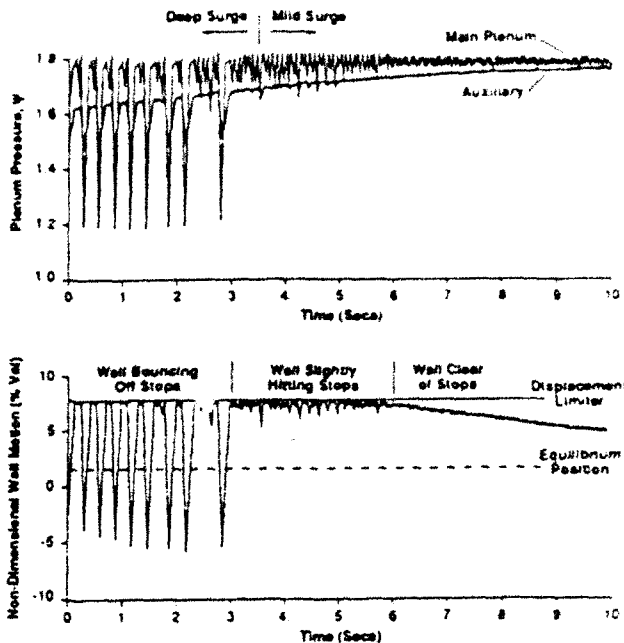


Fig. 21 Experimental time history showing suppression of fixed wall system deep surge when wall is released (optimized system, $B = 0.91$)

shown in Fig. 21, where fixed wall surge is suppressed by equalizing the auxiliary and main plenum pressures, thus freeing the wall from the displacement limiters. The time traces in Fig. 21 show the wall bouncing on the stops as the auxiliary plenum pressure equalizes. When the wall clears the stops, the deep surge cycle is suppressed. Although not shown, the wall continues to move toward its steady-state equilibrium position as the pressures in the auxiliary and main plenums equalize.

Two other points should be made about the time history shown in Fig. 21. First, the time scale over which the surge suppression occurs is considerably longer than any time scale associated with the system oscillations because it is set by the filling time (through the small equalization tube) of the auxiliary plenum. Second, as seen in previous figures, the deep surge regime is one in which the oscillations are strongly nonlinear, with mass flow oscillations greater than the time averaged mass flow. This indicates that the use of tailored structure can suppress surge even when the oscillations have large amplitude. In this connection it should be noted that similar behavior has been found by Pinsley et al. (1991) and Ffowcs Williams and Huang (1989) using different active control schemes. Such behavior emphasizes that successful use of dynamic control is not restricted to the small amplitude regime.

Dynamic Response of System Components

Compressor Behavior. One of the major assumptions used in modeling the compression system is that the compressor remains on its steady-state characteristic during transient operation, at least for frequencies on the order of the Helmholtz frequency. To check this, the unsteady pressure rise versus mass flow relation (i.e., the compressor transfer function) can be calculated directly from the unsteady data and compared to the quasi-steady slopes. The unsteady data were taken from operating points exhibiting small amplitude limit cycles. The instantaneous pressure rise versus mass flow slope was determined from measurements of inlet mass flow and plenum pressure, due corrections being made for the inertia of the fluid in the inlet duct. Only self-excited oscillations were examined, so that measurements were obtained only at or near the system resonant frequency where there was an acceptable signal-to-noise ratio.

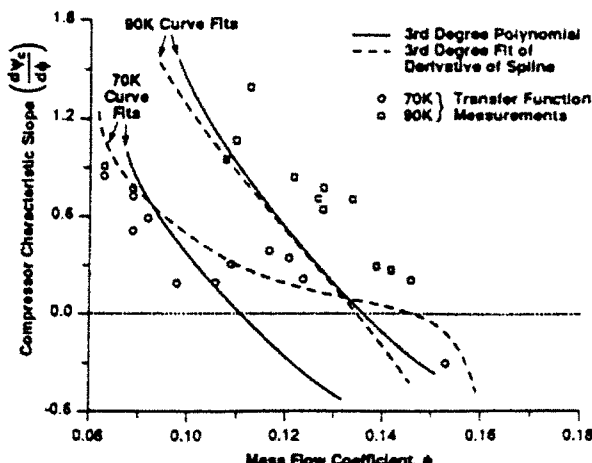


Fig. 22 Measured compressor transfer function and compressor characteristic slope values obtained from curve fits to steady-state data

The compressor slope, as measured, yielded a real and imaginary part. The real part represents the instantaneous slope of the compressor characteristic. The imaginary part can be viewed as a lag term, similar to that discussed by Fink (1988), which accounts in a rudimentary fashion for the unsteady aerodynamics within the compressor. The real part of the transfer function is plotted versus steady state mass flow coefficient for the 70K and 90K speedlines in Fig. 22. The data are from both fixed and movable wall systems, indicating that, as would be expected, the presence of the wall has no noticeable effect on the instantaneous characteristic slope. Also plotted in the figure are the slopes resulting from two methods of fitting the steady-state data; the derivative of a third-order polynomial curve fit, and a third-order polynomial fit of the derivative of a cubic spline fit of the steady-state compressor data. (It is important to note that, as can be inferred from Fig. 22, accurate determination of the slope is difficult to do.) As shown, the compressor characteristic slopes determined from the steady-state data and those determined from unsteady data are in reasonable agreement. In particular, the unsteady data fall within the variance between the two steady-state slopes calculated by curve fits. The assumption of quasi-steady behavior thus appears to be an adequate representation of the instantaneous compressor slope over the range of flow coefficients investigated.

The time lag for both the 70K and 90K speedlines was approximately 5–10 ms, corresponding to 0.065–0.13 Helmholtz resonator periods. The compressor throughflow time can be estimated at approximately 3.0 ms. The lag term is thus on the order of the throughflow time of the compressor and it seems plausible to attribute the lag to unsteady aerodynamic effects within the compressor passages. This is in agreement with the conclusions of Fink (1988), who determined that a lag term on the order of compressor throughflow time was needed for agreement between the predicted and experimental behavior of a compression system in deep surge. Fink also found that a lag term of this order should have a negligible effect on system stability over the range of B -parameter investigated, so it appears that the quasi-steady compressor slope is adequate for predicting the onset of surge.

Another assumption used in the present treatment is that the wheel speed remains constant for perturbations in mass flow and pressure rise. This is not strictly correct because pressure and mass flow perturbations vary the power requirements of the compressor, and hence cause the wheel speed to vary. Fink (1988) assessed this assumption and showed that variable wheel speed had a stabilizing effect on the compression system. The degree of stabilization was shown to be a function of a nondimensional parameter, defined as

$$\text{Wheel inertia parameter} = \frac{2\rho_0 L A_m R^2}{I}$$

where I is the moment of inertia of the wheel and R_T is the tip radius. Using Fink's results, variations in wheel speed were found to have negligible effect on the stability of the compression system used in the present experiments.

An alternative way to address this point is to note that if the wheel speed and pressure fluctuations were strongly coupled, the nondimensional pressure rise and wheel speed variations during mild surge would be roughly the same order. However, for a typical (say 2.5 percent rms) pressure fluctuation, the measured wheel speed fluctuations are only 0.2 percent, an order of magnitude less. The assumption of constant wheel speed is thus adequate for modeling the small perturbation response, and hence linear stability, of the compression system.

Conclusions

Dynamic control using tailored structure has been shown to be effective in suppressing centrifugal compressor surge. The use of a movable plenum wall shifted the surge line to the left roughly 25 percent in flow over a significant portion of the corrected speed range examined. The effectiveness of surge suppression is a function of a set of nondimensional parameters, which govern the aeroelastic coupling of the wall to the compression system dynamics.

The present scheme was found to be robust, suppressing surge over a wide range of operating conditions with no adjustments to the parameters. Use of a movable wall was also demonstrated to lead to suppression of existing (highly nonlinear) surge cycles. In the stabilized region of the compressor map, surge was suppressed with no time average change in the compressor operating point.

The amount of control action (wall motion) required is a function of the nonlinearities in the wall dynamics, such as Coulomb friction and leakage. For the optimized configuration investigated in this research, the nominal limit cycle wall motion in the stabilized region was roughly 0.1 percent of plenum volume, with frequencies near the Helmholtz frequency. Pressure fluctuations in the stabilized region were on the order of 0.5 percent of the mean pressure rise of the compressor.

Time-resolved data were used to verify some of the major assumptions in the modeling of the compression system. Compressor transfer function measurements showed that a quasi-steady compressor characteristic gave a reasonable representation of the instantaneous compressor characteristic slope. These measurements also indicated that the improvement in surge margin is due to modification of the system dynamics, rather than a result of modifying the compressor characteristics by altering the local flow in the compressor. The smallness of the measured wheel speed variations supported the predictions that wheel speed variation would not significantly affect system stability.

In general, all aspects of the experimental investigations confirmed that the lumped parameter model of the compression system provided a useful description of the system dynamics, both with and without the movable plenum wall.

The physical mechanism responsible for the surge suppression with the flexible wall is unsteady energy dissipation due to the wall motion.

The maximum stable compressor characteristic slope is better measure of the effectiveness of this control scheme rather than the minimum stable mass flow coefficient. The steady-state mass flow coefficient has little effect, in an explicit way, on the stability of the compression system with the movable wall, and the dominant influence of mass flow is through the relation between mass flow and compressor slope implied by the compressor characteristic.

Nonlinear solution of the system equations showed the existence of small-amplitude limit cycles in the stabilized region in agreement with measurement. These limit cycles were found to result primarily from Coulomb friction and leakage.

Acknowledgments

This project was conducted under a grant from the Air Force Office of Scientific Research, Dr. J. M. McMichael and Capt. H. Helin, program managers. This support is gratefully acknowledged. Financial support for D. L. Gysling was provided by the Air Force Research in Aero Propulsion Technology (AFRAPT) program, AFSOR-85-0288. The authors also wish to express their appreciation to Dr. G. R. Guenette for his extremely useful technical advice and assistance throughout this research.

References

Bathe, K.-J., and Wilson, E. L., 1976, *Numerical Methods in Finite Element Analysis*, Prentice-Hall, Inc., Englewood Cliffs, NJ, p. 322.

Chen, G. T., 1987, "Active Control of Turbomachinery Instabilities—Initial Calculations and Results," M.S. Thesis, Department of Aeronautics and Astronautics, MIT, Cambridge, MA.

Dean, R. C., Jr., and Young, L. R., 1977, "The Time Domain of Centrifugal Compressor and Pump Stability and Surge," *ASME Journal of Fluids Engineering*, Vol. 99, pp. 53-63.

Emmons, H. W., Pearson, C. E., and Grant, H. P., 1955, "Compressor Surge and Stall Propagation," *ASME Transactions*, Vol. 77, pp. 455-469.

Epstein, A. H., Ffowcs Williams, J. E., and Greitzer, E. M., 1989, "Active Suppression of Compressor Instabilities," *J. Propulsion and Power*, Vol. 5, pp. 204-211.

Ffowcs Williams, F. E., and Huang, X., 1989, "Active Stabilization of Compressor Surge," *J. Fluid Mech.*, Vol. 204, pp. 245-262.

Fink, D. A., 1988, "Surge Dynamics and Unsteady Flow Phenomena in Centrifugal Compressors," Ph.D. Thesis, Department of Aeronautics and Astronautics, MIT, Cambridge, MA.

Gysling, D. L., 1989, "Dynamic Control of Centrifugal Compressor Surge Using Tailored Structure," M.S. Thesis, Department of Aeronautics and Astronautics, MIT, Cambridge, MA.

Greitzer, E. M., 1981, "The Stability of Pumping Systems—The 1980 Freeman Scholar Lecture," *ASME Journal of Fluids Engineering*, Vol. 103, pp. 193-242.

Halfman, R. L., 1962, *Dynamics*, Addison-Wesley Publishing Company, Inc., Reading, MA, p. 335.

Pinsley, J. E., 1988, "Active Control of Centrifugal Compressor Surge," M.S. Thesis, Department of Aeronautics and Astronautics, MIT, Cambridge, MA.

Pinsley, J. E., Guenette, G. R., Epstein, A. H., and Greitzer, E. M., 1991, "Active Stabilization of Centrifugal Compressor Surge," *ASME Journal of Turbomachinery*, Vol. 113, this issue.

Stenning, A. H., 1980, "Rotating Stall and Surge," *ASME Journal of Fluids Engineering*, Vol. 102, pp. 14-20.

APPENDIX

Derivation of the Equations of Motion for the Movable Plenum Wall System

Consider the compression system shown in Fig. 1(b). The following assumptions are used: The flow in the inlet ducting is one-dimensional, incompressible, inviscid, and unsteady; the plenum pressure is spatially uniform and plenum processes are isentropic; the fluid inertia in the throttle is negligible; the compressor follows a quasi-steady characteristic; and the throttle pressure drop mass flow relation is parabolic.

The momentum equation applied to the compressor duct yields

$$P_0 + \Delta P_c - P_p = \frac{L_c}{A_{in}} \frac{d\dot{m}_1}{dt} \quad (A1)$$

where L_c is the equivalent length of the compressor duct. Mass conservation in the plenum yields

$$\dot{m}_1 - \dot{m}_2 = \frac{d(\rho_p V_p)}{dt} \quad (A2)$$

The pressure drop across the throttle can be written in terms of the throttle mass flow as

$$\Delta P_t = \frac{1}{2} \frac{\dot{m}_2^2}{\rho_p A_t^2} \quad (A3)$$

Finally, the motion of the wall is given by

$$m\ddot{q} + c\dot{q} + kq = (P_0 - P_{\text{plenum}})A_p \quad (A4)$$

where q is defined as the position of the wall away from the equilibrium position of the wall.

Writing the fluid dynamic variables as mean ($\bar{\quad}$) plus small perturbations ($\delta \quad$) and linearizing the compressor and throttle characteristics about a time-mean operating point yields equations for the perturbation quantities:

$$\left(\frac{d\Delta P_c}{dm} \right) \delta\dot{m}_1 - \delta P_p = \frac{L_c}{A_{in}} \frac{d(\delta\dot{m}_1)}{dt} \quad (A5)$$

$$\delta\dot{m}_1 - \dot{m}_2 = \frac{\bar{V}_p}{\bar{A}_p} \frac{d\Delta P_p}{dt} + \bar{P}_p A_p \frac{d\delta q}{dt} \quad (A6)$$

In Eq. (A6), the isentropic assumption has been used, and volume change has been expressed as the product of plenum area A_p and perturbation displacement δq .

We introduce the following nondimensional quantities:

$$\phi = \frac{\dot{m}}{\rho_0 A_{in} U} \quad \tau = \omega_H t$$

$$\psi_c = \frac{\Delta P_c}{\frac{1}{2} \rho_0 U^2} \quad B = \frac{U}{2\omega_H L_c}$$

$$\psi_t = \frac{\Delta P_t}{\frac{1}{2} \rho_0 U^2} \quad \delta\eta = \frac{A_p \delta q}{\bar{V}_p}$$

$$\psi = \frac{P_p - P_0}{\frac{1}{2} \rho_0 U^2} \quad M = \frac{U}{\bar{A}_p}$$

Using these equations, Eqs. (A5) and (A6) can be written as

$$\left(\frac{d\psi_c}{d\phi} \right) \delta\phi_1 - \delta\psi = \frac{1}{B} \frac{d\delta\phi_1}{d\tau} \quad (A7)$$

and

$$\delta\phi_1 - \delta\phi_2 = B \frac{\delta\psi}{d\tau} + \bar{P}_p \frac{B}{\rho_0 M^2} \frac{d\delta\eta}{d\tau} \quad (A8)$$

The throttle pressure drop equation can be written as

$$\delta\psi = \frac{\rho_0}{\bar{\rho}_t} \left(\frac{d\psi_t}{d\phi} \right) \delta\phi_2 \quad (A9)$$

$$\delta\psi = \frac{\rho_0}{\bar{\rho}_t} \left(\frac{\bar{\phi}^2}{2\bar{V}_p} \right) \delta\phi_2$$

For the wall motion, we define the following nondimensional control parameters:

$$W = \frac{\rho_0 A_p^2 L_c^2}{m \bar{V}_p}$$

$$\zeta^* = \frac{c}{2m\omega_p}$$

$$Q^* = \frac{\omega_p}{\omega_H}$$

The wall dynamics can then be written in nondimensional form as:

$$\frac{d^2\delta\eta}{d\tau^2} + 2\zeta^* Q^* \frac{d\delta\eta}{d\tau} + Q^{*2} \delta\eta = WB^2 \delta\psi \quad (A10)$$

Using the algebraic relation between $\delta\psi$ and $\delta\phi_1$, the throttle characteristic can be used to eliminate $\delta\psi$ from the set of nondimensional equations. In addition, we can define

$$\delta v = \frac{d\delta\eta}{d\tau}$$

as a nondimensional wall velocity to convert Eq. (A10) into two first-order equations. Rearranging these equations, and making use of Eq. (A9), yields the following stability matrix:

$$\begin{bmatrix} B\left(\frac{d\bar{\psi}_c}{d\bar{\phi}}\right) - s & \frac{2B\bar{\psi}}{\bar{\phi}} & 0 & 0 \\ \frac{1}{B}\frac{\bar{\phi}}{2\bar{\psi}} & -\frac{1}{B2\bar{\psi}} - s & 0 & -\frac{\bar{\rho}_p}{\bar{\rho}} \frac{1}{M^2} \frac{\bar{\phi}}{2\bar{\psi}} \\ 0 & 0 & -s & 1 \\ 0 & WB^2 \frac{2\bar{\psi}}{\bar{\phi}} & -Q^2 & -2\zeta Q - s \end{bmatrix} \begin{bmatrix} \delta\phi_1 \\ \delta\phi_2 \\ \delta\eta \\ \delta v \end{bmatrix} = \begin{bmatrix} 0 \\ 0 \\ 0 \\ 0 \end{bmatrix}$$

The control parameters Q^* and ζ^* are referenced to the Helmholtz frequency of the compression system, which varies slightly with operating conditions. They can be modified so that they remain independent of operating conditions. Thus, substitution of the following corrected control parameters yields the stability matrix given as Eq. (10):

$$Q = Q^* \sqrt{\frac{\rho_0}{\bar{\rho}_p}} \text{ and } \zeta = \zeta^* \sqrt{\frac{P_p}{P_0}}$$

For reference, we also note that expanding the determinant for the 2×2 stability matrix describing the fixed wall compression system leads to the characteristic equation shown below:

$$s^2 + \left[\frac{1}{2\bar{\psi}} B \left(\frac{d\bar{\psi}_c}{d\bar{\phi}} \right) \right] s + \left[1 - \left(\frac{d\bar{\psi}_c}{d\bar{\phi}} \right) \frac{\bar{\rho}}{2\bar{\psi}} \right] = 0$$

(A11)

Dynamic instability occurs when the first term in brackets becomes negative. The condition for this is

$$\left(\frac{d\bar{\psi}_c}{d\bar{\phi}} \right) > -\frac{1}{B^2 \frac{2\bar{\psi}}{\bar{\phi}}}$$

which is the fixed wall stability limit.

Dynamic Control of Rotating Stall in Axial Compressors Using Aeromechanical Feedback

D. Gysling, E.M. Greitzer, J. Dugundji

During the past year, dynamic control of rotating stall in axial flow compressors has been successfully demonstrated. Based on results from a two-dimensional model of the rotating stall dynamics of axial compressors, a device was designed and constructed to extend the stable flow of a single-stage axial flow compressor. This control strategy modifies the unsteady, non-axisymmetric fluid dynamics of the compression system with a circumferential array of discrete jets located axially upstream of the compressor. The amount of high momentum fluid injected upstream of the compressor is regulated by reed valves. The cantilevered reed valves, modeled in their first cantilevered bending mode as mass-spring-damper systems, are driven by unsteady pressure perturbations in the flow field upstream of the compressor. The reed valve dynamics form an aeromechanical feedback loop that determines the coupling between the rotating stall dynamics of the compression system and the high momentum air injected into the face of the compressor.

The basic theory used in the design of this control strategy is similar to the theory used to design the movable IGV control scheme, successfully used to stabilize rotating stall by Paduano (1990) and Haynes (1992). However, several distinct differences exist which will add to the knowledge base for controlling rotating stall in axial flow compressors. The unique features of this control strategy include:

- 1) Aeromechanical (or structural) feedback is employed for the first time.
- 2) The control law used is implemented on a local basis; previous methods have used modal-based control laws.
- 3) Static pressure is used as the sensed variable; previous method have used mass flow as the sensed variable.
- 4) The feedback law used is a second order, in time, dynamic compensator; previous methods have used proportional control laws.

5) High momentum jet actuators are used for the first time.

The effect of dynamic mass injection on the rotating stall dynamics of the compression system were analyzed using the Moore-Greitzer model. The model consists of three basic components: a potential upstream flow field, the compressor (with feedback incorporated), and a rotational downstream flow field. The effect of the dynamic control strategy was incorporated by modifying the pressure rise and mass flow boundary conditions across the compressor.

The high momentum fluid injected upstream of the compressor was assumed to mix out before entering the compressor, thereby modifying the local (around the circumference) total pressure and mass flow entering the compressor. The feedback is incorporated by modeling the reeds' response to non-axisymmetric pressure perturbations in the upstream flow field.

The stability of the compression system was determined using a small perturbation, linearized eigenvalue analysis. With the dynamic control strategy, the stability of the system to non-axisymmetric disturbances is a function of the original compression system parameters plus a set of control parameters. These parameters are:

$\partial\psi/\partial\phi$	slope of compressor speedline
λ, μ	fluid inertia parameters
ϕ	mass flow coefficient
n	harmonic number
W	reed valve mass parameter
Q	reed valve frequency parameter
ξ	reed valve critical damping ratio
ϕ_B	injection velocity parameter

A parameter optimization study was performed which predicted that significant stabilization could be achieved with physically realizable values for the control parameters. Based on these results, a device was designed to match these non-dimensional control parameters for use on the single-stage compressor at the Gas Turbine Lab. The physical device is a steel structure housing 24 discrete reed valves placed on the casing wall immediately upstream of the

compressor. A schematic of the device is shown in Fig. 1. The reed valves were fabricated from graphite epoxy composite material to achieve the low mass and relatively high frequency required by the design study. Additional, non-linear simulations indicated that minimizing the coulomb friction in the reed valve motion was essential. To this end, low friction, adjustable, pneumatic dashpots were used to provide the damping for each reed valve. The high pressure air used for the injection is supplied by a source external to the compressor through a single, variable pressure supply plenum.

The compressor was instrumented to record steady-state and time-resolved measurements. The steady-state data recorded includes compressor pressure rise, mass flow, and wheel speed, and injected mass flow and momentum. A radial traverser is also available to measure the axial velocity distribution and the inlet boundary layer. Additional instrumentation is available for measuring time-resolved pressure, mass flow, and reed valve displacement.

Initial experimental results are as follows. Although the amount of steady-state mass flow injected into the face of the compressor does not explicitly appear in the stability analysis, experimentally it was found to significantly affect the stability boundary of the compression system. This is due to the change in the steady-state pressure rise versus mass flow characteristic resulting from the steady-state mass injection. Thus, in order to isolate the stability improvement due to dynamic feedback, the increase in stable flow range due to dynamic feedback was determined by comparing the stalling flow coefficient with the reed valves rigid to the stalling flow coefficient with the reed valve free to respond to pressure perturbations. The comparison was made with the same amount of steady-state mass injected. Figure 2 shows the stability boundary for the compression system with and without structural feedback. As shown, the stable flow range was increased by 7% in this case. This figure is representative of the largest flow range extension achieved to date.

The two-dimensional theory predicts that increasing the momentum of the injected fluid will increase the range extension. However, as the momentum of the injected fluid is increased, the amount of stabilization due to dynamic feedback decreases. Research is continuing to resolve

this issue.

Time-resolved pressure, mass flow, and reed deflection measurements are currently being studied to further characterize the effects of dynamic mass injection. The time-resolved measurements include:

- 1) stall inception transients
- 2) reed valve deflection / pressure transfer functions
- 3) upstream mass flow / pressure transfer functions
- 4) hub and tip hot-wire traces to determine three-dimensionality of flow field.

Although the effects of the dynamic mass injection control strategy developed in the research have not been fully characterized at this point, initial results show that this control strategy is a viable method to extend the stable flow range of compression systems.

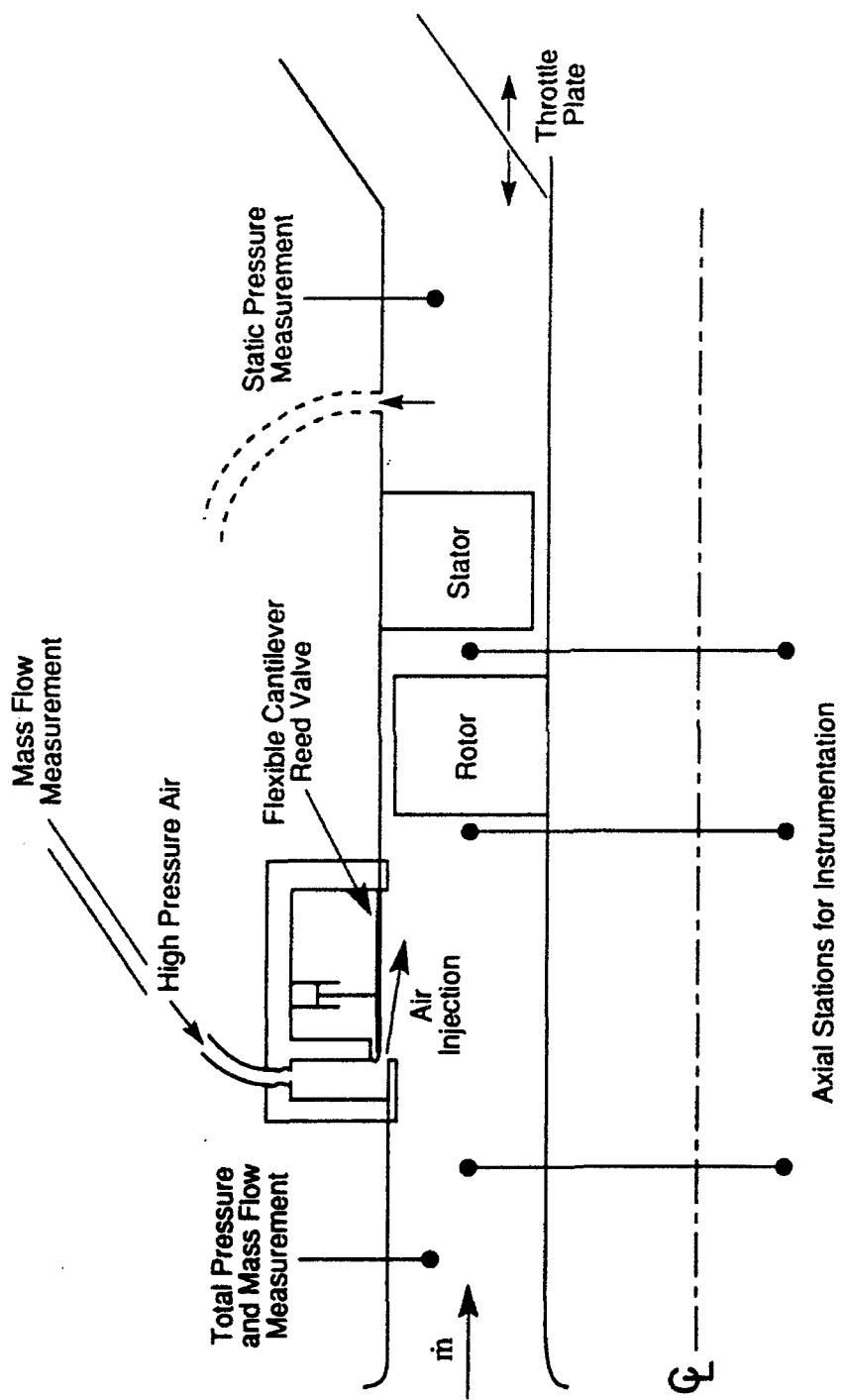


Fig. 1: Structural control experimental setup on a single-stage compressor.

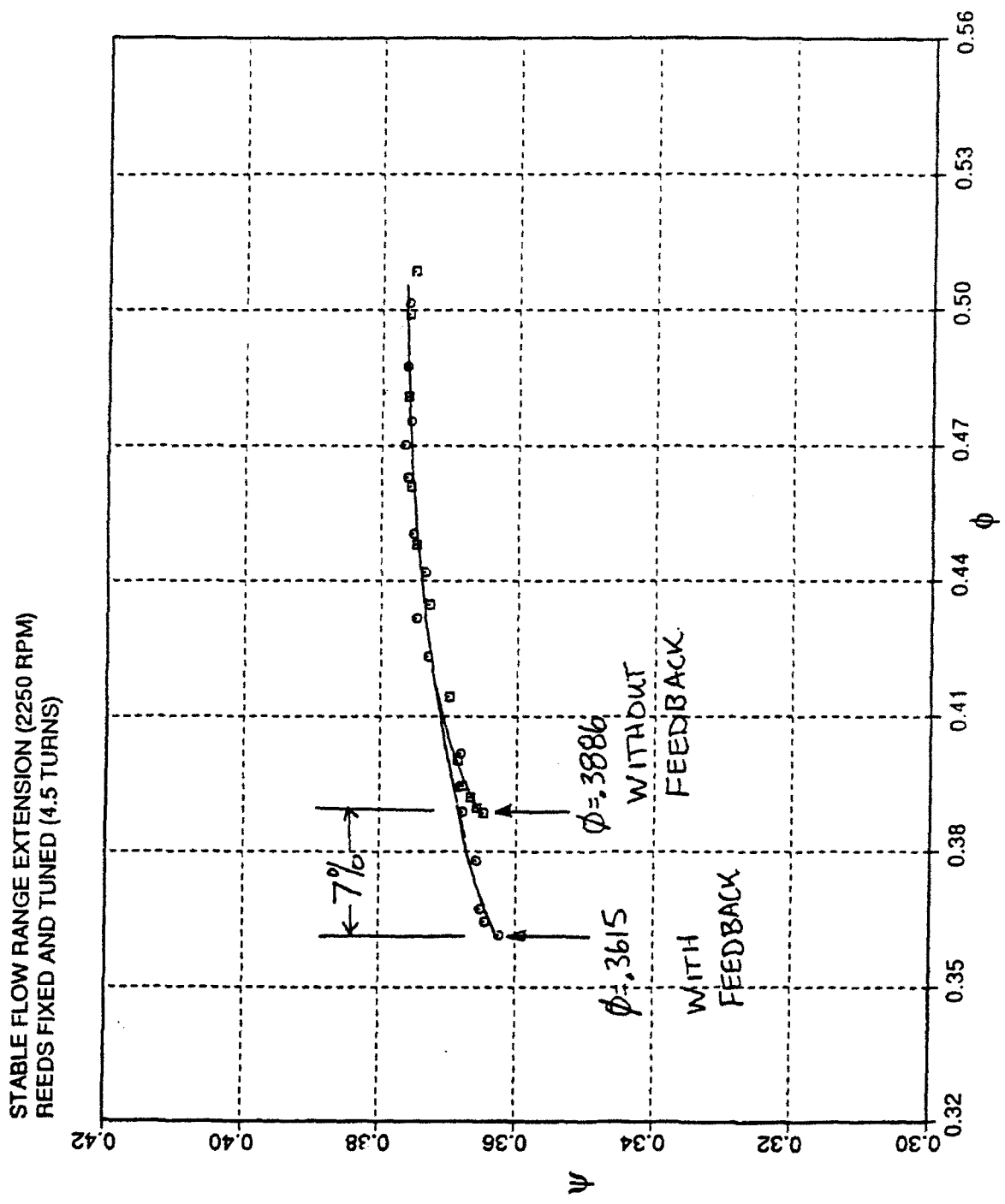


Fig. 2: Measured compressor characteristic with and without structural control.